

Partitioned Algorithms using Vortex Particle Methods for Fluid–Structure Interaction of Thin-walled Flexible Structures

DISSERTATION

zur Erlangung des akademischen Grades
Doktor-Ingenieur (Dr.-Ing.)

an der Fakultät Bauingenieurwesen
der Bauhaus-Universität Weimar

vorgelegt von
Samir Chawdhury
geboren am 03 Juni 1984
in Netrokona, Bangladesch

Mentor: Prof. Dr. Guido Morgenthal

Weimar, June 2020

EHRENWÖRTLICHE ERKLÄRUNG

Ich erkläre hiermit ehrenwörtlich, dass ich die vorliegende Arbeit ohne unzulässige Hilfe Dritter und ohne Benutzung anderer als der angegebenen Hilfsmittel angefertigt habe. Die aus anderen Quellen direkt oder indirekt übernommenen Daten und Konzepte sind unter Angabe der Quelle gekennzeichnet.

Bei der Auswahl und Auswertung folgenden Materials haben mir die nachstehend aufgeführten Personen in der jeweils beschriebenen Weise entgeltlich/unentgeltlich geholfen:

Keine.

Weitere Personen waren an der inhaltlich-materiellen Erstellung der vorliegenden Arbeit nicht beteiligt. Insbesondere habe ich hierfür nicht die entgeltliche Hilfe von Vermittlungs- bzw. Beratungsdiensten (Promotionsberater oder anderer Personen) in Anspruch genommen. Niemand hat von mir unmittelbar oder mittelbar geldwerte Leistungen für Arbeiten erhalten, die im Zusammenhang mit dem Inhalt der vorgelegten Dissertation stehen.

Die Arbeit wurde bisher weder im In- noch im Ausland in gleicher oder ähnlicher Form einer anderen Prüfungsbehörde vorgelegt.

Ich versichere ehrenwörtlich, dass ich nach bestem Wissen die reine Wahrheit gesagt und nichts verschwiegen habe.

Weimar, den 30.06.2020

Signature

.....

Samir Chawdhury

Acknowledgements

Abstract

Fluid–structure interaction (FSI) is a multiphysics study of mutual interaction between deformable structure and surrounding or internal fluid flow. Proper understanding of FSI phenomena is crucial in many engineering fields. The increasing trend of extremely flexible and lightweight structures, such as long-span cable-supported bridges, super-tall towers and chimneys, large membrane roofs, requires accurate prediction of wind–structure interaction in the design process to avoid potential damage of important structures.

The grid-free Vortex Particle Method (VPM) has been established as an accurate and efficient computational fluid dynamic (CFD) simulation technique to model flow around complex geometries. Existing FSI models of VPM have been in the context of two-dimensional (2D) and pseudo-three-dimensional (pseudo-3D) multi-slice formulations. They are based on linear structural behaviour and limited to rigid cross-sections only. In this study, the VPM is extended with new developments to enhance its applicability for coupled FSI simulations of thin-walled flexible structures. The partitioned algorithms are employed to implement the coupling of flow solvers, 2D and pseudo-3D VPM, with advanced structural models.

Initially, the 2D VPM is coupled with corotational finite element formulation, which is to include geometric nonlinear effects for large-displacement FSI of thin plate systems. Fundamentally, at each simulation step, the fluid forces are projected from the surface panels to the FE nodes at the mid-surface of the thin body. The nodal displacements are projected as feedback to the surface panels to update the required boundary conditions. The coupled solver is validated on benchmark large-displacement FSI problems such as the flag-type flapping of cantilever plates in axial flow and Kármán vortex street. The validated extension of 2D VPM is successfully employed for analysing diverse and complex aeroelastic interactions of different thin-walled systems such as a) inverted and T-shaped cantilevers with/without tip mass, b) flexible membrane systems, and c) umbrella-type structures.

Secondly, the pseudo-3D VPM is extended similarly according to the procedure of 2D VPM, however, in a slice-wise manner. Importantly, the pseudo-3D VPM is proposed for FSI analysis of linear shell-structures. Modal superposition technique is applied because of its computational efficiency. The novelty is the inclusion of 3D natural vibration modes in the structural analysis. The validated method is utilised for aeroelastic interaction of shell-type structures such as large membrane roof and solar chimneys.

Furthermore, two new extensions of 2D VPM are developed for modelling of inflow fluctuations that can be used as inflow condition in FSI analysis. While the first extension allows modelling of low-frequency pulsating incoming flow, the second extension reproduces turbulent wakes from bluff bodies. Finally, the FSI model of 2D VPM is applied exclusively to a distinct application field: small-scale aeroelastic energy harvesting. The aero-electromechanically coupled behaviour is modelled for different thin and flexible prototype harvesters. An analysis framework is shown useful for optimisation of harvester performance for different inflow conditions. This work indicates that the developed numerical techniques are beneficial not only for fundamental investigations but also for aeroelastic interaction of large-scale thin-walled mega structures.

Kurzfassung

Die Fluid–Struktur-Kopplung, FSK (oder FSI im internationalen Kontext) ist ein multiphysikalischer Effekt der gegenseitigen Wechselwirkung zwischen verformbarer Struktur und umgebender oder interner Fluidströmung. Das richtige Verständnis der FSI-Phänomene ist in vielen technischen Bereichen von entscheidender Bedeutung. Der zunehmende Trend zu extrem flexiblen und leichten Strukturen, wie z.B. weitgespannte seilunterstützte Brücken, superhohe Türme und Schornsteine, große Membrandächer, erfordert eine genaue Vorhersage der Wind–Struktur-Kopplung (WSK) im Entwurfsprozess, um potenzielle Schäden an wichtigen Strukturen zu vermeiden.

Die gitterfreie Vortex-Partikel-Methode (VPM) wurde als genaue und effiziente numerischen Strömungsmechanik (CFD im internationalen Kontext) Simulationstechnik zur Modellierung der Strömung um komplexe Geometrien herum etabliert. Bestehende FSI-Modelle der VPM wurden im Zusammenhang mit zweidimensionalen (2D) und pseudodreidimensionalen (Pseudo-3D) Mehrschichtformulierungen erstellt. Sie basieren auf linearem Strukturverhalten und sind nur auf starre Querschnitte beschränkt. In dieser Studie wird das VPM um neue Entwicklungen erweitert, um seine Anwendbarkeit für gekoppelte FSI-Simulationen von dünnwandigen flexiblen Strukturen zu verbessern. Die partitionierten Algorithmen werden eingesetzt, um die Kopplung von Strömungslösern, 2D und Pseudo-3D VPM, mit fortschrittlichen Strukturmodellen zu implementieren.

Zunächst wird der 2D VPM mit einer korotationalen Finite-Elemente-Formulierung gekoppelt, die geometrisch nichtlineare Effekte für FSI mit großer Verschiebung von dünnen Plattensystemen beinhalten soll. Grundsätzlich werden bei jedem Simulationsschritt die Fluidkräfte von den Oberflächenplatten auf die FE-Knoten in der Mittelfläche des dünnen Körpers projiziert. Die Knotenverschiebungen werden als Rückkopplung auf die Oberflächenplatten projiziert, um die erforderlichen Randbedingungen zu aktualisieren. Der gekoppelte Solver wird anhand von FSK-Benchmark-Problemen mit großen Verschiebungen validiert, wie z.B. das fahnenartige Flattern von Cantilever-Platten in axialer Strömung und Kármán Wirbelstraße. Die validierte Erweiterung von 2D VPM wird erfolgreich zur Analyse vielfältiger und komplexer aeroelastischer Wechselwirkungen verschiedener dünnwandiger Systeme eingesetzt, wie z.B. a) invertierte und T-förmige Cantilever mit/ohne Spitzenmasse, b) flexible Membransysteme und c) schirmartige Strukturen.

Zweitens wird die Pseudo-3D-VPM nach dem Verfahren der 2D-VPM in ähnlicher Weise erweitert, jedoch scheibenweise. Wichtig ist, dass die Pseudo-3D VPM für die FSI-Analyse von linearen Schalenstrukturen vorgeschlagen wird. Die modale Überlagerungstechnik wird wegen ihrer rechnerischen Effizienz angewendet. Das Novum ist die Einbeziehung von 3D-Eigenschwingungsmoden in die Strukturanalyse. Die validierte Methode wird für die aeroelastische Wechselwirkung von schalenartigen Strukturen wie großen Membrandächern und Solarkaminen eingesetzt.

Darüber hinaus werden zwei neue Erweiterungen von 2D VPM zur Modellierung von Einströmschwankungen entwickelt, die als Einströmbedingung in der FSK-Analyse verwendet werden können. Während die erste Erweiterung die Modellierung von niederfrequent pulsierender Einströmung ermöglicht, reproduziert die zweite Erweiterung turbulente Nachläufe von Steilkörpern. Schließlich wird das FSI-Modell der 2D-VPM ausschließlich auf ein bestimmtes Anwendungsgebiet angewandt: die kleinräumige aeroelastische Energiegewinnung. Das aero-elektro-mechanisch gekoppelte Verhalten wird für verschiedene dünne und flexible

Prototyp-Harvester modelliert. Es wird ein Analyserahmen gezeigt, der für die Optimierung der Harvesterleistung für verschiedene Einströmbedingungen nützlich ist. Diese Arbeit zeigt, dass die entwickelten numerischen Techniken nicht nur für grundlegende Untersuchungen, sondern auch für die aeroelastische Wechselwirkung großflächiger dünnwandiger Megastrukturen von Nutzen sind.

Contents

Acknowledgements	V
Abstract	VII
Table of Contents	XI
List of figures	XV
List of tables	XXIII
1 Introduction	1
1.1 Background and motivation	1
1.2 Objectives, methodologies and contributions	3
1.3 Outline of the thesis	5
2 Wind effects on structures	7
2.1 Introduction	7
2.2 Atmospheric boundary layer	7
2.3 Bluff body aerodynamics	9
2.4 Aeroelastic vibration phenomena	10
2.4.1 Limited amplitudes phenomena	11
2.4.2 Divergent amplitudes phenomena	12
2.5 Nonlinear aeroelasticity	13
2.6 Summary	14
3 Numerical methods for fluid–structure interaction simulation	15
3.1 Introduction	15
3.2 Coupling mechanisms for FSI simulations	16
3.2.1 Monolithic approaches	16
3.2.2 Partitioned approaches	17
3.2.3 Conforming and non-conforming mesh	18
3.2.4 Large displacement FSI simulations	18
3.3 Numerical analysis of fluid and structure	19
3.3.1 Modelling of fluid motion	19
3.3.2 Structural analysis using finite element methods	20
3.4 The Vortex Particle Method	20
3.4.1 Governing equations of fluid motion	21
3.4.2 The Boundary Element Method	23
3.5 Application of Vortex methods	25
3.5.1 Aerodynamic analysis of bluff bodies	25

3.5.2	Studies of deformable bodies using vortex methods	27
3.6	Summary	28
4	Partitioned extensions using Vortex Particle Methods for FSI simulations	29
4.1	Introduction	29
4.2	A large-displacement FSI model using 2D VPM	30
4.2.1	Modelling of flow around thin and deformable geometry	30
4.2.2	Nonlinear finite element analysis using corotational beam	34
4.2.3	Presentation of immersed thin structures in the fluid domain	38
4.2.4	Calculation of the nodal forces for the structure analysis	39
4.2.5	Projection of motion from mid-surface to boundary panels	41
4.2.6	Fluid–structure coupling	43
4.2.7	Validation of the enforcement of velocity boundary condition	44
4.3	The pseudo-3D VPM for FSI simulations of flexible thin-shell structures	50
4.3.1	Multi-slice modelling of flow around deformable geometry	50
4.3.2	A linear structural model for pseudo-3D multi-slice solver	52
4.3.3	Slice-wise presentation of thin structures in fluid flow	54
4.3.4	Slice-wise fluid–structure coupling	57
4.4	A simplified aeroelectromechanical coupled model	57
4.5	Methods of inflow fluctuations for FSI simulation	58
4.6	Summary	59
5	Fluid–structure interaction simulations of thin-walled structures	61
5.1	Introduction	61
5.2	Validation of the two-dimensional coupled solver	61
5.2.1	Flexible cantilever in von Kármán vortex street	61
5.2.2	Flutter instability of cantilevered flexible plate	66
5.2.3	Aeroelastic motion of inverted flexible cantilever plate	68
5.3	Rotational flutter of inverted T-shaped cantilever with tip mass	73
5.4	Aeroelastic motion of different inverted cantilevers	74
5.5	Coupled interactions of flexible membrane systems	78
5.5.1	Flow over a building with elastic membrane roof	78
5.5.2	Aeroelastic motion of flexible 2D membrane umbrellas	84
5.6	Validation of pseudo-3D VPM for FSI simulation	92
5.6.1	Flexible cantilever in von Kármán vortex street	92
5.6.2	Identification of analytical critical flow speed of inverted flag	96
5.6.3	Flapping of skewed inverted cantilever plate	98
5.7	Vortex-induced vibration of clamped circular pipes using pseudo-3D VPM	100
5.7.1	System description and the resonance wind speed	100
5.7.2	Single-slice VIV analysis using 2D SDOF model	102
5.7.3	VIV of clamped circular pipe using pseudo-3D VPM	103
5.7.4	Ovalling response of circular pipe at higher wind speeds	106
5.8	Aeroelastic analysis of a thin-walled membrane roof	109
5.9	Pseudo-3D aeroelastic analysis of solar chimney	116
5.9.1	The solar chimney power plants	116

5.9.2	Loads on solar chimneys and stability concerns	117
5.9.3	Analyses of aeroelastic response of 1500 m solar chimneys	118
5.10	Summary	128
6	Aeroelastic energy harvesting	129
6.1	Introduction	129
6.2	Vibration energy harvesting	130
6.2.1	Background	130
6.2.2	Conversion mechanisms	130
6.3	Brief review on aeroelastic energy harvesting	132
6.3.1	Flutter/airfoil-based aeroelastic energy harvesters	132
6.3.2	Energy harvesting from vortex-induced vibration	133
6.3.3	Galloping-based energy harvesters	133
6.3.4	Harvesters based on wake galloping	134
6.4	Torsional flutter-based T-shaped energy harvesters	134
6.4.1	Torsional flutter	134
6.4.2	A reference T-shaped electromagnetic energy harvester	135
6.4.3	Identification of flutter wind speed of T-shaped harvester	135
6.5	Modelling and simulation of T-shaped electromagnetic energy harvesters . . .	139
6.5.1	Electrical damping effects in equation of motion	140
6.5.2	Modelling of energy outputs and validation	141
6.6	Physical optimization of T-shaped energy harvesters	144
6.6.1	Influential electrical parameters	145
6.6.2	Effect of physical shape on flutter-based T-shaped harvesters	146
6.7	A framework for optimisation of electrical parameters as preliminary study . .	148
6.7.1	Preliminary analysis of electromagnetic energy harvesters	149
6.7.2	Studies on different cantilevers for preliminary assessment of piezoelec- tric harvesting	152
6.8	Summary	155
7	Modelling the effect of free stream fluctuations on aeroelastic interactions	157
7.1	Introduction	157
7.2	Pulsating incoming flow	158
7.2.1	Background	158
7.2.2	A New Numerical Technique in VPM for Pulsating Flow	158
7.2.3	Flow fluctuations using vorticity carrying particles	161
7.2.4	Quality assessment	163
7.2.5	Convergence of the proposed numerical scheme	165
7.2.6	The influence of flow characteristics	168
7.2.7	Influence of periodic fluctuations on T-shaped harvesters	168
7.2.8	Application of pulsating flow on flexible T-shaped harvester	174
7.2.9	Pulsating flow on flexible cantilever in Kármán vortex street	176
7.2.10	Summary	178
7.3	The flow reproduction method	178
7.3.1	Introduction	178

7.3.2	A new numerical method for reproduction of flow simulation	179
7.3.3	Validation study and efficiency of flow reproduction	182
7.3.4	Quality assessment	190
7.3.5	Wake buffeting analysis	192
7.3.6	Aeroelastic interaction of T-shaped harvester in fluctuating wind	194
7.3.7	Summary	196
8	Conclusions	199
8.1	Summary	199
8.2	Conclusions	202
8.3	Recommendations for future studies	204

List of Figures

1.1	The Tacoma Narrows Bridge before (left) and after the collapse (right) (picture courtesy: University of Washington Libraries, Special Collections).	1
1.2	The collapse of three tall cooling towers in Ferrybridge/England (left), the moment of collapse of one tower	2
2.1	Alan Davenport wind loading chain.	7
2.2	Flow around streamlined body (left) and bluff body (right).	9
2.3	Schematic of structural response against wind speed.	11
3.1	Schematic of the boundary element discretization for a circular cross-section. The surface vortex sheet strength	23
3.2	The simulation of flow around static bluff bodies using VPM: (a) flat plate at $Re = 10^3$, (b) flat plate at $Re = 10^4$, (c) circular cylinder at	26
3.3	Extensions on dynamic analysis models within the existing framework of in-house CFD solver based on VPM	27
4.1	A partial schematic presentation of the boundary element discretisation of a thin cantilever flexible plate of thickness h , which is flapping	31
4.2	The outlook of coupled FSI algorithm only from the 2D vortex particle method.	32
4.3	The schematic presentation of structural nodes and elements at the mid-surface of the deformed thin plate, which has been shown	35
4.4	Reference and corotational configuration of a typical beam element.	36
4.5	Identification of projection element for each boundary panel and the sign of surface normal vector to the element.	39
4.6	Projection of fluid pressure from the boundary panels to the structural nodes: (a) the schematic shows the projection	41
4.7	Update of the geometry based on the projection of grid points of boundary panels due to the motion at the mid-surface of the thin elements.	42
4.8	Projection of the velocity components from the nodal displacements at n_1 and n_2 to the control point p of a panel.	43
4.9	Flowchart of 2D coupled VPM for large-displacement FSI simulations.	45
4.10	Flow around an inclined flat plate in free stream flow considering static and imposed oscillation	46
4.11	Comparison of the resultant flow field U at different time in case of static and forced oscillation analyses while the numerical models used are of particular concern	47
4.12	Comparison of the velocity components U_x and U_y at different monitored locations	48

4.13	Comparison of the velocity field due to the rotational motion of flat plate in uniform flow	49
4.14	Schematic description of newly extended pseudo-3D VPM for multi-slice FSI simulation of thin-walled shell-type flexible structures	51
4.15	Identification of projection element for each boundary panel and the sign of surface normal vector corresponding to local axis of the projecting element, as shown	55
4.16	Flowchart representation of coupled numerical algorithm for pseudo-3D multi-slice simulations.	58
5.1	The interaction between the vortex shedding of rigid square section with the attached flexible cantilever plate	62
5.2	Convergence study of finite element discretisation: 1st natural vibration frequency is compared based on the number of element	63
5.3	The particle maps (left of (a-c)) and corresponding flow fields (right of (a-c)) are shown for different	64
5.4	The simulation of cantilever beam under the vortex shedding from upstream square: (a) the time history of the vertical	65
5.5	Study on the frequency of response of cantilever tip: (a) frequency spectrum of the displacement time history	65
5.6	The flutter-induced flapping of a cantilevered flexible plate: (a) the plate in conventional flag configuration under axial flow	67
5.7	The instability and post-critical vibrations of a flag-type cantilever plate in axial flow	69
5.8	Schematic configuration of a cantilever plate (length $L \times$ height H) is shown in inverted flag	70
5.9	Schematic presentation of the deflected modes for an inverted flag with the increase in incoming flow speed	70
5.10	Coupled FSI simulations of the inverted flag under axial flow	72
5.11	Visualisation of the flapping of inverted cantilever plate: (a-b) shows the particle map (left) and corresponding instantaneous	73
5.12	The comparison of the vertical tip displacement of the simulated T-shaped cantilever to identify the critical flutter wind speed.	74
5.13	Flow visualisation around moving T-shaped inverted cantilever under free stream flow	75
5.14	Schematic presentation of different inverted cantilever systems in axial flow: The effect of the tip mass and vertical tip plate	76
5.15	Comparison of maximum vertical tip displacement (left) and response frequency (right) of three specific systems under different wind speeds.	77
5.16	The fluttering modes of inverted T-shaped cantilever beam at different wind speeds: 6 m/s (left), 8 m/s (middle), and 25 m/s (right).	77
5.17	The schematic of uniform flow over a membrane roof of a building.	78
5.18	The flow around rigid building and static membrane roof deformed under 32% dead load: (a) the discretisation of surface panels	80
5.19	Coupled simulation of the membrane roof at flow velocity 13.75 m/s: (top) the vertical displacement at the centre of the roof	81

5.20	Coupled simulation of the membrane roof at 13.75 m/s: (a-b) the particle map (top) and the flow field (bottom) around	81
5.21	The effect of gravity forces on system identification: comparison of membrane displacement at centre and lowest bending frequency	82
5.22	Free vibration analyses are performed using a geometrically nonlinear finite element model of a membrane roof. Two loading scenarios are considered . . .	83
5.23	Coupled analysis of the membrane roof of a building under different flow velocities: the time history of the vertical displacement	85
5.24	A schematic presentation of two-span membrane system under uniform flow. .	86
5.25	The convecting particles in free stream flow of 10 m/s around the membrane roof.	86
5.26	Aeroelastic analysis of two-span membrane roof with a roller-type central support (a); the coupled simulations are performed	87
5.27	Aeroelastic response of two-span membrane roof with a hinged-type central support (a); the coupled simulations are performed	88
5.28	System configuration for the flow over a membrane roof.	89
5.29	Geometrically nonlinear finite element model of membrane umbrella for eigenvalue analysis: (a) the modelled system, (b) steel frame	89
5.30	Aeroelastic response of two-span membrane roof under different wind velocities: (a) 10 m/s, (b) 20 m/s, and (c) 30 m/s. For each wind speed	90
5.31	Particle maps influenced by the sequential motion of the membrane at 30 m/s.	91
5.32	The trajectories of nodal response for the membrane and steel frame. The red dotted lines show the original position of the structural nodes.	92
5.33	The coupled response of the membrane supports at 30 m/s: (a) left support, (b) centre support, and (c) right support.	93
5.34	The pseudo-3D VPM analysis: the interaction between a flexible cantilever beam and vortex shedding from attached rigid square cylinder	94
5.35	The schematic shows the system discretisation of the system in each simulation slice. The surface of the rigid square and flexible plate is discretised	94
5.36	The multi-slice visualisation of flexible cantilever plate in Kármán vortex street: (top) the particle maps, and (bottom) the velocity	95
5.37	The tip displacement of the cantilever plate at the mid-slice ($\xi_{z_i} = 0.5$) position (left), and the normalized frequency	96
5.38	Schematic presentation of 7-slice simulation: the flapping of inverted cantilever plate.	96
5.39	Normalized natural vibration modes and frequencies of the reference inverted cantilever plate model	97
5.40	The vortex street around the the cantilever plate at different slices due to the free stream flow.	97
5.41	The vertical tip displacement of the inverted cantilever plate at the central simulation slice ($\xi_z = 0.5$) under different dimensional	98
5.42	Schematic presentation of a skewed inverted cantilever for pseudo-3D VPM analysis: (a) the modification over the reference inverted	99
5.43	Normalized natural vibration modes and frequencies of the skewed inverted cantilever plate model	99

5.44	Pseudo-3D VPM analysis of a skewed inverted cantilever: the time histories of tip displacements	100
5.45	Vortex-induced vibration analysis of a both-end clamped circular pipe using 7-slice pseudo-3D VPM with flexible formulation:	101
5.46	The finite element modelling of the both-end clamped circular pipe and the natural vibration modes associated	102
5.47	Simulation of flow passed a static circular section: (a) the shedding of vortices behind a static circular cylinder at	103
5.48	Single-slice VIV analysis of a rigid circular section using 2D VPM with SDOF model: the normalized vertical displacement of the circular pipe	104
5.49	A 2D single-slice coupled FSI simulations of circular cylinder: (a) the peak vertical response and (b) vortex shedding frequencies at different flow velocities.	105
5.50	Pseudo-3D multi-slice simulation of a both end clamped circular pipe: the instantaneous flow fields around the circular cylinders at each slices	106
5.51	Multi-slice VIV analysis of flexible and long circular cylinder using pseudo-3D VPM with MDOF model: the normalized vertical	107
5.52	The shell buckling at the midspan of circular pipe is shown for two different phases under wind speed	108
5.53	The superposition of the surface displacements at the midspan ($\xi_z = 0.5$) of the circular pipe under the free stream wind velocities	109
5.54	Pseudo-3D multi-slice VPM model for aeroelastic coupled simulation of the flexible and long circular pipe under 45 m/s	110
5.55	The collapse of AFAS football stadium in Alkmaar, Netherlands due to strong wind (Picture courtesy: BBC sports, 10 th August, 2019).	111
5.56	Schematic configuration of a membrane roof system under free stream flow U_∞ . The roof is considered curved in a parabolic way	111
5.57	The FE model of the cantilever curved roof: (a) the thin roof is modelled by flexible membrane which is supported by a steel frame	113
5.58	Instantaneous particle map of pseudo-3D roof system under laminar flow of 30 m/s.	113
5.59	The pseudo-3D coupled simulation of the membrane roof: (a) the time histories of tip displacement at different slices of the roof under wind speed of 30 m/s	114
5.60	The pseudo-3D coupled simulation of the membrane roof: (a) the time histories of tip displacement at different slices of the roof under wind speed of 40 m/s	115
5.61	The free vibration analysis of the roof after the imitation of LCO at 40 m/s: (a) the time histories of tip displacement, and (b) the frequencies	116
5.62	Schematic solar chimney power plant.	117
5.63	Variants of solar chimneys of different height.	118
5.64	Details of a 1000 m solar chimney.	119
5.65	The finite element modelling of 1500 m tall solar chimneys with 3D and top views: (left) the system without any stiffening, (right) the stiffening	121
5.66	Analysis of the finite element model of 1500 m tall solar chimney (hollow configuration): the natural vibration modes and frequencies	122
5.67	Pseudo-3D aeroelastic analysis of 1500 m tall solar chimney (hollow configuration) under the wind speed of 30 m/s	123

5.68	Comparison of relative horizontal and vertical displacements at the top slice considering the monitored nodes	124
5.69	Analysis of the finite element model of 1500 m tall solar chimney (with PT tendon at regular interval): the natural vibration modes and frequencies	125
5.70	Aeroelastic response of a 1500 m tall solar chimney at wind speed of 70 m/s (stiffened SC): the time histories of horizontal	126
5.71	The aeroelastic response of 1500 m tall solar chimney under the wind speed of 70 m/s.	126
5.72	Aeroelastic analyses of 1500 m solar chimney at different wind speeds: comparison of horizontal and vertical response time histories	127
6.1	Schematic representation of the energy harvesting: (a) piezoelectric harvester, and (b) electromagnetic generator.	130
6.2	Schematic purely rotational motion of a bridge deck.	134
6.3	Electromagnetic energy harvesting from fluttering response of T-shaped cantilever systems: (a) the experimental wind tunnel set-up of a prototype T-shaped electromagnetic energy harvester	136
6.4	Modeling of T-shaped cantilever harvester: (a) the actual deformed shape of the flexible harvester	137
6.5	The flutter derivative A_2^* of the cantilever harvester obtained from forced vibration simulation	137
6.6	The use of simplified rigid beam model to identify the critical flutter wind speed based on the vertical tip displacement of the T-shaped harvester.	138
6.7	The particle maps at wind speed 5 m/s in case of simplified rigid beam model.	138
6.8	Discretisation of the T-shaped cantilever harvester: (top) the discretisation scheme of the cantilever system for the flow solver and structural solver together	139
6.9	Coupled simulation of flexible T-shaped cantilever system: the flow fields around the deformed body are shown for sequential three vibration phases.	140
6.10	Fully coupled simulation of the T-shaped system under different wind speeds: Identification of critical onset flutter wind speed based on the aeroelastic coupled response	140
6.11	The damping of the prototype harvester: (top) total damping of the harvester estimated in reference study	142
6.12	Comparison of the time histories of the tip responses (left) and predicted voltage outputs of the harvester considering different electrical resistances	143
6.13	Comparison of the energy outputs of the reference prototype T-shaped harvester under different wind speeds and electrical resistances	144
6.14	Identification of critical flutter onset load resistance (R_L) of the prototype harvester: critical R_L identified based on	145
6.15	The influence of vertical plate height H_{vp} on power output of reference T-shaped harvester: (a) the reference harvester, (b) the modified harvester	146
6.16	Modification in length and thickness of the reference T-shaped harvester, and corresponding changes in dynamic properties and electrical damping ratios	147
6.17	Comparison of the modelled power output of the studied harvesters along with the reference harvester under the wind speed of 8 m/s and load resistance	148
6.18	Comparison of influential response parameters of T-shaped cantilever with tip mass under different incoming flow	149

6.19	The average peak vertical tip displacements (a) and response frequency (b) of the T-shaped cantilever	150
6.20	The predicted power outputs of T-shaped cantilever harvester are compared in (left) and (right) for different electrical damping under U_∞ of 10 m/s and 15 m/s.	150
6.21	The electrical damping for different coupling coefficients $Nl\beta$ and load resistances R_L considering $R_C = 300 \Omega$	151
6.22	Coupled analysis of a geometrically optimized T-shaped harvester under different wind speeds	152
6.23	Schematic representation of piezoelectric energy harvesting from the vibration of cantilever beams under	152
6.24	Analysing the potential of piezoelectric energy harvesting of different cantilever systems for a wide range of wind speeds	153
6.25	Preliminary investigation on the potential of piezoelectric energy harvesting of different cantilever systems	154
7.1	The schematic of a proposed numerical scheme for the simulation of pulsating incoming flow within the framework	159
7.2	Study on the induced velocity field due to the regular seeding of the particles: (a) the discrete-time histories	162
7.3	Periodic flow fluctuations by releasing predefined vortex particles ($u_m/U_\infty = 0.15$, $fL/U_\infty = 0.1042$):	164
7.4	Quality assessment of the modelled periodic flow that has been presented . . .	166
7.5	Convergence study to validate the proposed numerical scheme by simulating a target sinusoidal flow	167
7.6	The influence of the number of particles (N_P) on the time histories of particle strength	167
7.7	The quality of the modelled flow is presented with respect to the targeted peak velocity amplitude and the frequency of flow fluctuations.	169
7.8	Dynamic motion of the harvester under steady and periodic incoming flow: comparison of the incoming field and the flow field	171
7.9	Study on the dynamic motion of the harvester under steady U_∞ and periodic incoming flow	172
7.10	Comparison of the vertical displacements of the modelled harvester under steady U_∞ and periodic incoming flow	173
7.11	The effect of the fluctuation frequency on the motion of modelled harvester: the envelopes are compared for vertical displacement under	174
7.12	The dynamic motion of the harvester under periodic flow of high fluctuations at very low frequency	175
7.13	The study on flexible T-shaped harvester under pulsating flow, which is composed of three different low frequencies	176
7.14	Study on the influence of pulsating flow on Kármán vortex street and further on coupled response of flexible cantilever: (a) schematic problem	177
7.15	Flexible cantilever response in Kármán vortex street influenced by low frequency periodic flow	177
7.16	Schematic of flow reproduction method: An upstream section ($B_1 \times D_1$) in free stream flow U_∞ , a downstream section ($B_2 \times D_2$) for wake buffeting . . .	179

7.17	Circulation around a typical square sampling-cell from the velocity sampling system	180
7.18	The reproduction simulation of flow past a square section by sequential seeding of precalculated vortex particles into the free stream flow: The comparison of .	183
7.19	Convergence study of FRM: The original flow field (a) is reproduced in four different scenarios by releasing	185
7.20	Computationally effective techniques in flow reproductions: Implementation of particle remeshing in flow reproduction	186
7.21	The influences of strength reduction factor ($\alpha_{r,f}$) on the quality of flow reproduction based on the comparison of characteristic flow profiles	188
7.22	The comparison of instantaneous fluctuating velocity components $u(t)$ and $w(t)$	189
7.23	Spectrum of time history of fluctuating velocity components $u(t)$ (left) and $w(t)$ (right) from the signals shown in Fig. 7.22.	189
7.24	Reproduction of simulations of different flow phenomena	190
7.25	The reproduced flow quality influenced by the location of the velocity sampling system or the particle release location (l_r) based on characteristic flow profiles	191
7.26	The effect of computationally effective techniques on the quality of flow reproduction based on the comparison	192
7.27	Normalized spectrum of the lift coefficient time history: the upstream square section in the original simulation at Reynolds number $Re = 500$	193
7.28	Dynamic simulations of the downstream section under different inflow conditions	193
7.29	Fluctuating velocity components of reproduced wakes from upstream bodies: (left) velocity time history, and (right) frequency spectrum.	195
7.30	Coupled simulation of flexible harvester in the reproduced wakes: (a) instantaneous particle map and flow field around	195
7.31	Fluctuating velocity components of random free-stream turbulence: (left) velocity time history, and (right) frequency spectrum.	196
7.32	Coupled simulation of flexible harvester in the free-stream random turbulent flow: (a) instantaneous particle map and flow field around	197

List of Tables

1.1	The FSI models are summarized based on the combination of coupling between fluid and structural solver and the incoming flow conditions.	6
4.1	Numerical parameters: the forced oscillation of an inclined flat plate.	46
5.1	Benchmark FSI problem of aeroelastic motion of an elastic cantilever attached to a square bluff body	62
5.2	Benchmark FSI problem of aeroelastic motion of an elastic cantilever attached to a square bluff body: numerical parameters	63
5.3	Comparison of current results with those in the open literature for the elastic flexible cantilever	66
5.4	Physical parameters of a cantilevered flexible plate in axial flow (mass ratio $\mu = 0.5$).	67
5.5	The flapping of cantilever plate in conventional flag configuration: numerical parameters for 2D coupled VPM analysis.	68
5.6	The physical parameters of the reference inverted cantilever plate	71
5.7	The analysis of flapping of an inverted cantilever plate in axial flow: numerical parameters for 2D coupled VPM analysis.	71
5.8	Flow over a building with elastic membrane roof: the dimensions and physical properties of fluid and membrane.	78
5.9	Flow over a building with elastic membrane roof: numerical parameters for 2D coupled VPM analysis.	79
5.10	Physical properties for the fluid and solid (membrane) two-span membrane system.	86
5.11	The numerical parameters of fluid and structural solvers for aeroelastic coupled simulation of two-span membrane system.	86
5.12	Flexible cantilever plate in Kármán vortex street: physical and material properties of the fluid and flexible plate.	94
5.13	Flexible cantilever plate in Kármán vortex street: numerical parameters for pseudo-3D coupled VPM analysis.	95
5.14	The flapping of an inverted cantilever plate in axial flow: numerical parameters for pseudo-3D VPM analysis.	97
5.15	The VIV analysis of both-end clamped thin circular pipe: the dimensions of the problem and physical properties for solid and fluid.	101
5.16	Vortex-induced vibration of clamped circular pipe: numerical parameters for pseudo-3D coupled VPM analysis.	105
5.17	The physical properties and considered dimensions for the cantilever roof system.	112
5.18	Aeroelastic response analysis of a membrane roof: numerical parameters for pseudo-3D coupled VPM analysis.	112

5.19	The physical dimensions of 1500 m solar chimney	120
5.20	Numerical parameters for aeroelastic response analyses of 1500 m tall solar chimneys.	122
6.1	Physical dimensions and dynamic properties of the reference prototype T-shaped electromagnetic energy harvester.	135
6.2	Fully coupled simulation of the T-shaped cantilever harvester: numerical parameters.	139
7.1	Simulation to induce additional constant velocity component to the free stream flow: numerical parameters.	162
7.2	Study on the harvester motion depending on the mean flow and the fluctuation amplitude: numerical parameters.	170
7.3	Study on the harvester motion depending on the mean flow and the fluctuation amplitude: numerical parameters.	175
7.4	Physical properties for the fluid and solid domains of the benchmark	182
7.5	Convergence study: numerical parameters associated with reproduction simulations performed by seeding different number of particles.	184
7.6	Adaptive numerical techniques in FRM: Numerical parameters associated with reproduction simulations.	187
7.7	Run-time comparison of simulations using different FRM techniques. Here, NP represents the average number of particles in simulation domain	187
7.8	Comparison of Run-time of the wake buffeting simulations using different computationally effective techniques in FRM.	194

Chapter 1

Introduction

1.1 Background and motivation

Fluid–structure interaction (FSI) is a multiphysics study that focuses on the mutual dependence between deformable structure and surrounding or internal fluid flow. The flapping flag and the falling of a leaf are amongst the daily life FSI examples. FSI frequently encounters in many areas of civil, mechanical, aerospace and biomechanical engineering such as the aeroelastic phenomena in long-span bridges, tall towers, chimneys, and lightweight membrane systems, the motion of wind-turbine blades, the fluttering of aeroplane wings, the flow-induced vibration of marine risers, heat exchanger tubes, and the blood vessel dynamics, etc.

Structures under wind action can exhibit a variety of aerodynamic phenomena, which can lead to destructive and catastrophic events. Under specific wind–structure interaction (WSI) scenario, the aerodynamic forces can insert on a structure as a consequence of its motion, also known as self-excited forces, which cause aeroelastic instability. The incident that took attention of the bridge engineers worldwide is the historical Tacoma Narrows Bridge disaster (Fig. 1.1) in 1940, which was not entirely comprehended back at that time due to the lack of understanding of self-excited forces. Furthermore, three of a group of eight tall thin-walled cooling towers (375 ft high) collapsed in Ferrybridge/England in 1965 (c.f. Fig. 1.2), which



Figure 1.1: The Tacoma Narrows Bridge before (left) and after the collapse (right) (picture courtesy: University of Washington Libraries, Special Collections).

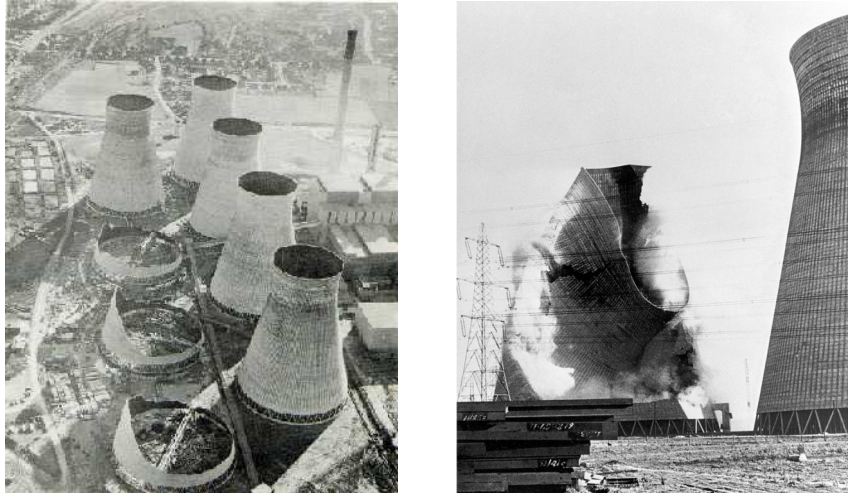


Figure 1.2: The collapse of three tall cooling towers in Ferrybridge/England (left), the moment of collapse of one tower (right) (picture courtesy: www.halinaking.co.uk).

was due to disregarding of wind action enhanced by powerful Kármán vortex street. Four towers which were on the windward side survived the wind action, but those behind were affected strongly by the vortices induced from the upstream bodies.

The design criteria of megastructures, such as long-span cable-supported bridges, super-tall buildings, towers and chimneys, large membrane roofs are governed by the aeroelastic interaction phenomena. Advancement in the computer-based numerical modelling as well the improvement in the wind-tunnel test aid to push the boundary limit of these structures. The desires to go beyond, however, introduces explicit challenges for their safety and performances, mainly when they are in demand to be increasingly aesthetic, and flexible. The vast majority of these structures are built in the atmospheric boundary layer, which implies that they are exposed to high turbulence flow and other effects of climate changes due to the surge of extreme events. Accurate prediction of WSI in the design process is crucial to avoid potential damage of important structures.

While the wind effects on civil engineering structures are of significant concern, the WSI has been used for large-scale wind power generation in many parts of the world. Due to the increasing demand for energy, Professor J. Schlaich of Stuttgart University proposed a solar chimney power plant (SCPP) in 1978 for solar-based electrical energy in the deserts. Conceptually, the efficiency of power generation depends largely on the chimney height and the enlargement of the heat collector area at the base. The feasibility studies on such large thin-walled chimneys proposed for different heights of 1000–1500 m and diameters of 120–170 m. Such a tall vertical cantilever tower, apart from several other critical design issues, is strongly susceptible to aeroelastic buckling of thin shells. Accurate modelling and analysis of coupled behaviour have been a significant concern.

The application fields of WSI have not been limited to large-scale wind energy harvesting. In recent years, aeroelastic responses or limit cycle oscillation (LCO) of thin-plate systems have been converted to electrical energy. It has been an active research area of the last decade because of the boom in structural health monitoring, which is influenced further by the advancements in wireless sensor networks. The harvesters offer green power as an alternative to the traditional limited-life batteries, which can save maintenance costs, particularly for extensive network systems. However, the sustainable motion of aeroelastic energy harvesters is a prerequisite for energy extraction. Proper understanding of the aero-electro-mechanically

coupled interaction of thin-walled harvesters is necessary for study on energy optimisation.

It is challenging to analyse FSI problems using analytical methods since they are intrinsically nonlinear and time-dependent. Experimental studies are always considered as a standard procedure; however, the advantages that make the numerical methods increasingly widespread are their ability to predict the full-scale aerodynamic behaviour, modelling of complex shapes, and detailed visualisation of interesting flow phenomena around bluff or moving flexible bodies. They hold further some preferred components, such as low cost and easy controlling of input parameters for fluid and structural models.

The numerical methods to solve FSI problems can broadly be classified as *monolithic* and *partitioned* based on the coupling algorithm. The monolithic algorithms solve the governing equations of fluid and structural dynamics simultaneously, and therefore, they are highly robust and stable. However, monolithic algorithms are computationally costly and require substantial expertise for code preservation. In contrast, partitioned algorithms are extensively used since they allow synthesizing independent computational schemes for the fluid and the structural dynamics subsystems. However, the stability of the coupled method requires special attention. With the advancements of the computational fluid dynamics (CFD) and computational structural mechanics, significant research on FSI has been performed. However, it is still challenging to answer many of the fundamental questions in FSI concerning appropriate coupling scheme, accuracy, robustness, performance, and applicability of the simulation techniques, which indicates the need for further developments.

The Vortex Particle Method (VPM) has been established as an accurate and efficient CFD simulation technique to model flow around complex geometries. The particle-based VPM has been a viable alternative to grid-based schemes for its strength in preserving rotational flow features which drive separation, reattachment and vortex shedding behaviour. The existing FSI implementations of VPM, which are mainly in the context of two-dimensional (2D) and pseudo-three-dimensional (pseudo-3D) formulations, have successfully been used for the analysis of aeroelastic interactions of line-like flexible structures such as long-span cable-supported bridges and towers. The existing 2D VPM can perform FSI simulation of rigid cross-sections with 3 degrees of freedom only. The pseudo-3D VPM, as the name suggests, uses multiple slices of 2D VPM simulations along the longitudinal direction of the structure to represent the full-scale 3D FSI phenomena. Even though vortex methods have successfully been used for bluff-bodies and in bridge aerodynamics; there exist no noticeable contributions in VPM for FSI analysis of deformable geometry that can be widely accepted in practical applications. The possibility of analysing flow around thin-walled flexible bodies would allow VPM to investigate a new class of FSI problems such as the flow-induced bending of a thin-plate or the deformation of thin-walled shell structures.

1.2 Objectives, methodologies and contributions

The main objective of this study is to extend the applicability of VPM for coupled FSI simulations of thin-walled flexible structures under steady and fluctuating incoming flows. The initial task is to extend the 2D VPM such that the flow-induced large motion of flexible thin bodies can be analysed. The subsequent task is to extend the pseudo-3D VPM for multi-slice FSI analysis of shell-type systems. In addition to validation of the extended FSI models, it is important to demonstrate their suitability to different FSI problems and application field of thin-walled structures. The final and compelling task is to investigate the interaction between fluid and structure influenced by inflow fluctuations.

In this context, the flow around deforming thin bodies is analysed using the 2D and pseudo-3D implementations of VPM. The structural behaviour is modelled and analysed using the Finite Element Method (FEM). The partitioned numerical approach is considered because of the flexibility of using different mathematical procedures for solving fluid and solid mechanics. The advantage of VPM is that the method is primarily grid-free; there is no need for conforming of mesh at the interface of fluid and structure. The structural equations are formulated and analysed at the mid-surface of the thin element because of its efficiency of handling large deformation. It is important to note that the coupled numerical extensions are based on non-conforming mesh since the interface of fluid and structure is separate. The accuracy of such models largely depends on the appropriate projection of information from one interface to another, and satisfaction of the required boundary conditions.

The interest of this study includes applying the FSI models under both laminar and fluctuating incoming flows. The VPM allows accommodating vorticity carrying particles in the free stream flow, which can create flow fluctuations. However, the particles need to be released in specific procedures to achieve desired fluctuations in the free steam flow.

The thesis separates the existing FSI models of VPM from the new contributions that allow the extended coupled methods to analyse FSI of thin-walled flexible structures. The latest additions of the VPM, the governing equations of structural analysis, and the coupling of the fluid and structural models are explained in the same chapter. The validation of the coupled methods and their application are displayed in the next chapters for different FSI problems. Finally, the thesis presents two further numerical extensions of VPM that allow modelling of inflow fluctuations along with their application in FSI simulations.

The numerical extensions, the methodology, and the contribution of this research are summarized as follows:

- A partitioned algorithm of 2D VPM for large-displacement FSI simulation of thin-walled flexible systems.

It is a newly developed partitioned FSI model using 2D VPM. The model is implemented mainly for large-displacement coupled interactions of thin-plate systems. The 2D VPM with immersed interface technique is utilised for analysis of flow around deformable bodies; the method ignores across-flow effects. The 2D corotational finite element formulation is used to analyse the geometric nonlinear motion of thin-plate systems.

- A partitioned algorithm using pseudo-3D VPM for FSI analysis of linear shell-type structures.

It is another new extension of VPM in the context of pseudo-3D multi-slice FSI analysis. Here, the structural equations are solved using superposition of uncoupled natural vibration modes, and therefore, the method is for linear structures. The novel contribution is the inclusion of 3D vibration modes of shell structures in contrast to the existing line-like structural model based on beam elements. This new extension allows simulating FSI problems of thin-walled shell structures such as large membrane roofs, tubes, towers, and chimneys, etc.

- A simplified aeroelectromechanical coupled model within the framework of 2D coupled VPM.

The 2D coupled VPM, which is developed for large-displacement FSI problems of thin-walled systems, is employed in a simplified fashion for aero-electro-mechanical coupled

analysis. The method is presented for analysing the flow-induced motion of flexible aeroelastic energy harvesters.

- An extension of 2D VPM for simulation of pulsating incoming flow.

It is a new numerical extension within the framework of 2D VPM to simulate pulsating incoming flow by seeding precalculated vortex particles into the free stream. The method uses the natural convection of the vortex particles, regularly released from two distant seeding points near the upstream boundary. The technique can be applied to investigate the behaviour and performance of small-scale energy harvesters in low-frequency periodic incoming flows.

- A new extension of 2D VPM for the reproduction of turbulent wakes of an original flow simulation for buffeting and FSI analysis.

It is another unique extension of 2D VPM which allows complex transient flow features computed by an original VPM simulation to be recreated for use as inflow conditions in FSI simulations. It is facilitated by recording velocity-time signals of the original simulation and computing time traces of vortex particles to be released into the secondary simulation near its upstream domain boundary. The method is recommended to apply for FSI simulations of a wake buffeting problem.

The thesis presents analyses of several FSI of thin-walled systems, apart from the benchmark studies, and discusses the new insights into the coupled mechanisms. The understanding of the large-displacement coupled motion of different thin and flexible cantilever plates permits the proposal of an optimisation scheme for aeroelastic energy harvesters. The optimisation framework is prescribed as a preliminary study on aeroelastic energy harvesters such that one can predict the potential of energy harvesting of a prototype system based on the target wind speeds. The investigation on the aeroelastic LCO of thin-plate systems influenced by the low frequency periodic incoming flow shows a new understanding of coupling mechanism.

A framework of a different combination of models is displayed in Table 1.1. Depending on the inflow condition and target application field, the coupled model can be chosen for specific aerodynamic and aeroelastic analysis.

The list of peer-reviewed publications by the author and co-authors are listed at the end.

1.3 Outline of the thesis

The layout of this thesis is as follows. Chapter 2 discusses briefly on the atmospheric wind, the essential aspects of bluff body aerodynamics, and the wind effects on structure such as different aeroelastic phenomena.

The coupling mechanism of FSI methods, their advantages and limitations, mesh treatment, surface discretisation algorithms are addressed briefly in Chapter 3. Furthermore, the thesis presents the governing equations of the VPM, the existing implementations, and the application of VPM in the literature.

Chapter 4 presents all the new changes added to the flow solver, which are in the context of 2D and pseudo-3D VPM. The governing equations of the structural solver and the kinematics of the corotational beam element are briefly addressed. The chapter describes step by step the coupling between the flow and structure solvers, the projection of information, the satisfaction

of the boundary conditions. The validation of the enforcement of the boundary conditions is necessarily presented.

Chapter 5 presents the validation of the coupled solvers, i.e. the 2D and pseudo-3d VPM, with several benchmark FSI problems along with some application studies.

The application of the 2D coupled VPM solver is presented in Chapter 6 for modelling, analysing, and optimisation of the performance of aeroelastic energy harvesters.

Two new numerical extensions of VPM are displayed in Chapter 7 for modelling of incoming flow fluctuations using the particle seeding in the upstream of the simulation domain.

The summary and conclusions of the research are discussed in Chapter 8, along with recommendations for further studies in the research direction.

Numerical model	Incoming flow condition		Flow solver		Structure solver	
	free stream	fluctuating /periodic	2D VPM	pseudo-3D VPM	geometrically nonlinear	linear modes
2D coupled VPM (nonlinear) FSI model for large-displacement of thin-walled flexible systems	•		•		•	
2D coupled VPM (linear) FSI model for small-displacement of thin-walled flexible systems	○		○			○
Pseudo-3D VPM (linear) FSI model for shell-type flexible structures (open geometry: plate, roof)	•			•		•
Pseudo-3D VPM (linear) FSI model for shell-type flexible structures (closed geometry: chimney, tube)	•			•		•
2D coupled VPM (nonlinear) aero-electro-mechanically coupled model for thin-walled aeroelastic energy harvesters	•		•		•	
2D coupled VPM (nonlinear) aero-electro-mechanically coupled analysis of harvesters in fluctuating flows: (1) pulsating incoming flow, (2) reproduced wakes.		•	•		•	

Table 1.1: The FSI models are summarized based on the combination of coupling between fluid and structural solver and the incoming flow conditions. Here, the filled circles (•) shows the models that have been utilized in this study. The unfilled circles (○) shows the possible models, the analysis results of which are not presented in the thesis.

Chapter 2

Wind effects on structures

2.1 Introduction

The wind loads and their effects on civil engineering structures involve, in some instances, considerable complexities that special attention must be taken into account to ensure safety and serviceability requirements. Over the last decades, the understanding wind effects on bridges, buildings and notable structures has progressed significantly due to the extensive research and experimental studies. However, there is a growing demand for constructing super-long-span cable-supported bridges, large flexible roofs, tall towers, and chimneys. Additionally, the considerable increase in destructive wind storms due to global climate change enhances the vulnerability of structures against wind hazard has become a significant challenge to aeroelastic engineers [257].

The Davenport's wind loading chain described an approach [27, 69, 70, 129] to evaluate wind loads and the wind-induced response of structures using a string of roughly five links or factors (see Fig. 2.1). They were discussed to be the local statistical wind climate, the terrain roughness and topography, the aerodynamic characteristics of the shape of the structure, and the increase of load due to potential wind-induced resonant vibrations. This chapter describes a brief discussion of the atmospheric wind and its description in terms of different statistical properties initially. A short overview of bluff-body aerodynamics follows further with several aeroelastic phenomena.



Figure 2.1: Alan Davenport wind loading chain.

2.2 Atmospheric boundary layer

The atmospheric boundary layer is the region of the lower troposphere where the wind flow significantly affected by friction of the earth's surface. The shape of the earth and its position relative to the sun are responsible for differences in the amount of solar heat received by the

atmosphere over various surface areas, which fundamentally causes the motion of air with respect to the surface and exerts a horizontal drag force upon the moving air.

The wind speeds in the atmospheric boundary layer vary randomly with time. It is common to study the wind field by decomposing into a mean wind speed along the direction of the mean wind and three perpendicular turbulence components in a sufficiently long averaging time. Assuming that x, y , and z represent the longitudinal, lateral and vertical direction, respectively, for the wind velocity components u, v and w . The total velocity at a point in the atmosphere is a function of the position and time; $\mathbf{U}(\mathbf{x}, t)$. The wind velocities which vary only with z for a given point (x, y, z) and time t can be expressed as:

$$\mathbf{U}(\mathbf{x}, t) = \{\bar{U}(z) + u(\mathbf{x}, t), v(\mathbf{x}, t), w(\mathbf{x}, t)\} \quad (2.1)$$

where, $\bar{U}(z)$ is the mean wind speed depending on height z above the ground. It is generally assumed that the non-zero mean component exists only in longitudinal flow direction.

The following parameters of the atmospheric turbulence are of interest in various applications: the mean wind, the turbulence intensity; the integral scales of turbulence; the spectra of turbulent velocity fluctuations; and the cross-spectra of turbulent velocity fluctuations. For the modelling of the mean profile and the description of turbulent characteristics of the atmospheric boundary layer, numerous approaches exist and further references are available in [217]. However, the statistical parameters that have used in this thesis are briefly discussed.

Turbulence intensity

The level of fluctuations in the wind field can be measured by its turbulence intensity which is the ratio of the standard deviation of each fluctuating component to the mean wind speed. The turbulence intensity components can be expressed as follows

$$I_u(z) = \frac{\sigma_u(z)}{\bar{U}(z)}, \quad I_v(z) = \frac{\sigma_v(z)}{\bar{U}(z)}, \quad I_w(z) = \frac{\sigma_w(z)}{\bar{U}(z)}, \quad (2.2)$$

where, the standard deviations $\sigma_u(z)$, $\sigma_v(z)$ and $\sigma_w(z)$ for the turbulence components in the longitudinal direction, lateral horizontal direction, and vertical direction can be written as:

$$\sigma_u(z) = \sqrt{\frac{1}{T} \int_0^T u^2 dt}, \quad \sigma_v(z) = \sqrt{\frac{1}{T} \int_0^T v^2 dt}, \quad \sigma_w(z) = \sqrt{\frac{1}{T} \int_0^T w^2 dt}. \quad (2.3)$$

Covariance and Correlation

Covariance and correlation are two important properties of turbulence wind, reflecting the statistical relation of fluctuating wind velocities between two points in space. The covariance between the turbulence winds at two different heights, z_1 and z_2 , is defined as follows

$$\text{cov}(u(z_1), u(z_2)) = \frac{1}{T} \int_0^T [U(z_1, t) - \bar{U}(z_1)] [U(z_2, t) - \bar{U}(z_2)] dt. \quad (2.4)$$

Thus, the covariance is the product of the fluctuating velocities at the two heights, averaged over time. Note that the mean values, $\bar{U}(z_1)$ and $\bar{U}(z_2)$, are subtracted from each velocity in the right-hand side of Eq. (2.4). Note that in the special case when z_1 is equal to z_2 , the

right-hand side is then equal to the variance (σ_u^2) of the fluctuating velocity at the single height. The correlation coefficient is defined as follows

$$\text{corr}(u(z_1), u(z_2)) = \frac{\text{cov}(u(z_1), u(z_2))}{\sigma_u(z_1) \cdot \sigma_u(z_2)}. \quad (2.5)$$

2.3 Bluff body aerodynamics

The flow of fluid over solid bodies is something that frequently occurs in our surroundings. The shape of the body has a profound influence on the flow over the body and velocity field. The aerodynamic characteristics such as the flow around bluff bodies are substantially different from streamlined bodies, c.f. Fig. 2.2. The flow around the airfoil can be seen streamlined, which is closely following the contours of the body. The flow separation from the surface of the airfoil can be seen only by a thin boundary layer. In contrary, for the rectangular bluff section, the flow is separated at the leading-edge corners. Most of the civil engineering structures such as buildings, towers and bridges are bluff in form. Therefore, it is necessary to percept the aerodynamics of bluff bodies to make further advancement in the field of wind engineering [135].

A large number of physical phenomena and problems exists in fluid dynamics depending on the characteristics of fluid and boundary conditions. In the boundary layer, i.e. the region of flow separation and turbulent wakes, the viscous and rotational effects play the most significant role [50]. The irrotational flow is the simplest of all forms of fluid flow occurs in the absence of viscosity. It is based on potential flow theory; this model has been of much use in the analytical study of streamlined bodies [174]. The viscosity of air at meteorological pressures and temperature is quite low; however, the viscous effects occur in the formation of boundary layers. If air flows over and along a smooth stationary surface, experimental evidence suggests that the air in contact with the surface adheres to it. It causes hindrance of the air movement in a layer near the surface referred to as the boundary layer. The importance of viscous effects is generally expressed by Reynolds number ($\mathcal{R}e$), which is an essential non-dimensional parameter in all branches of fluid mechanics as follows

$$\mathcal{R}e = \frac{U_\infty L}{\nu}, \quad (2.6)$$

where U_∞ is the flow velocity, L is the length scale, and ν the kinematic viscosity of the fluid. It expresses the ratio of the inertia forces to the viscous forces of a particle of fluid on an element. The viscous forces play a decisive role on the aerodynamics at low Reynolds number, whereas at high Reynolds number the inertia forces dominate over the fluid viscous forces. The flow separation occurs when the inertial forces adequately decelerate the fluid particles. The presence of adverse pressure gradients in the flow allows occurring this deceleration. For

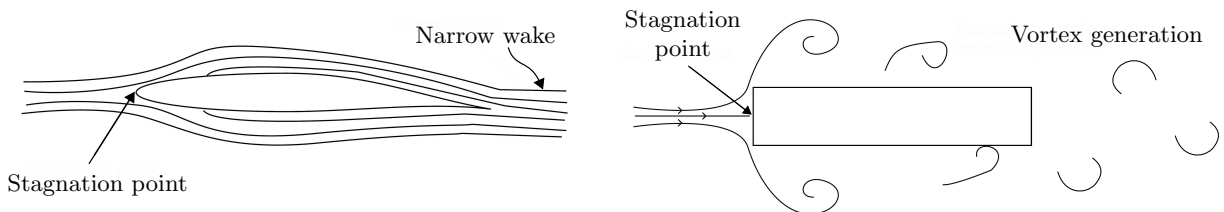


Figure 2.2: Flow around streamlined body (left) and bluff body (right).

a bluff body with sharp edges, the flow separation initiates by the location of the edges, and flow re-attachment may or may not occur. Even if it does, it might not be influenced by the Reynolds number [150]. In case of a circular cylinder, which is a bluff body with curved surfaces, the positions of the separation of local surface boundary layers are much more dependent on viscous forces than is the case with sharp-edged bodies [119]. The separation layers generate discrete vortices, which shed into the wake flow behind the bluff body.

The Reynolds number for flows of practical interests ranges from nearly zero to as high as 10^8 or 10^9 . A gradual increase of Reynolds number of the flow over an obstacle generally produces a widely varying sequence of flow phenomena [217]. At sufficiently high Reynolds numbers the circulation region introduced by the separation becomes unstable and an oscillating wake composed of large-scale eddies, the von Kármán vortex street, forms downstream of the body. For a given cross-sectional shape, the frequency of vortex shedding, f_s , is proportional to the approaching flow speed, and inversely proportional to the width of the body [119]. It may be expressed in a non-dimensional form, known as the Strouhal Number (St) as follows

$$St = \frac{f_s D}{U_\infty}, \quad (2.7)$$

where U_∞ is the far upstream velocity. D is the section depth. The Strouhal Number varies with the shape of the cross-section, and for circular and other cross-sections with curved surfaces, it varies with the Reynolds Number. The vortex shedding pattern from bluff-bodies at different Re was displayed in [150, 156, 178, 179, 182].

2.4 Aeroelastic vibration phenomena

Aeroelastic instabilities involve aerodynamic forces that act upon the body as a consequence of its motion. Such forces are termed motion-induced or self-excited [72, 100, 217], in which the motion of the structure generates aerodynamic forces. The wind-induced vibration mechanisms can be classified based on force excitation into four mechanisms: forced vibration, self-excited vibration, a combination of forced and self-excited vibration, and random vibration. The aeroelastic phenomena commonly observed in long-span bridges are the galloping, torsional flutter, coupled flutter, vortex-induced vibration (VIV), buffeting, etc. However, they are not limited to bluff bodies only; the motions of flexible bodies such as rods, tubes, pipes, and elastic cantilever plates all exhibit coupled aeroelastic vibration phenomena.

In another representation, which is based on the stability, response amplitude and the range of wind velocity where it occurs, the wind-induced vibration and its effects on structures can be distinguished as depicted in Fig. 2.3. Here, the limited amplitudes phenomena show the dynamic response of structures due to the aerodynamic forces; the influence of motion-induced forces are generally negligible. The VIV, buffeting and rain wine-induced vibrations are among the examples of limited amplitudes phenomena. The limited amplitude phenomena often discussed with the comfort and serviceability issues; however, they can lead to the ultimate failure of the system due to fatigue damage. The divergent amplitude problems are usually aeroelastic instability problems in which motion-induced forces play a significant role. There are three types of such phenomenon that can occur in bridge sections: torsional flutter, coupled flutter and galloping.

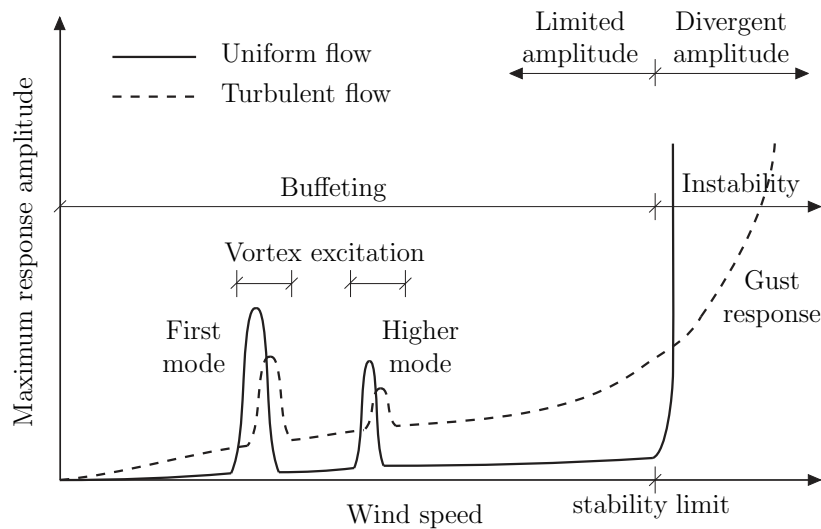


Figure 2.3: Schematic of structural response against wind speed [1].

2.4.1 Limited amplitudes phenomena

Vortex-induced vibrations

Vortex-induced vibrations (VIV) are the response of a structure which is induced by the interaction with the vortex shedding of the flow. In a long-span cable-supported bridge, the interaction of the bridge with vortex shedding may result in “lock-in” phenomenon in which the large-amplitude crosswind response at a reasonably wide range of wind velocities [136]. VIV is one of the major issues in long-span bridge vibration, which usually occurs at low wind speeds and low turbulence conditions [100, 257]. Though the VIV response of a system generally belongs to limited amplitude, however, the response should be controlled to a specific limit to ensure the regular operation and to avoid fatigue damage to the bridge. It is often, therefore, suggested to break the shedding pattern by using deflectors to minimise the system response.

Apart from the bluff bodies, the large-amplitude response of inverted cantilever plate systems was reported as VIV. The synchronisation of vortex shedding frequency occurred when tested in wind tunnel experiment and numerical analysis [142, 201].

Buffeting response

A structure immersed in a wind field subjects to static and dynamic wind forces caused by mean and fluctuating wind speeds, respectively. Buffeting is a random vibration caused by fluctuating winds. The consideration of the buffeting responses of a long-span bridge usually is dominant to determine the size of structural members. The buffeting forces from turbulent wind and self-excited forces due to the wind-bridge interaction should be considered to model the action of buffeting wind load. Extreme buffeting may cause fatigue problem in bridge components and affect the functionality of the bridge.

Vortex-induced wake buffeting

Structural members, when located in the wake of an upstream bluff body, can oscillate by the vortices shed from the upstream body with much larger amplitudes [252]. The wake

flow is generally an extremely complex flow system composed of unsteady and non-uniform fluid motion. Wake buffeting depends mostly on the development of the wake in between the space of upstream and downstream bodies. In the case of two bodies close to each other, the buffeting response is the effect of combined wakes of two bodies. However, when they are far apart, it is the wake of the upstream body hitting on the downstream one that has the dominant effect. A reasonable possibility for improving wake buffeting seems to be the utilisation of approaches which may decrease the vortex energy and disorder periodicity of the wake fluctuation.

2.4.2 Divergent amplitudes phenomena

Flutter

Flutter is a self-feeding aeroelastic phenomenon which is potentially destructive to long-span cable-supported bridges. The aerodynamic forces generated on the bridge deck coupled with its motion. If the energy input by the aerodynamic forces at high wind speeds in an oscillation cycle becomes more substantial than that dissipated by the mechanical damping of the structural system, the amplitude of vibration will grow, which can lead to the Ultimate Limit State of the bridge and ultimately to collapse [257].

The expression of classical flutter is initially employed to the thin airfoil. It indicates an aeroelastic phenomenon in which two degrees of freedom (DOFs) of a structure, which are torsional and vertical, can couple together in a flow field and oscillates in an unstable fashion with a single frequency. The flutter phenomena will depend on phase lag or degree-of-coupling among the modes [100]. The smaller frequency separation between the coupled modes increases the risk of flutter to occur [86].

Torsional flutter is single-degree-of-freedom (SDOF) aeroelastic instability with rotational motion. The mechanism of torsional flutter is related to aerodynamic damping of rotational motion. Torsional flutter occurs when the total damping (mechanical and aerodynamic) of the system in torsional motion becomes zero.

Panel flutter is a self-excited, dynamic-aeroelastic instability of thin plate or shell-like components. The flapping flag is a daily life example.

Galloping

The galloping is a large-amplitude aeroelastic phenomenon observed particularly with slender structures in the direction perpendicular to the flow at frequencies much lower than those of vortex shedding from the same section [217, 257]. It is often known as ‘translational galloping’, ‘cross-wind galloping’ or ‘bending flutter’. It is a common instability mode for non-circular cross-sections, for example, rectangular or ‘D’ sections or the effective sections of some ice-coated power line cables.

Wake galloping

Wake galloping is a phenomenon of two cylinders in which the flow induces the oscillations of a downstream cylinder in the turbulent wake of an upstream cylinder. Wake galloping may occur only under specific conditions where the frequencies of the response of the downstream cylinder are low compared to its vortex-shedding frequencies and to those of the cylinder located upstream. The wake galloping is generally large-amplitude limit cycle oscillations

(LCO). Wake galloping can happen to stay cables in a cable-stayed bridge, or to the hangers of a suspension bridge.

Torsional divergence

Torsional divergence is a non-oscillatory phenomenon and described by torsional instability which happens at some critical divergence wind velocity. The twisting moment increases with the increase in wind velocity, which in turn increases the angle of attack relative to the structure and increases the twisting moment furthermore. Therefore, it is not an issue of ultimate structural strength; instead, the phenomenon depends upon the structural flexibility and the way the aerodynamic moments develop [217]. In case of a bridge section, the torsional divergence occurs suddenly at the critical wind velocity and leads to ultimate collapse [257]. The torsional divergence wind velocity of the civil engineering structure is generally much higher than the design wind speed.

2.5 Nonlinear aeroelasticity

For the last decades, nonlinear aeroelasticity has been a subject of great interest. The linear models, both theoretical and experimental, have successfully been utilised for analysing aeroelastic problems for many years. The outcome of nonlinear aeroelastic behaviour most commonly relates to the limit cycle oscillations (LCO), considered as one of the simplest dynamic bifurcations. The LCO phenomenon is characterised by periodic oscillations of generally moderate to large amplitudes [170]. The variety of possible nonlinear aeroelastic behaviours include higher harmonic and subharmonic resonances, jump-resonances, entrainment, and change of periods to double [82].

The nonlinear aeroelastic LCO can be triggered by either or both the structural and the aerodynamic origins [82]. A single nonlinear mechanism may be mainly responsible for the LCO. However, it is difficult to know which nonlinearity is dominant without analysing appropriate mathematical and experimental wind tunnel models. The nonlinearity is often welcoming because without the LCO the catastrophic flutter can lead to loss of the flight vehicle [82, 83].

In most cases, these nonlinear effects are small, and therefore, the linear models worked well. However, sometimes nonlinear effects are more critical, and occasionally, they are crucial. For example, the flutter instability of cantilevered flexible plate in axial flow is known for many years. It is a canonical problem, often known as plate or shell flutter that leads to limit cycle motions of moderate amplitude. The flutter motion of this thin plate does not usually lead to immediate catastrophic failure. The structure has a nonlinear stiffening due to the tension induced by mid-plane stretching of the plate that arises from its lateral bending [82].

In contrast to a plate flutter of a plate in conventional flag configuration, [142] introduced the large-amplitude LCO of an inverted cantilever. The system is with a free leading edge and a clamped trailing edge. The system exhibits large-amplitude flapping over a finite band of flow speeds. The flapping behaviour was identified as VIV in [201]. Recently, the flapping of inverted cantilever systems has been investigated for small-scale energy harvesting [183, 215]. The fluttering of T-shaped inverted cantilever plate is also another example of nonlinear aeroelasticity problem of large-amplitude LCO [55, 149, 186]. In recent years, the nonlinear effects of wind-structure interactions of long-span suspension bridges are becoming a crucial concern as the span-length increasing to predict the aeroelastic behaviours [254].

2.6 Summary

This chapter has summarized some fundamental aspects of wind effects on structures. The formation of wind and some frequently used statistical parameters to define wind properties are discussed very briefly. The flow characteristics when passes bluff bodies is fundamental issue in fluid dynamics and the key points has been addressed. Furthermore, different types of aerodynamic response phenomena that can happen to structures when immersed in wind flow have been discussed based on their response patterns. A short discussion on nonlinear aeroelasticity concludes this chapter.

Chapter 3

Numerical methods for fluid–structure interaction simulation

3.1 Introduction

The coupled problem of fluid flow that interacts with a flexible moving structure plays remarkable roles in many scientific and engineering fields. For most fluid–structure interaction (FSI) problems, it is impossible to obtain analytical solution. The experimental investigations are limited in scope, and therefore, the numerical simulations are often used to investigate the fundamental physics related to the intricate interaction between fluids and structures. Advancements in computational algorithms, the progress in computer capacity coinciding with the understanding of flow and structural modelling have made these coupled simulations feasible. However, an extensive study of such problems remains a challenge due to their strong nonlinearity and multidisciplinary nature [120].

Despite the common origin of continuum mechanics, the fluid and structure both have their background of theories and mathematical descriptions, which is in terms of partial differential equations. Many numerical algorithms look for synthesizing individual computational approaches for fluid dynamics and structural dynamics subsystems. The interaction between the two simulation modules introduces a lot of complications. It is a critical issue to select the suitable models for fluid and structure based on the application field to develop an efficient interface to perform coupling between two models [134].

The numerical methods to analyse FSI problems can be classified into two approaches based on the coupling mechanism: monolithic approach and partitioned approach. This chapter focuses briefly on different coupling approaches of FSI simulations with a discussion on their advantages and limitations. The review follows further on the treatment of mesh at the interface and the numerical strategies to deal with large-displacement FSI problems. The thesis presents in next chapter partitioned extensions of Vortex Particle Methods (VPM) for FSI simulations thin-walled flexible structures. Therefore, the governing equations of VPM and the existing FSI implementations of VPM for bluff bodies are briefly presented.

3.2 Coupling mechanisms for FSI simulations

Numerous algorithms in computational fluid dynamics (CFD) attempt to integrate independent computational methods for the fluid mechanics and structural dynamic subsystems [134]. This procedure is associated with being full of complications related to the interaction between the two analysis modules. Depending on the application case, the initial task is to determine suitable numerical models for fluid and structure and to develop an efficient interface to execute the coupling between two models.

The numerical analysis of the FSI problem are based on the exchange of information between the fluid and structure models in iterative loops. It means the flow-induced loads from the fluid domain must be applied to the discretised structural model [196]. The solution of the structural solver allows the modification of boundary conditions which must be updated or projected from the deformable structure to the fluid boundary.

The numerical solution of a coupled field results in a system of nonlinear algebraic equations. The coupling mechanism of the fluid and structure solver to solve those equations of FSI problems may be broadly classified into two approaches: the monolithic approach [114, 121, 125, 200], and partitioned approach [71, 120, 238, 253, 255].

3.2.1 Monolithic approaches

The monolithic method is the direct approach in which the equations of motions for fluid and structure are viewed as a single set of equations. The kinetic boundary conditions at the interface are solved simultaneously within the fluid and the structure domains. It is driven by the idea of a closed discretisation of the overall FSI system.

The primary advantage of a monolithic approach is that the fluid and structure are perfectly synchronised while advancing a single time step [30]. It usually leads to enhanced robustness, stability, and more significant allowable time steps. For a monolithic discretisation of an FSI problem, the overall system of equations, comprising the discrete flow and structural variables, and their coupling components can be expressed as follows

$$\begin{bmatrix} K_F & K_{FS} \\ K_{SF} & K_S \end{bmatrix} \begin{Bmatrix} u_S \\ u_F \end{Bmatrix} = \begin{Bmatrix} f_S \\ f_F \end{Bmatrix}, \quad (3.1)$$

where the diagonal blocks K_F and K_S represent the fluid and structure internal equations. The off-diagonal blocks K_{FS} and K_{SF} contain the coupling of the unknowns between fluid and structure [103]. The approach is robust, unconditionally stable with rapid convergence and less restriction on the permissible time step. The method can potentially achieve better accuracy for a multidisciplinary problem [114, 124, 125, 200]. However, the monolithic methods may require substantially more resources and expertise to develop and maintain such a specialized code. Therefore, they are believed to be computationally expensive and less suitable for large-scale problems [134]. However, Heil et al. [114] demonstrated that the monolithic solvers could be competitive even in test cases with very weak FSI, for which partitioned solvers converge reliably. The efficiency of monolithic solvers was discussed to be dependent on the provision of efficient preconditioners. However, the different characteristics of the individual fields cannot be taken into account. Furthermore, the monolithic approach generally suffers from software modularity.

3.2.2 Partitioned approaches

In recent years, remarkable advancements have been witnessed for individual discipline in both computational fluid dynamics and computational structural mechanics. Therefore, the numerical FSI analysis is attempted often in the context of partitioned methods, where already existing advanced fluid and structure solvers are jointly employed. The coupling is performed in time loops mainly by exchanging information between the solvers in an alternating fashion for the simulation time step. The partitioned method, in contrast to the monolithic approach, provides excellent flexibility of selecting code or software for solving the structure and fluid equations. The recent advancements and reduction in computational costs for modelling of both fluid and solid structures have made the partitioned schemes more popular for analysing FSI problems [77, 107, 112, 134, 137, 160, 196, 233, 253].

The partitioned approaches can be classified into two types: the fully coupled approach and the loosely coupled approach depending on the satisfaction of the coupling conditions in the immersed interface.

Fully-coupled approach

If the interaction between fluid and structure is strong, it is necessary to perform iterations between the flow solver and the structural solver to calculate the solution of the coupled problem. The fully-coupled approach ensures that the continuity of stress at the fluid-structure interface is satisfied within the desired convergence threshold. The fully-coupled approach is often expressed as a strongly-coupled FSI algorithm. It is generally preferred for FSI problems with strong interactions like the blood flow in arteries. This approach retains the synchronisation of the monolithic scheme; at the same time, the method also holds the advantages of a partitioned scheme [30]. It represents an improved code with maintainability and algorithmic flexibility for physically different systems.

Loosely coupled approach

In case of weak interaction between the motion of fluid and structure such as the aeroelastic instabilities of flexible thin-plates, there is no need for additional coupling iterations. The loosely coupled approaches are robust for such FSI problems with large mass ratio (structural density considerably larger than the fluid density). The error of such an approach depends only on the accuracy of the temporal discretization scheme. The loosely coupled approaches have successfully been reported in the literature on an array of aeroelasticity problems. In contrast, when the mass ratios are in order of one or lower, fully-coupled iterations are required to enhance the robustness of FSI problems [107].

The update of the fluid and structure solution are lagged, or staggered, resulting in a lower computational cost per time step than a fully coupled approach. Important to note that the two systems are never entirely in phase, and this introduces a temporal error in addition to the truncation error of the fluid and structure integration schemes. Care should be taken to maintain both accuracy and stability when constructing a loosely coupled method. Unless the time lag is sufficiently small, spurious numerical solutions may exist.

In this thesis, the loosely coupled partitioned approach is used for the numerical analysis of aeroelastic interactions of different thin-walled flexible structures. As it is stated earlier, one of the fundamental advantages of partitioned methods is the flexibility of choosing available software or code for solving the fluid and structure equations. However, it may require small

intrusions into the source codes of the individual solver to create the coupling environment. The coupling procedure itself is not, by any means, a straightforward thing. Since the solvers are separated, they both use their discretisation method, can lead to non-matching grids, different stability requirements on time step widths and requirements of interface data. Furthermore, the accuracy of coupling depends on the quality of projection of information from one interface to another.

The modelling of flow around bodies with low viscosity fluid may be highly turbulent and requires very small simulation time steps for the converged solution. In contrast, the structure can advance with much larger time steps if the displacements are small. In the case of large-displacement FSI problems with high response frequency, it is necessary to use a tiny time step for the structure solver to achieve a converged solution. Therefore, the sub-cycling of time step can be applied for fluid or structure solver depending on the FSI problem.

3.2.3 Conforming and non-conforming mesh

The decomposition of the domains is a standard numerical approach to speed up complex coupled simulations. The matching of the meshes at the fluid-structure interface is usually not desirable since a much finer mesh is required in case of flow solver when compared to the structural solver [71]. Based on the treatment of meshes, two contrasting approaches towards a general classification of the FSI solution procedures are the conforming and non-conforming mesh methods [238].

The conforming mesh methods consider the interface conditions as physical boundary conditions, which considers the location of the interface as part of the solution, and requires meshes that conform to the interface [120]. As the solution is advanced, the update of the mesh is necessary due to the movement and deformation of the solid structure.

The non-conforming mesh methods, on the other hand, uses the boundary location and related interface conditions as constraints which are imposed on the model equations so that non-conforming meshes can be employed. As a consequence, the fluid and structure equations can be solved conveniently and separately from each other with their grids, and re-meshing is not essential.

Different research groups may probably take care of numerical codes or solvers quite distinct in terms of methodology. The use of non-matching discretisation allows exploiting the vast experience of the new development of solvers for each field, such as the use of different discretisation size and element in [196]. In another example in [184], the aeroelastic response of flexible airfoil (NACA0012) was analysed using a geometrically nonlinear 1D beam model. Therefore, the meshes can be non-matching; however, an appropriate interpolation/projection step has to be carried out to facilitate the transfer of information between the fluid and structure domains [71].

3.2.4 Large displacement FSI simulations

The fluid domain is generally described in a Eulerian frame of reference, and the solutions are obtained in fixed grid/mesh points. Difficulties arise when the fluid field changes shape or when flexible/moving bodies are present inside the fluid domain. There have been different proposed techniques and investigation in literature for handling moving interfaces and in particular the interfaces of a solid elastic structure embedded in a fluid [238]. The Arbitrary

Lagrangian–Eulerian (ALE) approach and Immersed Boundary (IB) methods are two general numerical techniques for simulating complex flow with deformable boundaries [107].

Arbitrary Lagrangian–Eulerian (ALE) approach

The ALE is a conventional boundary conforming approach that allows the arbitrary motion of grid/mesh points with respect to their reference frame [81, 116, 127]. The solid body and the flow are meshed separately, and in which, a Lagrangian mesh follows the material points to discretise the solid body. The fluid points at the fluid–structure interface are moved similarly in a Lagrangian manner to correspond to the instantaneous configuration of the solid body. Since the mesh conforms at the interface, the boundary conditions of the flow at the solid surface can be imposed straightforwardly.

The ALE approach is well suited for simulating the flow of high Reynolds number since it can capture the position of moving fluid–structure interface very accurately. The refinement of the flow mesh near the solid surface can be performed locally to resolve the boundary layer. However, the computational efficiency of the scheme reduces in case of significant deformation problems due to the requirement of remeshing the moving mesh frequently. Furthermore, the substitution of solutions from the deteriorated mesh to the new mesh may introduce artificial diffusion, causing loss of accuracy [238]. Especially in case of a solid body with complex shape and large deformations, it is necessary to update the mesh topology frequently through extensive computations. In such situations, the methods that are based on fixed and non-body-conformal grids may provide more attractive alternatives [233].

Immersed Boundary (IB) methods

The non-boundary conforming IB method, which was firstly introduced in [189], provide an alternative approach for simulating FSI problems involving complex geometries and arbitrarily large deformations. In contrast to the ALE technique, where the fluid–structure interface is accurately captured, IB methods do not require any changes of the fluid mesh/grid.

IB methods are especially attractive for simulations of complex flows in engineering and biology because they do not require remeshing and can readily handle arbitrarily large deformations, c.f. [221]. This solid boundary interacts with the fluid employing local body forces applied to the fluid at the position of the solid points. This body force imposes the kinematic constraint that the velocity at each of these solid points is coupled to the (interpolated) fluid velocity at that point. The introduction of these body forces has become the basic idea behind several non-boundary-fitting FSI methods. Throughout the years, the IB methods have been successfully applied in many application fields [107, 108, 233, 266].

3.3 Numerical analysis of fluid and structure

3.3.1 Modelling of fluid motion

There are many approaches, but the most important of which are finite difference (FD), finite volume (FV), finite element (FE) methods, Boundary Element Methods (BEM). More details on the method can be found in [22, 98].

On structured grids, the FD method is very simple and effective. It is the oldest method for solving partial differential equations. The partial derivatives are replaced with a truncated

Taylor series expansion. The restriction to simple geometries is a significant disadvantage in complex flows. Finite Volume Methods (FVM), a natural choice for CFD problems, are based on the discretisation of the Navier-Stokes equations in their conservative form. The solution domain is formulated using a finite number of contiguous control volumes (CVs). The conservation equations are enforced on each CV as well as the overall flow volume. The FV methods can accommodate unstructured mesh, so the FV codes rendering them suitable for complex geometries, however, with extra computational effort. Finite element methods (FEM) are based on potential energy considerations of the system employing variational expressions.

The Boundary Element Method (BEM) is a numerical method for solving linear partial differential equations by the discretisation of an integral equation that is both mathematically equivalent to the original partial differential equation [174]. The BEM consists of an integral equation, and therefore, the reformulation of the PDE is necessary. Furthermore, this equation is defined on the boundary of the domain and an integral that relates the boundary solution to the solution at points in the domain. The computational efficiency of the BEM is one reason for the increased attention.

3.3.2 Structural analysis using finite element methods

FEM is one of the most important developments in applied mechanics for analysis of any given physical phenomenon in two or three space variables. They are very appealing to engineers because of their simplicity, compactness, and result-oriented features. An extensive system can be subdivided into smaller and simpler parts, typically known as finite elements. Extensive reviews on the method can be found in [35, 56].

In the linear analysis, the force-displacement relationship holds linear. This approach is practically applicable to the structural problems in which the stresses stay in the elastic zone of the used material. The stiffness matrix remains constant throughout the analysis.

The analyses of linear structures can be approximated furthermore by a superposition of a small number of its eigenmodes. Modal superposition is a powerful technique that helps for reducing the computation cost.

In the nonlinear analysis, the force-displacement relationship is nonlinear, which may be due to geometrical nonlinearity, large deformations, or material nonlinearity. Consequently, the stiffness matrix needs to be updated throughout the analysis.

In geometrically nonlinear analysis, the changes in geometry due to structural deformations are considered in the formulation of the constitutive and equilibrium equations. Material nonlinearity is associated with the inelastic behaviour of a structure, generally characterized by a force-deformation relationship.

3.4 The Vortex Particle Method

This section provides the formulation of the classical Vortex Particle Methods (VPM), which has been used in this study for the analysis of fluid motion. The VPM are based on the vorticity discretization of the velocity field by particles. The Lagrangian formulation of the governing Navier–Stokes equations determines the evolution of the computational elements. The major advantages that the classical vortex method enjoys over grid-based methods are

an automatic adaptivity of the computational elements and low numerical dissipation [174]. Vortex methods are mesh-free, which is in the context of describing the boundaries of the computational domain using a surface mesh only. More details about the vortex methods are available in [64].

A computer program ‘VXflow’ was developed in Morgenthal [174] based on the VPM for numerical analysis of bluff body aerodynamics. The efficiency of the solver was enhanced further in Morgenthal and Walther [177]. The governing equations of the VPM and the existing implementations for analysing different aerodynamic interaction phenomena are presented here briefly. In this study, this numerical scheme is extended further for FSI simulation of thin-walled flexible structural systems which will be discussed in the next chapter.

3.4.1 Governing equations of fluid motion

The flow field is governed by the unsteady Navier–Stokes (NS) equations, and for incompressible unsteady flow of a viscous fluid, the continuity and momentum equations can be described in terms of velocity $\mathbf{u}(\mathbf{x}, t)$ as:

$$\nabla \cdot \mathbf{u} = 0, \quad (3.2)$$

$$\frac{\partial \mathbf{u}}{\partial t} + (\mathbf{u} \cdot \nabla) \mathbf{u} = -\frac{1}{\rho} \nabla p + \nu \nabla^2 \mathbf{u}, \quad (3.3)$$

where ρ is the fluid density, p is the pressure and ν is the kinematic viscosity. It is found advantageous to describe the dynamics of the fluid flow in terms of the evolution of the vorticity field. The vorticity $\boldsymbol{\omega}$ is the curl of velocity field \mathbf{u} of a flow, such that

$$\boldsymbol{\omega} = \nabla \times \mathbf{u}. \quad (3.4)$$

For two-dimensional flows, the NS Eq. (3.3) in terms of the vorticity can be written as:

$$\frac{\partial \omega}{\partial t} + (\mathbf{u} \cdot \nabla) \omega = \nu \nabla^2 \omega. \quad (3.5)$$

This eliminates the pressure term, which provides a lot of computational advantages. For inviscid flow Eq. (3.5) can be rewritten in substantial derivative notation:

$$\frac{D\omega}{Dt} = 0. \quad (3.6)$$

Here, equation (3.6) allows the use of gridless numerical scheme and discretization of particle elements in Lagrangian manner. The velocity field can be expressed in terms of stream function Ψ and vorticity such that it results in Poisson equation

$$\nabla^2 \Psi = -\omega. \quad (3.7)$$

The use of Green’s functions is a common approach for solving the Poisson equation to obtain

the velocity distribution from a field of vorticity. By taking the curl of the solution $\Psi(\mathbf{x})$, the velocity field in \mathcal{R}^2 can be computed using Biot-Savart relation

$$\mathbf{u}(\mathbf{x}) = \mathbf{U}_\infty - \frac{1}{2\pi} \int_{\mathcal{D}} \frac{\omega(\mathbf{x}_0) \times (\mathbf{x}_0 - \mathbf{x})}{|\mathbf{x}_0 - \mathbf{x}|^2} d\mathcal{D}_0. \quad (3.8)$$

For a moving body immersed in fluid flow, the kinematic velocity boundary condition at the solid surface states that the surface is impermeable

$$\mathbf{u}_B \cdot \mathbf{n}_0 = u_{n_0}, \quad (3.9)$$

$$\mathbf{u}_B \cdot \mathbf{t}_0 = u_{t_0}, \quad (3.10)$$

where \mathbf{n} is the surface unit normal vector, u_0 is the surface velocity and t_0 is the surface unit tangential vector.

Vorticity boundary values

The vorticity on the surface of the solid bodies which satisfies the velocity boundary condition is found through the Biot-Savart relation

$$\int_{D_B} \frac{\omega_0(x_0) \times (x_0 - x)}{|x_0 - x|^2} d\mathcal{D}_{B_0} = I(x_B) - A_d [u(x_B) - U_\infty] \quad (3.11)$$

With the use of a surface vorticity sheet γ_0 , the Fredholm integral equation in vector form can be expressed from Eq. (3.11) as follows

$$\int_B \frac{\gamma_0 \times (\mathbf{x}_0 - \mathbf{x})}{|\mathbf{x}_0 - \mathbf{x}|^2} d\mathcal{B}_0 = \mathbf{I} - 2\pi [\mathbf{u}_0 - \mathbf{U}_\infty], \quad (3.12)$$

in which the components of the vector equation (Eq. (3.12)) are Fredholm integral equations in the unknown γ_0 .

The simulation of phenomena governed by the two-dimensional Euler equations are the first and simplest example in which vortex methods have been successfully used. The vortex particle methods (VPM) involve with several components which are kinematics, convection, boundary conditions imposed using boundary elements, and the modelling of diffusion.

Discretisation of the vorticity field

The classical 2D vortex method is based on the discretization of the vorticity field by a finite sum of N_p Lagrangian particles located at \mathbf{x}_p which can be expressed as follows

$$\omega(\mathbf{x}, t) = \sum_{p=1}^{N_p} \delta(\mathbf{x} - \mathbf{x}_p(t)) \Gamma_p, \quad (3.13)$$

where $\omega(\mathbf{x}, t)$ is the vorticity at position \mathbf{x} and time t , δ is the Dirac delta function, Γ_p is the

strength of p th particle, and $\mathbf{x}_p(t)$ is the position. The use of Eq. (3.13) in Eq. (3.8) yields

$$\mathbf{u}(\mathbf{x}_p) = \mathbf{U}_\infty - \frac{1}{2\pi} \sum_{p=1}^{N_p} \frac{\mathbf{e}_z \times (\mathbf{x}_p - \mathbf{x})}{|\mathbf{x}_p - \mathbf{x}|^2} \Gamma_p = \mathbf{U}_\infty - \sum_{p=1}^{N_p} \mathcal{K}(\mathbf{x}_p - \mathbf{x}) \Gamma_p, \quad (3.14)$$

where \mathcal{K} is the velocity kernel. The Gaussian core which was used can be expressed as follows

$$\mathcal{K}_\sigma(\mathbf{r}) = \frac{\mathbf{e}_z \times \mathbf{r}}{2\pi|\mathbf{r}|^2} \left[1 - \exp\left(-\frac{|\mathbf{r}|^2}{\sigma^2}\right) \right] \quad (3.15)$$

The vorticity transport equation (Eq. 3.5) is solved using an operator splitting technique. The first step involves the solution of the inviscid Euler equation

$$\frac{\partial \omega}{\partial t} + (\mathbf{u} \cdot \nabla) \omega = 0, \quad (3.16)$$

which is approximated by the convection of the vortex elements. The second step of the fractional step algorithm involves the solution of the diffusion problem

$$\frac{\partial \omega}{\partial t} = \nu \nabla^2 \omega, \quad (3.17)$$

which is solved using the random walk technique.

3.4.2 The Boundary Element Method

This section discusses briefly on the use of boundary element method for the discretization of immersed bodies in flow field. The geometry of immersed bodies is discretized assuming piecewise linear panels ($\mathbf{x}_i, i = 1, \dots, N_i$) of approximately uniform length ($\Delta s_i = |\mathbf{x}_{i+1} - \mathbf{x}_i|$). This creates a polygon of N_i panels of lengths Δs_i . The surface vorticity (γ_i) is discretized as sheets of linearly varying vorticity along the panels, as shown in Fig. 3.1.

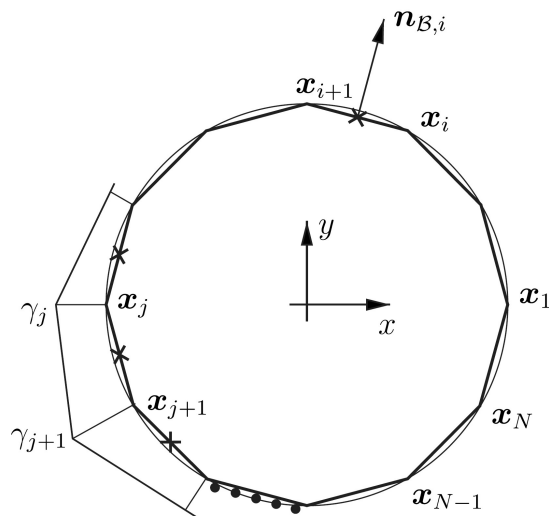


Figure 3.1: Schematic of the boundary element discretization for a circular cross-section. The surface vortex sheet strength is linear along a panel. The boundary condition is enforced at the panel centre point (•). Also indicated (d) are the blobs created from the surface sheet strength and to be released in the next step [177].

The enforcement of the no-penetration velocity boundary condition requires the solution of the Fredholm integral equation (Eq. (3.12)),

$$\left(\int_B \frac{\boldsymbol{\gamma}_0 \times (\mathbf{x}_0 - \mathbf{x})}{|\mathbf{x}_0 - \mathbf{x}|^2} d\mathbf{B}_0 \right) \cdot \mathbf{n} = (\mathbf{I} - 2\pi [\mathbf{u}_0 - \mathbf{U}_\infty]) \cdot \mathbf{n}. \quad (3.18)$$

where $\boldsymbol{\gamma}_0$ is the unknown surface vorticity. The bound vortices are obtained from equation $\boldsymbol{\mathcal{M}}\boldsymbol{\gamma}_0 = \mathbf{b}$, in which $\boldsymbol{\mathcal{M}}$ is the influence matrix that contains the influence coefficients [147] in order to describe the mutual induction of the vortex sheets while the right-hand side (\mathbf{b}) contains all external influences such as the induced velocities on the panels from the free stream contribution. The detailed components of the equation $\boldsymbol{\mathcal{M}}\boldsymbol{\gamma}_0 = \mathbf{b}$ for a body can be expressed as follows

$$\begin{bmatrix} m_{1,1} & \dots & m_{1,j} & \dots & m_{1,N_l} \\ \vdots & \ddots & \vdots & \ddots & \vdots \\ m_{i,1} & \dots & m_{i,j} & \dots & m_{i,N_l} \\ \vdots & \ddots & \vdots & \ddots & \vdots \\ m_{N_l,1} & \dots & m_{N_l,j} & \dots & m_{N_l,N_l} \\ \frac{1}{2}(\Delta s_1 + \Delta s_{N_l}) & \dots & \frac{1}{2}(\Delta s_j + \Delta s_{j-1}) & \dots & \frac{1}{2}(\Delta s_l + \Delta s_{l-1}) \end{bmatrix} \begin{Bmatrix} \gamma_1 \\ \vdots \\ \gamma_i \\ \vdots \\ \gamma_{N_l} \end{Bmatrix} = \begin{Bmatrix} b_1 \\ \vdots \\ b_i \\ \vdots \\ b_{N_l} \\ \Gamma_{system} \end{Bmatrix} \quad (3.19)$$

where $m_{i,j}$ is the normal component of the velocity induced at the i th panel by the j th panel. The induced velocity can be obtained from a simple integration of the mutual influence. The expression for the generic component $m_{i,j}$ in eq. (3.19) reads:

The components b_i entail the influence of the free vorticity, inflow velocity and rotation/deformation of the body surface can be easily computed. The circulation of the system is

$$\Gamma_{TOT} = - \left(\sum_{i=1}^{N_l} \Gamma_p - 2A\Omega \right), \quad (3.20)$$

where Γ_p is the circulation carried by the volume particles, Ω is the angular velocity of the body of area A and the term $2A\Omega$ accounts for the circulation incurred by the rotation of the body. The obtained system of equations is over-determined and can be solved in a least squares sense by converting it as follows:

$$\boldsymbol{\mathcal{M}}^T \boldsymbol{\mathcal{M}} \boldsymbol{\gamma} = \boldsymbol{\mathcal{M}}^T \mathbf{b}, \quad (3.21)$$

for the least squares solution of an inconsistent system $\mathbf{A}\mathbf{x} = \mathbf{b}$ of m equations and n unknowns. For an arrangement of panels which do not change their relative position, which is the case of a single body moving without deformation, the influence matrix $\boldsymbol{\mathcal{M}}$ does not change. It is therefore assembled at the beginning of a simulation and $\boldsymbol{\mathcal{M}}^T \boldsymbol{\mathcal{M}}$ computed, inverted and stored. The transpose $\boldsymbol{\mathcal{M}}^T$ is also stored as it is multiplied by the right-hand side vector at each time step. The surface vorticity found by solving this system is assigned to the nodes on the boundary $\Gamma_{0_t} = \frac{1}{2} (\gamma_{0_t} \Delta s_i + \gamma_{0_{t+1}} \Delta s_{i+1})$ and subsequently released into the flow. More details about the fundamental equations and methodological steps of the flow solver can be found in Morgenthal [174], Morgenthal and Walther [177]

3.5 Application of Vortex methods

The nature of the aerodynamic conditions and its effects on civil engineering structures can be very complicated. Therefore, the reliable prediction of dynamic loads and structural response is a significant challenge. Vortex methods have attracted remarkable attention in recent years mainly for applications in bluff body aerodynamics, such as the analysis of aerodynamic problems in long-span bridges.

3.5.1 Aerodynamic analysis of bluff bodies

Most past works on vortex methods were directed towards developing techniques [62, 63, 90, 144, 145, 163, 198, 209]. Extensive details of the vortex methods can be found in Cottet et al. [64]. There had also been several studies on 3D flow simulation [104, 146, 190, 191]. Several studies utilized GPU for accelerated performance of VPM such as in [175, 198, 199]

The impulsively started flow past a circular cylinder has been a benchmark case, and several studies had been performed in [51, 144, 154] using vortex methods. The knowledge of the flow field around bluff structures is of major importance in the fields of civil and wind engineering. Unsteady flow around the square and rectangular section cylinders using a two-dimensional (2D) discrete vortex method in [156, 231], and the study outcome have been found quite satisfactory with results taken from various experimental data. The flow past a flat plate, both fixed and in heave or pitch motion are simulated in [244] using vortex methods to study on the boundary layer growth, vortex shedding and interaction between free shear layers.

The 2D vortex method was used further for analysing aeroelastic analysis in bridge decks; the flow around static different bridge cross-sections as well as the cross-sections undergoing forced oscillatory cross wind and twisting motion were investigated in [151, 152, 244] for assessment of drag coefficient, Strouhal number and aerodynamic derivatives for application in aeroelastic analyses.

The existing implementation of VPM with the boundary element technique was used for modelling of flow past bluff bodies in Morgenthal [174], Morgenthal and Walther [177]. A number of studies on fundamental problems of fluid mechanics had been presented in Morgenthal [174] such as the study on boundary layer of static flat plate (see Fig. 3.2(a-b)), the flow around circular cylinders (see Fig. 3.2(c)). The ability of the method to simulate flow around complex geometry such as cactus was modelled (see Fig. 3.2(d)). Applications of the computer code to aeroelastic phenomena in the field of wind engineering of long-span bridges were presented in Morgenthal [173], Morgenthal and Walther [177]. The solver was successfully used in Abbas and Morgenthal [2], Kavrakov and Morgenthal [139], Morgenthal [173, 174] for analyses of complex aerodynamic phenomena in long-span bridges.

The VPM was extended recently with a novel adaptive solution strategy in Milani [167], Milani and Morgenthal [168] to ensure a balance of accuracy and computational efficiency in resolving flows dominated by structural bodies of different scales. The efficiency of the method depends on high spatial numerical discretization near the fluid-structure interface and a progressive coarsening of vorticity field away from the bodies (see Fig. 3.3(a)).

A pseudo-three-dimensional (3D) extension of VPM was presented in Morgenthal et al. [175] for the numerical aerodynamic analysis of line-like structures such as long-span bridges (see Fig. 3.3(b)). Several two-dimensional (2D) simulations are performed for sections along the structure. The in-plane forces and displacements are coupled to a 3D dynamic represen-

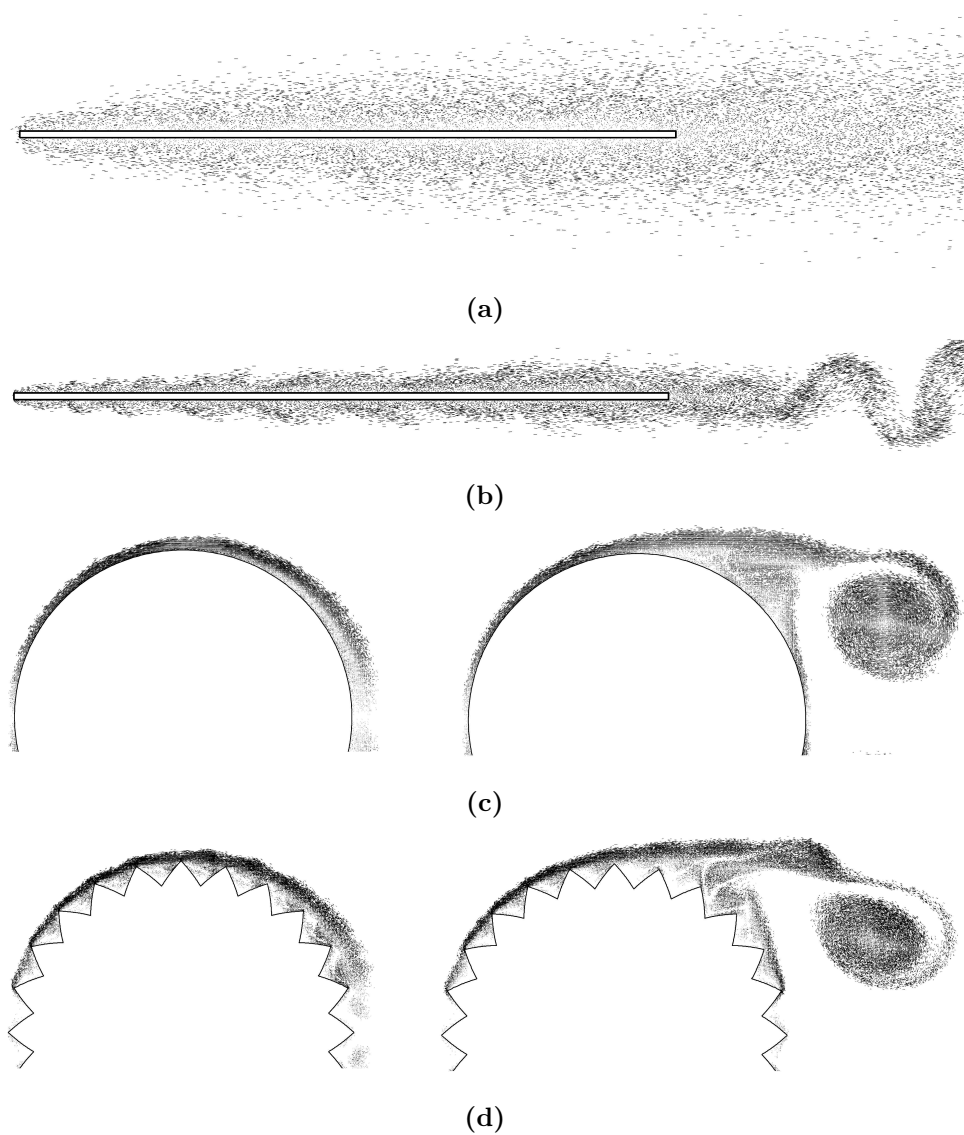


Figure 3.2: The simulation of flow around static bluff bodies using VPM: (a) flat plate at $Re = 10^3$, (b) flat plate at $Re = 10^4$, (c) circular cylinder at $Re = 3000$, and (d) cactus section at $Re = 3000$ [174].

tation of the structure to perform fully coupled fluid–structure interaction simulations (see Fig. 3.3(c)).

The seeding of pre-calculated vortex particles was utilised within the mentioned VPM-based CFD solver to model inflow turbulence for buffeting and wake buffeting analyses, c.f. Chawdhury and Morgenthal [52], Kavrakov et al. [138], Kavrakov and Morgenthal [140, 141], Morgenthal et al. [175], Tolba and Morgenthal [234, 236]. The concept of seeding particles within the framework of VPM was introduced in Prendergast and McRobie [192], Prendergast [193] for modelling of 2D unsteady wind. The particles were pre-calculated from statistically generated target wind field. The method was further employed in Hejlesen et al. [115], Rasmussen et al. [197] for the simulation and estimation of the aerodynamic admittance in bridge aerodynamics. The particle seeding technique within the framework of the presented VPM based solver was shown in Chawdhury and Morgenthal [52] for reproduction of a simulated flow field. The further extension of the solver in pseudo-three-dimensional (pseudo-3D) context was shown in Morgenthal et al. [175], Tolba and Morgenthal [234] for analysing the aeroelastic

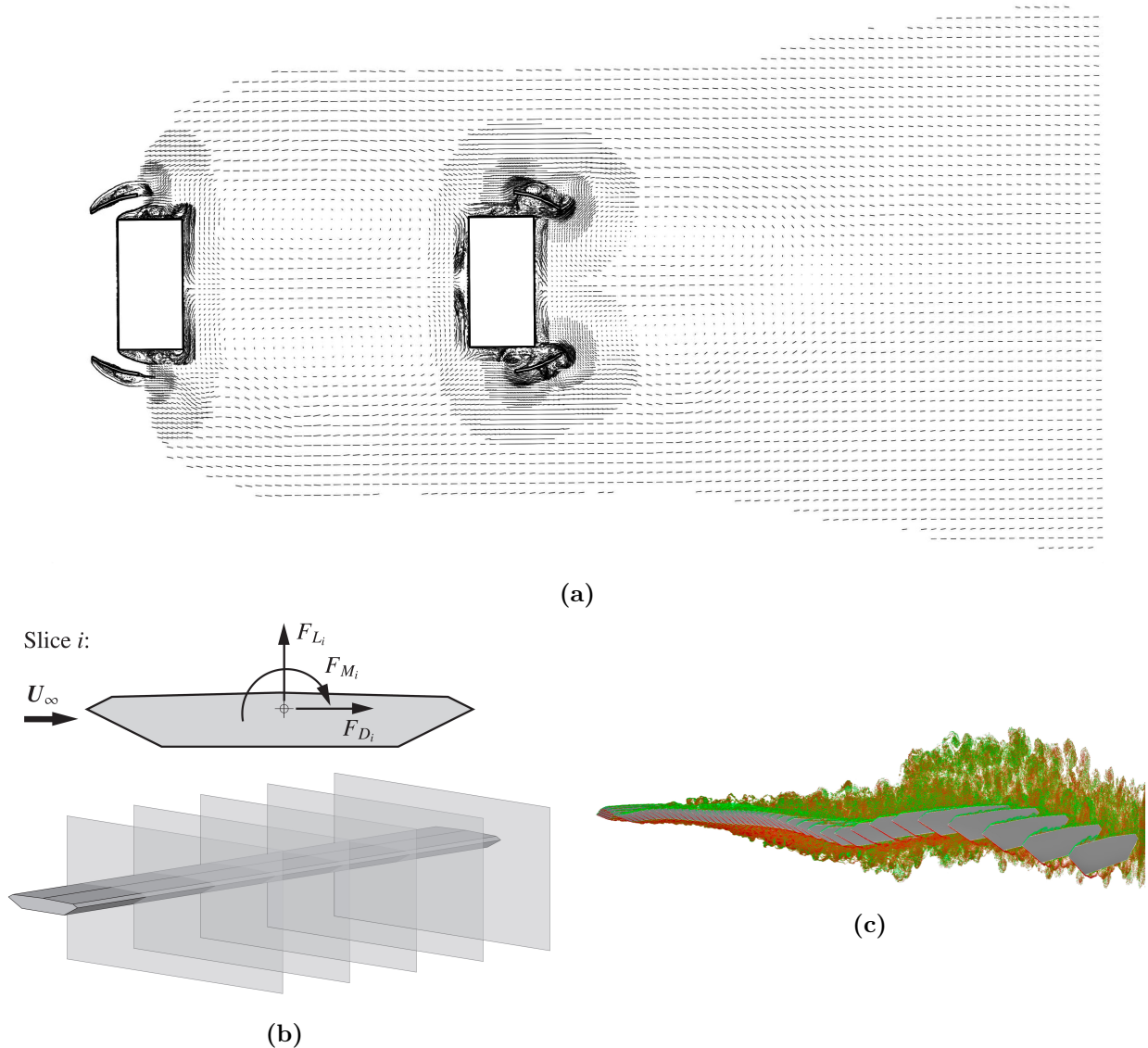


Figure 3.3: Extensions on dynamic analysis models within the existing framework of in-house CFD solver based on VPM: (a) the particle maps after applying adaptive solution techniques to Alcónetar bridge arch section with flow deflectors [168], (b) Schematic of the pseudo-3D method: standard CFD slice analysis and multi-slice arrangement along the structure [175], (c) instantaneous particle map for the pseudo-3D flutter analysis under laminar flow during LCO at maximum positive rotation [140].

response of bridges due to the turbulent wind. In contrast to the previous studies, in which the particles were seeded to model 2D or 3D turbulent flow field, the particles are seeded in this study to simulate periodic flow fluctuation, specifically along the flow direction.

3.5.2 Studies of deformable bodies using vortex methods

The numerical analysis of FSI problems can be extremely challenging when a flexible body undergoes large deformations. The FVM is commonly used flow solver for such coupled analysis. Over the last decades, VPM has been used successfully for bluff body aerodynamics as well as FSI simulations of bluff bridge decks. However, very few uses of VPM have been found in the literature regarding the FSI problems with deformable bodies. It is probably due to the inefficiency of VPM in 3D for FSI simulations when compared to grid-based methods

such as FVM. However, there are several FSI problems, such as line-type flexible structures, the coupled behaviour of which can be predicted in 2D with satisfaction and computational efficiency.

Among a few studies of vortex methods of FSI simulations, Yamamoto et al. [258] used the discrete vortex method (DVM) and investigated the hydroelastic interactions that take place between oscillating flexible cylinders and fluid forces. In Eldredge [89], the coupled solutions of fluid and body dynamics in problems of biolocomotion were analysed. The added mass effects from the fluid were considered with the intrinsic inertia of the body to allow for simulations of bodies of arbitrary mass, including massless or neutrally buoyant bodies. In Rossinelli et al. [198], the VPM was used to handle simultaneously multiple deforming and stationary bodies by simulating swimming entities swimming in an environment with fixed obstacles. The deformation of the flexible bodies was assigned earlier, and therefore, it was not a complete FSI simulation where the flow effects on the motion of the body.

Important to note that in the studies as mentioned above of deformable bodies, the modelled fluid had been water. In recent past, Sessarego et al. [211] described the development of a new aeroelastic code that combines a 3D vortex method for interactive rotor aerodynamic simulations, with the finite element structural dynamics model. It was presented for analysis of modern wind turbines. The model was used further in Sessarego et al. [210] for design optimization of a curved wind turbine blade.

The aeroelastic interaction of flexible body is quite challenging. In many cases, simplified assumptions are employed to be to use an existing model for FSI analysis. For example, the flutter-induced aeroelastic response of a flexible T-shaped cantilever was studied in Park et al. [186]. The study utilised the 2D FSI model of VPM, which was based on the rigid body only. Therefore, the flexible motion of the T-shaped section was approximated with the vibration of an equivalent rigid T-beam section. A simplified single degree of freedom (SDOF) model was used in VPM to model the coupled behaviour of the system (it is shown later in Sec. 6.4.3). The critical flutter wind speed was identified reasonably well when compared with the wind tunnel experiment. However, the nonlinear LCO of such a flexible system in higher wind speeds can not be predicted with a simplified model, which is necessary for the optimisation of harvester performance.

3.6 Summary

This chapter has described briefly different aspects of numerical models for FSI simulations. The coupling mechanisms depending on the interaction between fluid and structure have been discussed, including their advantages and disadvantages. The type of mesh treatment in FSI simulations has been reviewed together with the issue of large-displacement problems. The governing equations of the vortex particle method (VPM) and its existing implementations have been discussed since the VPM is extended and utilised throughout this thesis. Important to note that the VPM is limited to static and coupled FSI simulations of rigid cross-sections. The further extensions of the flow solver for FSI simulations of thin-walled flexible structural systems are presented in the following chapters, including the validation and different case studies.

Chapter 4

Partitioned extensions using Vortex Particle Methods for FSI simulations

4.1 Introduction

This chapter presents newly developed partitioned numerical extensions of Vortex Particle Methods (VPM) to analyse coupled interaction between the fluid and thin-walled flexible structural systems. In this context, the new extension of 2D VPM is proposed for analysing large-displacement FSI problems of thin plate systems. On the other hand, the extension of pseudo-3D VPM is newly implemented to analyse FSI simulations of shell-type structures.

Fluid–structure interaction (FSI) problems of thin and flexible bodies encounter across a broad range of Reynolds numbers and flow regimes. A flexible structure can exhibit a large-amplitude motion depending on the interaction between the fluid and structure. The development of a numerical model for analysing FSI problems is very challenging. It is essential not only to model the effects of the deforming body on the flow fields but also to analyse the flow-induced structural motion accurately. In particular, when a flexible structure undergoes large-displacement due to the interaction with the incoming flow, it is necessary to consider geometrical nonlinear effects of the structure.

The partitioned numerical approaches offer to synthesise between different advanced or appropriate fluid and structural models. However, the challenges exist the information exchange and boundary conditions between the solvers due to their differences in methods and distinctive architecture. The VPM offers appealing perspectives in terms of computational efficiency and resolution. Moreover, it is not a necessity to conform mesh at the boundary interface since the primary method is grid-less. Furthermore, the implementation of Boundary Element Method (BEM) allows to discretise and analyse the large-amplitude motion of deforming thin body very efficiently. The projection of information from mid-surface to the boundary surfaces requires special attention [107]. The enforcement of the no-penetration velocity boundary condition is necessary to solve the vorticity field [174] at every time step, since the discretised geometry of a deforming body may be continuously different.

In the following, the further modifications which are added to the flow solver based on VPM, the governing equations of the structural solver, and the coupling procedures between the flow

and structural solver are discussed in details. This chapter presents only the validation of the enforcement of required boundary conditions for the coupled solvers using forced oscillation analyses. The validation and application of the coupled solvers on FSI problem of thin bodies are presented in Chapter 5.

Within the framework of 2D coupled VPM, this chapter presents a brief introduction of a numerical model for the aero-electromechanical coupled analysis of aeroelastic energy harvesters. More details of the method and its application on energy harvesters, including performance optimizations, are presented in Chapter 6. Furthermore, two new extensions of 2D VPM, which are proposed for the simulation of inflow turbulence, are introduced only. However, the details are shown in Chapter 7 with the application of the coupled FSI models in inflow turbulence.

4.2 A large-displacement FSI model using 2D VPM

The section presents a newly developed partitioned numerical extension of the 2D VPM for large-displacement FSI analysis of thin-walled flexible structural systems. Initially, the discussion shows the modelling of flow around deforming moving geometry. Boundary discretisation of a moving body is a critical concern for accurate prediction of surface vorticity. The application of the BEM and the enforcement of required boundary conditions are highlighted. The corotational finite element formulation is used to consider geometrically nonlinear effects of flexible elements. The equation of motion is modelled at the mid-surface of the thin body. Since the interface of fluid and structure of the presented coupled model is non-conforming type, the procedure for the projection of information in between the solvers is an essential issue, and therefore, discussed step by step with several schematics. In brief, the section discusses, sequentially, the further modifications implemented to the flow and structure solvers, which are required for the coupled FSI algorithm.

4.2.1 Modelling of flow around thin and deformable geometry

Surface discretisation using Boundary Element Method

The interaction between the fluid and moving deformed body depends on several factors such as the change of shape of the structure, the relative movement between fluid and structure. An accurate representation of the vortex sheet on the moving deformed body is of major concern to model the flow effects.

For a thin flexible plate deforming largely under specific inflow condition, as shown in Fig. 4.1, the instantaneous boundary element discretisation is shown at initial time $t = t_0$ for the unchanged body, whereas at $t = t_n$ for the deformed body. Here, n indicates the simulation step such that $n = 1, 2, \dots, NT$, in which NT is the number of time steps. The geometry is discretized, in all cases, assuming piecewise linear panels (\mathbf{x}_i , $i = 1, \dots, N_{panel}$) of approximately uniform length ($\Delta_{s_i} = |\mathbf{x}_{i+1} - \mathbf{x}_i|$), as mentioned in previous chapter for rigid sections. Control or sampling points \mathbf{x}_{c_i} are defined at the middle of each panel i . It is the control point at which the velocity boundary condition is imposed (cf. Fig. 4.1).

In order to solve the vorticity distribution γ_0 on the surface panels, it is necessary to satisfy the velocity boundary conditions on the solid surface at the centre points of the each panels. It requires the calculation of induced velocity on the surface panels, and furthermore, the enforcement of the velocity boundary condition. An overview of the coupled algorithm

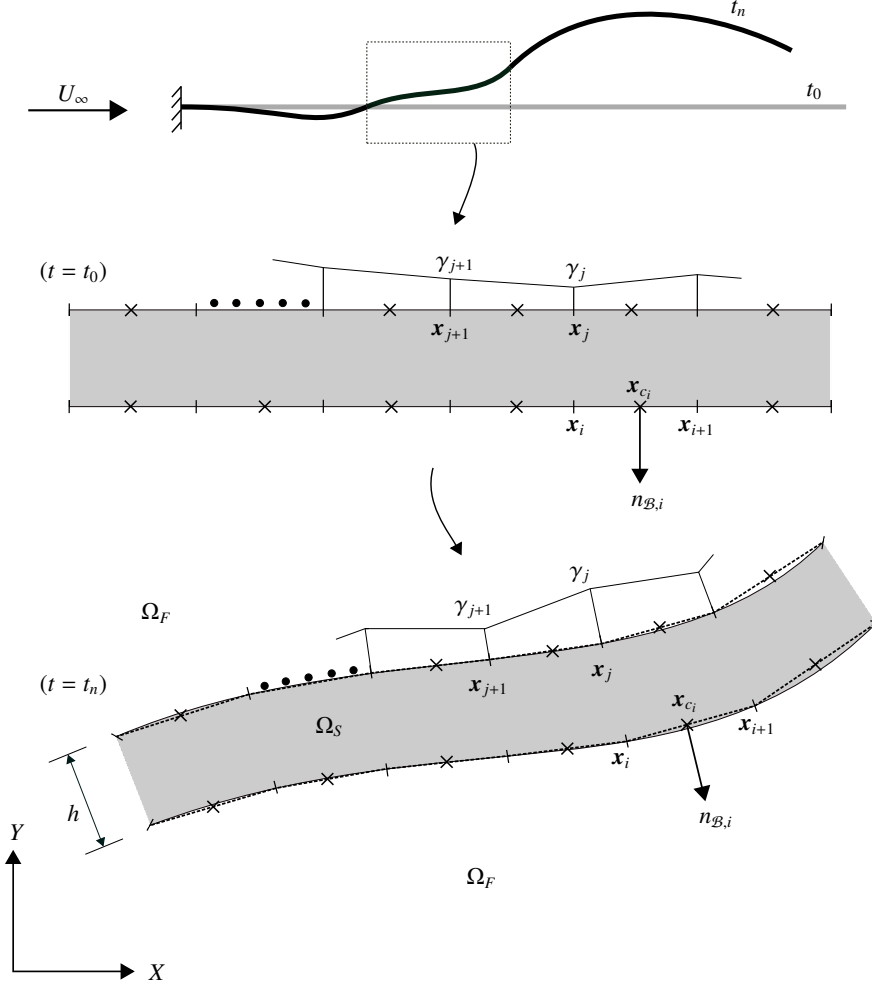


Figure 4.1: A partial schematic presentation of the boundary element discretisation of a thin cantilever flexible plate of thickness h , which is flapping in incoming flow U_∞ . Here, the instantaneous discretisation of the system is shown for two time instances: t_0 and t_n . The surface vortex sheet strength is considered linear along the surface panel. The boundary condition is enforced at the panel centre point (\times). The indicated blobs (\bullet) are created from the surface sheet strength and to be released in the next step. Here, Ω_F and Ω_S indicates the fluid and structural domain, respectively.

is visualised in Fig. 4.2; however, by focusing only on the 2D VPM. In the following, the modifications, which are implemented for the 2D extension of VPM to perform coupled FSI simulation, are highlighted according to their sequence (at every time step):

- Store flow-induced panel pressures on the surface for the structural solver.
- Import the solution from the structural solver, which is projected from the structural mesh to the boundary panels.
- Update the position of the deformed boundary panels and panel velocities,
- Restructure panel velocities in local coordinate to satisfy velocity boundary condition.
- Calculation of influence matrix based on the updated boundary panels.
- Solve for the new surface vorticity.

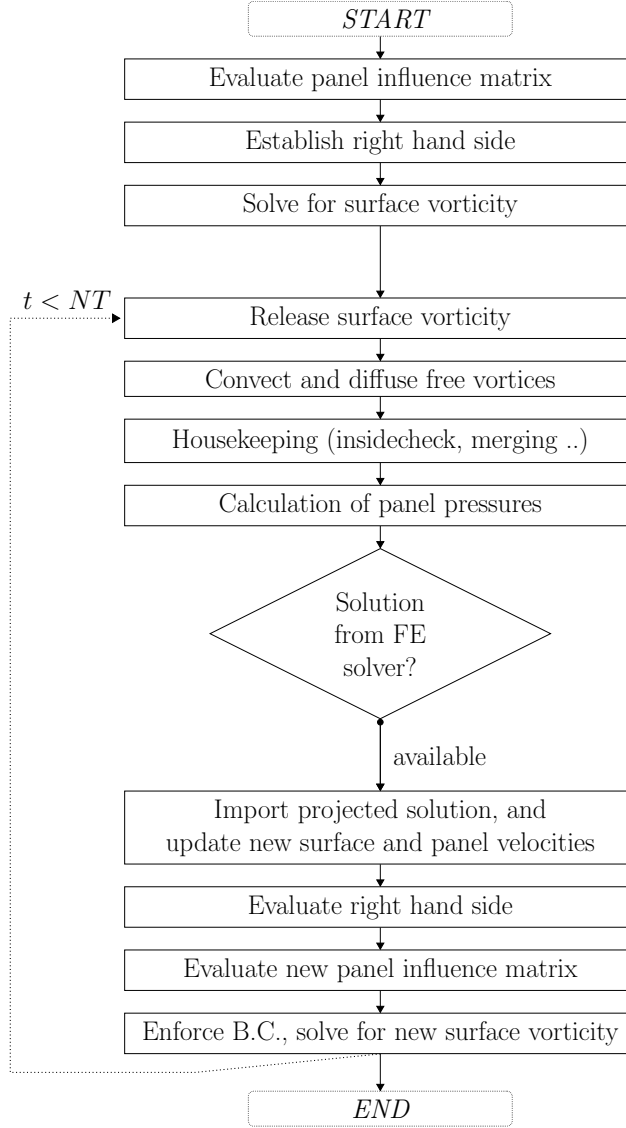


Figure 4.2: The outlook of coupled FSI algorithm only from the 2D vortex particle method.

Enforcement of boundary conditions and surface vorticity

The kinematic velocity boundary condition at the solid surface which means the surface is impermeable can be expressed as follows

$$\mathbf{u}(\mathbf{x}_{\mathcal{B}}) \cdot \mathbf{n}_{\mathcal{B}} = 0. \quad (4.1)$$

where $\mathbf{n}_{\mathcal{B}}$ is the surface unit normal vector. In case of 2D flow field, the vorticity on the surface of the solid bodies which satisfies the velocity boundary condition can be obtained through the Biot-Savart relation,

$$\int_{\mathcal{B}} \frac{\omega_0 \times (\mathbf{x}_0 - \mathbf{x})}{|\mathbf{x}_0 - \mathbf{x}|^2} d_{\mathcal{B}_0} = (\mathbf{I} - 2\pi [\mathbf{u}_0 - \mathbf{U}_{\infty}]) \quad (4.2)$$

where \mathbf{I} is the velocity induced on the surface by the vorticity in the fluid excluding the contributions from the surface \mathcal{B} . The vorticity on the surface can be considered in its

integral by defining the surface vortex sheet over a layer whose thickness h tends to zero as

$$\gamma_0 = \lim_{h \rightarrow 0} \int_0^h \boldsymbol{\omega} d\mathbf{n}. \quad (4.3)$$

where \mathbf{n} is the surface normal vector. The use of Eq. (4.3) in Eq. (4.2) results in the kinematic boundary condition,

$$\left(\int_B \frac{\gamma_0 \times (\mathbf{x}_0 - \mathbf{x})}{|\mathbf{x}_0 - \mathbf{x}|^2} d\mathcal{B}_0 \right) \cdot \mathbf{n} = (\mathbf{I} - 2\pi [\mathbf{u}_0 - \mathbf{U}_\infty]) \cdot \mathbf{n}. \quad (4.4)$$

This Fredholm integral equation (Eq. (4.4)) in vector form can be solved for the unknown γ_0 . With the assumption of linear variation of γ_0 , the influence of the vortex sheets on all the other panels can be approximated as follows

$$\mathcal{M}\gamma_0 = \mathbf{b} \quad (4.5)$$

where \mathcal{M} is the influence matrix describing the mutual induction of the vortex sheets, and includes a separate equation for the enforcement of the Kelvin theorem. The right-hand side (\mathbf{b}) contains all external influences, and the system of equations is solved in the least squares sense. The surface vorticity found by solving this system is assigned to the nodes on the boundary Γ_{0_i} and subsequently released into the flow.

Instantaneous solution of the surface vorticity

If an immersed thin plate undergoes large deformation in incoming fluid flow, as shown in Fig. 4.1, it is necessary to consider the mutual effects of deformed body and flow field in the coupled numerical analysis. For the extended coupled model, the no-penetration boundary condition is used, which was mentioned in the initial version of the code. However, the boundary condition needs to be satisfied now at every time step t_n such that

$$\left(\int_B \frac{\gamma_0 \times (\mathbf{x}_0 - \mathbf{x})}{|\mathbf{x}_0 - \mathbf{x}|^2} d\mathcal{B}_0 \right)_{t_n} \cdot \mathbf{n} = (\mathbf{I} - 2\pi [\mathbf{u}_0 - \mathbf{U}_\infty])_{t_n} \cdot \mathbf{n} \quad (4.6)$$

where γ_0 is the unknown surface vorticity of the deformed body at time t_n . With the assumption of linear variation of γ_0 , the influence of the vortex sheets on all the other panels can be approximated at time step t_n as follows

$$\mathcal{M}_{(t_n)}\gamma_{0(t_n)} = \mathbf{b}_{(t_n)}, \quad (4.7)$$

where $\mathcal{M}_{(t_n)}$, $\gamma_{0(t_n)}$, and $\mathbf{b}_{(t_n)}$ are the influence matrix, unknown surface vorticity, and right hand side vector, respectively, at time step t_n .

It is mentioned in previous chapter that for an arrangement of surface panels which do not change their relative position, i.e. in the case of a single body moving without deformation or an assembly of bodies undergoing a solid body motion, the influence matrix \mathcal{M} does not change. It is therefore for rigid bodies assembled at the beginning of a simulation and $\mathcal{M}^T\mathcal{M}$ computed, inverted and stored. The transpose \mathcal{M}^T is also stored as it is multiplied by the right-hand side vector at each time step.

For a coupled FSI analysis, particularly for large-displacement problems, it is challenging but necessary to account the shape modification effects on the flow field around the deformed

body. The continuous change of the geometry makes it necessary to formulate the influence matrix $\mathcal{M}_{(t_n)}$ in Eq. (4.7) and solving the vortices at every time step to calculate the influence of modified shape and its motion on the flow field accurately.

The new positions of the surface panels and control points are updated based on the projected structural solution from the mid-surface to the deformed boundary. The right hand side vector $\mathbf{b}_{(t_n)}$ is then calculated in local panel coordinate based on the updated geometry.

Inside check algorithm

Importantly, for a vortex particle it is strictly not possible to be convected into the body, and to ensure that it is necessary to perform the inside check on whether a vortex has travelled inside the solid region. The check was performed by considering an imaginary line from the vortex' position (x_p, y_p) to (x_p, ∞) . If the number of surface edges crossed by this line counted is odd, the vortex is inside, otherwise it is outside the body [174].

In case of flexible implementation of FSI algorithm, it is necessary to define many corner points than rigid bodies. In the previous implementation of VPM for rigid bodies, the section of the undistorted thin plate, as shown in Fig. 4.1, can be identified by four corner points. The boundary elements are determined further by equal discretisation of the edges of the section. In contrast, present implementation suggests to discretise the surface beforehand and to use the geometry nodes as the corner points, which is from the beginning of an analysis. Once the body experiences significant distortion, all the geometry nodes act as corner points and perform the inside check to ensure that a vortex has travelled inside the body.

4.2.2 Nonlinear finite element analysis using corotational beam

Accurate and efficient computation of structural response is necessary to study the stability analysis of thin-plates those undergo large displacements. Note that the previous coupled FSI implementation of 2D VPM has been based on linear structural vibration behaviour and with a maximum of three degrees of freedom (DOFs) of the whole rigid section. The analysis of large-amplitude motions of flexible thin systems requires a more advanced structural modelling approach to accurately predict the system vibrations, which is not possible with few DOFs. Consequently, a structural solver based on 2D corotational finite element (FE) formulation is coupled with the 2D VPM to account for the geometrically nonlinear effects accurately.

Modelling of structural motion

The structural responses of thin-walled flexible structures are approximated at the mid-surface of the thin element, as shown in Fig. 4.3. Two-node elastic beam-column element is used, in which each node has three degrees of freedom (d_x, d_y, α_z) : displacement components in horizontal and vertical directions, and in-plane rotation. The nodes (n_i) and elements (e_i) of the idealised model are shown at the centreline of the thin body. The equation of motion for a structural system with many degrees of freedom can be written as follows

$$\mathbf{M}\ddot{\mathbf{q}} + \mathbf{C}\dot{\mathbf{q}} + \mathbf{K}_t\mathbf{q} = \mathbf{f}_{\text{ext}}, \quad (4.8)$$

where \mathbf{q} , $\dot{\mathbf{q}}$, $\ddot{\mathbf{q}}$ are the vectors of nodal displacements, velocities and accelerations respectively; and \mathbf{M} , \mathbf{C} , \mathbf{K}_t , and \mathbf{f}_{ext} are the mass, structural damping, total tangent stiffness matrix, and external force vector, respectively.

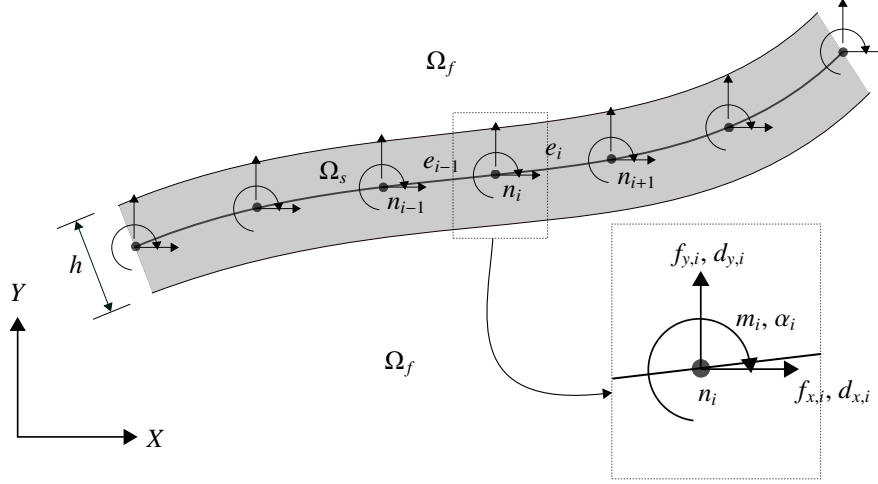


Figure 4.3: A partial schematic presentation of structural nodes and elements at the mid-surface of the deformed thin plate, which has been shown in Fig. 4.1.

The mass matrix \mathbf{M} of thin-walled beam system is formulated using lumped mass idealization. If the mass m of an element of length l is uniform, a point mass of $ml/2$ can be assigned to each nodes at the end of the element.

The proportional Rayleigh damping matrix is used which is a combination of the mass and the stiffness matrix as follows

$$\mathbf{C} = a_0\mathbf{M} + a_1\mathbf{K}. \quad (4.9)$$

This leads to the relation between damping ratio and frequencies as follows:

$$\xi_n = \frac{a_0}{2\omega_n} + \frac{a_1\omega_n}{2}. \quad (4.10)$$

The factors a_0 and a_1 can be evaluated by associating two specific natural frequencies ω_m and ω_n . Assuming the same damping ratio for both frequencies i.e. $\xi = \xi_m = \xi_n$, the proportionality factors can be simplified as:

$$a_0 = \frac{2\xi\omega_m\omega_n}{\omega_m + \omega_n}, \quad a_1 = \frac{2\xi}{\omega_m + \omega_n} \quad (4.11)$$

The two modes can be selected which are considered to be participating more in the response or have sufficient difference between the frequencies. The modes which have frequencies in-between these two modes will have relatively low damping and will participate more in the response; however, the modes out of this frequency range will have very high damping resulting in reduced effect in the overall response.

Kinematics of the corotational beam

A corotational formulation combined with Euler-Bernoulli hypothesis is used with the inclusion of axial force. This coupled model is particularly implemented for thin-walled systems those are exposed to high axial forces, deforms largely, (for example the aeroelastic fluttering motion of thin T-shaped cantilever system), and displays geometrical nonlinear effects in dynamic response. The efficiency of the method to deal with nonlinear dynamic behaviour of beam structures has been reported in several studies [37, 122, 153, 232].

Here, the kinematics of the corotational beam is explained briefly. The detailed formulation for corotational 2D beam can be found in [153, 208]. The notations used are defined in Fig. 4.4. The coordinates for the nodes 1 and 2 in the global coordinate system (X, Y) are (x_1, y_1) and (x_2, y_2) . The vector of global displacements is defined by

$$\mathbf{q}_g = [u_1 \ w_1 \ \theta_1 \ u_2 \ w_2 \ \theta_2]^T \quad (4.12)$$

while the vector of basic element displacements in local coordinates is defined by

$$\bar{\mathbf{q}}_1 = [\bar{u} \ \bar{\theta}_1 \ \bar{\theta}_2]^T \quad (4.13)$$

with

$$\bar{u} = l_n - l_o, \quad (4.14)$$

$$\bar{\theta}_1 = \theta_1 - \alpha = \theta_1 - \beta - \beta_o, \quad (4.15)$$

$$\bar{\theta}_2 = \theta_2 - \alpha = \theta_2 - \beta - \beta_o, \quad (4.16)$$

where l_o and l_n denote the initial and current lengths of the element, α denotes the rigid rotation angle. The definition of the parameters can be expressed as

$$l_o = [(x_2 - x_1)^2 + (y_2 - y_1)^2]^{1/2}, \quad (4.17)$$

$$l_n = [(x_2 + u_2 - x_1 - u_1)^2 + (y_2 + w_2 - y_1 - w_1)^2]^{1/2}. \quad (4.18)$$

The current angle of the local system with respect to the global system is denoted as β and is given by

$$c = \cos \beta = \frac{1}{l_n} (x_2 + u_2 - x_1 - u_1), \quad (4.19)$$

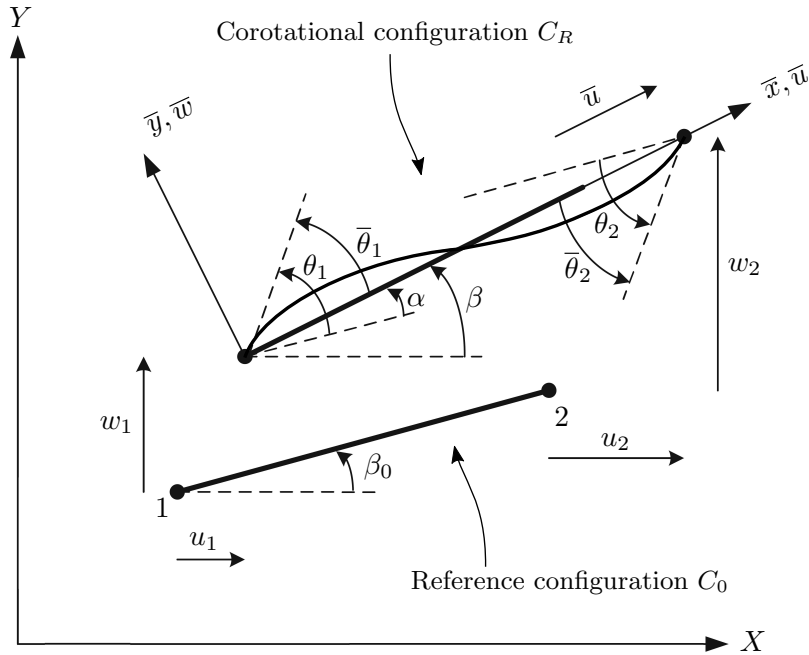


Figure 4.4: Reference and corotational configuration of a typical beam element.

$$s = \sin \beta = \frac{1}{l_n} (z_2 + w_2 - z_1 - w_1). \quad (4.20)$$

The transformation matrix \mathbf{B} is defined such that $\delta \bar{\mathbf{q}}_l = \mathbf{B} \delta \mathbf{q}_g$ with \mathbf{B} as follows

$$\mathbf{B} = \begin{bmatrix} -c & -s & 0 & c & s & 0 \\ -s/l_n & c/l_n & 1 & s/l_n & -c/l_n & 0 \\ -s/l_n & c/l_n & 0 & s/l_n & -c/l_n & 1 \end{bmatrix}, \quad (4.21)$$

The relationship between the local and global internal forces vectors \mathbf{f}_l , \mathbf{f}_g can be expressed as follows

$$\mathbf{f}_g = \mathbf{B}^T \mathbf{f}_l \quad \text{with } \mathbf{f}_l = [N \quad M_1 \quad M_2]^T. \quad (4.22)$$

The total global stiffness matrix can be expressed as the sum of global and geometric stiffness

$$\mathbf{K}_t = \mathbf{K}_g^M + \mathbf{K}_g^G = \mathbf{B}^B \mathbf{K}_l \mathbf{B} + \frac{\mathbf{z}\mathbf{z}^T}{l_n} N + \frac{1}{l_n^2} (\mathbf{r}\mathbf{z}^T + \mathbf{z}\mathbf{r}^T) (M_1 + M_2), \quad (4.23)$$

where

$$\mathbf{r} = [-c \quad -s \quad 0 \quad c \quad s \quad 0]^T, \quad (4.24)$$

$$\mathbf{z} = [s \quad -c \quad 0 \quad -s \quad c \quad 0]^T, \quad (4.25)$$

\mathbf{K}_l is the local tangent stiffness matrix. These relations are independent on the choosing of different beam theories.

Numerical time integration

The equation of motion (Eq. (4.8)) is solved for the full system matrix under the external fluid forces in time domain. The implicit Newmark time integration with Newton–Raphson iterations [57, 180] is used in which for an incremental solution of the system $\Delta \mathbf{q}^{i+1,j}$ between iteration $j+1$ and j can be obtained from

$$\left[\mathbf{K}_t + \frac{\gamma}{\beta \Delta t} \mathbf{C} + \frac{1}{\beta (\Delta t)^2} \mathbf{M} \right]^{i+1,j} \Delta \mathbf{q}^{i+1,j} = \mathbf{f}_{\text{ext}}^{i+1} - \mathbf{f}_{\text{int}}^{i+1,j} = \mathbf{R}^{i+1,j}, \quad (4.26)$$

with the residual,

$$\begin{aligned} \mathbf{R}^{i+1,j} = & \mathbf{f}_{\text{ext}}^{i+1} - \mathbf{f}_{\text{int}}^{i+1,j} - \\ & - \left[\frac{1}{\beta (\Delta t)^2} \mathbf{M} + \frac{\gamma}{\beta \Delta t} \mathbf{C} \right] (\mathbf{q}^{i+1,j} - \mathbf{q}^i) + \left[\frac{1}{\beta \Delta t} \mathbf{M} + \left(\frac{\gamma}{\beta} - 1 \right) \mathbf{C} \right] \dot{\mathbf{q}}^i + \\ & + \left[\left(\frac{1}{2\beta} - 1 \right) \mathbf{M} + \left(\frac{\gamma}{2\beta} - 1 \right) \mathbf{C} \right] \ddot{\mathbf{q}}^i. \end{aligned} \quad (4.27)$$

where, Δt is the time step, the subscripts i , $i+1$ indicate the time level $t^{i+1} = t^i + \Delta t$. The parameters β and γ define the variation of acceleration over a time step Δt and determine the stability and accuracy characteristics of the method.

The average acceleration method ($\gamma = 0.5$; $\beta = 0.25$) is used as the time integration strategy, which is well known “unconditionally stable condition” irrespective of time step for linear systems. The solution of the system can be written as $\mathbf{q}^{i+1,j+1} = \mathbf{q}^{i+1,j} + \Delta \mathbf{q}^{i+1,j}$ to update

the displacements. The algorithm is advanced to the next time level when the iterative process is declared converged which is by reaching a specified tolerance limit of the iterative process. In this study, an open-source software OpenSees [76, 161], which is a framework for structural and geotechnical models with wide range of algorithms and solution methods, has been employed to carry out the geometrically nonlinear structural dynamic analysis.

4.2.3 Presentation of immersed thin structures in the fluid domain

An essential feature of the proposed coupled FSI algorithm is that it employs the FE formulation for thin beam elements in which the structural equations are formulated and solved at the mid-surface of the thin structure, as it has been shown in Fig. 4.3. A similar mid-surface approach was demonstrated in Gilmanov et al. [107] with the implementation of coupling between curvilinear immersed boundary method and rotation-free FE formulation, however using triangular thin shell elements.

The mid-surface approach is chosen due to its efficiency in handling thin-walled structural elements. The flow solver based on VPM is mesh-less, which uses background grid only to speed-up the velocity computation, and therefore the coupling process is quite convenient since the matching of the meshes at the interface is not necessary.

There are algorithmic challenges in the proposed coupled model since BEM is designed to use normal vectors (\mathbf{n}) at the immersed interface (c.f. Eq. (4.6)). It is crucial to reconstruct velocity boundary conditions at the boundary nodes along the local normal of the surface panel, see Eq. (4.6).

It is challenging further to calculate the loads on the structure nodes imparted by fluid stresses at the fluid–structure interface. It is because, at every point on the boundary panels, there is a unique normal vector that points toward the fluid side of the interface, namely the positive wall normal vector [107]. In other words, the fluid pressures acting toward the fluid side of the interface are considered positive. For such a case, it is readily apparent that at each FE node at the mid-surface in the local coordinate of the beam element, it has both positive and negative wall-normal vectors (n_e^+ and n_e^-) pointing toward the fluid side of the interface, (see Fig. 4.5).

Based on the challenges mentioned above, the following two tasks have to be performed before proceeding to the calculation of the nodal forces on the structure elements:

- Identification of projection beam element for each surface panel on which the fluid pressure has to be projected.
- Identification of the sign of surface normal vector for each panel with respect to the local coordinate of the beam element, whether it is positive or negative for the element.

It is important to note that the boundary panels are expected to be equal and oriented in the anticlockwise orientation. In contrast, the FE formulation at the mid-surface can employ different element size with any node–element orientation. An algorithm is developed to identify the projection beam element and the normal surface vectors for each boundary panel, see Algorithm 1. They are obtained at the beginning of an analysis and stored for reuse in further time steps.

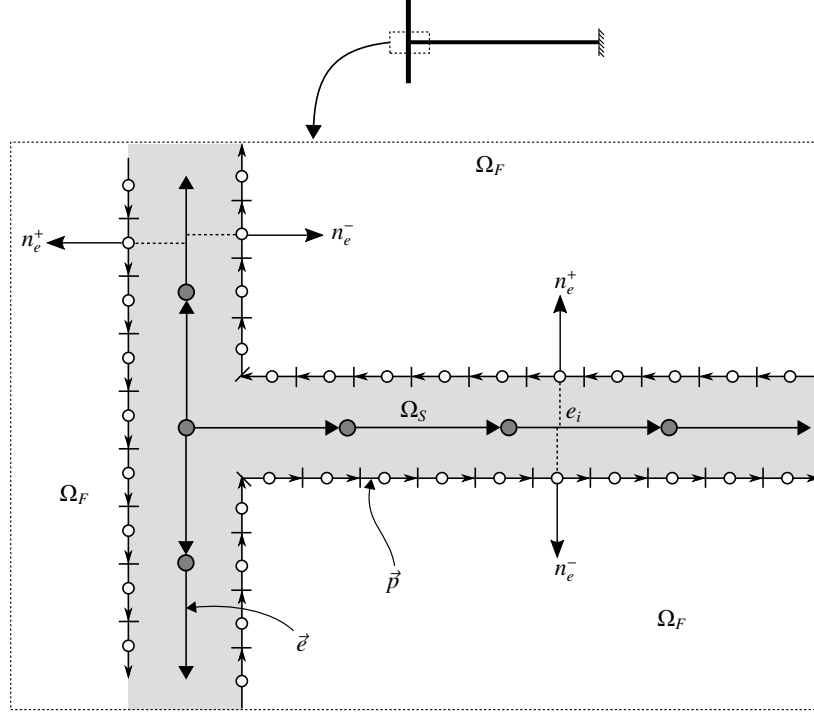


Figure 4.5: Identification of projection element for each boundary panel and the sign of surface normal vector to the element. The discretization of the fluid and structure is partially shown for a T-shaped cantilever system in fluid flow. Here, the filled circles (●) present the structure nodes, at which the surface loads has to be projected. The unfilled circles (○) shows the control points associated with the boundary panels. The vectors, \vec{e} and \vec{p} , represents the element vector and panel vector, respectively. The direction of the vector is defined based on the start node towards the end node.

The proposed coupled model is based on the thin elements of uniform thickness. In the case of beam thickness with tiny variation, the conditions of the angle between element and panel can be slightly adapted. However, the developed technique for the projection of information from one interface to other needs to updated if it is necessary to consider for the small inclination of panels for an FSI case.

4.2.4 Calculation of the nodal forces for the structure analysis

In order to perform the coupled analysis the fluid pressures induced on the surface panels have to be integrated and projected on the structural nodes at the mid-surface. If the pressure of a panel i is p_i , the total force normal on the panel F_i^\pm can be calculated as

$$F_i^\pm = p_i \Delta_{s_i} W_s, \quad (4.28)$$

where Δ_{s_i} and W_s are the panel length and the width of the structure. Since the panel and the beam element at the mid-surface are parallel, the magnitude of the normal force is same; however, the sign of the force can be changed depending on the sign of surface normal vector (c.f. Algorithm 1) such as

$$F_{(e,i)}^\pm = F_i^\pm \cdot n_{e,i}^\pm, \quad (4.29)$$

where $F_{(e,i)}^\pm$ is the normal force on the element e due to the pressures on a surface panel i ; $n_{e,i}^\pm$ is the sign of surface normal vector for panel i with respect to the local coordinate of

Algorithm 1: Identification of projection beam element for each boundary panel and the sign of surface normal vector corresponding to the element coordinate system.

- 1 Calculation of angle between the element vector and panel vector
 - 2 Calculation of distances between all FE nodes and boundary control points
 - 3 Iteration for each boundary panels, $i = 1, 2, \dots, N_{panel}$
 - find the closest FE node and its connecting other nodes
 - identification of the projection beam element (e) using the nodal distances and angle between element and panel (note: boundary panel and element are parallel)
 - 4 Identification of the sign of element normal vector based on the angle between panel and element
 - if angle = 0° , assign n_e^+ for the panel,
 - if angle = 180° , assign n_e^- for the panel,
 - if angle = 90° (generally the surface panels at the edges along the thickness),
 - (a) assign n_e^+ if the closest node is start node of the beam element,
 - (b) assign n_e^- if the closest node is end node of the beam element,
 - if angle $\neq 0^\circ \neq 90^\circ \neq 180^\circ$: the coupled method is not formulated for such cases (e.g. varying plate thickness).
 - 5 Store vectors of each panel index $panel_i$, corresponding projecting beam element e_{panel} , and the sign of surface normal vector as follows $\rightarrow [panel_i; e_{panel}; n_e^\pm]$
-

element e (the value of which is either 1 or -1).

For a random beam element, if the projected normal force $F_{(e,i)}^\pm$ acts to a point on the element, which bisects the element with distance l_a from the start node (n_1), whereas l_b from the end node (n_2). Using the finite element formulation, the local nodal forces for a element considering the point load on a both end fixed beam can be calculated as follows

$$F_{n_1(e,i)} = \frac{F_{(e,i)}^\pm * l_b^2}{l_e^3} (3l_a + l_b), \quad (4.30)$$

$$F_{n_2(e,i)} = \frac{F_{(e,i)}^\pm * l_a^2}{l_e^3} (l_a + 3l_b), \quad (4.31)$$

where l_e is the total length of the element; $F_{n_1(e,i)}$ and $F_{n_2(e,i)}$ are the distributed local normal forces at nodes n_1 and n_2 of element e , respectively.

Fig. 4.6 shows examples of projection of fluid force $F_{(e,i)}$ from the surface panel i to the structure element e at the mid-surface, and furthermore, the distribution of forces to the element nodes n_1 and n_2 .

The element local force vector (\mathbf{f}_i) is calculated by iterating over the surface panels, and finally, by summing up all the contributions to the element end nodes. When the projection of the loads for each panel to the FE nodes are over, the global force vector (\mathbf{f}_g) can be calculated using the element transformation matrix $[\mathbf{T}]$ as follows

$$\mathbf{f}_g = [\mathbf{T}]\mathbf{f}_i. \quad (4.32)$$

Since the presented coupled model uses the lumped mass formulation, and therefore, the rotational degrees of freedom are zero. This simplification allows to disregard the consideration

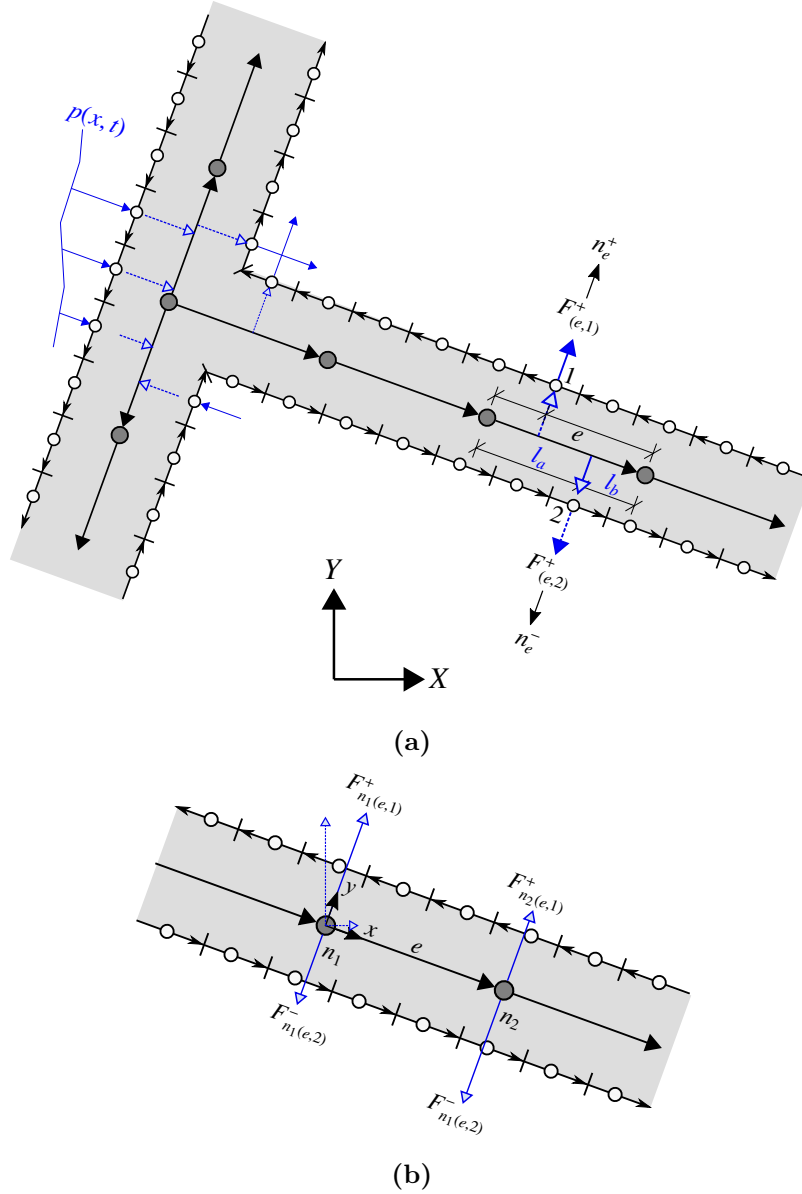


Figure 4.6: Projection of fluid pressure from the boundary panels to the structural nodes: (a) the schematic shows the projection of panel forces $F_{(e,i)}^{\pm}$ on two panels, in which $i = 1$ and 2. Here, $F_{e,1}$ and $F_{e,2}$ are the integrated panel forces that have to be projected at the nodes of the beam element e . According to the sign convention of the flow solver, $F_{e,1}$ and $F_{e,2}$ are positive since they are acting towards the fluid side of the interface. However, n_e^{\pm} determines the sign of the force at the mid-surface for the beam element. In (b), it shows the distributed nodal forces in local coordinate (xy) of element e . Once, the projection of the surface loads are added to all nodes in element coordinate, the nodal force vector can be transformed to the global coordinates (XY) . An example of force components are shown in global coordinate for $F_{n1(e,1)}$.

of bending moments at the element nodes, and they are assigned zero.

4.2.5 Projection of motion from mid-surface to boundary panels

The projection of the structural motion at the FE nodes in the mid-surface needs to be projected at the boundary nodes in order to update the geometry. The procedure is shown

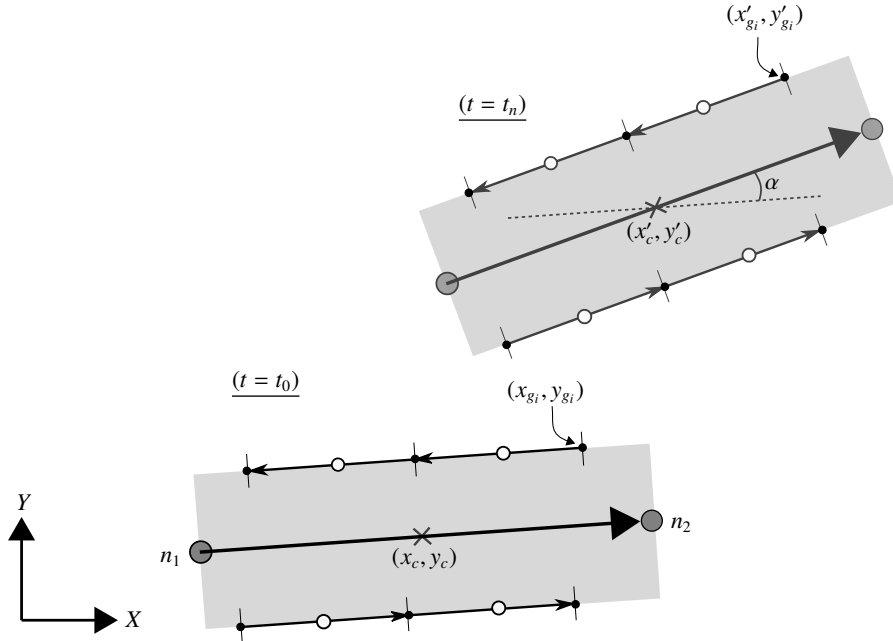


Figure 4.7: Update of the geometry based on the projection of grid points of boundary panels due to the motion at the mid-surface of the thin elements.

schematically in Fig. 4.7. The calculation is based on each panel and corresponding projecting element. At each simulation step, the geometry position of i^{th} grid point (x_{g_i}, y_{g_i}) can be found based on the summation of changed position of rotation centre (x'_c, y'_c) plus the change of coordinates due to the element rotation α . Here, the rotation centre is the mid-position of a beam element, and α is the rotation of element due to the structural solution at the FE nodes n_1 and n_2 . Important to note that the initial position of the geometry at t_0 acts as a reference for each simulation step. The equations that are used to calculate the grid positions are as follows

$$x'_{g_i} = x'_c + (x_{g_i} - x_c) \cos \alpha - (y_{g_i} - y_c) \sin \alpha \quad (4.33)$$

$$y'_{g_i} = y'_c + (x_{g_i} - x_c) \sin \alpha + (y_{g_i} - y_c) \cos \alpha \quad (4.34)$$

The structure may deform substantially; however, it is assumed that the linear panels those belong to a specific projecting beam element are unreformed. This means each segment of beam element and surrounding panels are approximated as rigid body motion with translation and rotation. Though the implementation allows variable length of beam element; however, the choice of beam element equal or smaller than the size boundary panel ensure the maximum projection accuracy.

The new position of the control points for each boundary panel is calculated based on the updated geometry since it is the mid-point of a panel.

The projection of the panel velocity from the FE nodes to the control point of a boundary panel is shown schematically in Fig. 4.8. At the normal direction of a panel, if the projection of control point bisects the beam element with a ratio of l_a/l_b , the panel velocities in global coordinate are calculated based on the solution at the start and end nodes of the element as follows

$$p_{vx} = v_{x_1} + \frac{l_a}{l_a + l_b} (v_{x_2} - v_{x_1}), \quad (4.35)$$

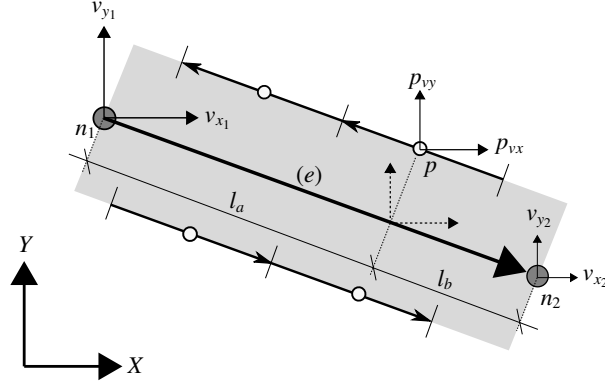


Figure 4.8: Projection of the velocity components from the nodal displacements at n_1 and n_2 to the control point p of a panel.

$$p_{vy} = v_{y1} + \frac{l_a}{l_a + l_b}(v_{y2} - v_{y1}). \quad (4.36)$$

It is important to note that the panel velocities are transformed further to the local coordinate of the panels to find the velocity normal component, however; after the update of the geometry. This is necessary to calculate the right hand side vector of Eq. 4.7 based on the updated geometry and other influences. The calculation of the panel acceleration is performed in the similarly as for the panel velocity.

4.2.6 Fluid–structure coupling

The fluid and structural equations are coupled with each other through the coupling of boundary conditions at the fluid–structure interface (Σ). The following equation shows the continuation of displacement

$$\mathbf{d}_s^\Sigma = \mathbf{d}_f^\Sigma \quad (4.37)$$

which is performed by projecting the displacement from the mid-surface to the geometry points of the boundary panels. The next condition is the continuation of the fluid forces

$$\mathbf{v}_s^\Sigma = \mathbf{v}_f^\Sigma \quad (4.38)$$

which is performed by projecting the integrated fluid pressures from the surface panel to the structure nodes. Furthermore, the continuation of the velocity at the interface

$$\mathbf{v}_s^\Sigma = \mathbf{v}_f^\Sigma \quad (4.39)$$

which is performed by projecting the velocity at the structural nodes at the mid-surface to the control point of the surface panels in global coordinates.

In this presented coupled numerical algorithm, some additional boundary conditions have to be satisfied due to the utilisation of BEM. In every time step t_n , the global panel velocities (p_{vx} and p_{vy}) needs to be restructured such that the normal velocity components ($p_v \cdot \mathbf{n}$) in updated panel coordinate on the solid boundary \mathcal{B} are enforced in the right hand side of the Eq. (4.6), which is repeated in the following

$$\left(\int_B \frac{\gamma_0 \times (\mathbf{x}_0 - \mathbf{x})}{|\mathbf{x}_0 - \mathbf{x}|^2} d\mathcal{B}_0 \right)_{t_n} \cdot \mathbf{n} = (\mathbf{I} - 2\pi [\mathbf{u}_0 - \mathbf{U}_\infty])_{t_n} \cdot \mathbf{n}. \quad (4.40)$$

It is necessary to calculate unknown surface vorticity at each time step. A summary of the overall algorithm of the 2D coupled VPM for FSI simulations is presented in Fig. 4.9.

For FSI problems of lower mass ratio ($\rho_s/\rho_f \approx 1$) when the interaction between fluid and structure is strong, e.g. the blood flow in human arteries, the numerical instabilities may be encountered in coupled time advancing schemes due to the added-mass effect of the fluid on the structure. It is mainly due to the additional fluid acceleration acting on the solid [26]. It was shown in [49] that the instability occurs irrespective to the coupling approaches, i.e. loose or strong. The additional iteration between fluid and solid solver with Aitken relaxation factor for the update of the displacement and velocity of interface for the sub-systems was shown in [26, 107] for performing strong coupling between fluid and structure solver. The relaxation technique was shown to accelerate the convergence of the algorithm. However, the additional iteration between fluid and solid solver, and the relaxation technique is not necessary for FSI problems with large mass ratio. In such a case, an accurate temporal discretization of the FSI problems is far more efficient to achieve stable solution [107]. The benchmark and other FSI test cases simulated in this study are of large mass ratio. Therefore, the additional sub-iterations between fluid and solid solver has not been considered.

4.2.7 Validation of the enforcement of velocity boundary condition

In the following, studies have been performed to check the quality of the proposed coupled algorithm regarding the satisfaction of the enforcement of velocity boundary condition (c.f. Eq.(4.2). In this context, the flow around a flat plate in uniform flow is analysed for two different scenarios: (a) translational oscillation of an inclined flat plate, and (b) rotational oscillation of a flat plate. The aim is to analyse both situations and compare the flow fields near the boundary layer, however, using the existing implementation of VPM for forced vibration analysis and the proposed coupled algorithm for 2D VPM. The motion of the rigid flat plate, in case of coupled VPM, is analysed through assigning the nodal displacement at the mid-surface of the thin flat plate.

Flow around an oscillating inclined flat plate in uniform flow

The flow around an inclined ($\theta = 15^\circ$) flat plate of length $L = 33$ m and thickness $h = 0.33$ m is simulated in free stream velocity for imposed motions. The aspect ratio of the system is 1:100. The time histories of the imposed translational motion of the inclined flat plate are shown in Fig. 4.10. The simulation type and numerical model are summarized as follows:

- Static analysis of inclined rigid plate in uniform flow (with no motion),
- Forced oscillation (same translational motion in horizontal and vertical direction) of inclined plate in uniform flow using rigid beam model,
- Similar forced oscillation of inclined rigid plate using presented flexible coupled model.

The purpose of the static analysis (no motion) is to use the flow field as a reference to display the influence of the imposed movement on the flow field. However; the aim is to compare the flow field in between the simulations, in which the motion is imposed. The simulation parameters are summarized in Table 4.1. The free stream velocity U_∞ is chosen low to ensure more influence on the flow field due to the imposed motion. The peak velocity of the motion (v) reaches up to 25 % of U_∞ (c.f. Fig. 4.10).

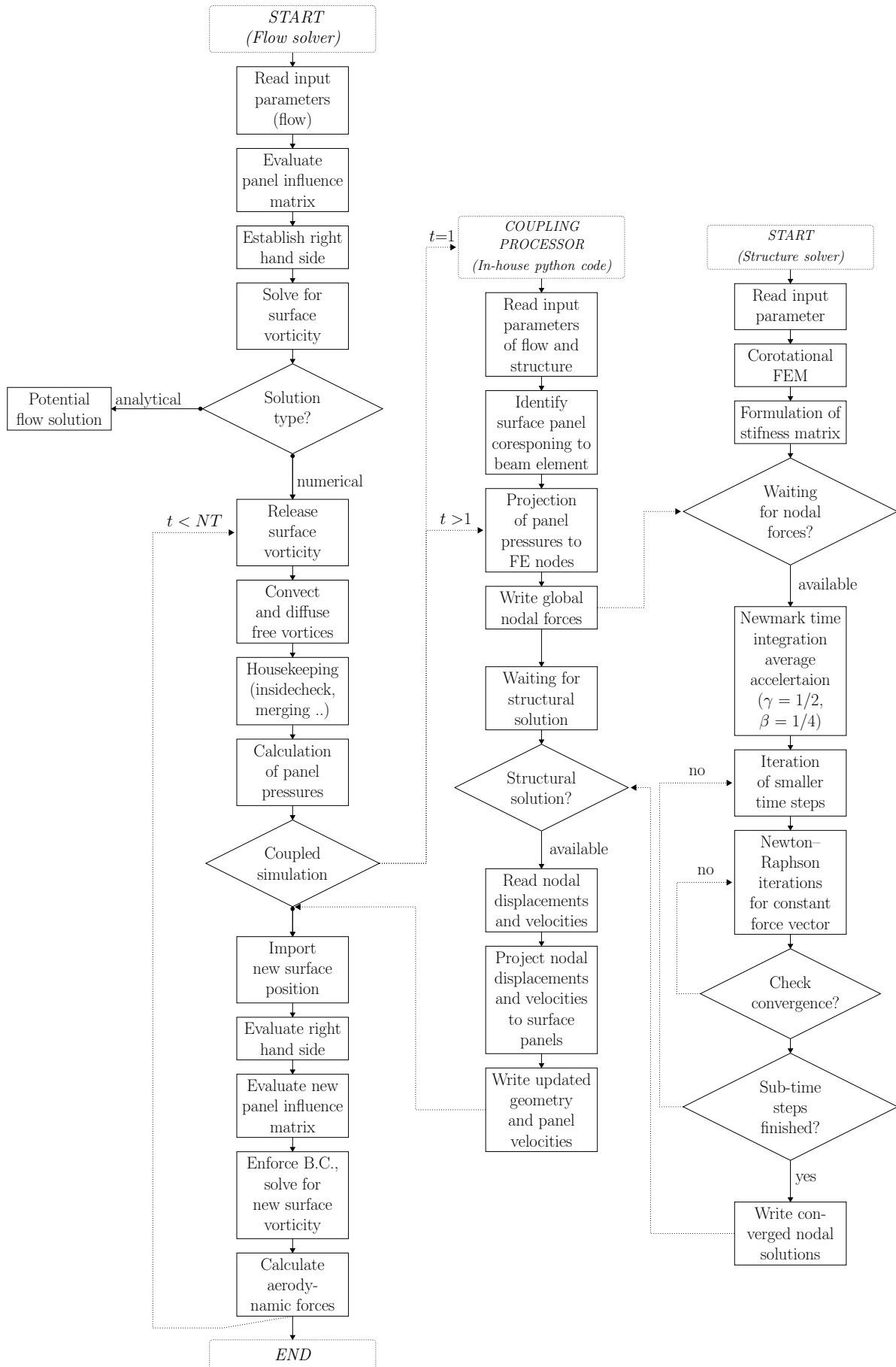


Figure 4.9: Flowchart of 2D coupled VPM for large-displacement FSI simulations.

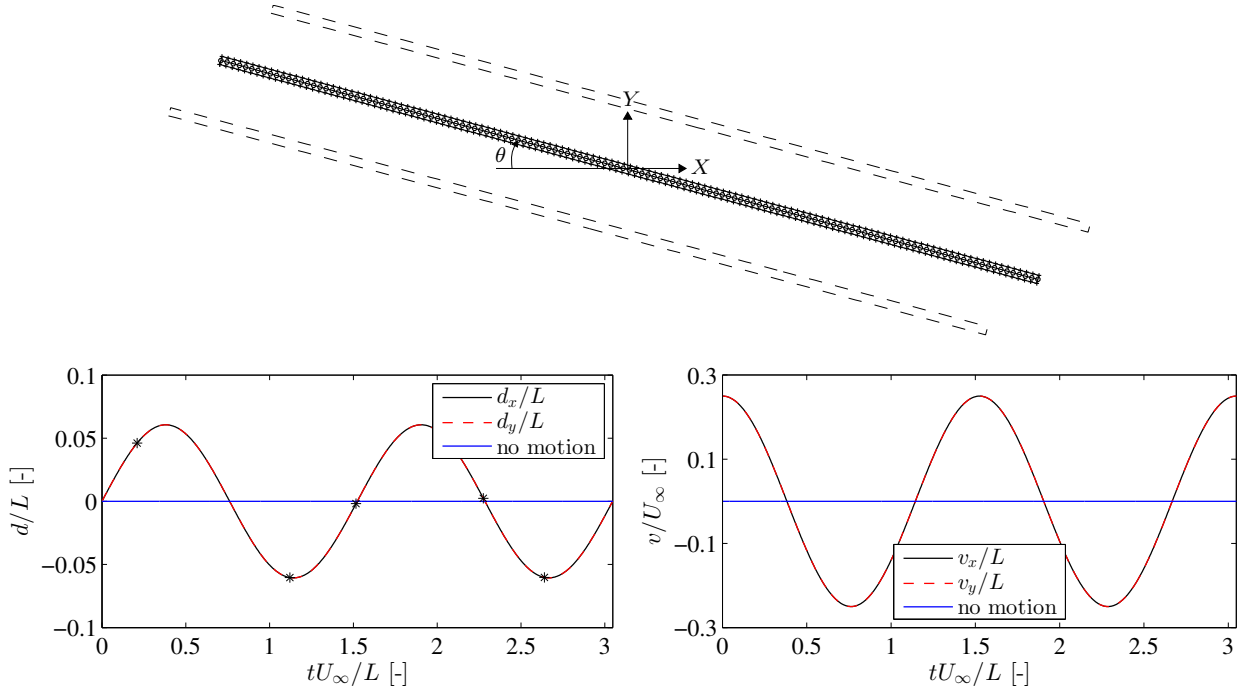


Figure 4.10: Flow around an inclined flat plate in free stream flow considering static and imposed oscillation: (top) the imposed motion of the system in X and Y direction based on the flexible coupled model; θ is the angle of attack for the incoming flow; (bottom-left) the time histories of imposed displacements, and (bottom-right) the time histories of corresponding imposed velocity. The star symbols (*) in the displacement time histories indicate the time at which the velocity fields are compared later in Fig. 4.11.

The resultant flow velocities $U = \sqrt{U_x^2 + U_y^2}$, in which U_x and U_y are the horizontal and vertical velocity components, for the studied cases are summarized in Fig. 4.11.

The static case is presented together with the forced oscillation to show how much closer the coupled beam model predicts the boundary layer in comparison with the rigid section model. The qualitative comparisons in Fig. 4.11 shows that the prediction of the boundary layer using the flexible coupled model is quite satisfactory.

The velocity fields are monitored at four locations, c.f. Fig. 4.12(a), and they are compared in Fig. 4.12(b-e). The comparison of the flow fields shows that the enforcement of the velocity boundary condition in the flexible coupled model is quite satisfactory. The small differences may be due to the differences in seeding of particles due to the random walk method. Furthermore, very small differences may be originated from the projection of the motion from mid-surface to the panel.

Test case	Numerical parameters		Value
All cases	Number of panels	N_{panel}	266
	Free stream velocity	U_∞	4 m/s
	Kinematic viscosity	ν	0.00015
	Non-dimensional time step	$\Delta t_f^* = \Delta t_f U_\infty / \Delta_s$	0.4
Coupled flexible model (mid-surface)	Number of beam elements	N_{elem}	132
	Length of beam element	l_{elem}	0.25 m

Table 4.1: Numerical parameters: the forced oscillation of an inclined flat plate.

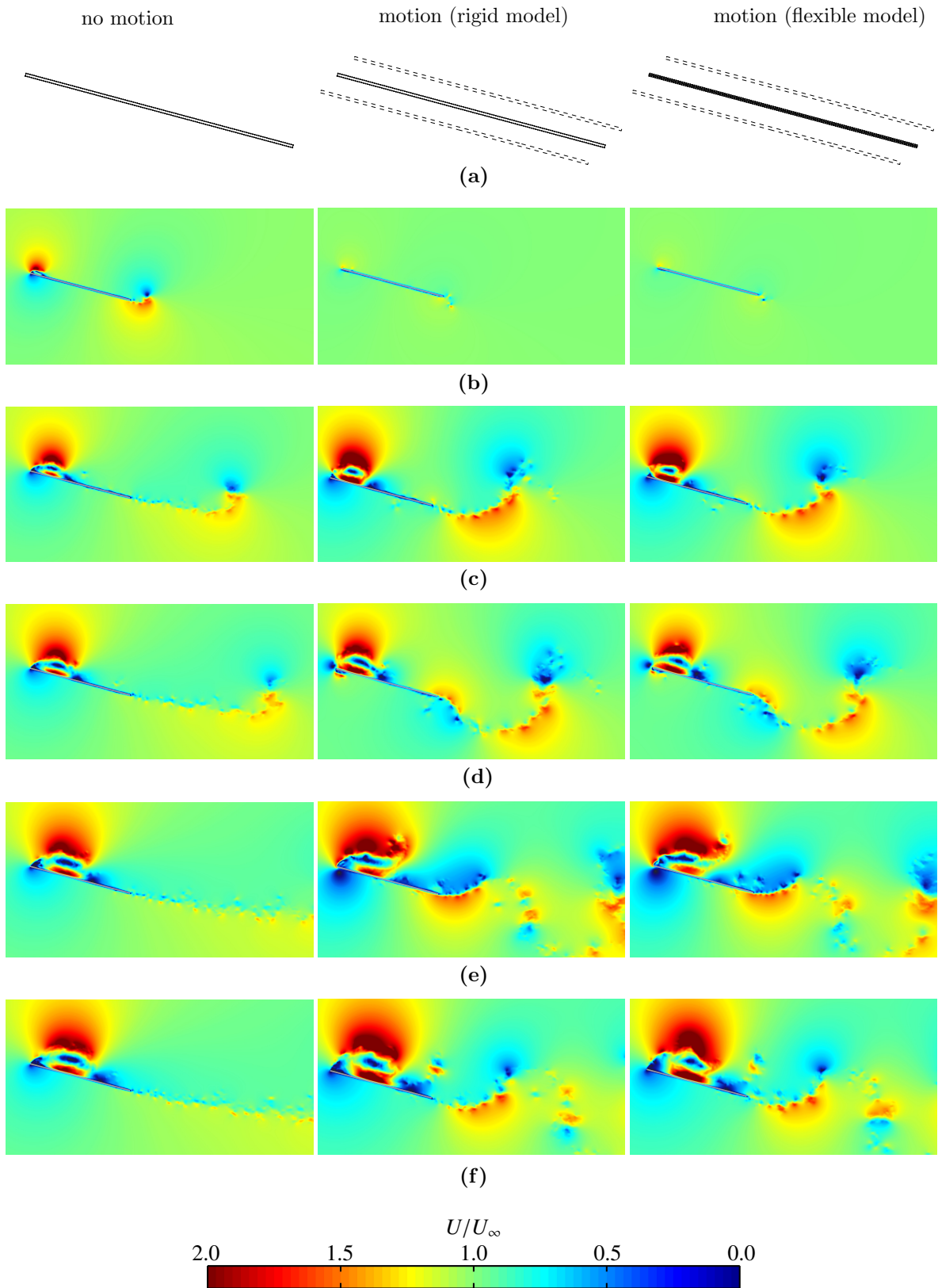


Figure 4.11: Comparison of the resultant flow field U at different time in case of static and forced oscillation analyses while the numerical models used are of particular concern: (a) the type of flow analysis and utilized numerical model. The flow fields are compared at different times such that $tU_\infty/L =$ (a) 0.18, (b) 0.38, (c) 1.14, (d) 1.9. The time histories of plate motion have been shown earlier in Fig. 4.10.

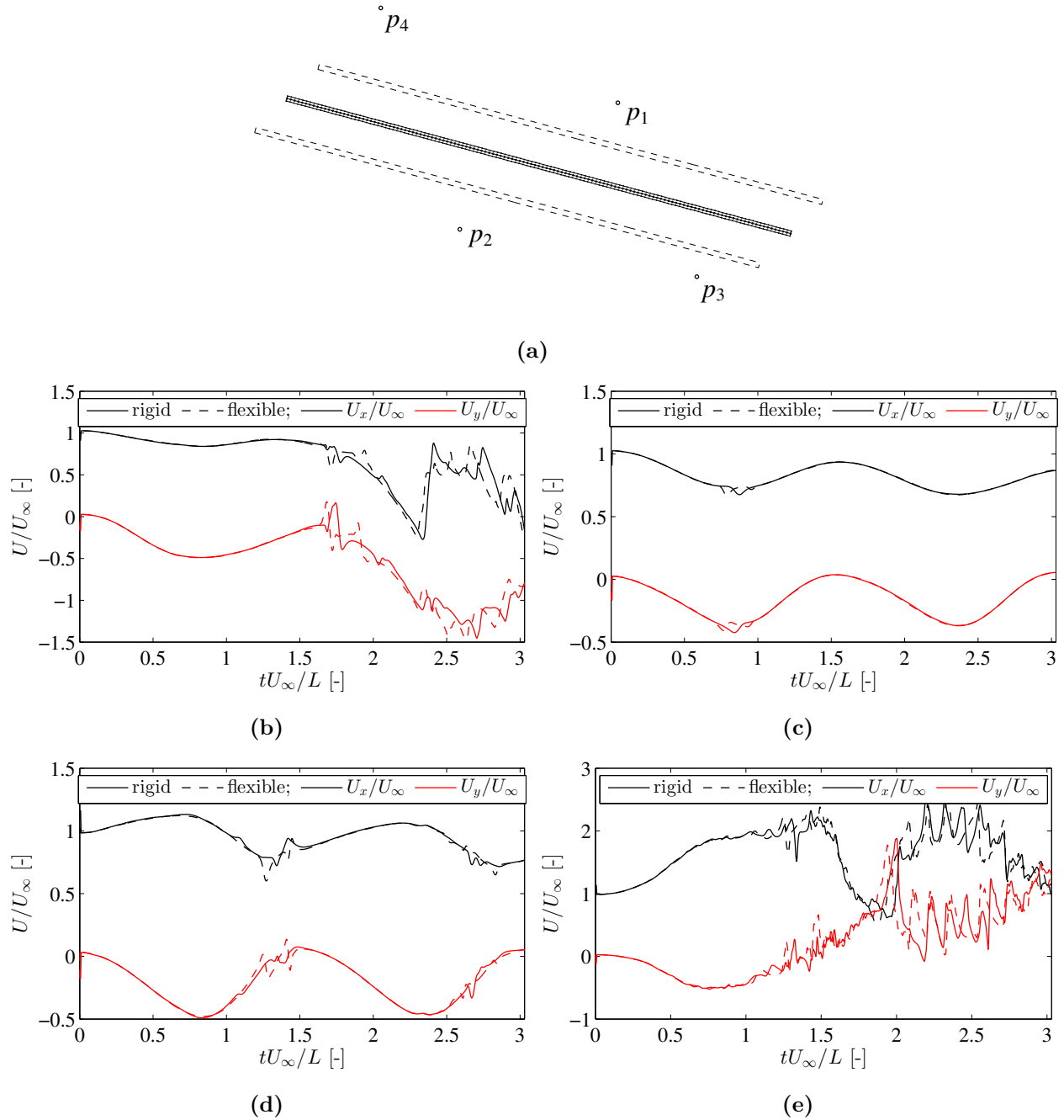


Figure 4.12: Comparison of the velocity components U_x and U_y at different monitored locations (p_1, p_2, p_3, p_4): (a) the position of the monitored points in the domain; the velocity time histories are shown based on rigid and flexible coupled model at different monitored points: (b) p_1 , (c) p_2 , (d) p_3 , and (e) p_4 .

Flow around rotational motion of a flat plate in uniform flow

The flow around a flat plate while rotating in the free stream velocity is analysed using the rigid and flexible coupled model. The velocity fields near the boundary layers are monitored for both numerical models. The study results are compared briefly in Fig. 4.13. The outcome for both studies shows that the implementation of the necessary boundary conditions is satisfactory for both translational and rotation imposed motion.

Here, both of the presented study cases shows that the motion-induced velocities are well-

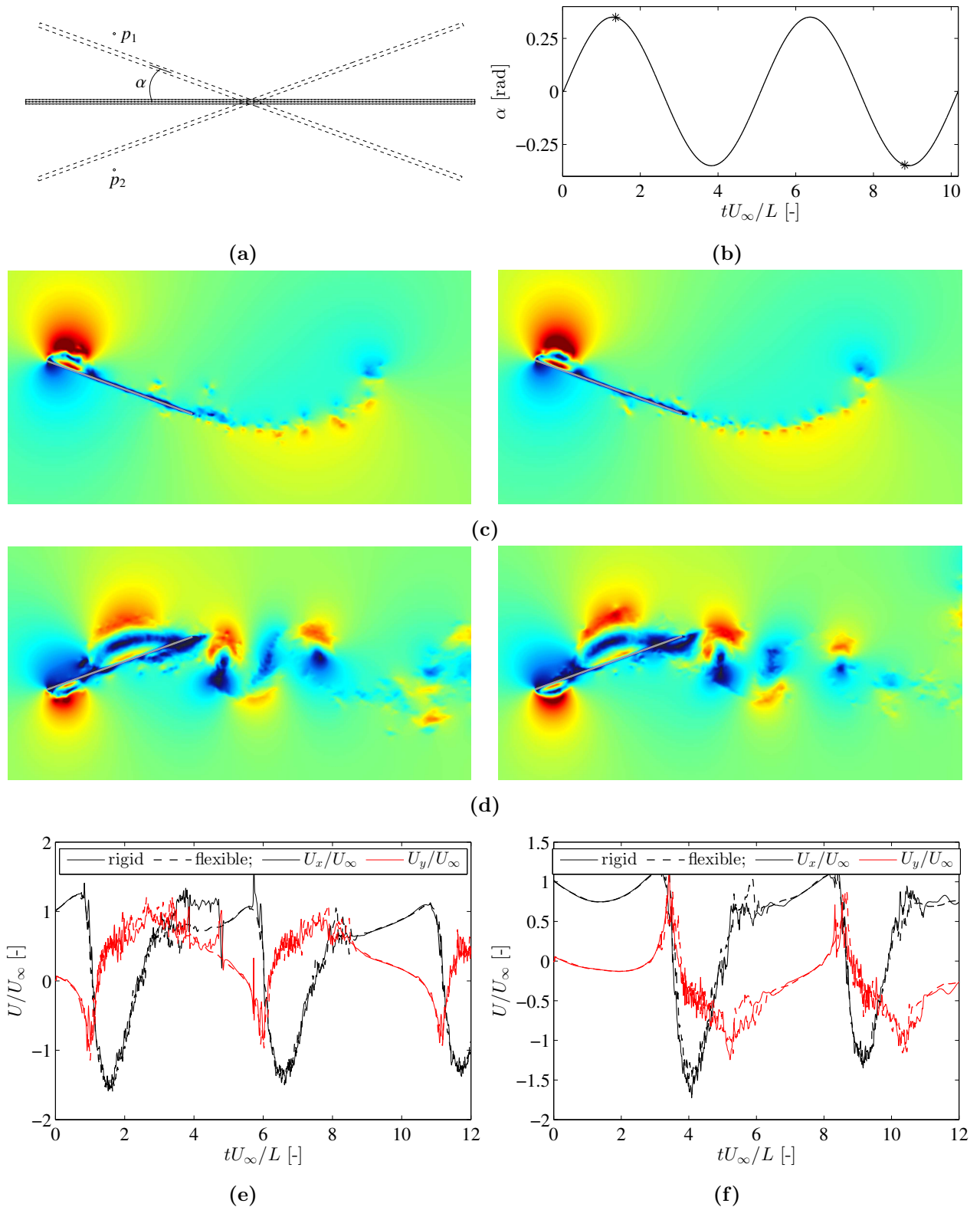


Figure 4.13: Comparison of the velocity field due to the rotational motion of flat plate in uniform flow: (a) the position of the monitored points in the domain; (b) the time history of the plate rotation (α); (c-d) the comparison of instantaneous resultant velocity fields (left: rigid model, right: flexible model) at times indicated by (*) in (b); the velocity components U_x and U_y at the monitored points such that (e) p_1 , and (f) p_2 .

modelled by the presented 2D coupled FSI model, though the study was not a coupled problem. However, it shows that the model can analyse motion-induced forces due to the motion of the deformed flexible body, which may be used for the calculation of aerodynamic derivatives.

The validation of the coupled algorithm for coupled dynamic analyses is presented later in Chapter 5 to several benchmark FSI problems of thin plate systems.

4.3 The pseudo-3D VPM for FSI simulations of flexible thin-shell structures

In the following, another extension of VPM is presented in the context of pseudo-3D multi-slice coupled model for complex FSI simulations of flexible thin-shell structures. The flow around immersed bodies is analysed using pseudo-3D VPM with boundary element discretisation, similarly as mentioned for the 2D coupled solver.

It is important to note that the limitation of the model is the absence of cross-coupling of flow in between the slices. The correlation can only come about through the structural coupling. Since the method allows the discretisation of flexible geometry independently for each flow slices, it is possible to use the previously mentioned coupling scheme of 2D VPM; however, in a slice-wise manner. The novelty is the inclusion of 3D shell vibration modes within the existing framework. The structural equations are formulated at the mid-surface of the thin shell elements and solved in the modal coordinate system.

The pseudo-3D VPM is presented schematically in Fig. 4.14 with some example cases of shell-type structures such as cooling tower or tall chimneys and cantilever roof system. Under particular aeroelastic loading scenario, such structures apart from the longitudinal flexible motion may deform in their shape in cross-section plane, which makes it necessary to consider the change of immersed geometry, as shown in Fig. 4.14(a). The modelling of the system response with the previous implementation, i.e. the rigid model using pseudo-3D VPM, is not possible since it uses the rigid cross-sections.

4.3.1 Multi-slice modelling of flow around deformable geometry

Discretisation of the surface in different flow simulation slices

In this extension of pseudo-3D VPM, the influence of changes in body shape and the surface motion are performed in a slice-wise manner to model the interaction between fluid and structure.

For a flexible circular tube-type structure, such as in Fig. 4.14(a), the instantaneous boundary element discretisation is shown in in Fig. 4.14(c) at time $t = t_0$ for the initial undistorted body, whereas at $t = t_n$ for the distorted body for a chosen flow simulation slice s . In case of shell structures like cantilever roof, such as in Fig. 4.14(b), the instantaneous boundary element discretisation for each flow simulation slice s can be performed based on the scheme shown in Fig. 4.1.

Similarly like the 2D coupled VPM solver, the geometry in each slice (s) of pseudo-3D VPM is discretized assuming piecewise linear panels (\mathbf{x}_i^s , $i = 1, \dots, N_{panel}$, $s = 1, \dots, N_{slice}$) of approximately slice-wise uniform length ($\Delta_{s_i}^s = |\mathbf{x}_{i+1}^s - \mathbf{x}_i^s|$). The control points $\mathbf{x}_{c_i}^s$ are

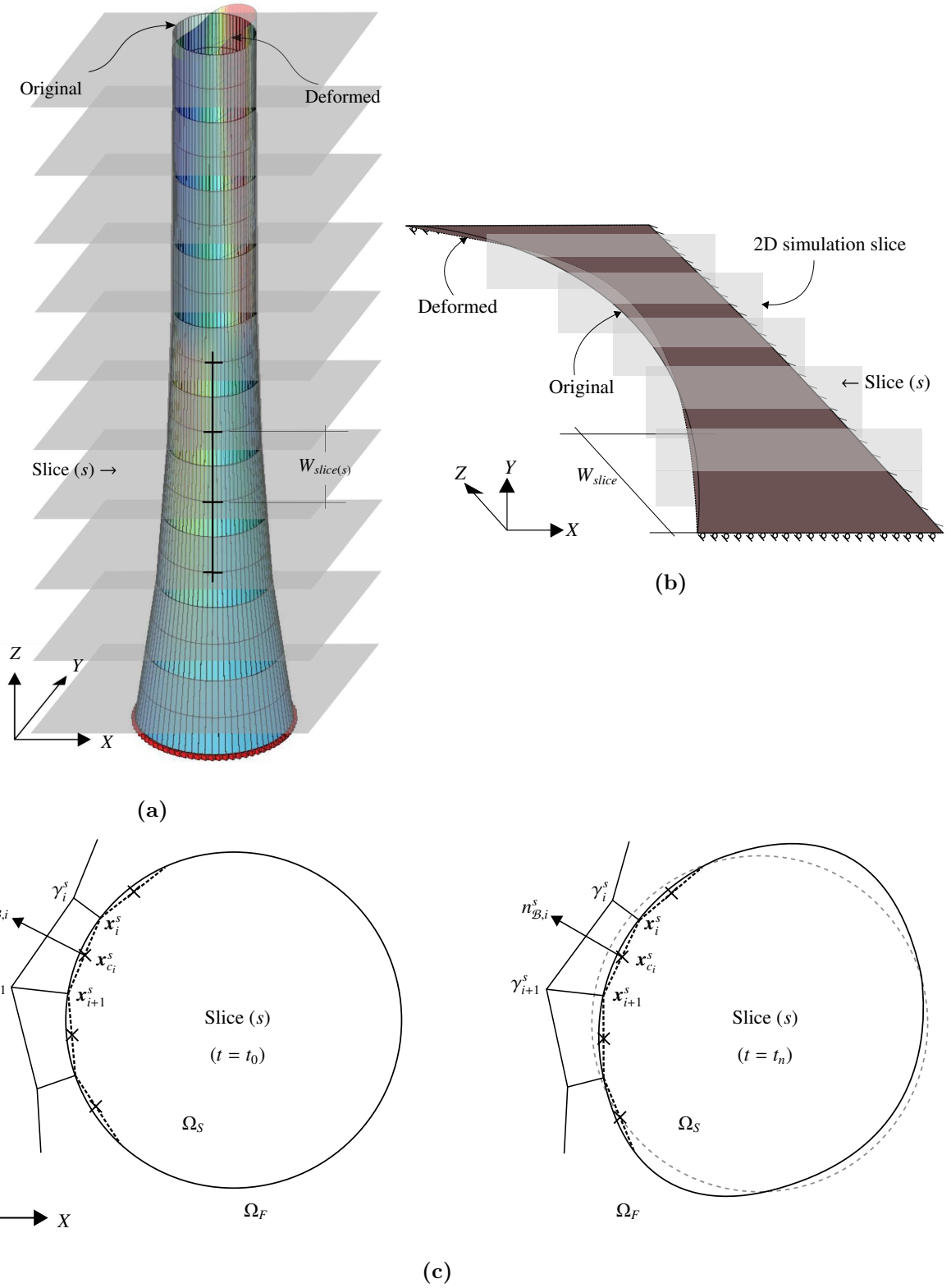


Figure 4.14: Schematic description of newly extended pseudo-3D VPM for multi-slice FSI simulation of thin-walled shell-type flexible structures: The vibration of a tall cooling tower and the orientation of the flow simulation slices are shown in (a), whereas the same information is shown in (b) for a large cantilever roof. (c) Slice-wise boundary element discretization is shown for the circular shell from (a), which is for a particular flow simulation slice s . In case a cantilever roof systems, such as in (b), the slice-wise boundary element discretization can be used as shown in Fig. 4.1. Here, W_{slice} is the slice width for which the surface pressures are considered same.

defined at the middle of each panel i of slice s . The velocity boundary condition is imposed at the control points of each slice at each time step (cf. Fig. 4.14(c)).

Instantaneous slice-wise solution of the surface vorticity

The no-penetration boundary condition is used in slice-wise manner, as mentioned earlier. In each flow analysis slices, the satisfaction of boundary condition requires the solution of the Fredholm integral equation at each time instant t_i for each slice s such that

$$\left(\int_B \frac{\gamma_0 \times (\mathbf{x}_0 - \mathbf{x})}{|\mathbf{x}_0 - \mathbf{x}|^2} d\mathcal{B}_0 \right)_{t_n}^s \cdot \mathbf{n} = (\mathbf{I} - 2\pi [\mathbf{u}_0 - \mathbf{U}_\infty])_{t_n}^s \cdot \mathbf{n}. \quad (4.41)$$

Here, the unknown surface vorticity (γ_0) of the deformed body needs to be solved at each slice s for each time step t_n , in which $n = 1, 2, \dots, NT$. With the assumption of linear variation of γ_0 , the influence of the vortex sheets of each slice on all the other panels can be approximated as follows

$$\mathcal{M}_{(t_n)}^s \gamma_{0(t_n)}^s = \mathbf{b}_{(t_n)}^s, \quad (4.42)$$

where $\mathcal{M}_{(t_n)}^s$, $\gamma_{0(t_n)}^s$, and $\mathbf{b}_{(t_n)}^s$ are the influence matrix, unknown surface vorticity, and right hand side vector, respectively, at time step t_n for slice s .

4.3.2 A linear structural model for pseudo-3D multi-slice solver

The section presents the use a linear structural analysis model for the coupled pseudo-3D multi-slice simulation. It is noteworthy that the existing multi-slice model is structured such that any number of slice can be chosen. Basically, it means that the same model can be used for both 2D single-slice and pseudo 3D multi-slice FSI simulations. Clearly, the structural model should be constructed based on standard shell elements from existing finite element libraries (c.f. Fig. 4.14).

Mode-generalized structural model

The superposition of generalized vibration modes is a powerful technique for performing dynamic response analyses of linear structures. It can reduce the computational time significantly. A system with few DOFs can be solved using full system as shown in Eq. (4.8). However, for large systems, especially when the displacements are linear it is usually advantageous to transform Eq. (4.8) to a smaller set of equations by expressing the displacements in terms of the first few natural vibration modes ϕ_n of the undamped system. The basic assumption in mode superposition is that the nodal displacements of the system are approximated by a linear combination of the first j eigenmodes such that

$$\mathbf{d}(t) = \sum_{n=1}^j \phi_n \mathbf{q}_n(t), \quad (4.43)$$

Here, $\mathbf{q}_n(t)$ are the modal amplitudes. The equation of motion related to time dependent forces can be expressed in modal coordinates as follows:

$$\mathbf{M}\phi_j \ddot{d}_j + \mathbf{C}\phi_j \dot{d}_j + \mathbf{K}\phi_j d_j = f_{ext}(t), \quad (4.44)$$

pre-multiplying with ϕ_j^T gives

$$\phi_j^T \mathbf{M} \phi_j \ddot{d}_j + \phi_j^T \mathbf{C} \phi_j \dot{d}_j + \phi_j^T \mathbf{K} \phi_j d_j = \phi_j^T f_{ext}(t), \quad (4.45)$$

or

$$\phi_j^T \mathbf{M} \phi_j \ddot{d}_j + 2\xi_j \omega_j \phi_j^T \mathbf{M} \phi_j \dot{d}_j + \omega_j^2 \phi_j^T \mathbf{M} \phi_j d_j = \phi_j^T f_{ext}(t), \quad (4.46)$$

where ω_j is the modal circular natural frequency, ξ_j is the modal damping ratio, ϕ_j is the mode shape, the subscript j is the mode number and f_L is the lift force vector, respectively. The Eq. (4.46) can be written as following

$$\tilde{\mathbf{M}} \ddot{d} + \tilde{\mathbf{C}} \dot{d} + \tilde{\mathbf{K}} d = \tilde{\mathbf{P}}(t), \quad (4.47)$$

where

$$\tilde{\mathbf{M}} = \phi^T \mathbf{M} \phi, \quad \tilde{\mathbf{C}} = \phi^T \mathbf{C} \phi, \quad \tilde{\mathbf{K}} = \phi^T \mathbf{K} \phi, \quad \tilde{\mathbf{P}}(t) = \phi^T f_{ext}(t) \quad (4.48)$$

with $\tilde{\mathbf{M}}$, $\tilde{\mathbf{C}}$, and $\tilde{\mathbf{K}}$ being diagonal matrices. The solution algorithm using the Newmark's algorithm is presented in Algorithm 2.

Algorithm 2: Newmark's method: linear system (Constant average acceleration method with $\gamma = \frac{1}{2}$, $\beta = \frac{1}{4}$)

Input: $\tilde{\mathbf{M}}, \tilde{\mathbf{C}}, \tilde{\mathbf{K}}, \mathbf{f}_{ext}(t), \Phi$, timestep Δt

Output: $\mathbf{d}(t)$

1 Initial Calculations

→ Since the system starts from rest, $\mathbf{d}_0 = \dot{\mathbf{d}}_0 = \mathbf{0}$; therefore, $\mathbf{q}_0 = \dot{\mathbf{q}}_0 = \ddot{\mathbf{q}}_0 = \mathbf{0}$.

→ Calculate $\mathbf{a}_1, \mathbf{a}_2, \mathbf{a}_3$:

$$\begin{aligned} \rightarrow \mathbf{a}_1 &= \frac{1}{\beta(\Delta t)^2} \tilde{\mathbf{M}} + \frac{\gamma}{\beta \Delta t} \tilde{\mathbf{C}}; \quad \mathbf{a}_2 = \frac{1}{\beta \Delta t} \tilde{\mathbf{M}} + \left(\frac{\gamma}{\beta} - 1 \right) \tilde{\mathbf{C}}; \quad \mathbf{a}_3 = \\ &\left(\frac{1}{2\beta} - 1 \right) \tilde{\mathbf{M}} + \Delta t \left(\frac{\gamma}{2\beta} - 1 \right) \tilde{\mathbf{C}}. \end{aligned}$$

→ $\hat{\mathbf{K}} = \tilde{\mathbf{K}} + \mathbf{a}_1$.

2 Calculations for each time step, $i = 0, 1, 2, \dots$,

→ $\hat{\mathbf{P}}_{i+1} = \Phi^T \mathbf{f}_{ext}(i+1) + \mathbf{a}_1 \mathbf{q}_i + \mathbf{a}_2 \dot{\mathbf{q}}_i + \mathbf{a}_3 \ddot{\mathbf{q}}_i$

→ Solve $\hat{\mathbf{K}} \mathbf{q}_{i+1} = \hat{\mathbf{P}}_{i+1} \Rightarrow \mathbf{q}_{i+1}$

$$\rightarrow \dot{\mathbf{q}}_{i+1} = \frac{\gamma}{\beta \Delta t} (\mathbf{q}_{i+1} - \mathbf{q}_i) + \left(1 - \frac{\gamma}{\beta} \right) \dot{\mathbf{q}}_i + \Delta t \left(1 - \frac{\gamma}{2\beta} \right) \ddot{\mathbf{q}}_i$$

$$\rightarrow \ddot{\mathbf{q}}_{i+1} = \frac{1}{\beta(\Delta t)^2} (\mathbf{q}_{i+1} - \mathbf{q}_i) - \frac{1}{\beta \Delta t} \dot{\mathbf{q}}_i - \left(\frac{1}{2\beta} - 1 \right) \ddot{\mathbf{q}}_i$$

→ $\mathbf{d}_{i+1} = \Phi \mathbf{q}_{i+1}$

3 Repetition for the next time step. Replace i by $i + 1$ and implement the sub-steps of 2 for the next time step.

Modal Damping

In dynamic analysis, it is a common choice to provide the relative damping for each mode directly since it allows the calculation of the response using the superposition of uncoupled modal responses. The use of modal damping ratios gives a more control to assign a higher

damping value if, for physical reasons, they are expected to be strongly damped. The damping of a MDOF system with N DOFs the damping matrix can be expressed in terms of the modal damping ratios ξ_n with $(n = 1, \dots, N)$ [59]. In principle, the procedure can be explained by considering the complete diagonal matrix of generalized damping coefficients, given by pre and postmultiplying the damping matrix by the mode shape matrix:

$$\tilde{\mathbf{C}} = \phi^T \mathbf{C} \phi = \text{diag}(2\xi_1\omega_1 M_1, \dots, 2\xi_n\omega_n M_n) \quad (4.49)$$

For classically damped systems, the square matrix $\tilde{\mathbf{C}}$ is diagonal. There are few situations in dynamic analysis when the superposition of the uncoupled modal responses can not be used for response analysis. They situations are as follows

- non-linear response where the mode shapes are changing with change in the stiffness,
- linear system with non-proportional damping.

The use of the damping ratios are not therefore allowed to express the damping in aforementioned situations. An explicit damping matrix is necessary. In both of these circumstances, the most effective way to determine the required damping matrix is to first evaluate one or more proportional damping matrices. The classical damping matrix from modal damping ratios can be expressed as follows

4.3.3 Slice-wise presentation of thin structures in fluid flow

The proposed coupled FSI algorithm for pseudo-3D VPM employs the FE formulation for thin shell elements in which the structural equations are formulated and solved for the mid-surface of the thin structure, as it has been shown in Fig. 4.3. Since the 2D flow simulation slices are independent, the presentation of the immersed body and the coupling techniques are maintained as much as similar like the 2D coupled VPM. However, challenges still exist in the organisation of structural information for the flow solver in a slice-wise way.

Identification of projection element for the boundary panels

The challenges of using mid-surface approach in association with the BEM have been described in Sec. 4.2.3. It has been described about the necessity of identifying projection element for each panel and the sign of surface normal vector (n_e^\pm) according to the local coordinate of projection element. They have been shown for the calculation of the nodal forces from the pressures from surface panels. They have been shown further for updating geometry, boundary nodes, and panel velocities. Therefore, similarly like the 2D coupled model, the following two tasks have to be performed, however, in a slice-wise manner:

- Identification of projection element for all surface panels on which the fluid pressure has to be projected. This identification is performed for each 2D flow simulation slice.
- Slice-wise identification of the sign of surface normal vector for each panel with respect to the local coordinate of projection element.

The identification of projection element for each boundary panels is performed similarly as it has been described in Sec. 4.2.3. It is shown schematically in Fig. 4.15 for specific slice of shell structures, e.g. circular tower and roof shown in Fig. 4.14(a-b).

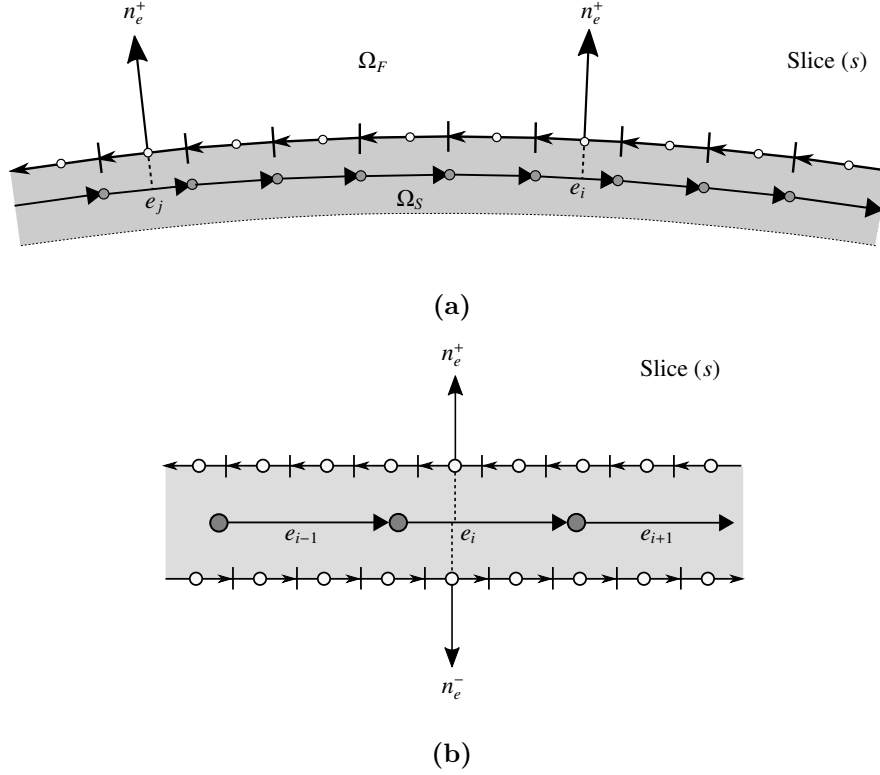


Figure 4.15: Identification of projection element for each boundary panel and the sign of surface normal vector corresponding to local axis of the projecting element, as shown in Fig. 4.5 for 2D coupled solver. Here, the schematics are shown for a slice s in which the structure is of closed circular shell in (a), whereas open shell in (b).

The Algorithm 1 can be used repeatedly for finding projecting elements for each surface panels, when the nodes and elements are defined according to the slices. In the end, the information is stored for each panel such that it contains the identity of projection element and the sign of surface normal vector with respect to the local coordinate of projection element.

It is important to note that the flow simulation slices are always a 2D plane. The structural nodes are expected to be considered in the flow simulation plane. This allows to consider projection element like the FE beam at the mid-surface for each slice. The aim is to exploit all the projection features of 2D coupled model to project information from one interface to another.

Calculation of nodal forces for the structural model

The calculation of the nodal forces for each 2D flow simulation slice is performed according to the procedure described in Sec. 4.2.4. If the pressure of a panel i in slice s is p_i^s , the total force normal on the panel $F_{i,s}^\pm$ can be calculated as

$$F_{i,s}^\pm = p_i^s \Delta_{s_i}^s W_{slice(s)}, \quad (4.50)$$

where $\Delta_{s_i}^s$ and $W_{slice(s)}$ are the length of i^{th} panel in slice s , and the slice width of the structure. The slice width $W_{slice(s)}$ is the dimension for which the pressure on the surface panel is considered same, see Fig. 4.14. If the distance between $(n-1)^{th}$ and $(n+1)^{th}$ slice is l , the width of slice n can be expressed as $W_{slice(n)} = l/2$.

The normal force $F_{(e,i,s)}^\pm$ on the projection element e for a slice s due to the pressures on a surface panel i is calculated as follows

$$F_{(e,i,s)}^\pm = F_{i,s}^\pm \cdot n_{e,i,s}^\pm, \quad (4.51)$$

where $n_{e,i,s}^\pm$ is the sign of surface normal vector for panel i with respect to the local coordinate of element e in slice s .

The calculation of the nodal forces $F_{n_1(e,i,s)}$ and $F_{n_2(e,i,s)}$ are performed using Eqs. (4.30-4.31), however, according to the slices. The formulation of the local force vector and the transformation to the global coordinate is performed similarly as mentioned in Sec. 4.2.4.

Structural vibration modes and flow simulation slices

The thin-walled structures can be modelled using 3-node or 4-node shell elements. However; it is important to note that the structural nodes should be in the plane of considered 2D VPM slice for flow analysis. To be consistent with the axis, the flow simulation slices are always considered in XY plane, which means the positions of the slices needs to be chosen along the Z -axis, see Fig. 4.14 for both cooling tower and roof. The structural nodes should be in the plane of flow simulation slice. Therefore, it is important to have a preliminary plan of flow simulation slices before developing the FE model of the structure.

If the FE model of the structure contains p number of potential XY plane along the Z -axis, a maximum p number of 2D flow simulation slices can be considered. For example, the cooling tower in Fig. 4.14 shows 21 possible position or plane for flow simulation slice; however, 10 slices have been used. The choice of slice number and position influence on the effective slice width, which is used for the integration of fluid pressure on the panels of a slice.

It is mentioned earlier that the structural equations are solved in modal coordinate system. It is therefore important to know the organisation of the mode shape vectors and how they are oriented with the flow simulation slices. If the FE model of the structure contains p number of potential slice plane, and each plane contains m number of FE nodes, the modal displacement vector for a natural vibration mode are organised as follows

$$\Phi = \begin{bmatrix} \phi_1 \\ \phi_2 \\ \dots \\ \phi_{p-1} \\ \phi_p \end{bmatrix}, \quad (4.52)$$

where ϕ_1, \dots, ϕ_p are the modal displacement vectors for the FE nodes in plane 1 to p . If $i = 1, \dots, p$, the modal displacement vector ϕ_i can be expressed as follows

$$\phi_i = \begin{bmatrix} d_{x(i,1)} & d_{y(i,1)} & d_{z(i,1)} & \alpha_{x(i,1)} & \alpha_{y(i,1)} & \alpha_{z(i,1)} \\ \dots & \dots & \dots & \dots & \dots & \dots \\ \dots & \dots & \dots & \dots & \dots & \dots \\ d_{x(i,m)} & d_{y(i,m)} & d_{z(i,m)} & \alpha_{x(i,m)} & \alpha_{y(i,m)} & \alpha_{z(i,m)} \end{bmatrix}. \quad (4.53)$$

When the structural solution is obtained using Eq. (4.43), the nodal displacements are obtained for the all the structural nodes. The projection of the nodal solution to the flow solver

needs a check on the position of the flow simulation slices if all of the structure planes are not used for the coupled analysis.

Projection of motion from mid-surface to boundary panels

It is mentioned earlier that the projection of information from mid-surface to boundary panels is performed in a way to re-use the algorithm of the 2D coupled solver. In each slice, the projection elements are utilised for updating geometry and panel velocities of the deformed body, which is according to the steps discussed in Sec. 4.2.5. According to the vibration modes, the structural solution provides system response in Z -axis. However, the structural nodes of a flow simulation slice remain in the XY plane, and therefore, the horizontal and across-flow responses are only updated.

4.3.4 Slice-wise fluid–structure coupling

The fluid and structural equations are coupled with each other through the coupling of boundary conditions at the fluid–structure interface (Σ) which are the continuation of displacement, forces, and velocities, as mentioned in Sec. 4.2.6, in a slice-wise way.

Furthermore, in every time step t_n , the global panel velocities (p_{vx} and p_{vy}) needs to be restructured such that the normal velocity components ($p_v \cdot \mathbf{n}$) in updated panel coordinate on the solid boundary \mathcal{B} are enforced in the right hand side of the Eq. (4.41), which is repeated in the following

$$\left(\int_B \frac{\gamma_0 \times (\mathbf{x}_0 - \mathbf{x})}{|\mathbf{x}_0 - \mathbf{x}|^2} d\mathcal{B}_0 \right)_{t_n}^s \cdot \mathbf{n} = (\mathbf{I} - 2\pi [\mathbf{u}_0 - \mathbf{U}_\infty])_{t_n}^s \cdot \mathbf{n}. \quad (4.54)$$

It is necessary to calculate unknown surface vorticity at each slice for each time step. The flowchart of the pseudo-3D coupled model is presented in Fig. 4.16.

4.4 A simplified aeroelectromechanical coupled model

Aeroelastic large-displacement limit cycle oscillations (LCO) of the thin plate systems can be exploited for energy harvesting to operate self-powered electronic devices and sensor nodes. They are designed in a way such that aeroelastic motion of the harvesters allows to generate electricity, more details on different harvesters are available in Chapter 6. The important point is that when the electricity generates in the circuit, it introduces electrical force and opposes the flow-induced motion of the harvester. This electrical force is proportion to the electrical damping, and the equation of motion of the harvester can be written in a simplified form as follows

$$\mathbf{M}\ddot{\mathbf{q}} + (\mathbf{C} + \mathbf{C}_e)\dot{\mathbf{q}} + \mathbf{K}\mathbf{q} = \mathbf{f}_{\text{ext}}, \quad (4.55)$$

where $(\mathbf{C} + \mathbf{C}_e)$ represents the sum of mechanical and electrical damping. The Rayleigh damping approach in Sec. 4.2.2 is used to calculate this total damping matrix using the total damping ratio $\zeta_t = \zeta_m + \zeta_e$, in which ζ_m and ζ_e are the mechanical and electrical damping ratios.

The validation of the method is shown in Chapter 6, which is based on the prediction of onset flutter wind speed and energy output of a reference prototype harvester in wind tunnel at different wind speeds. The method is shown further for optimization of harvester performance.

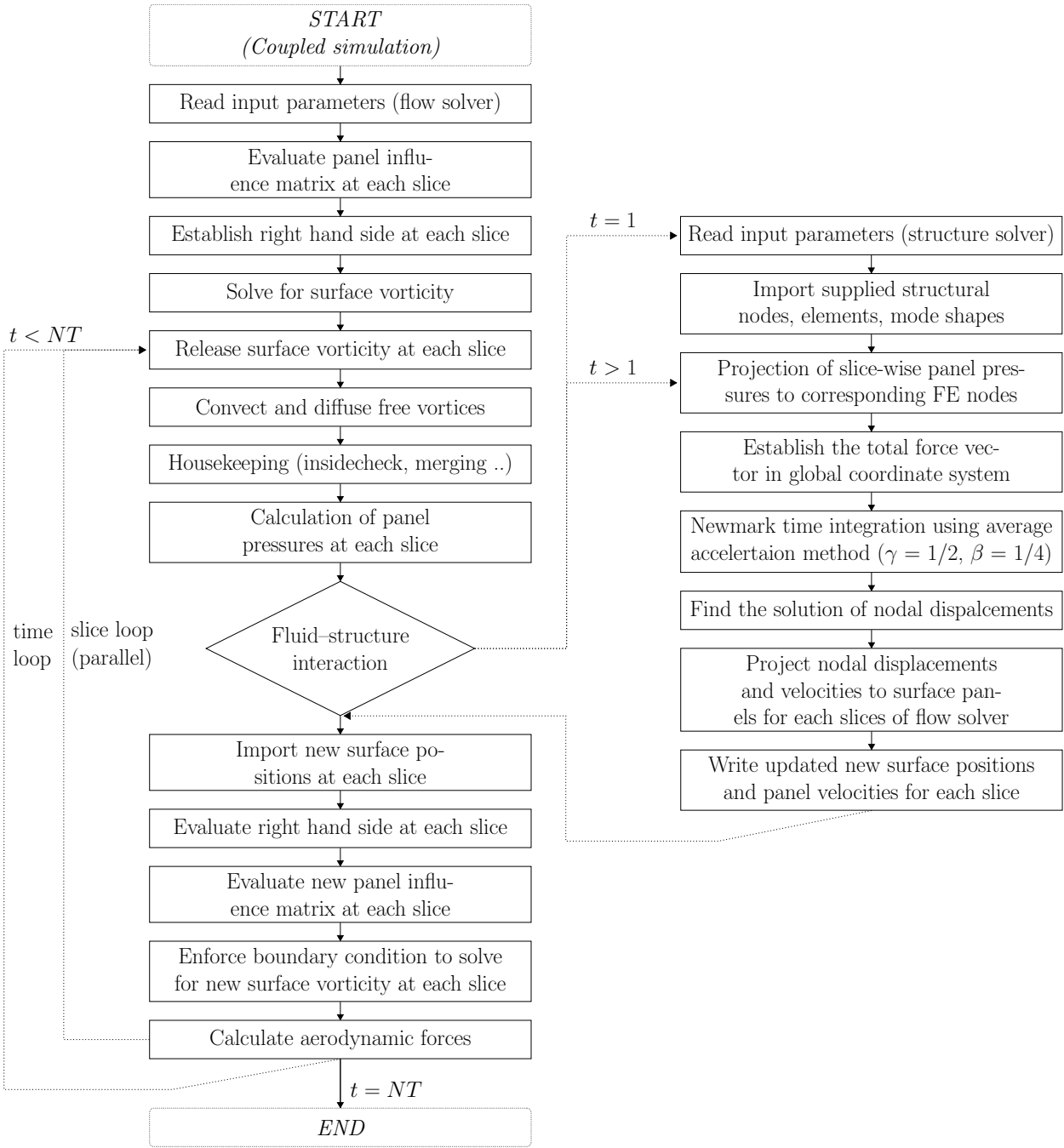


Figure 4.16: Flowchart representation of coupled numerical algorithm for pseudo-3D multi-slice simulations.

Finally, this aeroelectromechanical coupled model shown how to perform a preliminary design and asses the potential of harvesters (within a size limit) for electromagnetic and piezoelectric harvesting from wind loading.

4.5 Methods of inflow fluctuations for FSI simulation

In this thesis, two new numerical extensions are developed for inflow turbulence using the concept of seeding vortex particles to be used for FSI simulations of any type of geometries, i.e. rigid and/or flexible. While one proposed extension presents the simulation of pulsating incoming flow, the other one introduces the reproduction of turbulent wakes from upstream

bodies for computationally efficient wake buffeting analyses.

Within the framework of existing VPM, the vorticity carrying particles can be used for the simulation of inflow fluctuations. The concept of seeding particles was introduced in Prendergast and McRobie [192] and Prendergast [193] for modelling of 2D unsteady wind. The particles were pre-calculated from statistically generated target turbulent wind field. The method was further employed in Hejlesen et al. [115], Rasmussen et al. [197] for the simulation and estimation of the aerodynamic admittance in bridge aerodynamics.

The pulsating flow is modelled by seeding pre-calculated particles from two seeding points near the upstream boundary. The seeding mechanism and the orientation of the particles are handled such that they induce only horizontal velocity components around the domain centre while the vertical components are nearly cancelled out. The sinusoidal periodic flow is modelled by seeding the particles of varied strength and orientation, correspondingly. The simulation of incoming turbulent wakes, on the other hand, is modelled by seeding particles as a reproduction of an original wake flows from upstream bluff bodies. It is presented as an alternative efficient technique of simulating turbulent wakes for wake buffeting analysis.

Both of the numerical extensions, the methodology, numerical validation, and application in FSI simulations are presented more in details in Chapter 7.

4.6 Summary

This chapter has presented the new extensions of VPM for FSI simulation of thin-walled flexible systems. The 2D coupled extension of VPM has been delivered for large-displacement FSI problems since an advance structural solver based on corotational finite element formulation has been used that can include the nonlinear effects due to large deformation. The validation of the coupled model in terms of the enforcement of the boundary conditions are shown by modelling the flow around a rigid thin plate is analysed for imposed translational and rotational motion. Comparison of flow fields with a rigid model is very much satisfactory. The pseudo-3D VPM, on the other hand, with a structural model based on linearised vibration modes has been proposed for the FSI simulations of thin-walled shell-type structures.

Chapter 5

Fluid–structure interaction simulations of thin-walled structures

5.1 Introduction

This chapter presents numerical studies on several fluid-structure interaction (FSI) problems involving thin-walled flexible systems. Initially, the two-dimensional (2D) coupled extension of the Vortex Particle Methods (VPM) is used for analysing 2D FSI problems. The validation of the method is shown based on numerical simulations of several benchmark large-displacement FSI problems. Another numerical extension, which is the pseudo-three-dimensional (pseudo-3D) multi-slice model of VPM, is utilised to simulate the aeroelastic coupled motion of thin-walled shell-type structures such as roofs, long circular pipes, solar chimneys, etc. This multi-slice model is proposed for small-displacement FSI problems of geometrically linear structures. For all presented studies, the physical and numerical parameters of the coupled model are showcased in a tabular form to ensure the reproducibility of the results.

5.2 Validation of the two-dimensional coupled solver

In the following, the presented 2D partitioned solver is used for large-displacement FSI simulations of thin plate systems. As mentioned earlier in the previous chapter that the 2D VPM with immersed interface technique [174, 177] has been used for analysing flow around deformable bodies. The geometrically nonlinear plate motion is analysed using 2D corotational beam element. The coupled solver is validated on benchmark large-displacement FSI problems such as the flapping of cantilever plates in axial flow and Kármán vortex street.

5.2.1 Flexible cantilever in von Kármán vortex street

This 2D FSI problem in which a thin elastic cantilever plate is attached to the downstream side of a rigid square section has been reported extensively in the literature [77, 107, 124, 125, 137, 160, 242, 243]. Beyond a critical Reynolds number (Re), the bluff and rigid square in axial flow causes flow separation and vortices from the leading corners. These vortices induce

alternative drop and increase in pressure field behind the body, in turns time-dependent lift forces. It is well-known von Kármán vortex shedding which can excite an attached flexible cantilever beam to large-displacement oscillatory motion.

The geometry and inflow conditions of the reference FSI problem are presented schematically in Fig. 5.1(a) while the discretisation of the FSI problem for presented flow and structure solver is shown schematically in Fig. 5.1(b). The summary of the material parameters of fluid and solid are listed in Table 5.1. The inflow velocity corresponds to the Reynolds number $\mathcal{R}e = D_s U_\infty / \nu_f$ of 333, in which D_s is the length of the sides of the rigid square cylinder.

The surface of the rigid square and flexible plate within the flow solver is discretised together into a number of surface panels (Fig. 5.1(b)). The numerical parameters of the coupled simulation are summarised in Table 5.2 according to the flow and structure solver. The

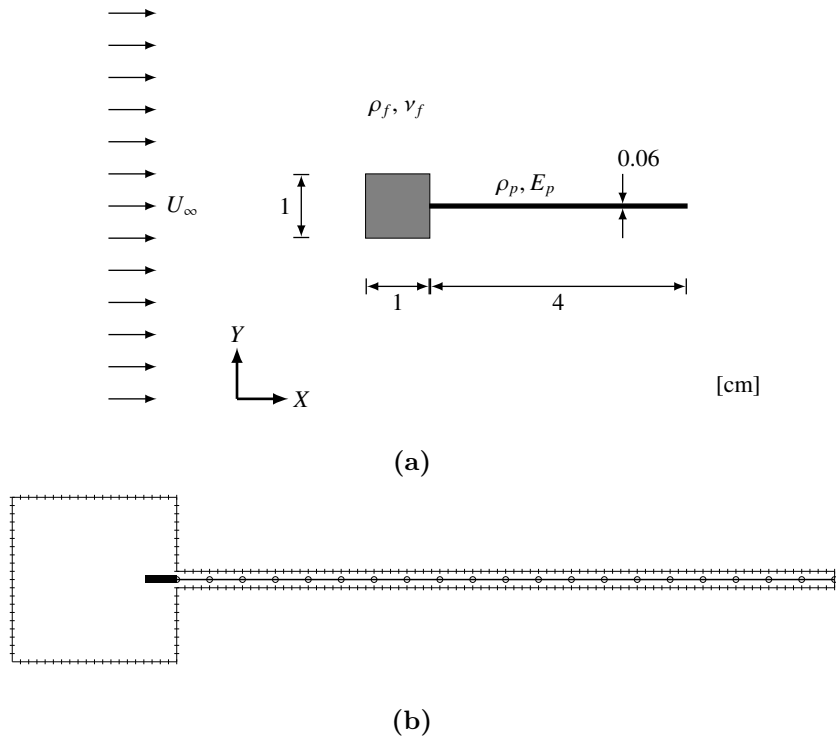


Figure 5.1: The interaction between the vortex shedding of rigid square section with the attached flexible cantilever plate:

- (a) schematic presentation of the problem with required physical dimensions,
- (b) the discretisation of the cantilever and rigid square for the 2D coupled VPM solver. Here, the surface discretisation is shown for the flow solver whereas the finite element discretisation is shown at the mid-surface of the flexible beam.

Physical and geometrical properties			Value
Solid	Density	ρ_s	100 kg/m ³
	Elastic modulus	E	2.5×10^5 Pa
	Depth of the square section	D_s	1 cm
Fluid	Density	ρ_f	1.18 kg/m ³
	Kinematic viscosity	ν_f	1.54×10^{-5} m ² /s
Flow	Free-stream flow	U_∞	0.513 m/s
	Reynolds number	$\mathcal{R}e$	333

Table 5.1: Benchmark FSI problem of aeroelastic motion of an elastic cantilever attached to a square bluff body: properties of the flow, fluid and solid.

Solver	Numerical parameters		Value
Flow	Length of the domain	l_d	60 cm
	Width of the domain	w_d	29.9413 cm
	Number of panels (rigid square and cantilever)	N_{panel}	242
	Panel size	$\Delta s/D_s$	0.05
	Non-dimensional time step	$\Delta t_f^* = \Delta t_f U_\infty / \Delta_s$	1
	Poissson grid	$N_x \times N_y$	511×255
	Number of particles (approx.)	$N_{particle}$	67,000 - 76,000
Structure	Number of beam elements	N_{elem}	40
	Length of beam element	l_{elem}	0.1 cm
	Non-dimensional time step	$\Delta t_s^* = \Delta_s U_\infty / \Delta_s$	1
	Number of sub-time steps		15

Table 5.2: Benchmark FSI problem of aeroelastic motion of an elastic cantilever attached to a square bluff body: numerical parameters for 2D coupled VPM analysis.

equation of motion of the structural nodes are considered at the mid-surface (Fig. 5.1(b)). The lumped mass approach is used to define the mass matrix. The 1st natural frequency of the cantilever beam (f_{n1}) according to the analytical formulation presented in [60] is found to be 3.0285 Hz. The convergence of f_{n1} compared to the analytical solution is shown in Fig. 5.2 for different number elements. It is observed that the use of 40 elements in the current study is sufficient for the structural model.

The Strouhal number ($St = f_s D_s / U_\infty$), a non-dimensional parameter to describe the frequency of vortex shedding (f_s), is found to be approximately 0.135 for the square cylinder at $Re = 333$. The corresponding vortex shedding frequency the square cylinder under the studied flow speed is found to be 6.92 Hz. From the theory of structural vibrations, it is well known that when the motion of the structure is excited by external force with a specific forcing frequency, the structure will oscillate with the same frequency as that of the imposed force. In the case of the attached cantilever to the square cylinder, the oscillation frequency can be governed by the interaction between the fluid and structure [107]. Moreover, the addition of the cantilever beam as well as its motion should modify the vortex shedding pattern and frequency contents.

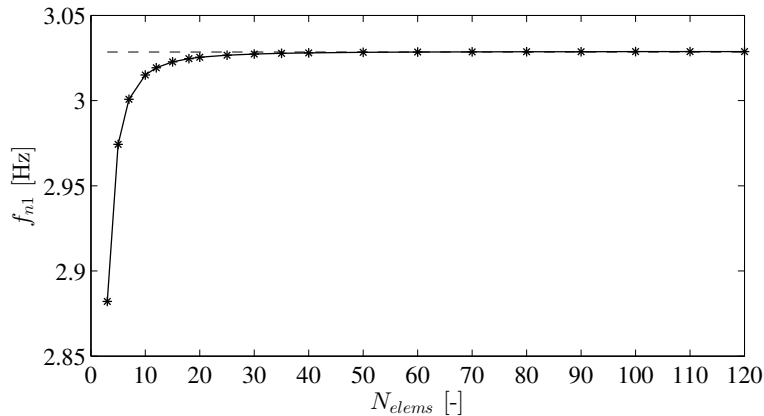


Figure 5.2: Convergence study of finite element discretisation: 1st natural vibration frequency is compared based on the number of element (N_{elems}) together with the analytical solution (—).

The oscillatory motion of the cantilever beam under the vortex shedding of a square cylinder is shown in Fig. 5.3 for different vibration phases. The adaptive particle remeshing strategy for VPM [168] is utilized to simulate the motion of the flexible cantilever beam. It is observed clearly from the particle maps in Fig. 5.3(a-c) that the particles are more in number near the fluid-solid interface and a gradual reduction away from the body. It allows the flow solver to resolve the flow field more precisely near the boundary layer. The time history of the displacement at the tip of the cantilever beam ($d_{y,t}$), the superposition of different vibration phases, and the convergence check for the structural solution are shown in Fig 5.4(a-c), respectively. For the convergence test of the solution for last iteration step is shown in Fig 5.4(c) with a tolerance limit of $1e-10$ chosen for energy increment (E_{incr}). The maximum number of sub-iteration to achieve the limit is found to be 3. Simulation is performed using a CPU system with Windows 7 operating system, 24-core with 2.66 GHz processor, and 64 GB RAM. The average run-time of the coupled simulation is calculated approximately 8.7 seconds per simulation time step.

The motion of the cantilever beam dominates the coupled motion since the coupled vibration

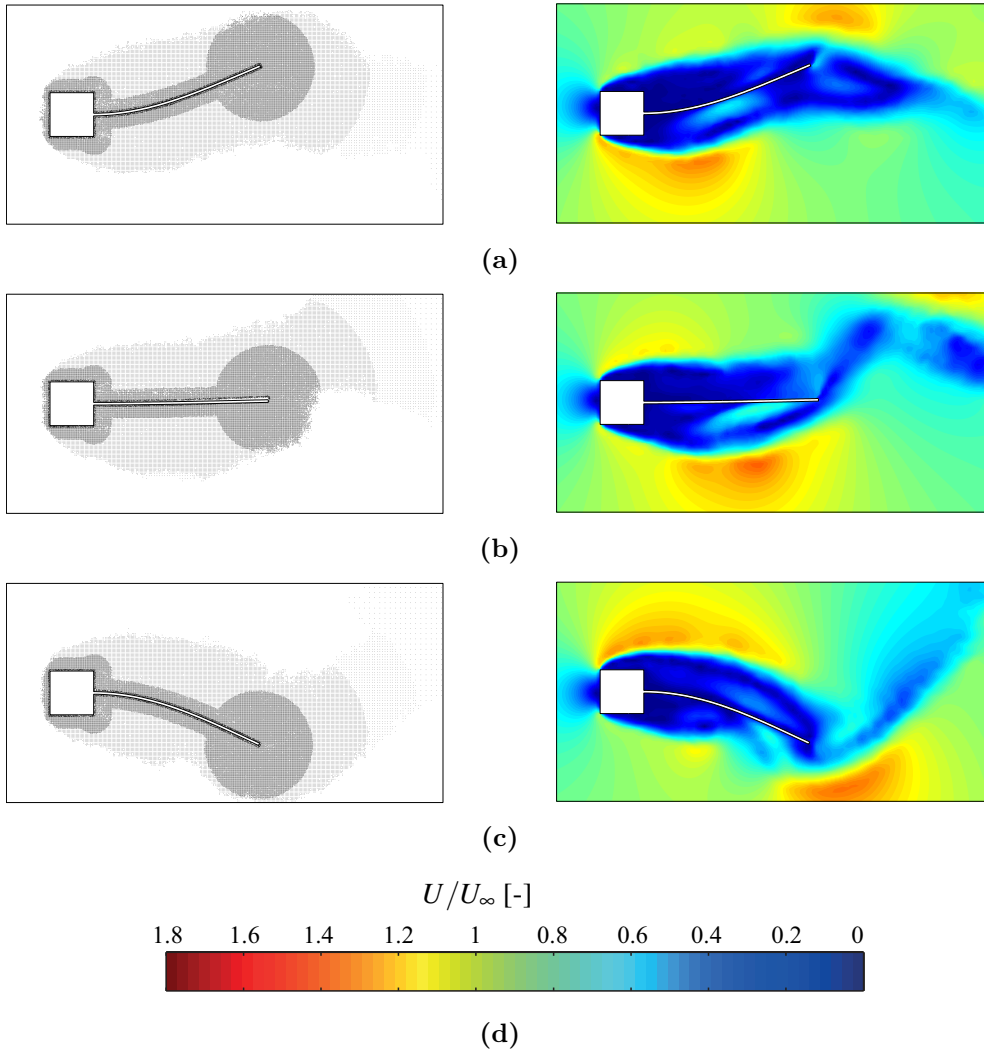


Figure 5.3: The particle maps (left of (a-c)) and corresponding flow fields (right of (a-c)) are shown for different vibration phases of the cantilever beam under the vortex shedding from a rigid square body. The non-dimensional velocity field U/U_∞ is shown in the colour chart (d).

frequency of the cantilever beam (3.12 Hz) is found slightly above the first natural frequency of the elastic appendix (see Fig. 5.5). This is due to the interaction with the vortex shedding

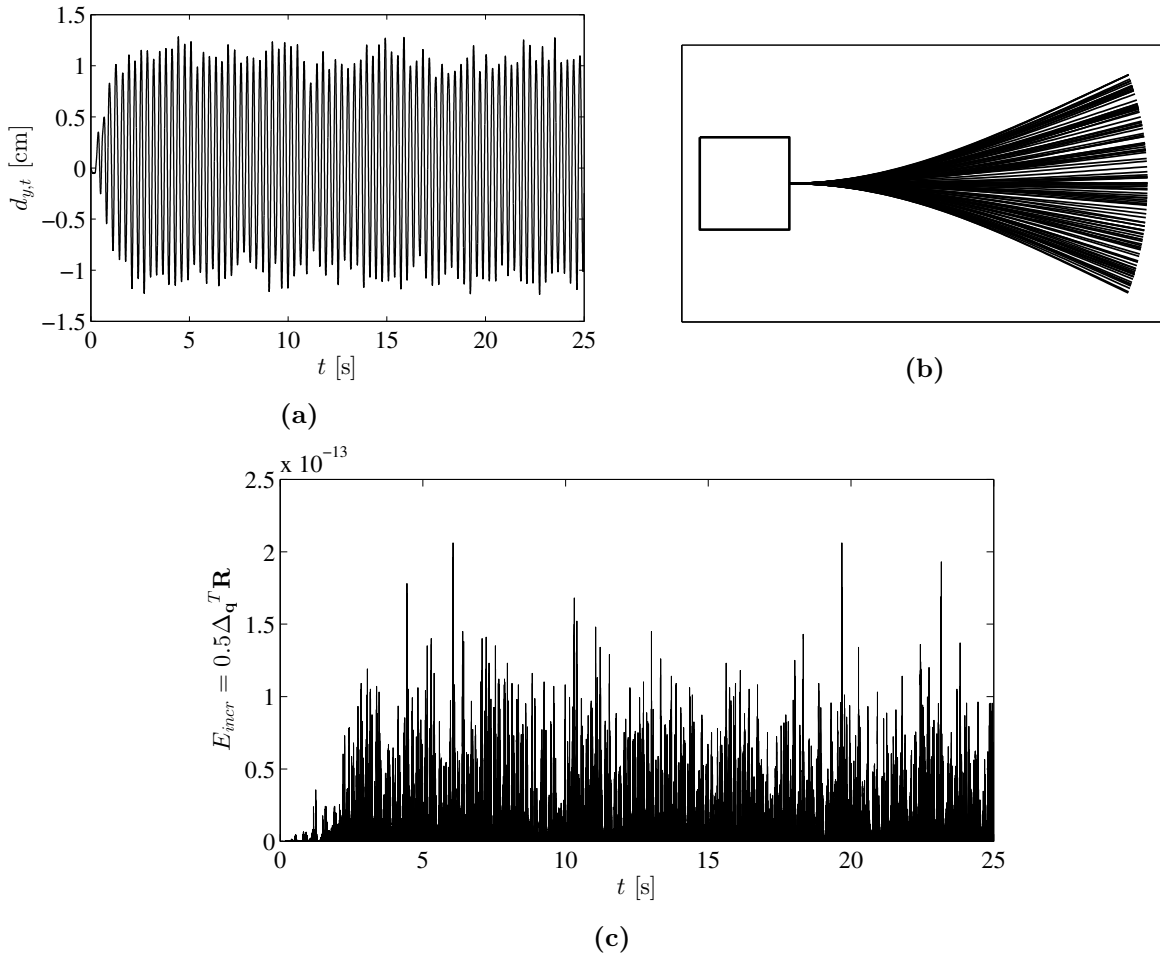


Figure 5.4: The simulation of cantilever beam under the vortex shedding from upstream square: (a) the time history of the vertical tip displacement, (b) the superposition of the vibration phases, and (c) the convergence test of energy increment E_{incr} , which is the dot product of solution vector and residual forces in last iteration step.

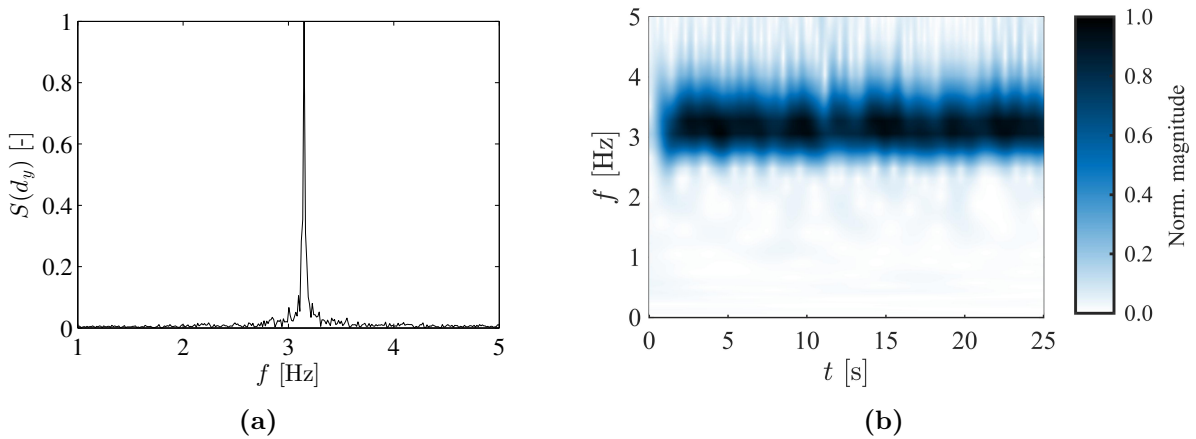


Figure 5.5: Study on the frequency of response of cantilever tip: (a) normalised frequency spectrum of the displacement time history, and corresponding wavelet transformation in (b) to show the change of frequencies over the time.

from the upstream square cylinder. As mentioned earlier that the resonance motion or a pure limit cycle oscillation behaviour should not be expected here. Therefore, it is observed in Fig 5.4(a) that the peak displacements are varying due to the coupled interactions. The long-term coupled beam tip displacement is observed to be in the range $|d_{y,t}|$ of 0.95 – 1.32 cm.

The tip displacement of the cantilever beam is found in good agreement with previous results from the literature. The oscillation frequency and the maximum displacement of the cantilever tip in the open literature are compared in Table 5.3. It is clear from the reference results presented in this table that there are differences in the outcome considering different numerical methods and their coupling approaches to handle such complex interactions.

Studies	Fluid flow	SD	Coupling	f [Hz]	$ d_{y,t} _{max}$ [cm]
Wall and Ramm [243]	Stabilized FEM	FEM	BGS ^a	2.77–3.22	1.12–1.32
Matthies and Steindorf [160]	FVM	FEM	BN ^b	3.125	1.00–1.35
Dettmer and Perić [77]	Stabilized FEM	FEM	NR ^c	2.94–3.125	1.10–1.40
Wood et al. [253]	FVM	FEM	BGS	2.94–3.125	1.10–1.20
Kassiotis et al. [137]	FVM	FEM	BGS	2.98	1.05
Habchi et al. [112]	FVM	FEM	BGS	3.25	1.02
Gilmanov et al. [107]	LES ^d	FEM	BGS	3.2	1.00–1.10
Current work	adaptive-VPM	FEM	NR	3.05–3.15	0.95–1.32

^a Partitioned Block Gauss–Seidel

^b Partitioned Block–Newton

^c Partitioned Newton–Raphson

^d Large Eddy Simulation

Table 5.3: Comparison of current results with those in the open literature for the elastic flexible cantilever attached to square bluff body case.

5.2.2 Flutter instability of cantilevered flexible plate

The flutter instability of cantilevered flexible plate immersed in axial flow is a canonical problem, which is shown in Fig. 5.6. In a fast-moving light fluid, the instability of a thin cantilevered plate occurs when the frequency of the lowest bending mode becomes equal to the frequency of aerodynamic oscillations [25].

This instability arises from the competition between the destabilizing effect of the aerodynamic pressure and the stabilizing effect of the bending rigidity of the structure [91, 166]. Example of such phenomenon includes: the paper in printing presses [249], medical applications [28, 123], and aeroelastic energy harvesters [84, 105, 164]. It is a challenging fluid-structure interaction problem of high-frequency fluttering, despite the fact that the system looks very simple [226]. The two-dimensional stability analysis of cantilevered plates in axial flow has also been modelled numerically in many studies [61, 94, 225–227]. The commonly used non-dimensional parameter to explain the critical behaviour of cantilever flag are the mass ratio of μ and reduced flow velocity U_R , which are defined as follows

$$\mu = \frac{\rho_f L}{\rho_s h}, \quad (5.1)$$

$$U_R = U_\infty L \sqrt{\frac{\rho_s h}{D}}, \quad (5.2)$$

where bending stiffness $D = Eh^3/[12(1 - \nu^2)]$, in which E and ν are, respectively, the Young’s modulus and Poisson ratio of the plate material. In present study, the structural models have been based on two-node Euler-Bernoulli beam element, which ignores the shear

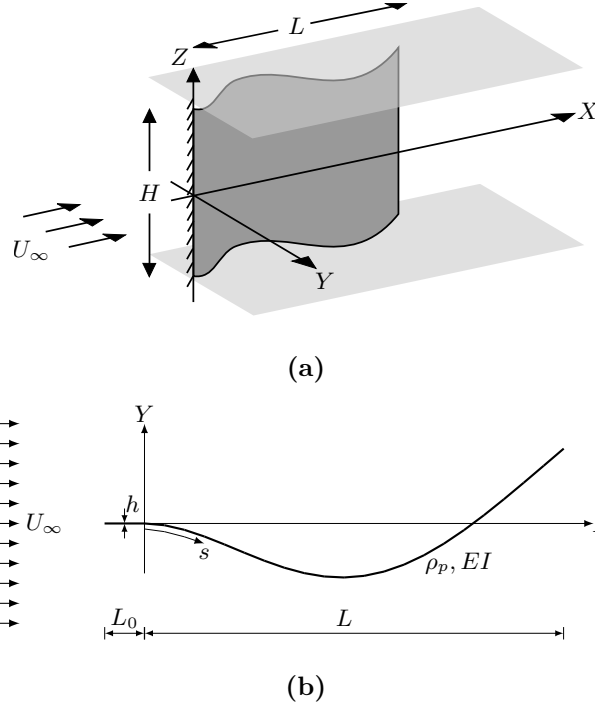


Figure 5.6: The flutter-induced flapping of a cantilevered flexible plate: (a) the plate in conventional flag configuration under axial flow U_∞ . The incoming flow acts on both surface of the plate, and the vortices shed from the trailing edge. (b) A 2D representation of the critical vibration mode.

deformation effects. However, the value of ν from reference studies is mentioned here, only to compare the present results with the reference results based on plate elements, for example in terms of non-dimensional parameter like U_R .

A thin cantilever plate of aluminium in conventional flag configuration is chosen from Tang et al. [227] to simulate as a reference system. The physical and geometrical properties of the plate are listed in Table 5.4. The value of μ which represents the relative magnitude of fluid to solid inertial forces is chosen 0.5. The numerical parameters of the coupled simulation considering the fluid and structure solver are summarized in Table 5.5. The natural frequencies of the first two vibration modes are found to be 1.196 Hz and 7.5 Hz. The flow velocity is gradually increased to identify the critical flutter wind speed, and also to study the behaviour of the system at post critical wind speeds.

At a critical flow velocity, the cantilever starts to flutter with large amplitude vibration

Physical and geometrical properties		Value	
Solid	Density	ρ_s	2840 kg/m ³
	Elastic modulus	E	7.056×10^{10} Pa
	Poisson ratio	ν	0.3
	Plate thickness	h	0.0005 m
	Plate length	L	0.58 m
	Plate height	H	0.2 m
	Support length	L_0	0.0058 m
Fluid	Density	ρ_f	1.226 kg/m ³
	Kinematic viscosity	ν_f	1.5×10^{-5} m ² /s

Table 5.4: Physical parameters of a cantilevered flexible plate in axial flow (mass ratio $\mu = 0.5$).

Solver	Numerical parameters		Value
Flow	Simulated free stream velocities	U_∞	6–13 m/s
	Length of the domain	l_d	4 m
	Width of the domain	w_d	1.99216 m
	Number of panels	N_{panel}	236
	Panel size	$\Delta s/h$	10
	Non-dimensional time step	$\Delta t_f^* = \Delta t_f U_\infty / \Delta_s$	0.5
	Poisson grid	$N_x \times N_y$	255×127
	Number of particles (approx.)	$N_{particle}$	60,000 - 75,000
Structure	Number of beam elements	N_{elem}	116
	Length of beam element	l_{elem}	0.005 m
	Non-dimensional time step	$\Delta t_s^* = \Delta t_s U_\infty / \Delta_s$	0.5
	Number of sub-time steps		20

Table 5.5: The flapping of cantilever plate in conventional flag configuration: numerical parameters for 2D coupled VPM analysis.

and exhibits a periodic LCO. The bifurcation diagram is shown in Fig. 5.7(a). The flutter amplitude increases monotonically with the increase in U_∞ . The initiation of fluttering is observed approximately at U_∞ of 8.25 m/s which is found slightly earlier than the identified fluttering limit of 9 m/s in Tang et al. [227]. The peak response amplitudes of the cantilever tip at higher wind speeds such as 10–13 m/s are found to be almost similar as [227]. The non-dimensional critical flutter threshold is calculated $U_{R(cr)} = 6.31$ corresponding to dimensional $U_{\infty(cr)}$ of 8.25 m/s. The flutter frequencies corresponding to the bifurcation diagram are shown in Fig. 5.7(b), which are close to the frequency of second vibration mode. The frequencies are observed increasing with the increase in U_∞ as experienced in [212, 249]. It is apparently due to the increase in positive aerodynamic stiffness for the flag-type system in the increasing axial flow. The time histories of the vertical tip displacement ($d_{y,t}$) of the cantilever beam are shown in Fig. 5.7(c, d) for U_∞ of 9 m/s and 13 m/s, respectively. The fluctuations are observed in LCO at 13 m/s which is due to the geometric nonlinearity at large displacement in higher wind speeds. The velocity–displacement ($v_{y,t}$ – $d_{y,t}$) relationship for the tip motion in vertical direction for U_∞ of 9 m/s and 13 m/s are shown in Fig. 5.7(e, f), respectively. Finally, the superimposed views of flutter modes are shown in Fig. 5.7(g, h) accordingly.

The identification of the critical flutter wind speed and tip responses of the cantilever have been found reasonably good compared to the reference study. The flag-type fluttering of the cantilever in lowest bending mode is the essence of this FSI problem which is observed in Fig. 5.7(g, h), and they are found quite comparable with the reference studies in the literature. From the limitation point of view, the presented model exhibits added-mass instabilities if the value of μ become more than 1. This is expected as the presented scheme is loosely coupled, and the added-mass instabilities can not be improved just by reducing the time steps. It needs more tight coupling between the fluid and structure solvers.

5.2.3 Aeroelastic motion of inverted flexible cantilever plate

Flapping mechanisms and influential parameters

In contrast to a cantilever plate in conventional flag configuration, the inverted cantilever with a free leading edge and a clamped trailing edge, displays large-amplitude flapping over a finite band of flow speeds, was introduced by Kim et al. [142]. Afterwards, Sader et al.

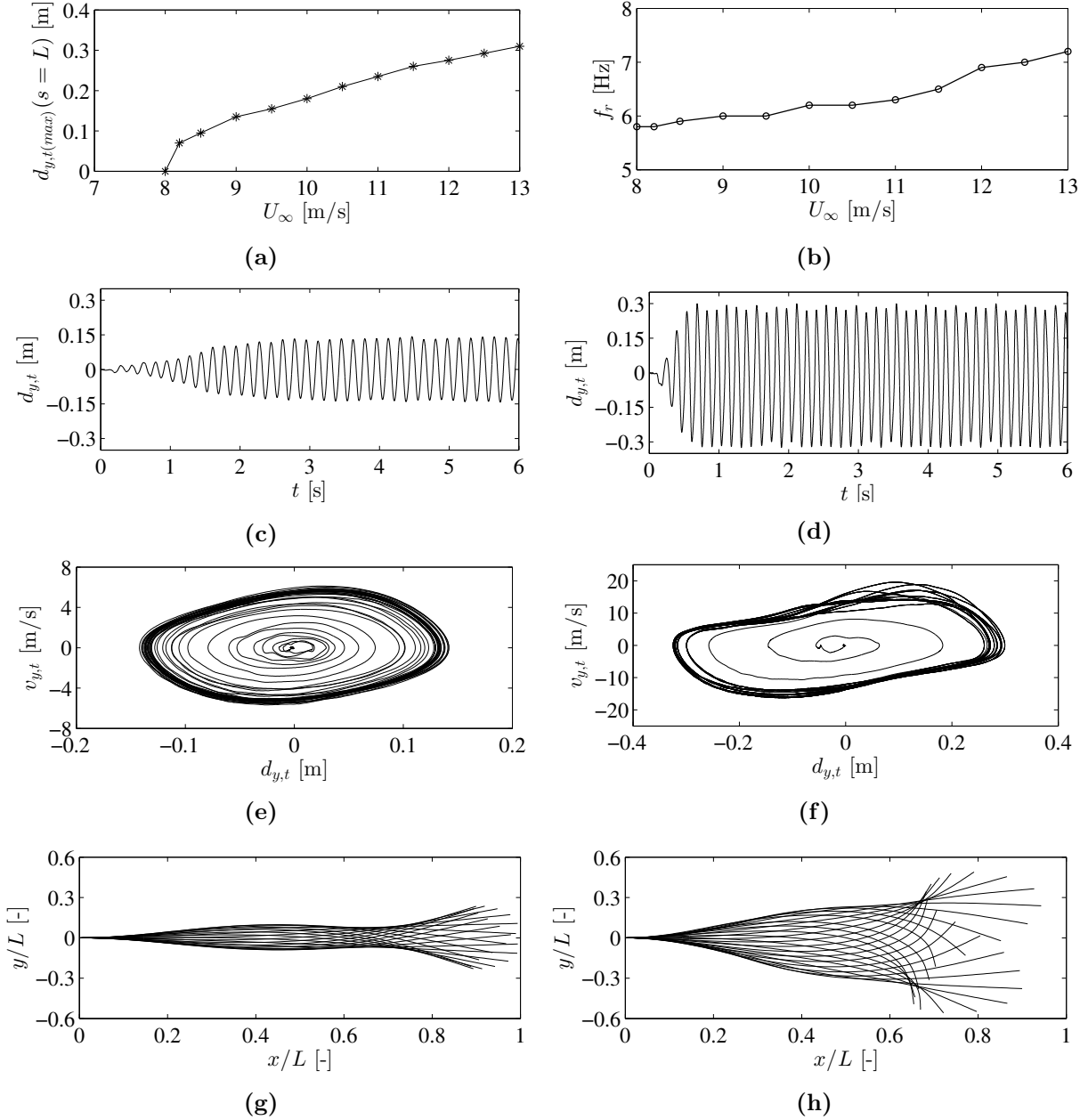


Figure 5.7: The instability and post-critical vibrations of a flag-type cantilever plate in axial flow ($L = 0.58$ m, $B = 0.2$ m, $\mu = 0.5$, $L_0/L = 0.01$): The bifurcation diagram and the flutter frequencies are shown in (a) and (b), respectively. The time histories of the vertical tip displacement are shown in (c) and (d) for U_∞ of 9 m/s and 13 m/s, respectively. The velocity–displacement plots for vertical tip displacement are shown in (e) and (f) in same order. Finally, the superimposed fluttering motion of the cantilever plate for U_∞ of 9 m/s and 13 m/s are shown in (g) and (h), respectively.

[201] studied extensively on several influential parameter to establish the reason behind the flapping mechanism. The schematic configuration of an inverted flag in axial flow is shown in Fig. 5.8 and its typical flapping behaviour are shown in Fig. 5.9.

The flapping of inverted flag was identified into two quasi-steady regimes, straight mode and fully deflected mode, and a limit-cycle flapping mode with large amplitude appears between the two quasi-steady regimes [142]. The classification of flapping of an inverted cantilever can be expressed based on its non-dimensional bending stiffness scaled by flow velocity and

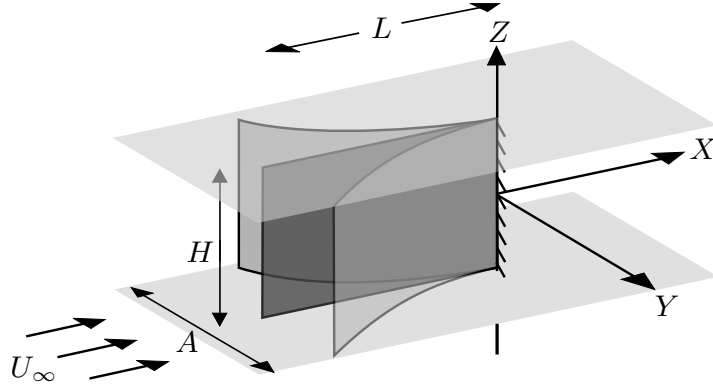


Figure 5.8: Schematic configuration of a cantilever plate (length $L \times$ height H) is shown in inverted flag configuration. The isometric view shows the peak-to-peak amplitude (A) of the cantilever tip in y -direction under axial flow U_∞ . The presented 2D coupled numerical model of the cantilever plate ignores the edge-effects, and it is visualized here by the confinement of the cantilever system in between the walls.

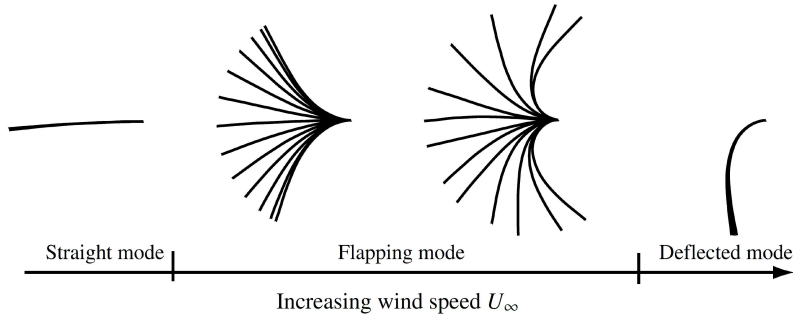


Figure 5.9: Schematic presentation of the deflected modes for an inverted flag with the increase in incoming flow speed [201].

plate length. The stability of a conventional flag depends on two non-dimensional dynamic parameters: μ in Eq. (5.1) and

$$\kappa = \frac{\rho U^2 L^3}{D}, \quad (5.3)$$

where κ specifies the dimensionless flow speed. The flapping mechanisms of inverted flag was established as a vortex-induced vibration in [201] after extensive studies using a combination of mathematical theory, scaling analysis and measurement. The aspect ratio was shown to be a influential parameter. A plate with small aspect ratio in a steady flow allows to generate edge vortices along and across the flow direction which reduces the overall lift. Therefore the bifurcation is largely affected by the aspect ratio. By performing eigenvalue analysis, the study results in Sader et al. [201] showed for infinite aspect ratio that the stability of an inverted flag lost at zero frequency when the non-dimensional flow speed $\kappa = 1.85$.

Two-dimensional simulation of reference inverted flag

In the following, the dynamics of a reference inverted cantilever plate which was studied in Sader et al. [201] has been investigated numerically using the presented coupled solver. The physical and geometrical properties of the plate are listed in Table 5.6. The numerical

properties of the coupled simulation considering the fluid and structure solver are summarized in Table 5.7. The inverted cantilever beam is simulated under different wind speeds. No edge-effects are considered in the analysis. Concerning edge-effects, the consideration of a 2D plate with infinite aspect ratio is analogous to the consideration of finite plate confined between the side walls (Fig. 5.8(a)).

The simulation results are displayed in Fig. 5.10 for both dimensional and non-dimensional incoming flow speeds. The transitions of the system response from stable to flapping and from flapping to deflected equilibrium are shown in Fig. 5.10(a) for different simulated flow speeds. The bifurcation is observed immediately after non-dimensional flow speed $\kappa = 1.85$. This is an agreement with the results from Sader et al. [201] since the present model doesn't consider the effect of vortices from the edges across the flow direction.

Fig. 5.10(b) shows the time histories of the tip displacements corresponding to flow speeds. The response frequencies of the cantilever tip are presented in Fig. 5.10(c) by applying a fast Fourier transform (FFT) to the displacement time histories. The shedding frequencies are presented in Fig. 5.10(d) by applying FFT to the time histories of the lift forces. It is seen in Fig. 5.10(c,d) that the response frequencies are synchronized with the vortex shedding frequencies which means the large amplitude responses are induced by the forces from periodic vortex shedding, as mentioned in [201].

The chaotic behaviour of the flag is shown in Fig. 5.10(a) for $\kappa = 6.27$ before going to the permanent deflected shapes, which is found quite similar to the one shown in [201]. The visualization of the vorticity field and the flow field in different vibration phases of

Physical properties		Value
Solid	Density	ρ_s 1200 kg m ⁻³
	Elastic modulus	E 2.4 GPa
	Plate thickness	h 0.13 mm
	Plate length	L 5.1 cm
	Plate width	B 6.4 cm
	Poisson ratio	ν 0.38
Fluid	Density	ρ_f 1.2 kg m ⁻³
	Kinematic viscosity	ν_f 1.54×10^{-5} m ² s ⁻¹

Table 5.6: The physical parameters of the reference inverted cantilever plate [201].

Solver	Numerical parameters	Value
Flow	Simulated free stream velocities	U_∞ 2–6 m/s
	Length of the domain	l_d 70 cm
	Width of the domain	w_d 34.9315 cm
	Number of panels	N_{panel} 206
	Panel size	$\Delta s/h$ 3.8462
	Non-dimensional time step	$\Delta t_f^* = \Delta t_f U_\infty / \Delta_s$ 1
	Poisson grid	$N_x \times N_y$ 511 \times 255
	Number of particles (approx.)	$N_{particle}$ 65,000 - 71,000
Structure	Number of beam elements	N_{elem} 102
	Length of beam element	l_{elem} 0.0005 m
	Non-dimensional time step	$\Delta t_s^* = \Delta t_s U_\infty / \Delta_s$ 1
	Number of sub-time steps	15

Table 5.7: The analysis of flapping of an inverted cantilever plate in axial flow: numerical parameters for 2D coupled VPM analysis.

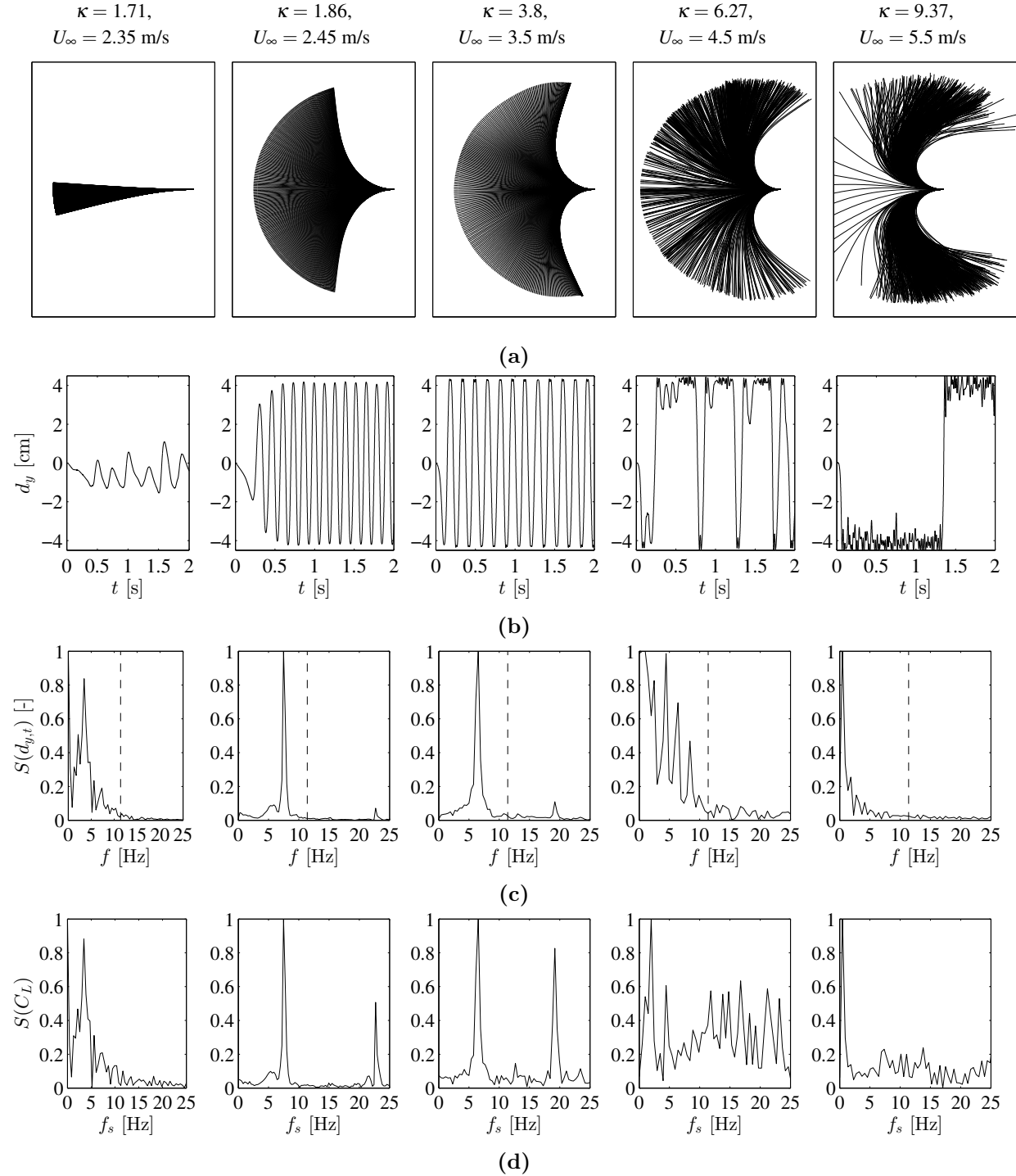


Figure 5.10: Coupled FSI simulation of the inverted flag under axial flow:

- (a) The sequential transition of the inverted flag from stable to periodic flapping, chaos, and deflected equilibrium under the axial flow. The dimensional and non-dimensional flow speeds, which are κ and U_∞ , are shown above the superposition of the vibration modes correspondingly.
- (b) The corresponding time history of the vertical peak displacements.
- (c) The normalised spectrum of the displacement time histories shown in (b). The dotted lines (– –) show the lowest bending frequency of the system.
- (d) normalised frequency spectrum of the lift forces.

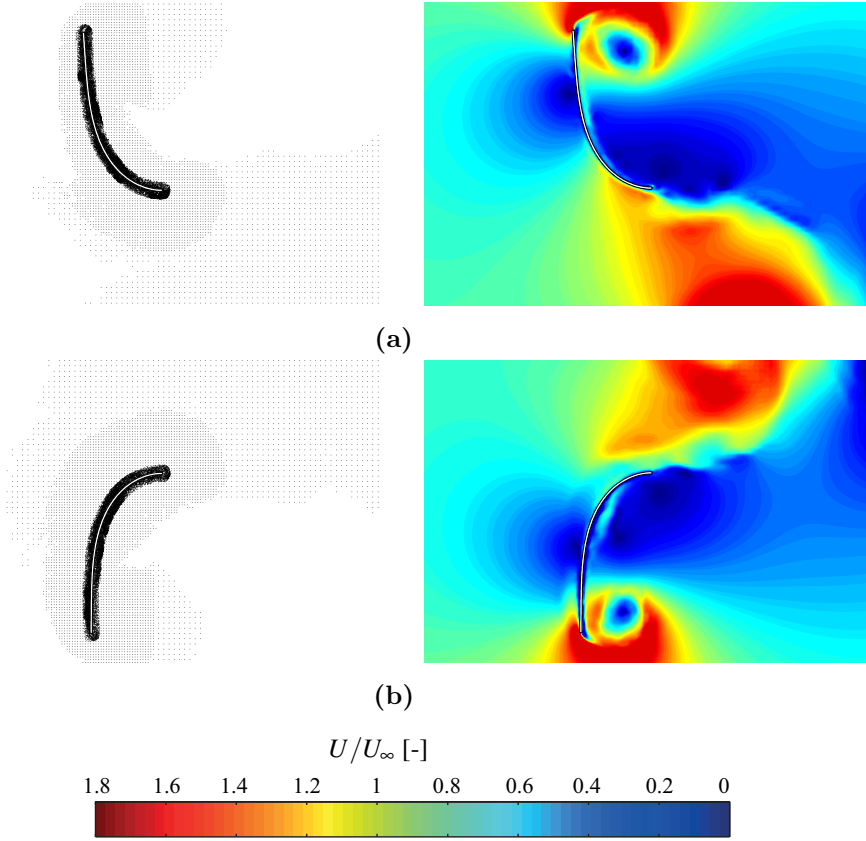


Figure 5.11: Visualisation of the flapping of inverted cantilever plate: (a-b) shows the particle map (left) and corresponding instantaneous velocity field (right) for different vibration phases. The visualisation is shown for flow velocity $\kappa = 1.86$.

the cantilever plate are shown in Fig. 5.11(a, b). The periodic vortex shedding is observed occurring after a diverging amplitude of the cantilever flag which is because of the sharp leading edge of the flag to incoming flow. This result indicates that the bifurcation of small aspect ratio inverted cantilever plate still occurs at $\kappa = 1.85$ if the sides of the plates are perfectly isolated. Above all, it is found to be a test case which can be easily considered for the validation of newly developed 2D coupled solver for FSI simulations.

5.3 Rotational flutter of inverted T-shaped cantilever with tip mass

The inverted T-shaped cantilever systems with tip mass are susceptible to one-dimensional (1D) torsional flutter which was studied extensively in [53, 149, 186] for small-scale energy harvesting. The equation of motion of torsional flutter is discussed later in Sec. 6.4.1, when this phenomenon will be discussed for aeroelastic energy harvesting.

In this study, the dimensions such as the length and width of the inverted T-shaped cantilever ($L \times W = 5.1 \text{ cm} \times 6.4 \text{ cm}$) are chosen according to the reference inverted cantilever presented in Table 5.6 of Sec. 5.2.3. A mass-less vertical plate ($W \times H_{vp} = 6.4 \text{ cm} \times 1 \text{ cm}$) is attached at the tip of the cantilever beam. The thickness of the beam is increased from 0.13 mm to 0.6 mm. A tip mass of 0.0116 kg is assigned at the cantilever tip to match the frequency of the inverted cantilever.

The inverted T-shaped cantilever is stimulated under different wind speeds to find the critical wind speed at which the unstable vibration initiates. The numerical properties of the coupled simulation considering the fluid and structure solver are just like before in Table 5.7, apart from $N_{panel} = 247$ and $l_{elem} = 123$ due to additional vertical plate. The vertical tip displacements of the T-shaped cantilever are shown in Fig. 5.12 under different wind speeds.

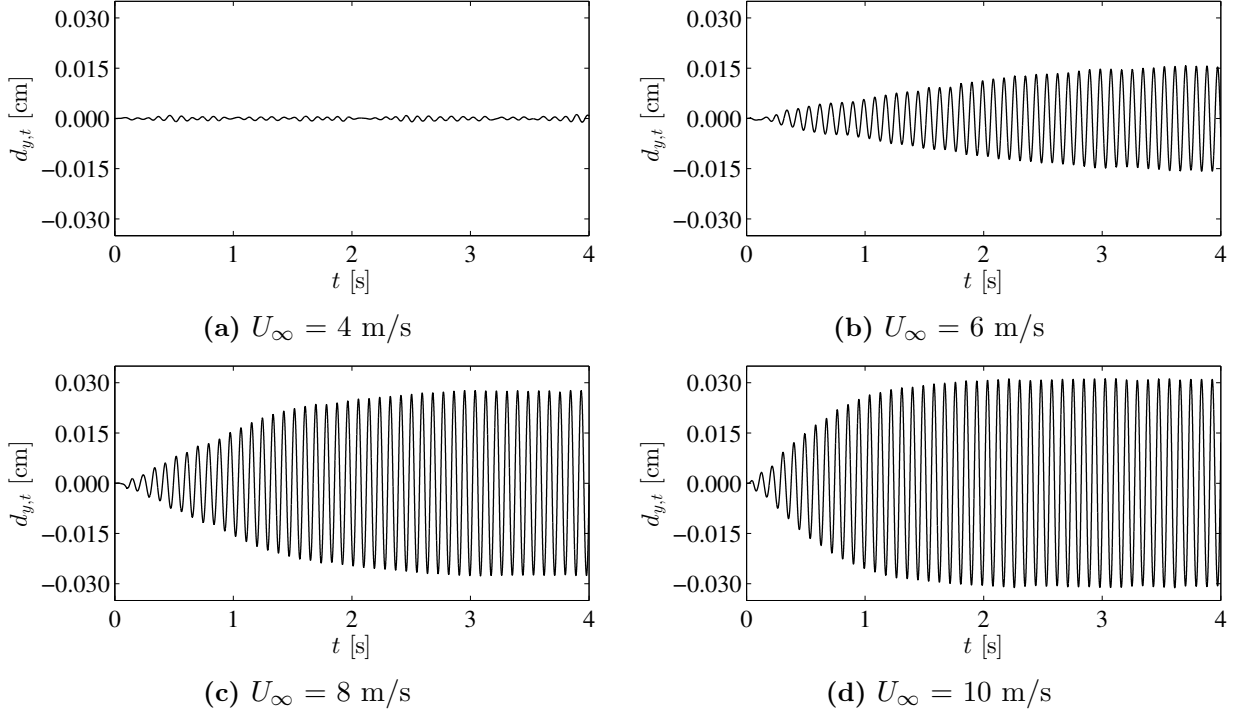


Figure 5.12: The comparison of the vertical tip displacement of the simulated T-shaped cantilever to identify the critical flutter wind speed.

It is observed from Fig. 5.12 that the system starts vibrating large amplitude at 6 m/s. At or above the critical flutter wind speed, the negative aerodynamic damping induced by the self-exciting aerodynamic forces exceeds the system damping and leads to unstable vibration. The total damping ratio of the system, which is sum of mechanical and aerodynamic damping, is calculated from the displacement time histories presented in Fig. 5.12. Using logarithmic decrement, the total damping ratios are calculated approximately -1.2 %, -1.8 %, -3.2 % under wind speeds 6 m/s, 8 m/s, and 10 m/s, respectively. The total negative damping is found to be increasing with the increase in wind speed, and therefore, the system starts vibrating large amplitude faster in fewer oscillation cycles as the flow speed increases. The vortex particles and flow field around the T-shaped cantilever are shown in Fig. 5.13.

The dynamics of the T-shaped cantilever in wind speed which is much higher than the critical flutter wind speed was not covered within the scope of the study. Therefore, the interest exists here to analyse the dynamics of the system in higher wind speeds until a permanent deflected mode appears.

5.4 Aeroelastic motion of different inverted cantilevers

The dynamics of inverted cantilever plates are studied here considering all possible combination of tip mass and mass-less vertical tip plate for the inverted cantilever, which is

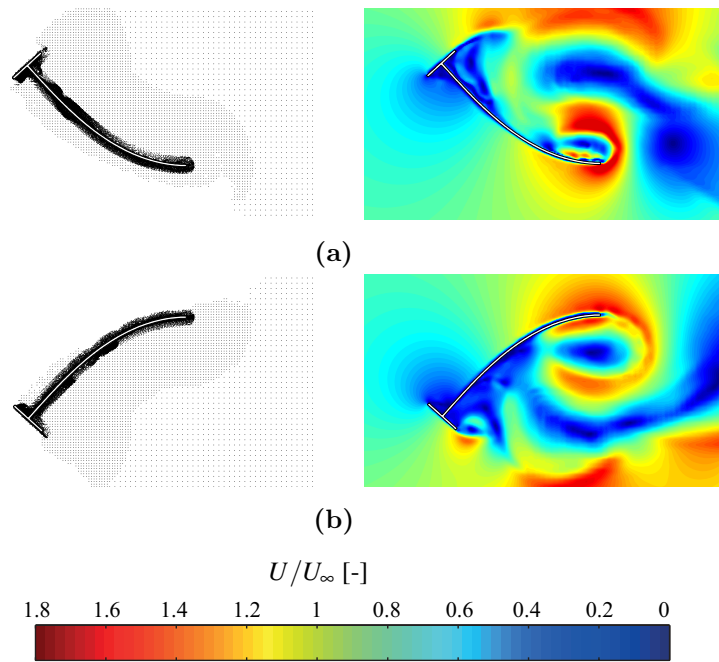


Figure 5.13: Flow visualisation around moving T-shaped inverted cantilever under free stream flow $U_\infty = 10 \text{ m/s}$: (a-b) particle maps (left) and corresponding flow fields (right).

schematically shown in Fig. 5.14. Four different inverted cantilever systems have been simulated under a wide range of wind speeds which are the reference inverted cantilever (inverted), the same with a mass-less vertical plate (T-shaped), the modified reference cantilever with tip mass (inverted with tip mass), and the last one with attached mass-less vertical plate (T-shaped with tip mass). The first natural frequency of the studied systems is kept approximately same. The interest here is to study the influence of tip mass and the vertical plate in the aeroelastic response of inverted cantilever systems.

The pattern of dynamic response for the studied systems is observed significantly different. The maximum amplitude of vertical tip displacements and the response frequency of the systems under different wind speeds are shown in Fig. 5.15. Each system is simulated for different wind speeds, however, up to a maximum one at which the system suffers the permanent deflected shape or loses the oscillatory motion.

The maximum tip displacements among the studied systems is observed from the reference inverted cantilever (Sec. 5.2.3). However, the flapping is observed for a narrow range of wind speeds (2.45 - 3.5 m/s). The system has suffered the deflected equilibrium under the wind speeds above 4.2 m/s. The frequency of vibration is almost half of the first natural frequency of the system during the flapping region. At wind speed lower than 2 m/s, the system is found vibrating with very small amplitude, however, in its own frequency (Fig. 5.15(b)). This again makes it sure that the amplitude and response frequency of the system is govern by the forces due to vortex shedding, especially, when the system starts oscillating large amplitude. Furthermore, the reference inverted beam is simulated considering a attached mass-less vertical plate at the cantilever tip.

The dynamic motion of this T-shaped cantilever is found similar as the reference inverted beam. The flapping initiates earlier at wind speed 2 m/s and the deflected mode is observed at wind speed 3 m/s (Fig. 5.15(a)). The vertical plate with two separation points is responsible for earlier generation of vortex shedding, and hence, early system response. This system also

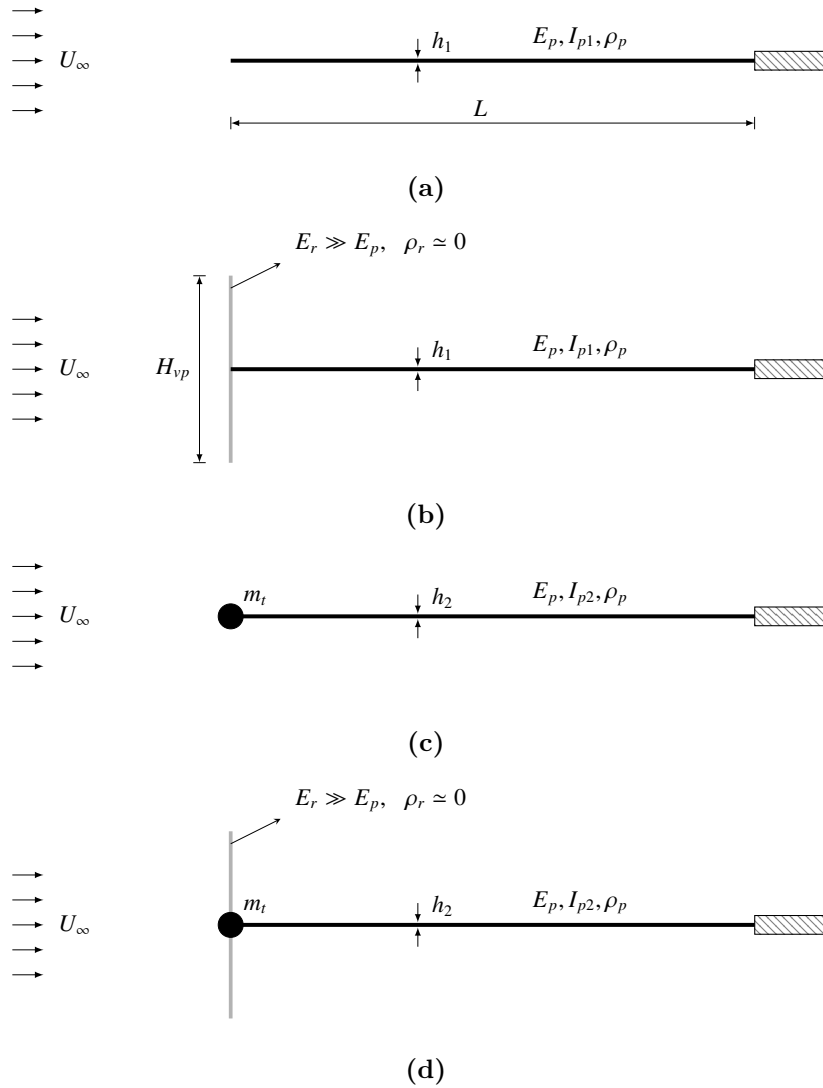


Figure 5.14: Schematic presentation of different inverted cantilever systems in axial flow: The effect of the tip mass and vertical tip plate in flapping mechanism of inverted cantilevers is of study interest. The basic inverted cantilever from Sec. 5.2.3, which is without tip mass and vertical plate, is considered as the reference system. A combination of concentrated tip mass (m_t) and/or vertical tip plate, which is nearly rigid and mass-less ($\rho_r = 0$), are shown in the following:

- (a) Reference inverted cantilever,
- (b) T-shaped reference inverted cantilever,
- (c) Modified inverted cantilever with tip mass, and
- (d) Modified T-shaped cantilever with tip mass.

follows the vortex shedding frequency at large vibration while vibrates with its own frequency at wind speed lower than 1.2 m/s (Fig. 5.15(b)).

The flapping of the modified inverted cantilever is found significantly influenced by the attachment of a tip mass only. Similarly, the flapping is influenced strongly by the vortex-shedding, however, at substantially large wind speed of 30 m/s. The increase in system damping due to the increased mass and stiffness is responsible for the need of high wind speed. The system is found vibrating with its natural frequency at wind speeds less than 15 m/s since response amplitude is very low. However, the response frequency is coupled when the wind speed is above 15 m/s (Fig. 5.15(b)).

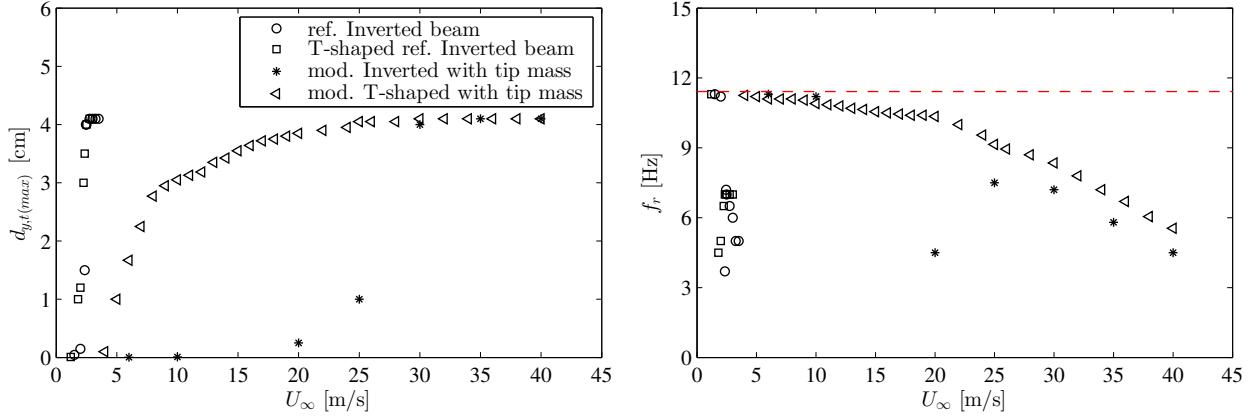


Figure 5.15: Comparison of maximum vertical tip displacement (left) and response frequency (right) of three specific systems under different wind speeds. Here, the dashed line (---) shows the first eigenfrequency of all three systems.

Interestingly, the previous system with the inclusion of mass-less vertical plate at the cantilever tip shows completely different aeroelastic behaviour. It is due to the susceptibility of the T-shaped system with tip mass to rotational flutter. The T-shaped cantilever with tip mass vibrates mostly in its first natural frequency whereas the other inverted cantilevers with vortex shedding frequencies, which are much lower than the first natural frequency of those systems. The response amplitude is observed increasing with the increase in wind speeds (Fig. 5.15(a)). As the wind speed approaches higher, a drop in response frequency is observed (Fig. 5.15(b)). It is due to the geometric nonlinearity that arises from high axial force due to the vertical plate facing the incoming flow in addition to large displacement.

The superposition of the vibration phases for the T-shaped cantilever is shown in Fig. 5.16 at different wind speeds. It is observed that both modified systems, which are the modified inverted cantilever and T-shaped cantilever with tip mass, show the deflected mode at just above 40 m/s.

The inverted T-shaped with tip mass cantilever exhibits LCO and vibrates for a wide range of wind speeds. The comparison of the cantilever systems in terms of response amplitude and oscillation frequency with respect to the inflow wind speed is essential and performed for the selection of a proper mechanical system for small-scale vibration energy harvesting.

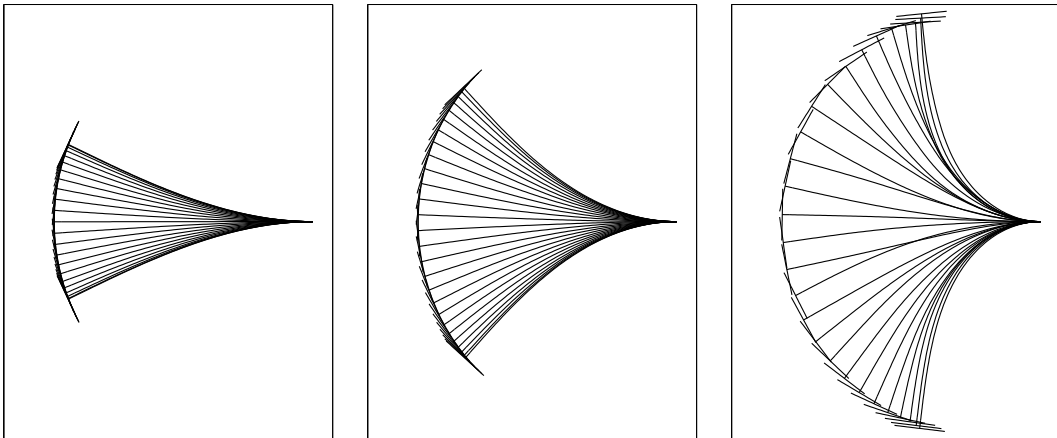


Figure 5.16: The fluttering modes of inverted T-shaped cantilever beam at different wind speeds: 6 m/s (left), 8 m/s (middle), and 25 m/s (right).

5.5 Coupled interactions of flexible membrane systems

5.5.1 Flow over a building with elastic membrane roof

This is an example of an elastic membrane roof that deals with viscous fluid flow around a building. Here, the flow interacts with the nonlinear vibration of the membrane roof prestressed by its gravity loads. It is a reference case study in which a monolithic coupled approach to fluid–structure interaction was modelled using space–time finite elements Hübner et al. [125]. Therefore, this test case can be considered as a validation study too.

A schematic of the problem is shown in Fig. 5.17. The geometric dimensions and physical properties of fluid and structure are summarized in Table 5.8. It is not possible to follow the parameters of the reference study strictly due to the limitation of the coupled VPM model, especially the definition of parabolic inflow condition. Here, the free stream flow velocity U_∞ is considered 13.75 m/s, which was the flow speed in reference study at the height of 5 m, which is the membrane level. The surface boundary layer is modelled using thin plates.

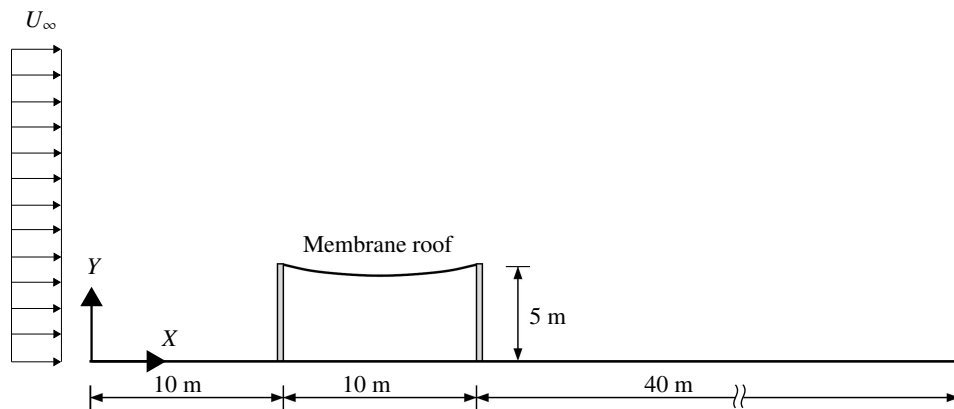


Figure 5.17: The schematic of uniform flow over a membrane roof of a building.

	Physical properties		Value
Membrane	Elastic modulus	E	10^9 Pa
	Density	ρ_s	1000 kg/m ³
	Poisson's ratio	ν	0
	Length of the membrane	L	10 m
	Thickness of the membrane	h	0.01 m
Fluid	Density	ρ_f	1.25 kg/m ³
	Kinematic viscosity	ν_f	0.1 m ² /s
Flow	Parabolic flow profile ([125])	$U_x(y=5\text{ m})$	13.75 m/s
	Free-stream flow (present study)	U_∞	13.75 m/s
	Reynolds number	Re	1375

Table 5.8: Flow over a building with elastic membrane roof: the dimensions and physical properties of fluid and membrane.

The numerical input parameters for the coupled numerical simulation are summarised in Table 5.9. Overall, 658 panels have been used for this simulation considering the rigid building, flexible membrane, and two rectangular thin rectangular sections as ground surface.

Solver	Numerical parameters		Value
Flow	Number of time steps	N_{step}	10,000
	Length of the domain	l_d	200 m
	Width of the domain	w_d	100 m
	Total number of boundary panels	N_{panel}	658
	Panel size	Δs	0.2 m
	Dimensional time step of flow solver	Δt_f	0.014545 s
	Non-dimensional time step	$\Delta t_f^* = \Delta t_f U_\infty / \Delta_s$	1.0
	Poissson grid	$N_x \times N_y$	255×127
Membrane	Number of particles	$N_{particle}$	110,000 - 130,000
	Number of beam elements	N_{elem}	50
	Length of element	l_{elem}	0.2 m
	Non-dimensional time step	$\Delta t_s^* = \Delta t_s U_\infty / \Delta_s$	1.0
	Number of sub-time steps		15

Table 5.9: Flow over a building with elastic membrane roof: numerical parameters for 2D coupled VPM analysis.

The membrane roof is considered to be prestressed by 32% of its dead load in order to be consistent with the reference study.

Flow simulation around rigid building and static membrane

Initially, the flow simulation is performed only around rigid building and static membrane to understand the vortex shedding pattern, velocity field, and frequency contents. The deformed shape of the membrane is considered under the mentioned 32% dead load. The separation zone develops at the leading edge of the building, whereas vortex shedding occurs at the trailing edge. The study results from different point of views are summarized in Fig. 5.18. The vortices stay for some times behind the building and increase until the diameter exceeds the building height (as mentioned in [125]), which are shown in the snap-shots of flow and particle fields close to the building.

The velocities are monitored using some velocity sampling points in front and behind the building. The mean plus/minus one standard deviation profiles ($(\bar{u} \pm \sigma_u)/U_\infty$) are shown in Fig. 5.18(c) for $U_\infty = 13.75$ m/s. The first 1000 time steps are however excluded from the statistical analysis. The velocity profiles show that the strong vorticity field generates behind the building, particularly near the ground surface. The vortices move downstream with the mean flow, leading to a periodical flow pattern. The vertical flow velocity and the flow frequencies of the monitored location just around the right top corner of the building ($x = 25$ m and $y = 5.3$ m) are shown in Fig. 5.18(d). The dominant frequency is found to be 0.125 Hz (c.f. Fig. 5.18(d)).

Fully coupled FSI simulation of rigid building with flexible membrane roof

In the coupled analysis, to reduce the effect of impulsively started flow, the fluid forces are gradually applied at the beginning by multiplying with a ramp function up to the simulation step 100. However, the dead load is applied from the start of the simulation.

The vortices move over the roof structure and induce membrane vibrations with large amplitudes, which interacts further with the fluid. Importantly, the large uplift response of the membrane is observed initially. However, after some time (35 s), a more or less periodical system behaviour occurs with frequencies of 0.9–1.0 Hz, and the vertical displacements of

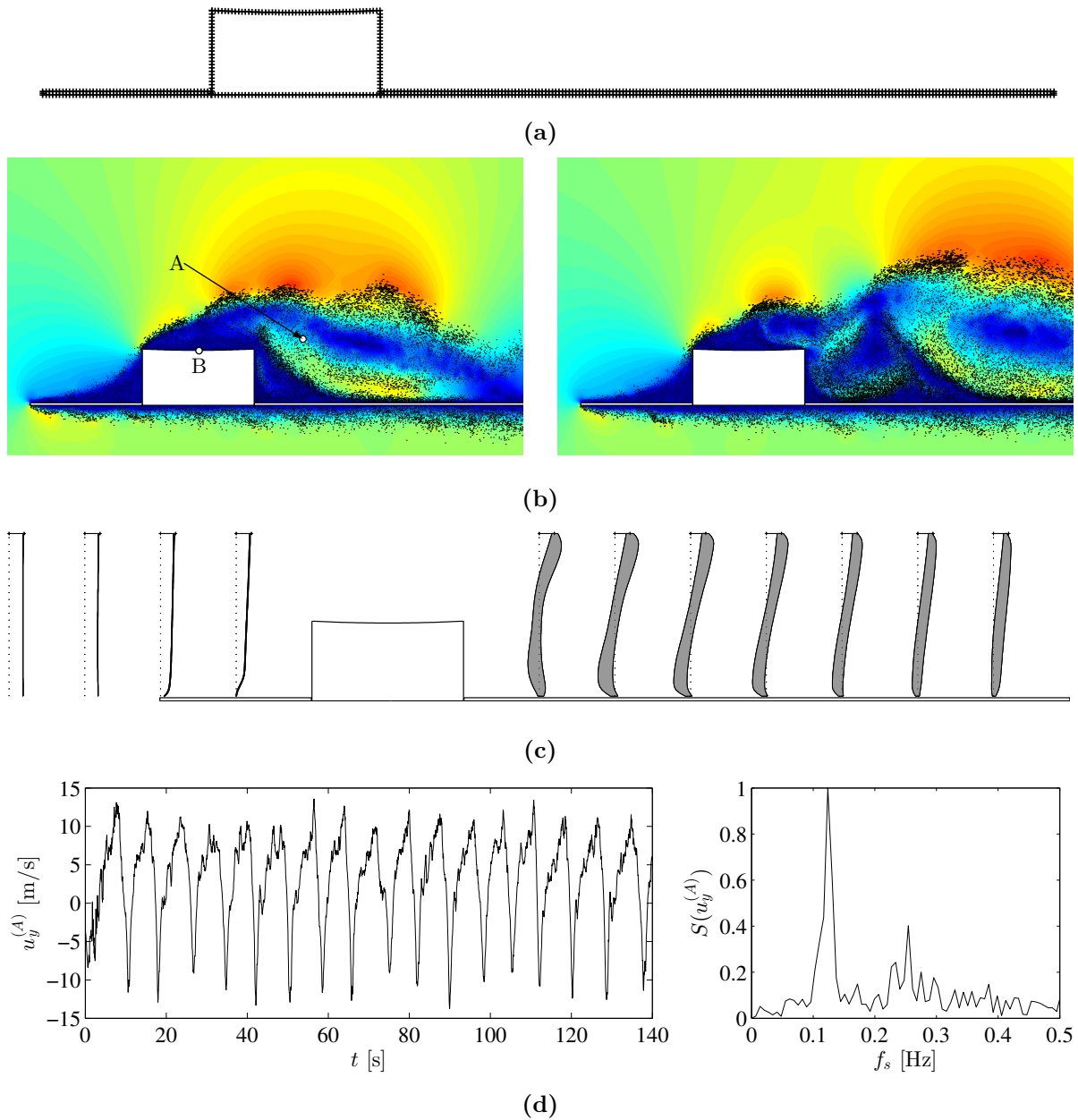


Figure 5.18: The flow around rigid building and static membrane roof deformed under 32% dead load: (a) the discretisation of surface panels for flow simulation; (b) the separation of flow at the leading edge, whereas the vortex shedding occurs at the trailing edge. The point B is shown in the centre of the membrane roof which is used later for monitoring coupled displacements. (c) The statistical velocity profiles $(\bar{u} \pm \sigma_u)/U_\infty$ are shown at the monitored section under $U_\infty = 13.75$ m/s. (d) The time history of the vertical flow velocity behind the building (monitored point A: $x = 25$ m, $y = 5.3$ m) (left) and the frequency spectrum of the velocity signal (right).

the membrane at the centre (d_y) are found to be 15–20 cm (see Fig. 5.19). The response amplitudes and the frequencies are found to be very much similar as they were mentioned in the reference study. The particle maps and the corresponding flow fields around the building while a complete oscillation of the membrane roof is done are visualised in Fig. 5.20.

Importantly, it is observed that the membrane vibrations and flow phenomena are not fully periodical. It is due to strong nonlinearities in membrane kinematics and fluid dynamics. The outcome of this study is very much satisfactory considering the fact that the results are com-

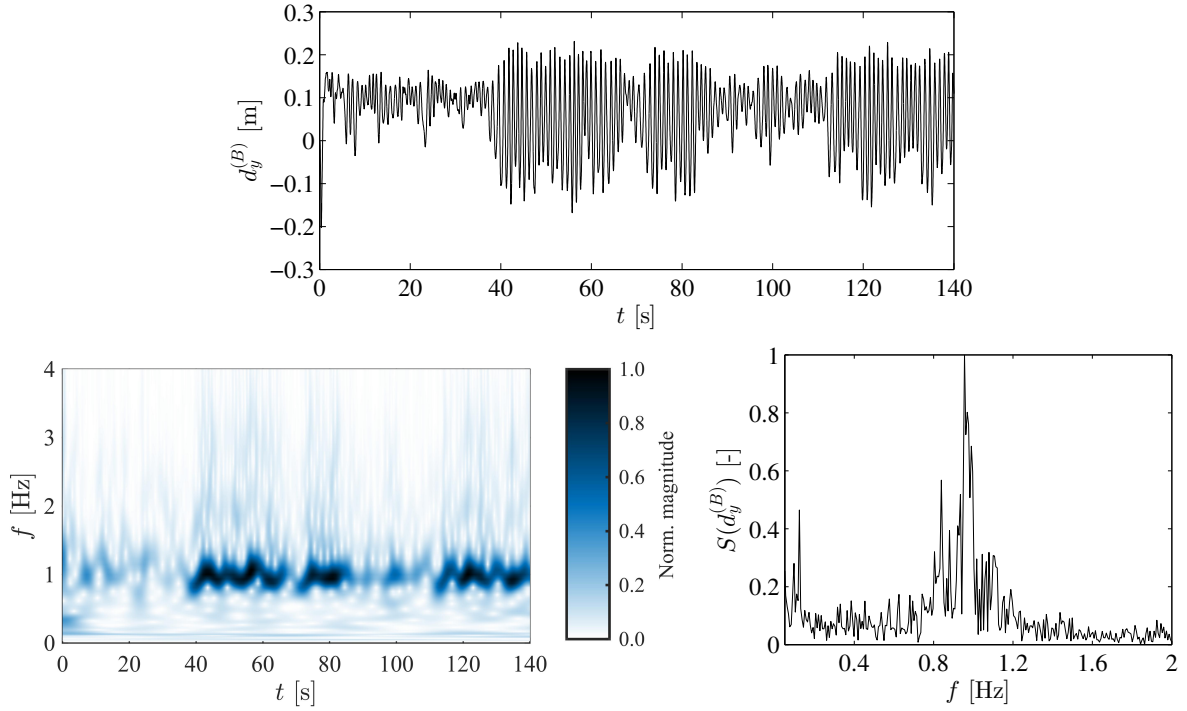


Figure 5.19: Coupled simulation of the membrane roof at flow velocity 13.75 m/s: (top) the vertical displacement at the centre of the roof, (bottom-left) the wavelet transformation of the displacement time history, (bottom-right) the frequency spectrum.

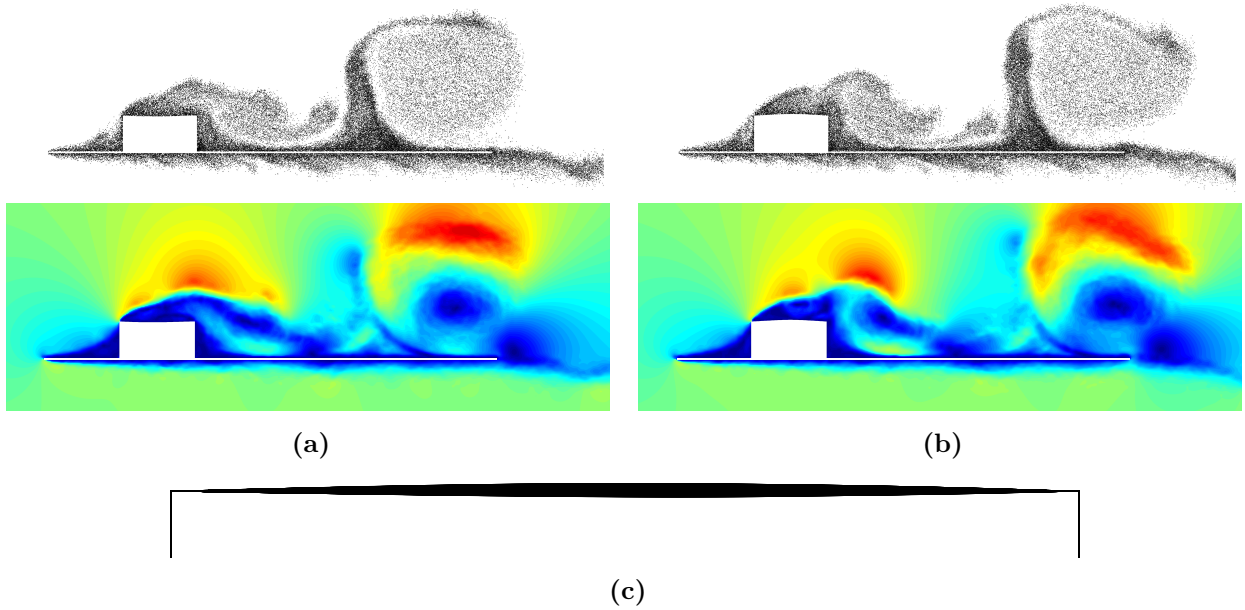


Figure 5.20: Coupled simulation of the membrane roof at 13.75 m/s: (a-b) the particle map (top) and the flow field (bottom) around the building while the membrane roof completed a half cycle oscillation, (c) envelope of the dynamic responses of the membrane roof.

pared with the study results which were obtained from monolithic FSI model. Furthermore, the simulation was for very low \mathcal{Re} with high viscosity fluid.

It was mentioned in Hübner et al. [125] that the response frequency of the coupled simulation is relatively high, mainly because of nonlinear membrane dynamics. However, there was not enough discussion on the coupled interactions.

Studies on membrane FE models to understand coupled FSI mechanism

This study is completely based on the structural model. Initially, a linear eigenvalue analysis is performed using the FE model of the membrane without considering the effect of 32% dead load. The first bending frequency is found to be 0.10 Hz. Afterwards, the geometrical non-linear effects are considered under the dead loads before performing the eigenvalue analysis, and the lowest bending frequency is obtained 1.6 Hz.

Fig. 5.21 shows the static displacement at the centre of the roof and the first natural frequency under the consideration of different percentage of dead loads. Clearly, the frequency of the membrane roof increases with the consideration of increasing dead load effects.

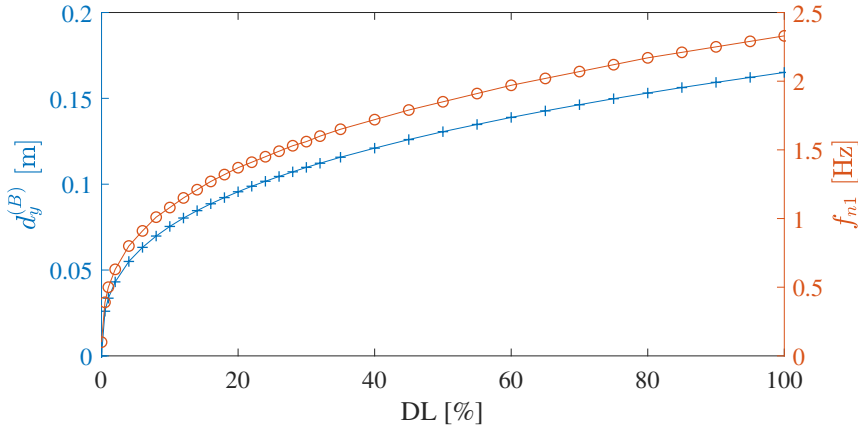


Figure 5.21: The effect of gravity forces on system identification: comparison of membrane displacement at centre and lowest bending frequency are compared under the consideration of different percentage of dead loads.

To understand the effect of membrane displacement on the instantaneous response frequency, the free vibration analyses are performed. Here, two different scenarios are considered: (a) removal gravity load effects after few steps, (b) continuation of at least 32% dead loads throughout the simulation. In both cases, the forces are applied gradually like a ramp function until the discontinuation or change point. The study results of free vibration analyses are presented in Fig. 5.22. A wavelet transformation of the displacement time history is presented to show the change of the frequency in time domain. A frequency spectrum of the signal is also shown.

In Fig. 5.22(a), the frequency is converging to 0.1 Hz, which is the lowest bending frequency obtained from the linear eigenvalue analysis. On the other hand, when 32 % dead loads effects are considered, c.f. Fig. 5.22(b), the midspan response and frequency are converging to 0.1122 m and 1.6 Hz, respectively. It is clear that the geometrical nonlinearity plays a big role here; the increase in response frequency is due to the increases in geometric stiffness.

Importantly, it is observed from the wavelet transformation of Fig. 5.22(b) that there is a presence of two response frequencies (approximately 1.26 Hz and 2.6 Hz) until $t = 13$ s. As soon as the effect of high frequency diminishes, there is a clear shift to single response frequency of 1.6 Hz.

Now, it can be observed that the membrane frequency in the coupled analysis is reduced to 0.9–1.0 Hz from 1.6 Hz. This is due to the strong coupling between the vortex shedding frequency of 0.125 Hz (c.f. Fig. 5.18(d)) and the membrane frequency of 1.6 Hz under 32 % dead loads.

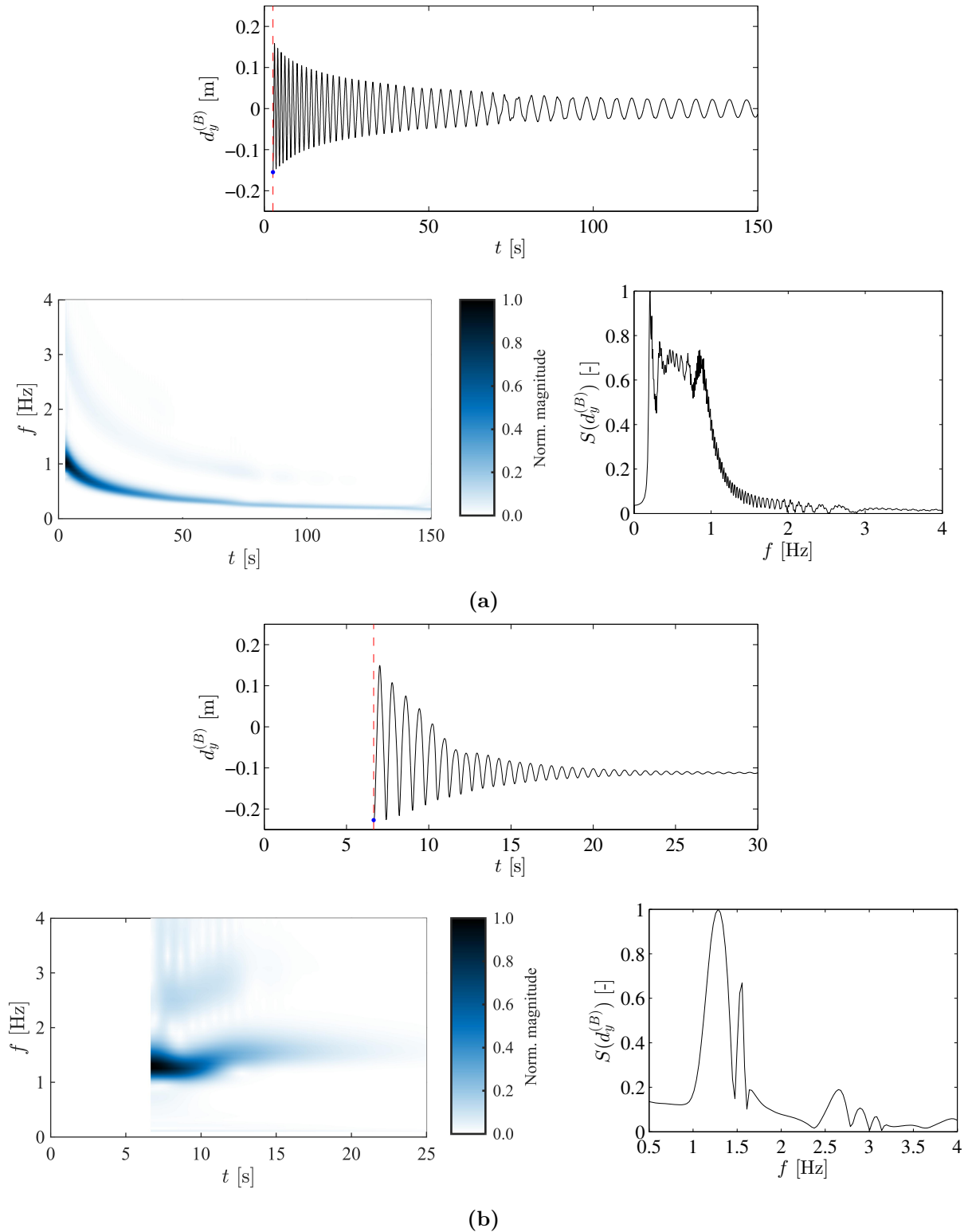


Figure 5.22: Free vibration analyses are performed using a geometrically nonlinear finite element model of a membrane roof. Two loading scenarios are considered: (a) full dead loads are applied until 2.65 s and removed afterwards, (b) full dead loads are applied initially up to 6.65 s and eventually continued with 32% of the dead loads. Here, for both scenarios in (a–b) the figure shows individually: (top) the displacement time history of the roof centre, (bottom-left) wavelet transformation of the time history, and (bottom-right) shows the normalised frequency spectrum.

FSI simulation of building with flexible membrane roof at different flow velocities

The flexible membrane roof is simulated furthermore under different flow velocities. The numerical parameters (c.f. Table 5.9), as well as the geometrical nonlinearity under 32 % of the dead loads, are considered the same as mentioned earlier. The response of the membrane roof at the centre and the response frequencies are compared in Fig. 5.23.

The coupled simulations are performed for four more flow velocities: 5 m/s, 10 m/s, 15 m/s, and 18 m/s. It is observed from Fig. 5.23 that the coupled frequencies of the vertical displacement at the centre of the membrane roof are quite different from each other. In the case of 5 m/s, the membrane stays mostly in the gravity direction. The coupled response frequency is comparatively high, however, dropped from 1.6 Hz to approximately 1.2 Hz. It is due to the fraction reduction of dead load effects by the fluid uplift forces (mean downward position from 0.1122 m to 0.1 m). The frequency with respect to the displacement of 0.1 m is nearly around (see Fig. 5.21).

At flow velocity 10 m/s, the oscillations are nearly periodic with response frequencies of approximately 0.7 Hz, which are almost half of the lowest bending frequency. The response amplitudes are observed in between 12 cm and -12 cm. However, the mean response is nearly zero, which corresponds to the frequency of 0.1 Hz (see Fig. 5.21). Additionally, the vortex shedding frequency is also low (0.125 Hz), the coupled motion is more dominated by the complex interaction of flow and geometric nonlinearity of the structure.

At flow velocities 13.75 and 15 m/s, the coupled motion is observed periodic similarly with response frequency approximately 1–1.1 Hz. The increase in response frequency is associated with the increase in mean response of the membrane due to the increase in uplift fluid pressure.

Finally, at flow velocity 18 m/s, the system oscillates with large amplitude mostly opposite to gravity direction, and therefore, the response frequencies increase again. However, a strong coupling between the flow and structure is still visible such as the presence of two dominant response frequencies in Fig. 5.23 (e). The low one is due to the frequency of vortex shedding, while the upper one is the frequency of the geometrically nonlinear structure.

5.5.2 Aeroelastic motion of flexible 2D membrane umbrellas

Aeroelastic response of two-span membrane systems

The aeroelastic coupled response of two-span membrane systems is analysed. The study is motivated by the flow over membrane roof, which has been presented in Sec. 5.5.1. A schematic of the current system is shown in Fig. 5.24. Though the internal support is shown roller-type, the system with an internal hinge support is also analysed. Initially, the membrane is considered elastic and straight. The deformed shape is obtained under the full dead loads. With the modifications over the previous study, the physical properties of fluid and solid are summarized in Table 5.10.

The first natural frequency of the membrane is found 0.2 Hz when the nonlinear effects of dead loads are ignored, whereas it is 1.52 Hz considering the geometrical nonlinear effects. Now, the aeroelastic coupled motion of the membrane system is analysed for different wind velocities. The numerical parameters of the coupled simulations are summarized in Table 5.11. The simulated flow velocities (U_∞) are: 10 m/s, 20 m/s, and 30 m/s. The vascularisation of the particle field in the free stream flow of 10 m/s is shown in Fig. 5.25.

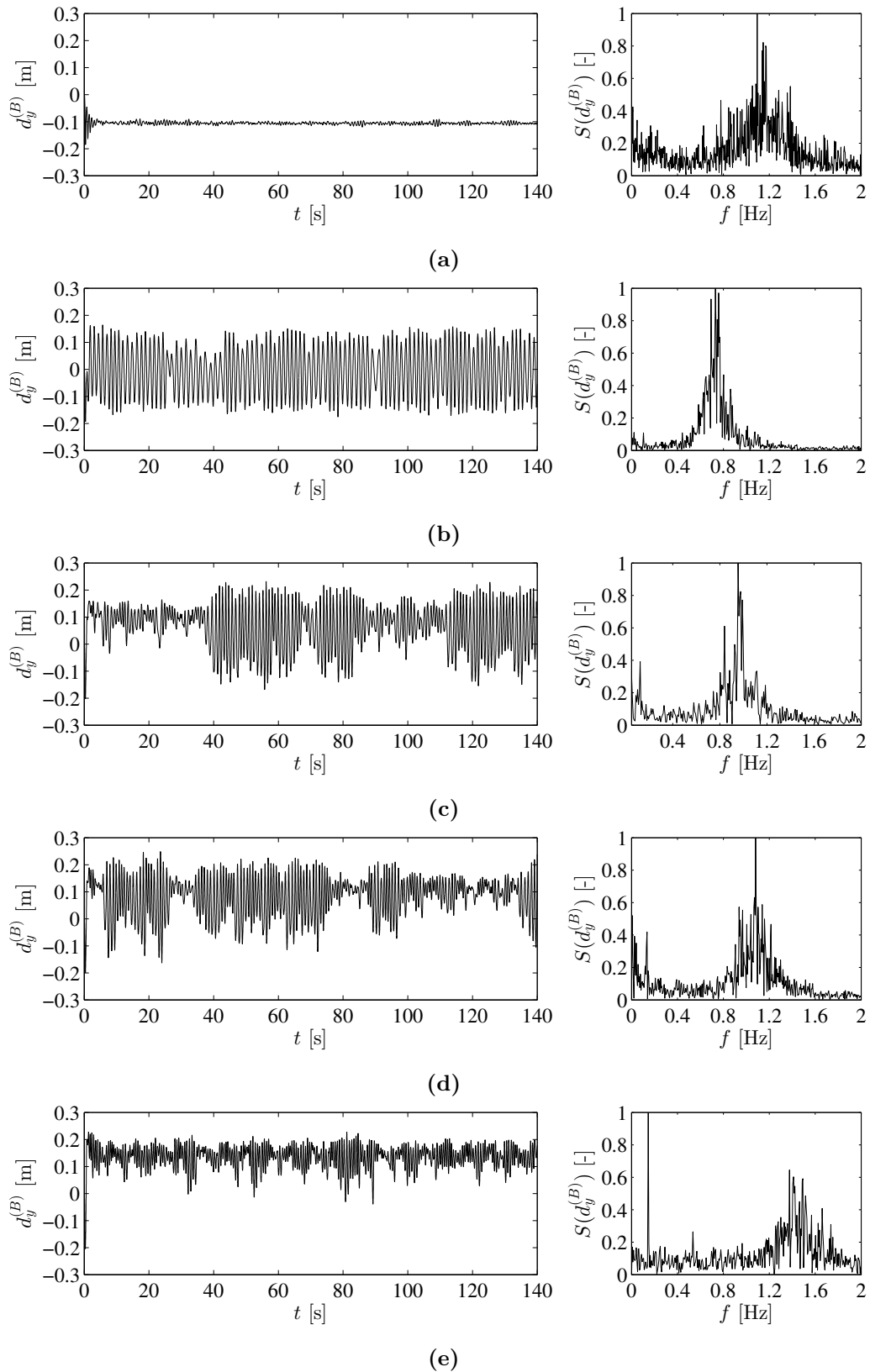


Figure 5.23: Coupled analysis of the membrane roof of a building under different flow velocities: the time history of the vertical displacement at the roof centre (left) and corresponding normalised frequency spectrum (right) are compared. Here, the flow velocities are: (a) 5 m/s, (b) 10 m/s, (c) 13.75 m/s, (d) 15 m/s, and (e) 18 m/s.



Figure 5.24: A schematic presentation of two-span membrane system under uniform flow.

Physical properties		Value	
Solid	Elastic modulus	E	2×10^9 Pa
	Density	ρ_s	1000 kg/m ³
	Thickness of the membrane	h	0.02 m
	Width of the membrane	W	8 m
Fluid	Density	ρ_f	1.2 kg/m ³
	Kinematic viscosity	ν_f	0.000015 m ² /s

Table 5.10: Physical properties for the fluid and solid (membrane) two-span membrane system.

The aerodynamic forces are applied as a ramp function up to the simulation step 500; however, the dead loads are applied since the beginning of the simulation. The aeroelastic coupled simulations of the membrane such as the superposition of the membrane vibrations, the response time histories at the centre of both spans, and their response frequencies are presented in Fig. 5.26.

The membrane response in both spans is relatively small at flow velocity 10 m/s. The coupled

Solver	Numerical parameters		Value
Flow	Simulated free stream velocities	U_∞	10–30 m/s
	Length of the domain	l_d	200 m
	Width of the domain	w_d	99.804 m
	Simulation time	t	80 s
	Number of panels	N_{panel}	404
	Panel size	Δs	0.2 m
	Non-dimensional time step	$\Delta t_f^* = \Delta t_f U_\infty / \Delta s$	2
	Poisson grid	$N_x \times N_y$	511 × 255
	number of particles	$N_{particle}$	150,000 - 170,000
	Structure	Number of beam elements	N_{elem}
Length of element		l_{elem}	0.201 m
Non-dimensional time step		$\Delta t_s^* = \Delta t_s U_\infty / \Delta s$	2
Number of sub-time steps			15

Table 5.11: The numerical parameters of fluid and structural solvers for aeroelastic coupled simulation of two-span membrane system.



Figure 5.25: The convecting particles in free stream flow of 10 m/s around the membrane roof.

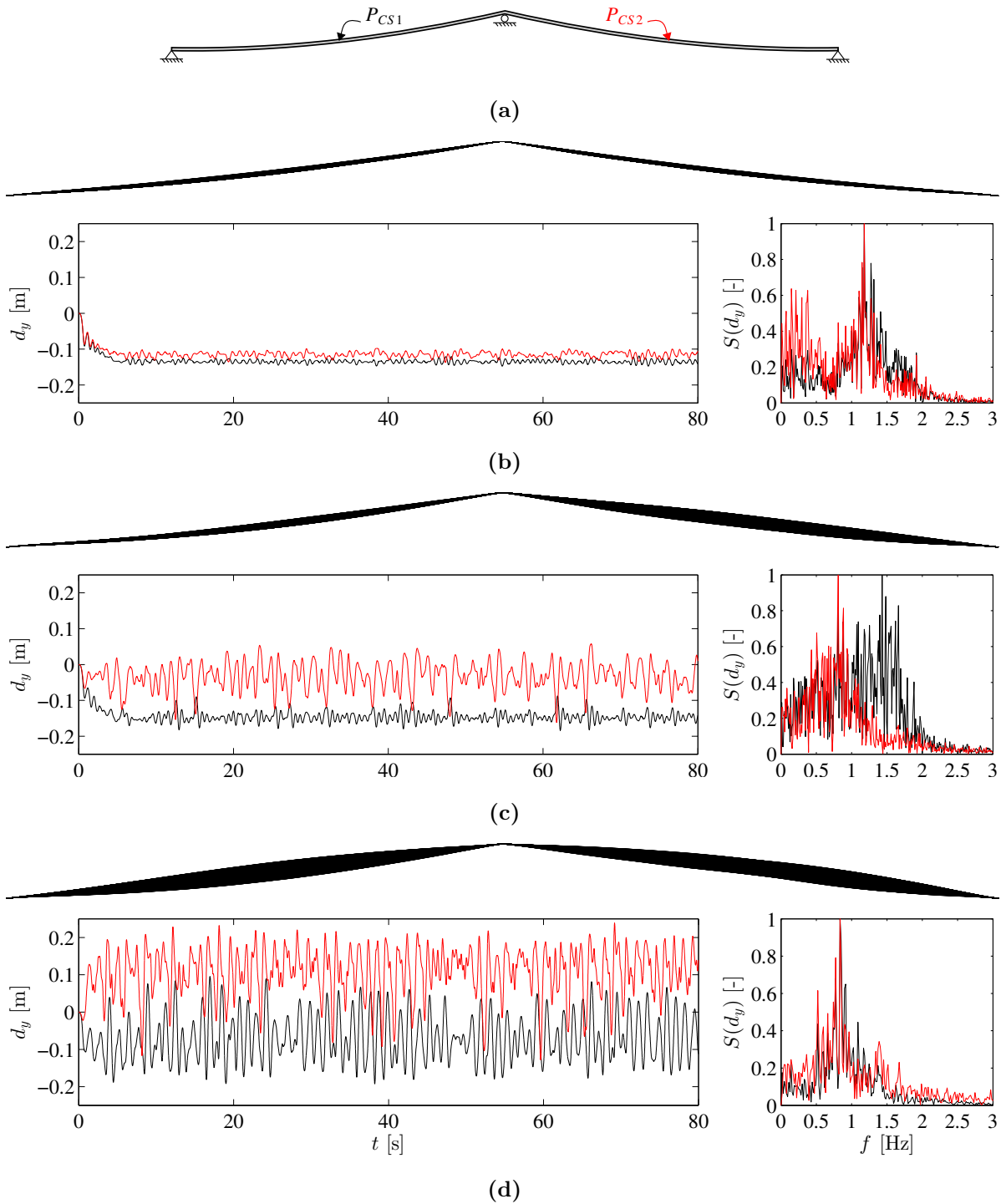


Figure 5.26: Aeroelastic analysis of two-span membrane roof with a roller-type central support (a); the coupled simulations are performed under different wind velocities: (b) 10 m/s, (c) 20 m/s, and (d) 30 m/s. Under each wind speed shown in (b-d) three figures are shown respectively: (top) envelope of the superposition of the membrane vibrations, (bottom-left) the displacement time histories at the span centres (P_{CS1} and P_{CS2}), (bottom-right) the frequency spectrum of displacement time histories. Here, black lines (—) are for the centre of 1st span, whereas red lines (—) are for the 2nd span.

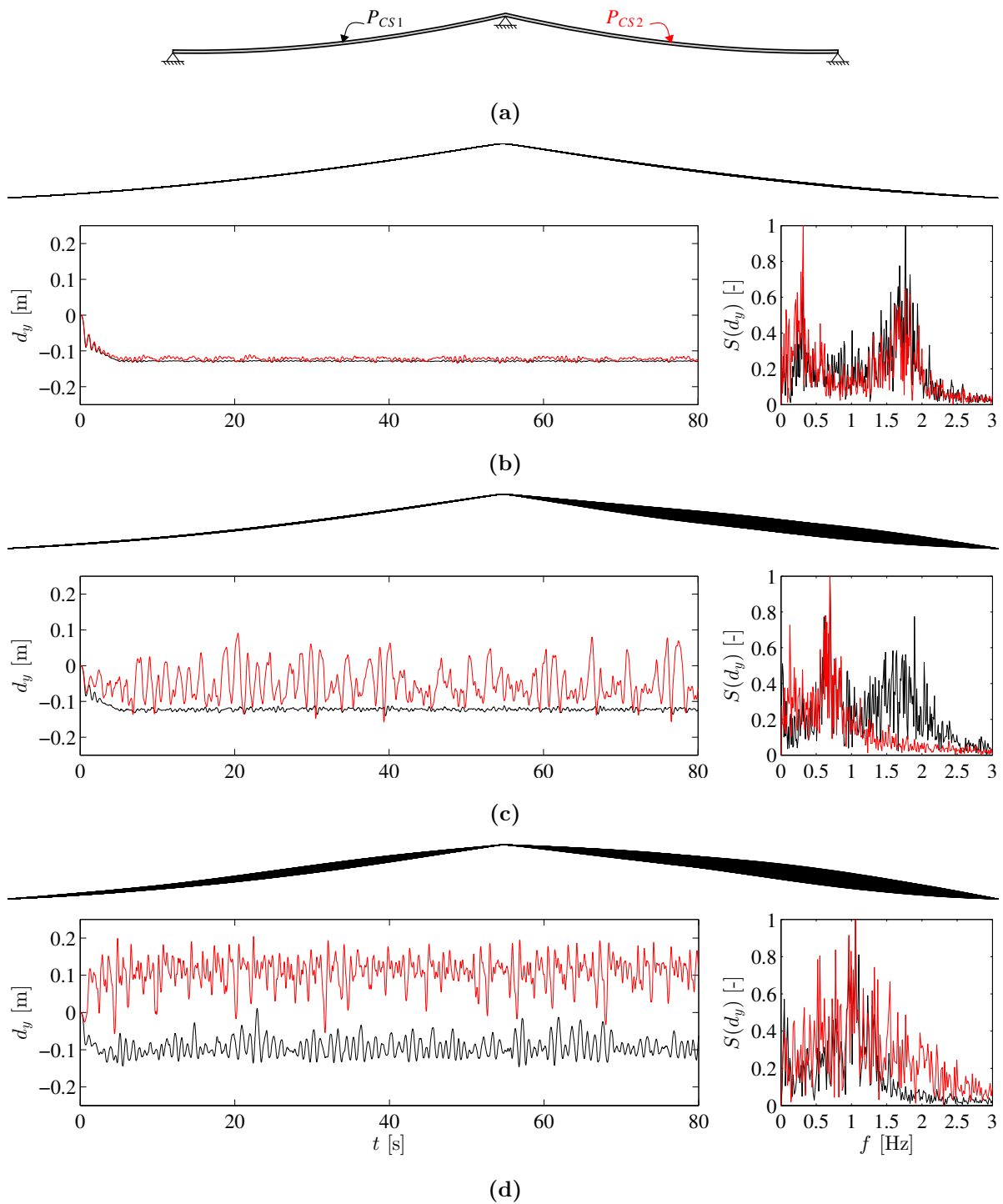


Figure 5.27: Aeroelastic response of two-span membrane roof with a hinged-type central support (a); the coupled simulations are performed under different wind velocities: (b) 10 m/s, (c) 20 m/s, and (d) 30 m/s. Under each wind speed shown in (b-d) three figures are shown respectively: (top) envelope of the superposition of the membrane vibrations, (bottom-left) the displacement time histories at the span centres (P_{CS1} and P_{CS2}), (bottom-right) the frequency spectrum of displacement time histories. Here, black lines (—) are for the centre of 1st span, whereas red lines (—) are for the 2nd span.

response frequencies are similar for both spans apart from the presence of low-frequencies in the second span, which is due to the vortex shedding. At flow velocity 20 m/s, the second span of the membrane system shows large motion, and therefore, frequencies are low and coupled. However, the first span acts as a streamlined section. Importantly, the response frequencies of the first span are observed slightly larger due to the axial tension induced by the response of the second. However, at 30 m/s the centre of both span starts vibrating large, and more precisely, with almost similar vibration amplitudes and coupled frequencies.

Now, similar studies on the two-span membrane system, however, considering that the internal support is fixed. The analysis results are presented in Fig. 5.27. The fluctuating responses at 10 m/s are very low in both spans, with the presence of low frequencies due to vortex shedding. At 20 m/s, the coupled motion is observed in 2nd span only. The first span shows almost no response. At flow velocity 30 m/s, the fluctuating response of the first span reduces significantly since there is no distribution of axial tension in between the spans due to fixed internal support (c.f. Fig. 5.26(d)).

Aeroelastic coupled motion of membrane umbrellas

With few modifications over the two-span membrane system, the coupled motion of an umbrella-type membrane roof is analysed. The schematic of the modified system is presented in Fig. 5.28; the membrane is supported using a steel frame. The membrane properties are considered the same as mentioned before in Table 5.10 while the beam cross-sections are

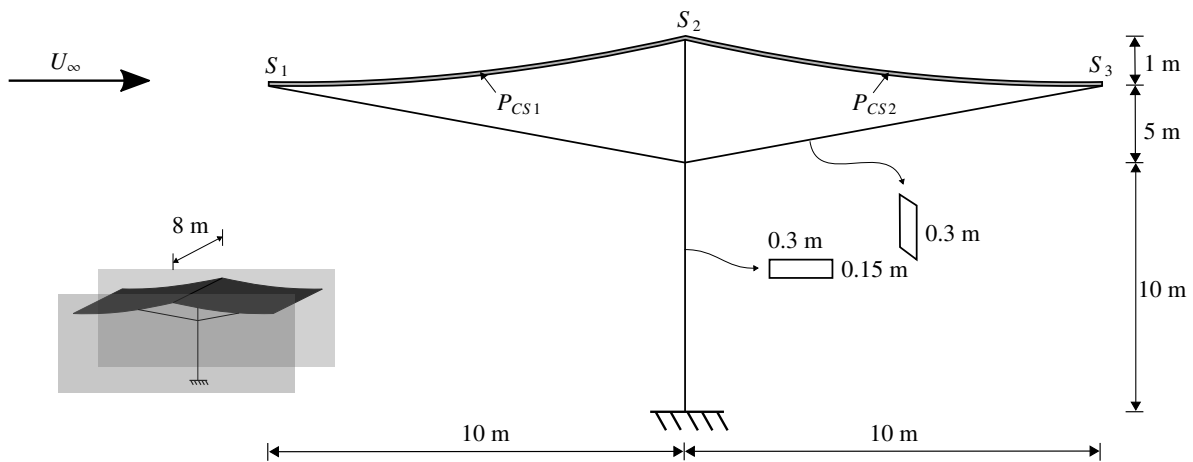


Figure 5.28: System configuration for the flow over a membrane roof.

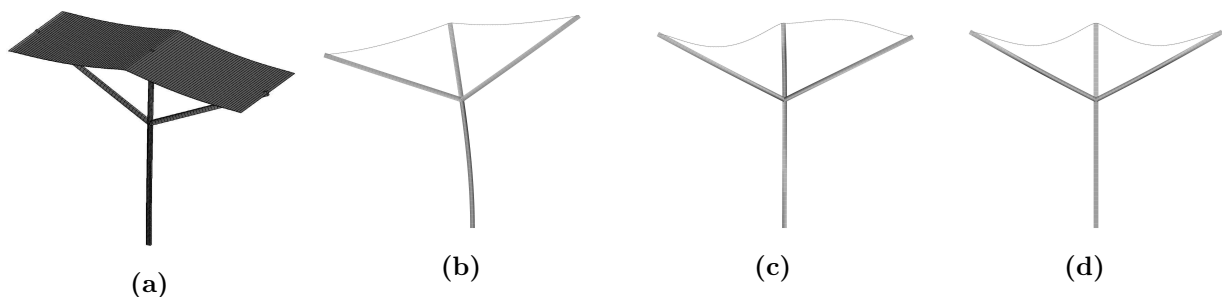


Figure 5.29: Geometrically nonlinear finite element model of membrane umbrella for eigenvalue analysis: (a) the modelled system, (b) steel frame mode $f_1 = 0.39$ Hz, (c) membrane mode $f_2 = 1.26$ Hz, and (d) membrane mode $f_3 = 1.39$ Hz.

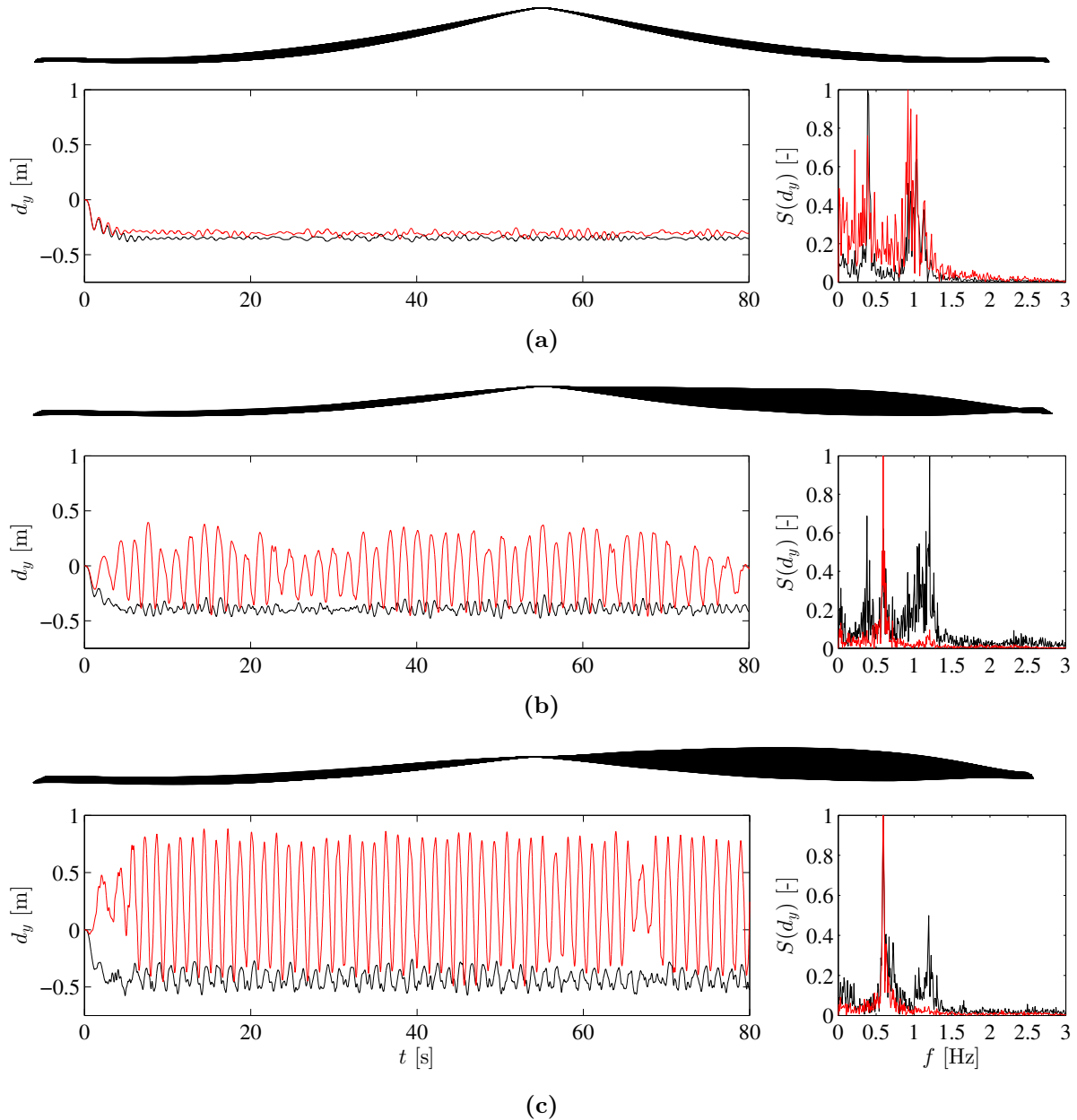


Figure 5.30: Aeroelastic response of two-span membrane roof under different wind velocities: (a) 10 m/s, (b) 20 m/s, and (c) 30 m/s. For each wind speed three figures are shown respectively:
 (top) superposition of the vibration phases,
 (bottom-left) displacement time histories of the centre of each span, and
 (bottom-right) the frequency spectrum of displacement time histories. Here, black lines (—) are for the centre of 1st span, whereas red lines (—) are for the 2nd span.

considered of steel ($E = 180 \times 10^9$ Pa). The width of the membrane roof is considered 8 m.

Important to note that the flow analysis is entirely 2D. Furthermore, the wind-induced nodal forces on the steel sections are not modelled. Basically, the discretisation scheme of the flow solver is the same as for the two-span membrane system. The wind forces are applied on the membrane structural nodes; however, the solution of the motion is analysed for all structural nodes including the steel frame. The FE model of the membrane umbrella is used for eigenvalue analysis. The natural vibration modes and corresponding frequencies are

presented in Fig. 5.29.

Similarly like the two-span membrane system, the umbrella is simulated for three flow velocities: 10 m/s, 20 m/s, and 30 m/s. The numerical parameters are considered the same as before in Table 5.11. Here, the number of elements for membrane and steel frame are used 100 and 238, respectively.

The outcome of the coupled simulations is presented in Fig. 5.30. At the flow velocity 10 m/s, the fluctuating responses of the membrane at the centre of the spans are quite small. However, the mean displacements are quite larger than before (0.3 m–0.35 m). It is due to the flexibility of the membrane support at the end positions. The response frequencies of both spans are quite similar; but, what is different from previous studies is the presence of the frequency of the steel frame. One of the response frequencies is the translation of the steel frame, which is more like rigid body motion for the membrane.

At 20 m/s, the second span starts oscillating larger while the first span is nearly unbiased, which is more like the two-span systems. The response frequencies at the centre of the second span are significantly reduced. However, there is the presence of two frequencies in case of the first span like at 10 m/s.

At 30 m/s, the response of the second span become significantly more substantial. However, the response of the first span is quite less. It is due to the fixation of the membrane at the central support. The coupled response of the second span is quite periodic. The particle maps influenced by the motion of the moving membrane at 30 m/s are shown in Fig. 5.31.

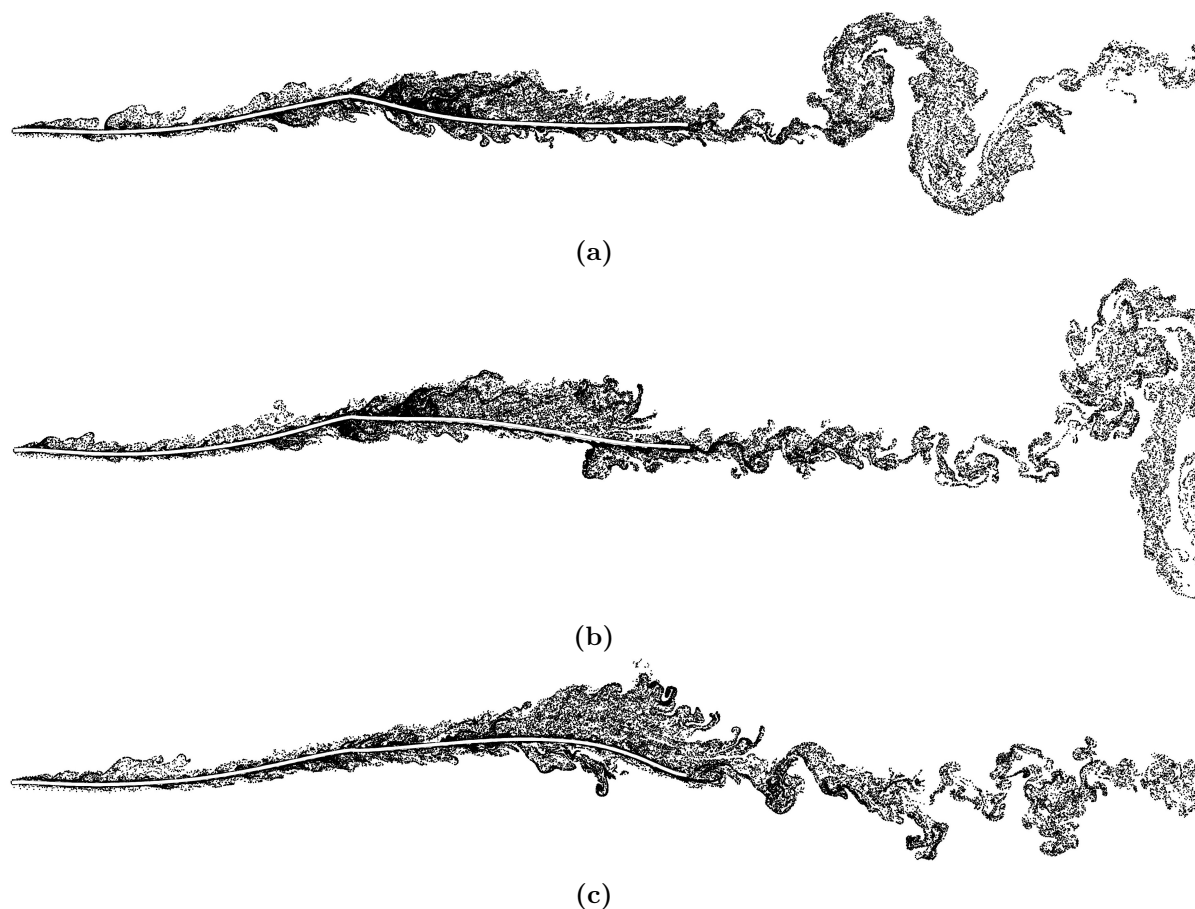


Figure 5.31: Particle maps influenced by the sequential motion of the membrane at 30 m/s.

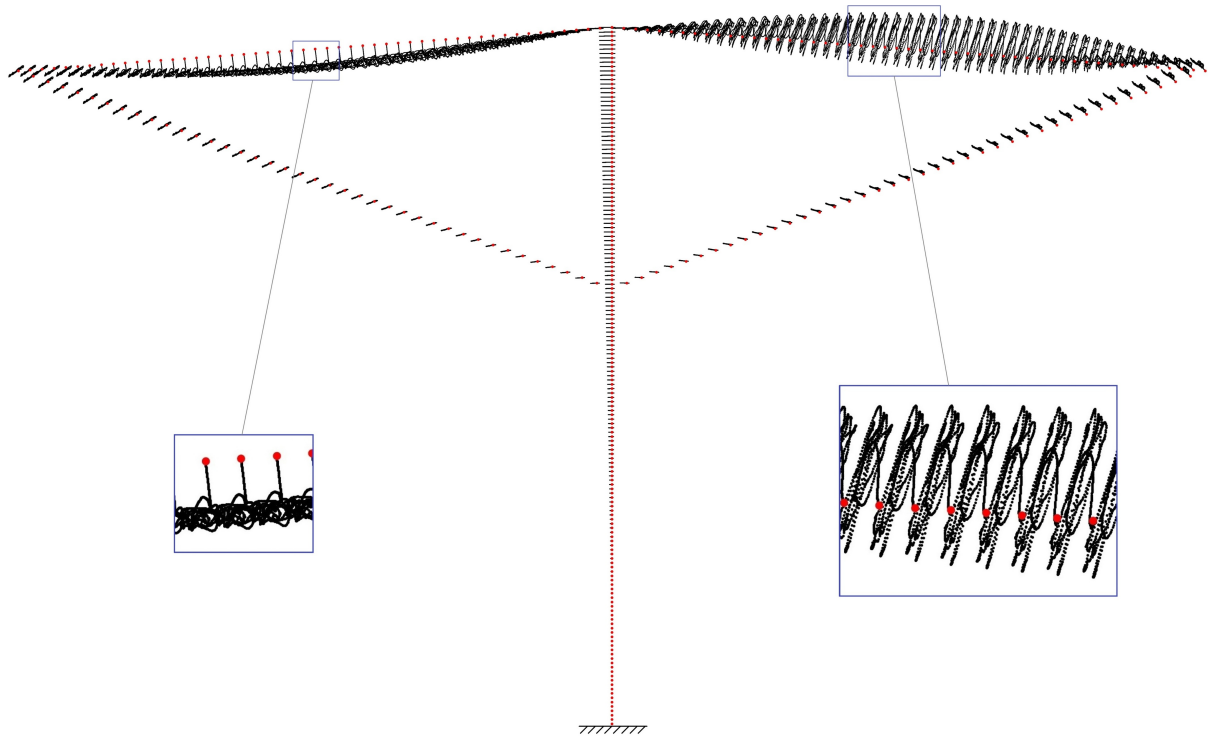


Figure 5.32: The trajectories of nodal response for the membrane and steel frame. The red dotted lines show the original position of the structural nodes.

The trajectories of the nodal response of the system, including the steel frame, are shown in Fig. 5.32.

The horizontal and vertical membrane responses at the supports, which are the left, centre and the right points are presented in Fig. 5.33 in case of $U_\infty = 30$ m/s. The fluctuating responses of left support are quite similar in both horizontal and vertical direction. However, the horizontal responses at the centre and the right support are mainly in a backward direction. The vertical responses at the centre are negligible and upward. However, the vertical responses at the right support are quite large in both directions. The response frequencies are mainly governed by the coupled response frequencies of the second span. There is a little influence of the lateral response frequency of the steel frame. The studies in this section show that even though the coupled model is 2D; however, it can simulate complicated aeroelastic interactions such as prestressed flexible membrane roofs.

5.6 Validation of pseudo-3D VPM for FSI simulation

5.6.1 Flexible cantilever in von Kármán vortex street

This is a 2D benchmark FSI problem that has been presented already in Sec. 5.2.1 for validation of the 2D coupled solver. It is considered again in this section for validation of the pseudo-3D multi-slice VPM model. The geometry and inflow conditions of the reference FSI problem are presented schematically in Fig. 5.34 in the context of pseudo-3D analysis. The summary of the material parameters of fluid and solid are listed again in Table 5.12.

The coupled motion of the flexible cantilever plate is simulated using 7 simulation slices. To simulate the 2D FSI problem in the context of pseudo-3D analysis, the plate width W of the system is considered 6 cm. However, to represent the 2D behaviour of the benchmark

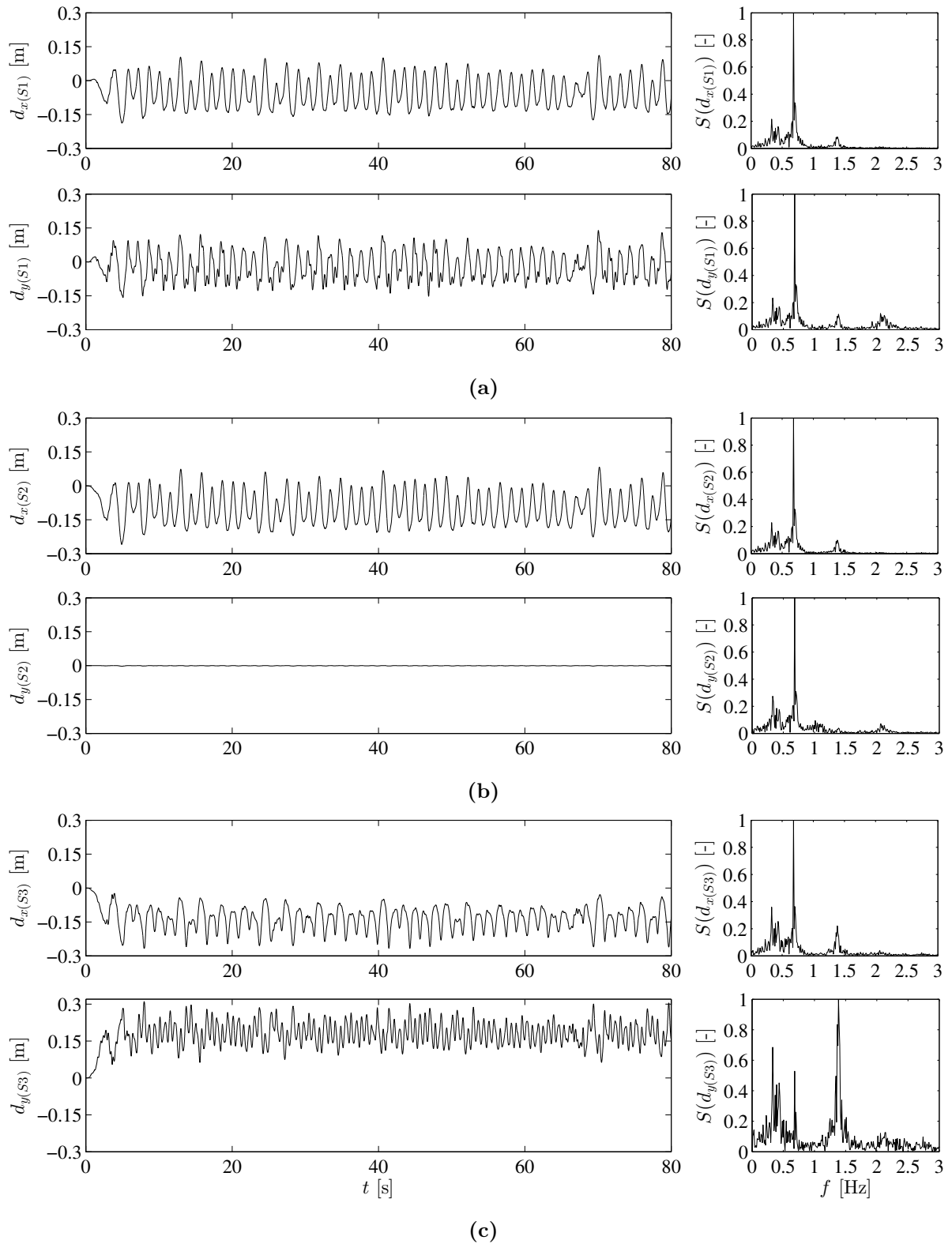


Figure 5.33: The coupled response of the membrane supports at 30 m/s: (a) left support, (b) centre support, and (c) right support.

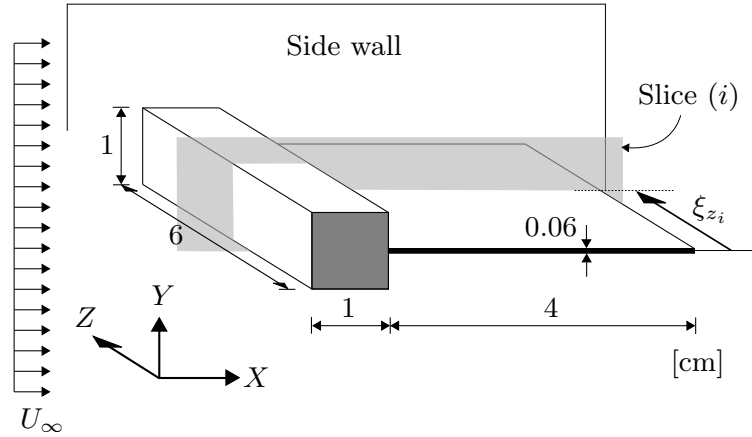


Figure 5.34: The pseudo-3D VPM analysis: the interaction between a flexible cantilever beam and vortex shedding from attached rigid square cylinder. The schematic presentation of the problem is shown with the physical dimensions. Here, ξ_{z_i} is the location of the slice i from the edge in Z -axis.

problem, the system is considered confined perfectly in between side walls, c.f. Fig. 5.34. The assumption is similarly needed for the presented pseudo-3D VPM formulation since the method can't consider the across-flow vorticity. The cantilever plate is discretised into 80 shell elements along the length while 6 elements along the width. The lowest natural vibration mode is of plate bending with a frequency of 3.04 Hz, which is found quite similar to the frequency mentioned in the literature. The discretisation of the system for fluid and structure solver is presented schematically in Fig. 5.35. The numerical parameters are summarised in Table 5.13

Geometry and physical properties			Value
Flexible plate	Density	ρ_s	100 kg/m ³
	Elastic modulus	E	2.5×10^5 Pa
	Plate length	L	4 cm
	Plate width	W	6 cm
	Plate thickness	h	0.06 cm
Fluid	Density	ρ_f	1.18 kg/m ³
	Kinematic viscosity	ν_f	1.54×10^{-5} m ² /s

Table 5.12: Flexible cantilever plate in Kármán vortex street: physical and material properties of the fluid and flexible plate.

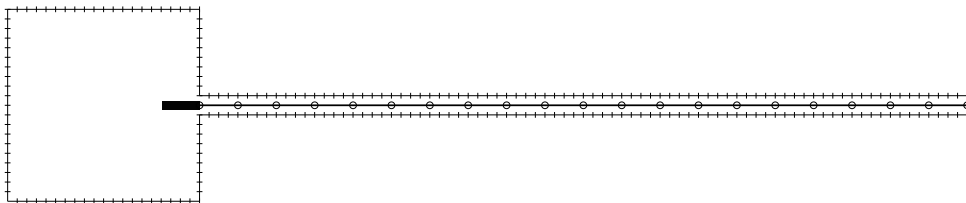


Figure 5.35: The schematic shows the system discretisation of the system in each simulation slice. The surface of the rigid square and flexible plate is discretised together in the case of the fluid solver. In contrast, the structural discretisation is at the mid-surface of the flexible plate.

Solver	Numerical parameters		Value
Flow	Free-stream flow	U_∞	0.513 m/s
	Number of simulation slices	N_{slice}	7
	Position of simulation slices	$\xi_{z_i} = Z_i/W$ ($i = 1, \dots, 7$)	0, 0.17, 0.33 0.5, 0.67, 0.83, 1
	Number of panel per slice (rigid square and cantilever)	$N_{pan(slice)}$	242
	Panel size per slice	$\Delta s_{(slice)}/L$	0.0125
	Non-dimensional time step	$\Delta t_f^* = \Delta t_f U_\infty / \Delta s_{(slice)}$	1.0
	Number of particles (approx.)	$N_{particle}$	525,000 - 560,000
Structure	Number of shell elements	N_{elem}	480
	Number of vibration modes	Φ_{num}	1
	Non-dimensional time step	$\Delta t_s^* = \Delta t_s U_\infty / \Delta s_{(slice)}$	1

Table 5.13: Flexible cantilever plate in Kármán vortex street: numerical parameters for pseudo-3D coupled VPM analysis.

The instantaneous vorticity field around the rigid square cylinder and the moving flexible plate at different simulation slices are shown in Fig. 5.36(top), whereas the instantaneous velocity fields are shown in Fig. 5.36(bottom) for the mid-slice ($\xi_{z_i} = 0.5$) only. The vertical tip displacement at the mid-slice and the response frequencies are presented in Fig. 5.37. The frequency of the coupled motion of the cantilever plate is found to be 3.19 Hz, which is slightly above the first natural frequency of the elastic appendix. The long-term maximum tip displacements $|d_{y,t}|_{max}$ are observed in the range of 1.05 – 1.135 cm, which is very good when compared to other studies and the nonlinear 2D VPM model in Table 5.3 in Sec. 5.2.1.

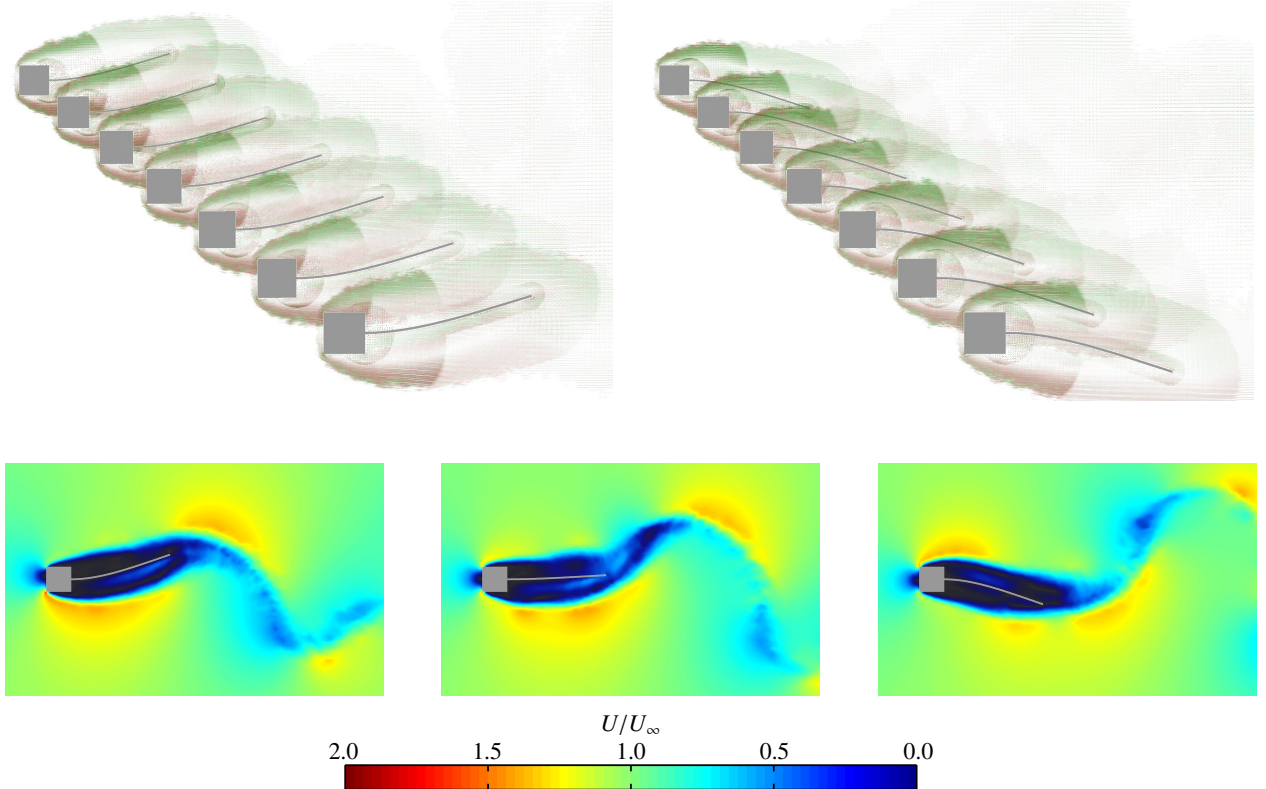


Figure 5.36: The multi-slice visualisation of flexible cantilever plate in Kármán vortex street: (top) the particle maps, and (bottom) the velocity field around the rigid section and moving flexible plate.

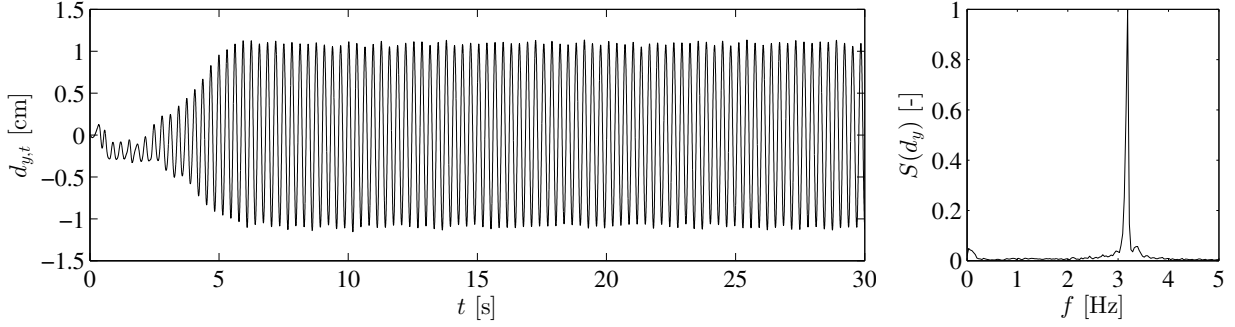


Figure 5.37: The tip displacement of the cantilever plate at the mid-slice ($\xi_{z_i} = 0.5$) position (left), and the normalized frequency spectrum of the displacement time history (right).

5.6.2 Identification of analytical critical flow speed of inverted flag

The dynamics of the reference inverted cantilever plate [201], which has been investigated in Sec. 5.2.3 using the 2D coupled solver, is simulated again, however currently using the multi-slice coupled model. The schematic multi-slice configuration of the inverted flag in axial is shown in Fig. 5.38. Knowing that the motion of the inverted flag is highly nonlinear, the aim of this study is therefore limited to the identification of critical wind speed at which the large-amplitude limit cycle oscillation initiates.

The reason of choosing this case again is the availability of an analytical critical non-dimensional flow velocity $\kappa = 1.85$, when there is not across-flow effects [201]. It has been mentioned earlier that the pseudo-3D VPM model can't model the across-flow effects. The physical and geometrical properties of the plate have been listed earlier in Table 5.6. The numerical parameters of the pseudo-3D coupled simulation are summarized in Table 5.14. The finite element model of the cantilever plate is based on 102 shell elements along the length while 8 elements along the width. The natural vibration modes and corresponding frequencies of the modelled system are shown in Fig. 5.39.

The visualization of the vorticity field in all the slices for different vibration phases of the cantilever plate are shown in Fig. 5.40. The vertical tip displacement of the cantilever at the mid-slice ($\xi_z = 0.5$) for different dimensional and non-dimensional wind speeds are displayed in Fig. 5.41. Even though four natural vibration modes have been used, including torsional and lateral bending type, the differential displacement in between the slices is found very negligible. The lowest bending mode governs the bifurcation, and it is observed exactly at wind speed $U_\infty = 2.45$ m/s, which is in non-dimensional unit $\kappa = 1.85$. It is an agreement with the analytical solution presented in [201] since the present model doesn't consider the effect of vortices from the edges across the flow direction.

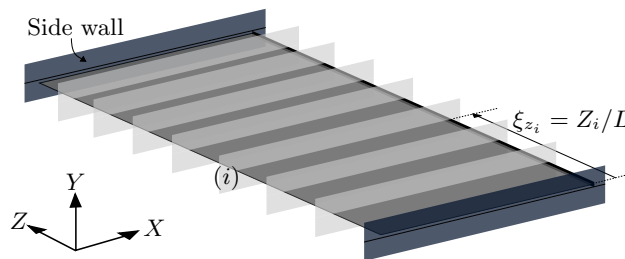


Figure 5.38: Schematic presentation of 7-slice simulation: the flapping of inverted cantilever plate.

Solver	Numerical parameters	Value	
Flow	Free-stream flow	U_∞	2.35–2.5 m/s
	Number of simulation slices	N_{slice}	7
	Position of simulation slices	$\xi_{z_i} = Z_i/W$ ($i = 1, \dots, 7$)	0.125, 0.25, 0.375, 0.5, 0.625, 0.75, 0.875
	Number of panel per slice	$N_{pan(slice)}$	206
	Panel size per slice	$\Delta s_{(slice)}/h$	3.8462
	Non-dimensional time step	$\Delta t_f^* = \Delta t_f U_\infty / \Delta s_{(slice)}$	1.0
	Number of particles (approx.)	$N_{particle}$	455,000 - 525,000
Structure	Number of shell elements	N_{elem}	816
	Number of vibration modes	Φ_{num}	4
	Non-dimensional time step	$\Delta t_s^* = \Delta t_s U_\infty / \Delta s_{(slice)}$	1

Table 5.14: The flapping of an inverted cantilever plate in axial flow: numerical parameters for pseudo-3D VPM analysis.

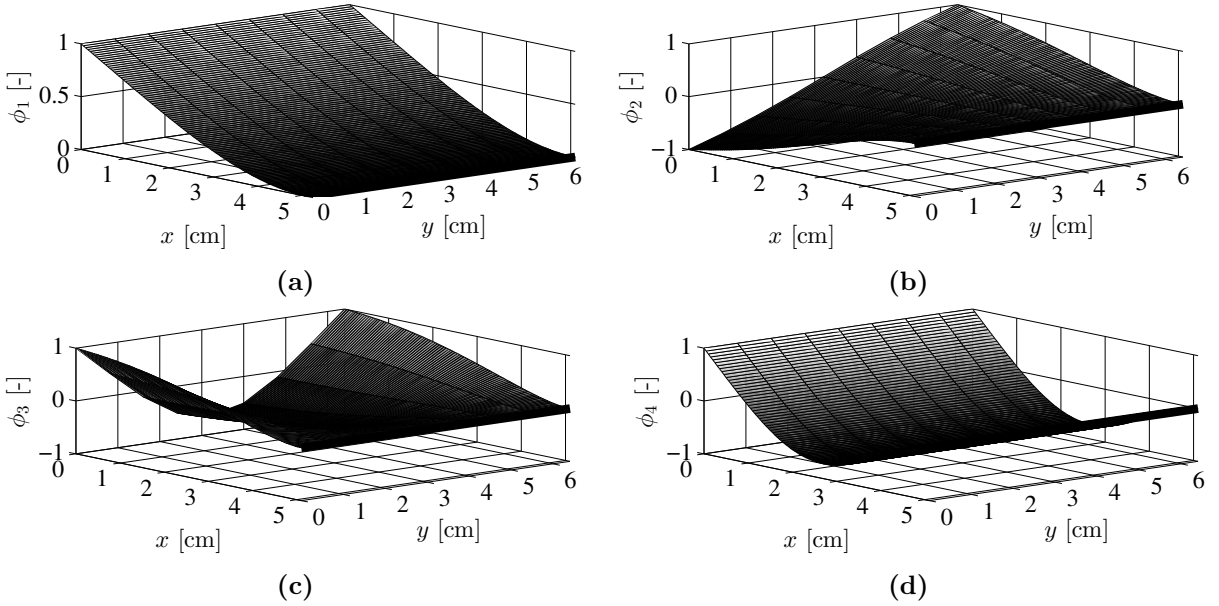


Figure 5.39: Normalized natural vibration modes and frequencies of the reference inverted cantilever plate model: (a) $f_1 = 11.53$ Hz, (b) $f_2 = 26.22$ Hz, (c) $f_3 = 62.77$ Hz, and (d) $f_4 = 72.24$ Hz.

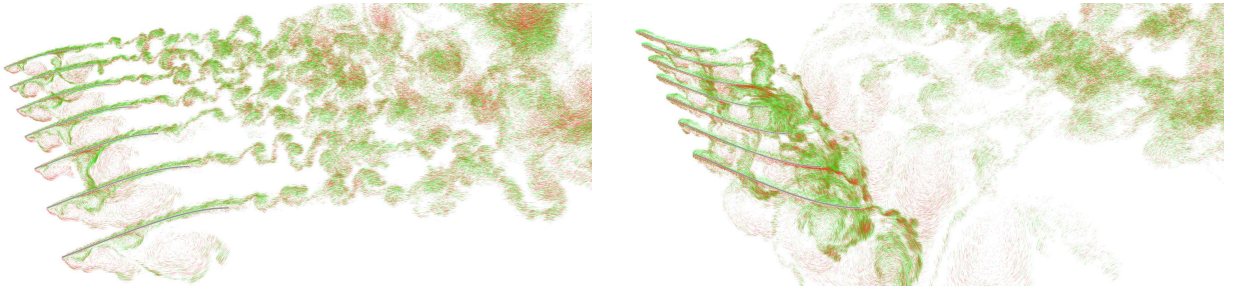


Figure 5.40: The vortex street around the the cantilever plate at different slices due to the free stream flow.

The coupled response frequencies of the cantilever are observed following the frequency of vortex shedding. The frequency of periodic motion of the cantilever plate at $U_\infty = 2.45$ m/s

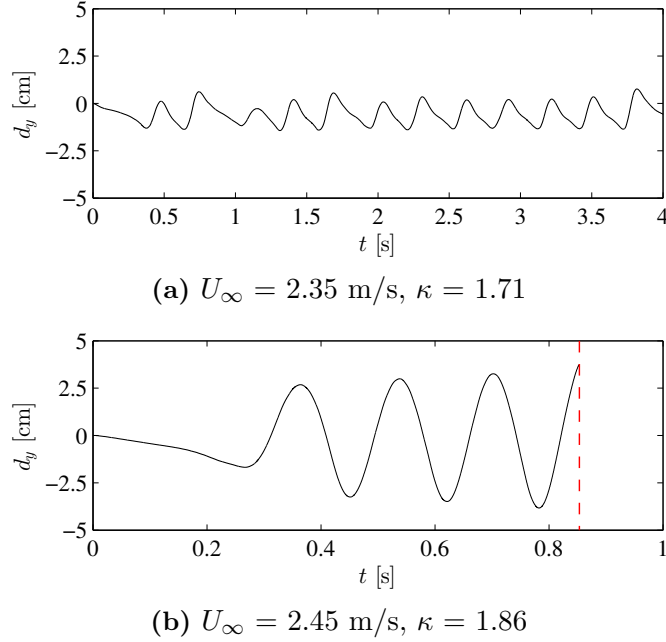


Figure 5.41: The vertical tip displacement of the inverted cantilever plate at the central simulation slice ($\xi_z = 0.5$) under dimensional (U_∞) and non-dimensional (κ) wind velocities. The critical wind velocity is identified as 2.45 m/s at which the large amplitude vibration initiates. The dotted lines in (b) shows the initiation of divergent amplitude.

is found approximately 6.5 Hz (c.f. Fig. 5.41(a)), which is slightly over the half of first natural frequency of the system (11.53 Hz). A minimum vertical tip displacement is necessary to induce the LCO behaviour. Therefore, the response of the system at $U_\infty = 2.35$ m/s seems to be a competition between the bending stiffness and the aerodynamic forces (Fig. 5.41(b)). Several very low frequencies are observed at $U_\infty = 2.35$ m/s. Similar fundamental behaviour was observed in [55, 201].

This particular test case has been analysed considering different number of slices such as 1, 2, and 4. It requires the change of the effective width of the slices accordingly. The critical wind speed at which the large amplitude flapping initiates is always identified very closely around 2.45 m/s ($\kappa = 1.86$) for all the studied cases.

5.6.3 Flapping of skewed inverted cantilever plate

The present study represents no validation study. Since the slice response of the inverted cantilever plate in the previous section shows unnoticeable differential displacement, the aim here is to analyse a skewed inverted cantilever plate such that the differential slice response can be displayed. A skewed inverted cantilever plate is therefore simulated under the axial wind using the pseudo-3D multi-slice numerical model. It is expected that a differential motion of the skewed plate may occur in between the slices since the length of the plate at each slice is different.

The length of the plate is adjusted at the top and bottom in order to make the cantilever skewed. A length modification ($\Delta L/L$) of 16 % is applied at the top and bottom edges such that $L_{top} = 4.284$ cm and $L_{bottom} = 5.916$ cm. The dimensions and multi-slice representation of the skewed inverted system are shown in Fig. 5.42. The coupled simulation is performed using 7 slices as before. The physical properties of the skewed inverted cantilever plate are

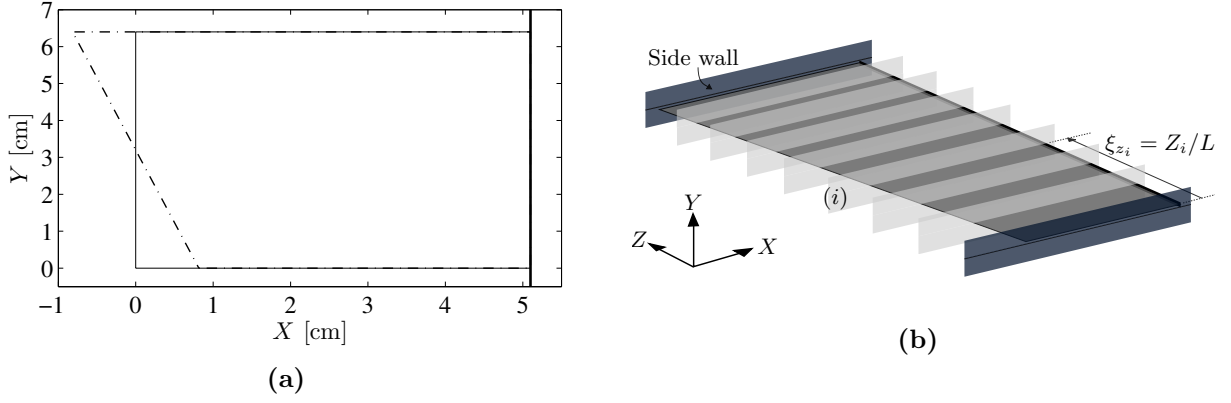


Figure 5.42: Schematic presentation of a skewed inverted cantilever for pseudo-3D VPM analysis: (a) the modification over the reference inverted cantilever (—) to have an skewed inverted cantilever (- · - ·). (b) The multi-slice schematic representation of the system.

chosen according to the reference inverted plate (Table 5.6). The numerical parameters of the pseudo-3D coupled simulation are almost same as mentioned in Table 5.14. The changes occur in the panel size and non-dimensional time step which are discussed in the next paragraph with the reasoning.

The cantilever plate is modelled again using 102 and 8 shell elements along the length and width, respectively. The natural vibration modes and corresponding frequencies of the modelled system are shown in Fig. 5.43. In the flow solver at each simulation slice 206 panels are used which means the size of the boundary elements Δs are different in slices ($\Delta s_{slice(min)}/h = 3.385$ and $\Delta s_{slice(max)}/h = 4.308$). However, in individual simulation slice the size of the panels are equal. In such a case, the non-dimensional simulation time step is normally considered or calculated based on the minimum average panel length such that $\Delta t_f^* = \Delta t U_\infty / \Delta s_{slice(min)}$.

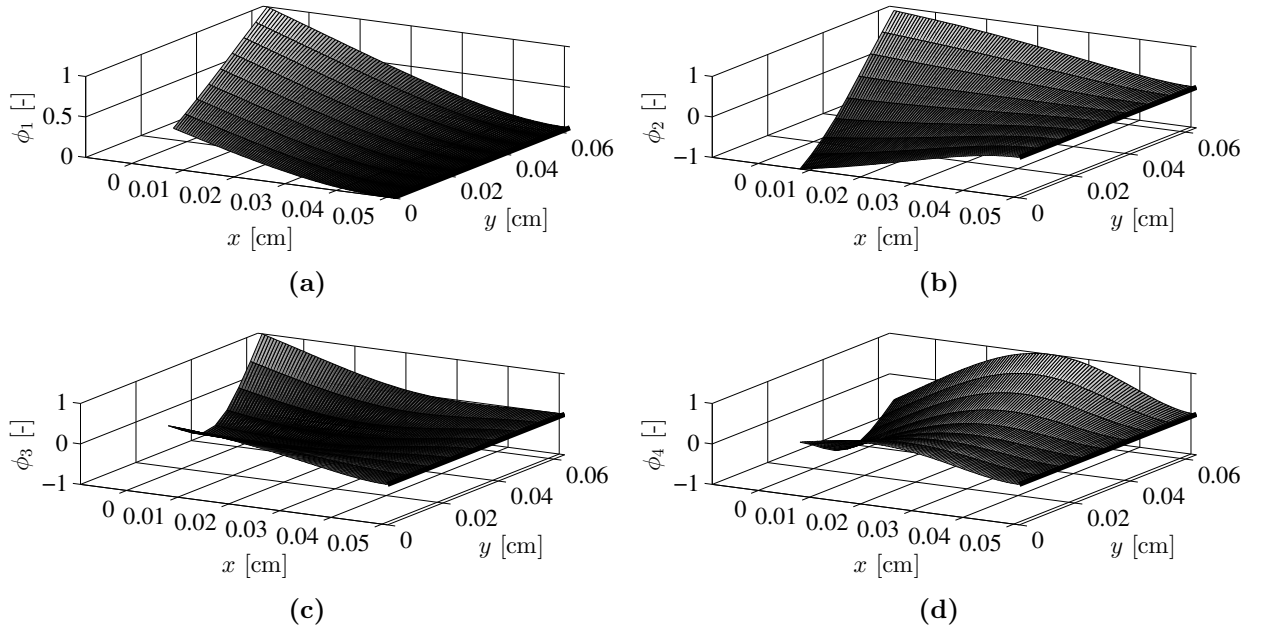


Figure 5.43: Normalized natural vibration modes and frequencies of the skewed inverted cantilever plate model: (a) $f_1 = 11.12$ Hz, (b) $f_2 = 26.91$ Hz, (c) $f_3 = 62.21$ Hz, and (d) $f_4 = 66.69$ Hz.

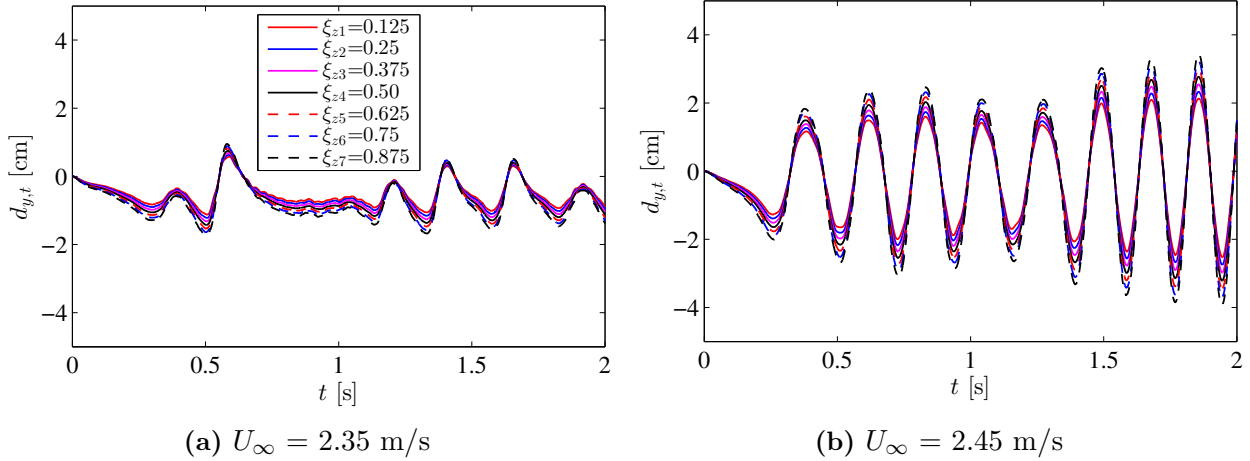


Figure 5.44: Pseudo-3D VPM analysis of a skewed inverted cantilever: the time histories of tip displacements at different slices under different incoming wind flows.

The coupled simulations are performed under different wind speeds. The displacement time histories of the cantilever tip for different slices are compared in Fig. 5.44 for 2.35 m/s and 2.45 m/s. The differential tip displacements are clearly observed at different slices. However, the critical wind speed for initiation of large amplitude LCO is identified at wind speed 2.45 m/s as before.

5.7 Vortex-induced vibration of clamped circular pipes using pseudo-3D VPM

In this section, the vortex-induced vibration (VIV) of an elastic and long circular pipe, which is clamped from both ends, is analysed under free-stream flow. This study is an application of the pseudo-3D VPM model for thin-walled circular sections, in which the fluid flows only around the outer surface. In this context, the aim is to analyse the VIV response of a clamped circular pipe considering two different models: (a) a 2D single-slice single-degree-of-freedom (SDOF) model (an existing 2D dynamic model for VPM), and (b) multi-slice analysis with flexible circular sections (presented pseudo-3D VPM model). This would allow performing a comparison of the outcome.

In the area of VIV of cylinders, the vast majority of research efforts in the past have been focused on the study on the transverse motion of flexibly mounted rigid bodies using SDOF model [203]. The understanding of FSI response of long flexible cylinder is crucial in the field of offshore engineering [126, 258]. The current study is not limited to analyse the cross-flow response of long flexible circular cylinders but also to study the ability of the proposed method of analysing ovaling effects of the circular shells.

5.7.1 System description and the resonance wind speed

A 42 m long circular pipe, which is clamped from both ends, has been analysed for VIV response. The schematic description as well as the multi-slice formulation of the system are shown together in Fig. 5.45. The position of the 2D simulation slices (ξ_z) are shown non-dimensionally along the longitudinal axis of the system. The dimensions and physical properties of the system are summarized in Table 5.15.

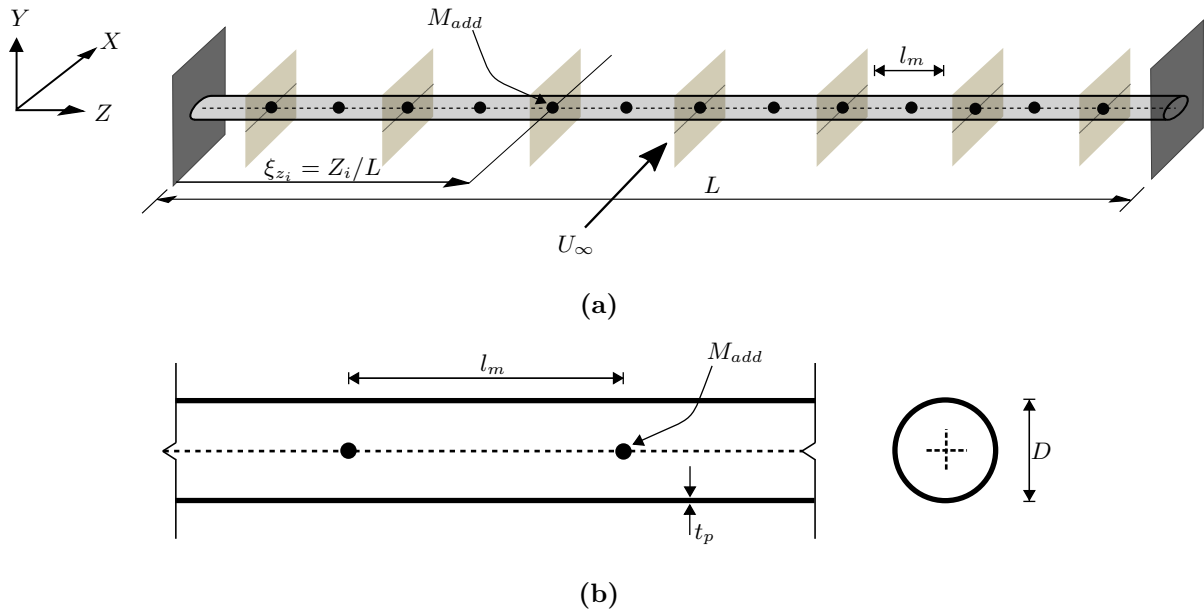


Figure 5.45: Vortex-induced vibration analysis of a both-end clamped circular pipe using 7-slice pseudo-3D VPM with flexible formulation: (a) the schematic of a long circular pipe of length L and diameter D . The filled circles (\bullet) along the centreline are additional masses (M_{add}) assigned at a distance of l_m . The slice locations are shown with a grey plane. (b) The close view of a partially selected portion of the system.

	Geometry and physical properties	Symbol	Value
Dimensions	Length of the circular pipe	L	42 m
	Distance between additional assigned mass	l_m	3 m
	Thickness of the pipe	t_p	5 mm
	Diameter of the pipe	D	1 m
Solid	Additional lumped mass	M_{add}	192 kg
	Density	ρ_s	8000 kg m ⁻³
	Elastic modulus	E	175 GPa
	Poisson ratio	ν	0.35
	Structural damping ratio	ζ	0.2 %
Fluid	Density	ρ_f	1.2 kg m ⁻³
	Kinematic viscosity	ν_f	1.5×10^{-5} m ² s ⁻¹

Table 5.15: The VIV analysis of both-end clamped thin circular pipe: the dimensions of the problem and physical properties for solid and fluid.

The mentioned 42 m long circular pipe is modelled in a structural solver based on the finite element approach. The model uses 160 shell elements along the circumference of the thin-walled circular section and 15 shell elements along the longitudinal axis. Additional mass is assigned for the shell nodes at a regular spacing to reduce the frequency of the system. At every 3 m distance (l_m) starting from the support, 1.2 kg of additional mass is assigned at each shell nodes (160 nodes). It means a total 192 kg of extra lumped mass is considered at every 3 m. The natural vibration modes and corresponding frequencies of the modelled system, which have been used for the pseudo-3D VPM simulations, are shown in Fig. 5.46. The vibration frequencies are found to be 2.73 Hz, 7.53 Hz, 9.37 Hz, and 9.51 Hz.

Static simulation of the circular cross-section is performed under free stream flow to study on the frequency contents of acting lift forces. For a large range of Reynolds number (\mathcal{Re}),

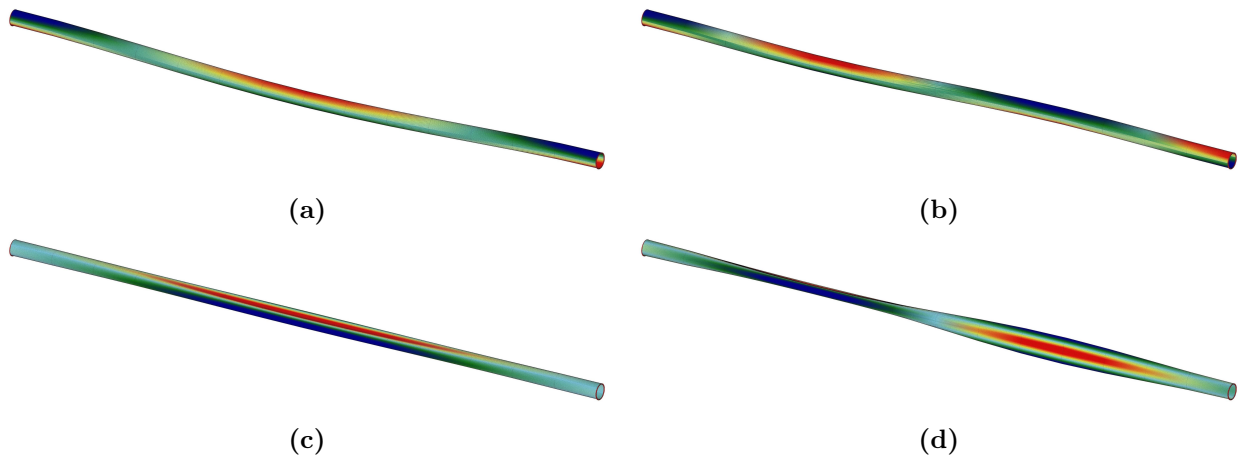


Figure 5.46: The finite element modelling of the both-end clamped circular pipe and the natural vibration modes associated with vertical bending and shell buckling: (a) $f_1 = 2.73$ Hz, (b) $f_2 = 7.53$ Hz, (c) $f_3 = 9.37$ Hz, and (d) $f_4 = 9.51$ Hz.

approximately up to 1×10^5 , the value of St for a circular cylinder can approximately be considered as 0.2. Above the mentioned Re , the St increases depending on the surface roughness. In case of smooth surface, St can be as high as up to 0.45.

A 2D static analysis of the rigid circular cross-section is performed under 12 m/s, which corresponds to the (Re) of 80,000. The circular section is discretized into 160 boundary panels. The length and width of the simulation domain are chosen $15 D$ and $7.5 D$. The number of vortex particles varies in between 100,000 and 120,000. The vortex shedding pattern and the Strouhal number are presented in Fig. 5.47. The values of St for the simulated circular cylinder are found to be in between 0.21 to 0.26, c.f. Fig. 5.47. Considering the lowest bending frequency of 2.73 Hz, the resonance flow velocities of the cylinder are found to be in between 10.5 m/s–13 m/s.

5.7.2 Single-slice VIV analysis using 2D SDOF model

The VIV response of the circular cylinder is modelled here using 2D VPM with simplified SDOF model considering the centre of the circular pipe. Here, the lowest bending frequency of 2.73 Hz is considered only. The coupled dynamic simulations are performed under different flow velocities. To keep $Re = 80,000$ for each studied flow conditions, the kinematic viscosity of the fluid is adjusted.

The time history of vertical displacement, the response frequencies, and the vortex shedding frequencies are displayed in Fig. 5.48 for several flow velocities. The system starts vibrating at or above 8 m/s, and the large responses are observed starting from 9 m/s. The maximum normalized vertical response ($d_{y(max)}/D$) is observed 0.129 at 11.5 m/s.

The response frequencies of the system mostly follow the lowest bending frequency of the circular pipe. However, at low flow velocities, when the system experience less response, the influence of vortex shedding is observed, c.f. the comparison of f_d and f_s in Fig. 5.48(a).

The comparison of normalized vertical displacement and governing vortex shedding frequency are compared in Fig. 5.49 under different simulated flow velocities. The peak response has dropped drastically above the flow velocity of 14 m/s (c.f. Fig. 5.49(a)) since the shedding frequencies (f_s) are far above the first bending frequency (c.f. Fig. 5.48(f) and Fig. 5.49(b)),

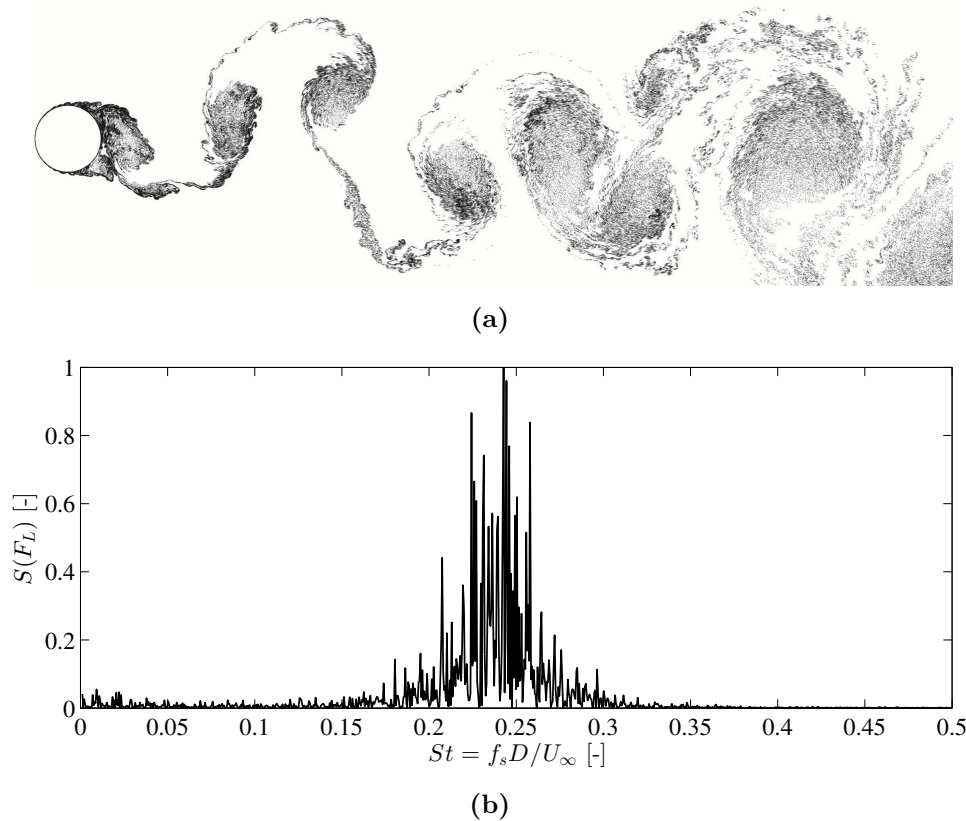


Figure 5.47: Simulation of flow passed a static circular section: (a) the shedding of vortices behind a static circular cylinder at Re of 80,000. (b) The spectrum of lift forces in order to identify the frequencies of vortex shedding.

and therefore, the resonance phenomena has been lost.

The important fact is that the vortex shedding frequencies f_s are found synchronized with the response/natural frequency (f_d or f_n) in between the flow speeds 8–13 m/s. The comparison between the shedding frequencies and the flow velocity are shown in Fig. 5.49(b). However, it is not like a conventional lock-in phenomenon. There is a presence of another frequency which is from the Kármán vortex street. This is due to the small VIV response of the system when compared to its length (only 0.3% of L).

5.7.3 VIV of clamped circular pipe using pseudo-3D VPM

The proposed pseudo-3D multi-slice VPM model is used here to model the coupled motion of the circular pipe. Here, four natural vibration modes of the clamped pipe are considered, which have been shown in Fig. 5.46, which means the shell buckling modes are also considered, c.f. Fig. 5.46(c-d). The numerical parameters associated with the 7-slice simulation is summarised in Table 5.16.

The instantaneous particle map and the corresponding flow field around the circular section in 7 slices are shown in Fig. 5.50. The outcomes of the pseudo-3D FSI simulations such as the time history of vertical displacement, the response frequencies, and the vortex shedding frequencies of the mid-slice ($\xi_{z_i} = 0.5$) are shown in Fig. 5.51.

The maximum normalized vertical response ($d_{y(max)}/D$) is observed 0.123 at 13 m/s. The vertical displacement is calculated as the average of vertical displacement from all shell nodes

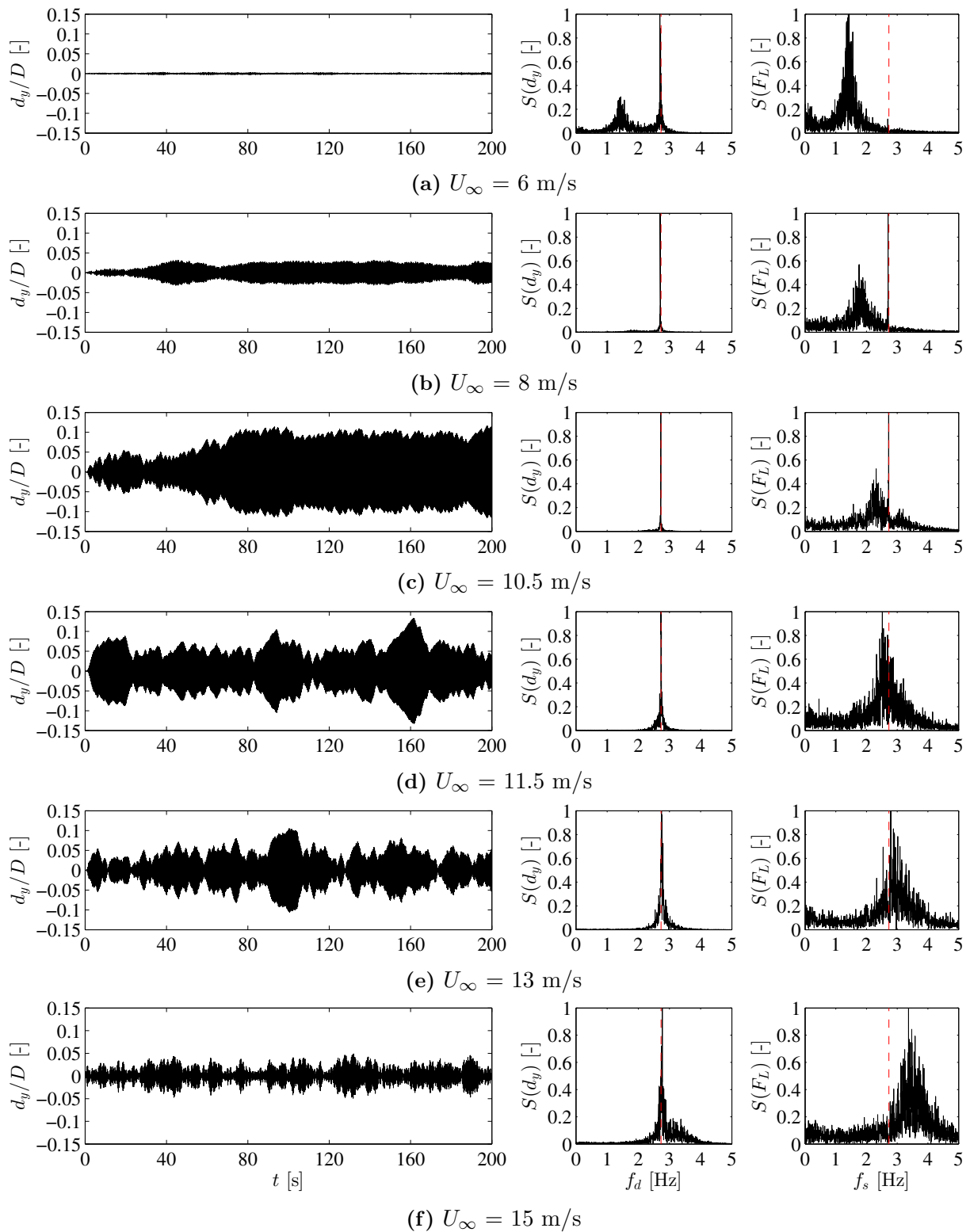


Figure 5.48: Single-slice VIV analysis of a rigid circular section using 2D VPM with SDOF model: the normalized vertical displacement of the circular pipe (left), the response frequency f_d (middle), and the vortex shedding frequency f_s (right) are compared in (a–f) under different free stream flow of 6 m/s to 15 m/s. The dotted red lines show the first natural frequency of the system.

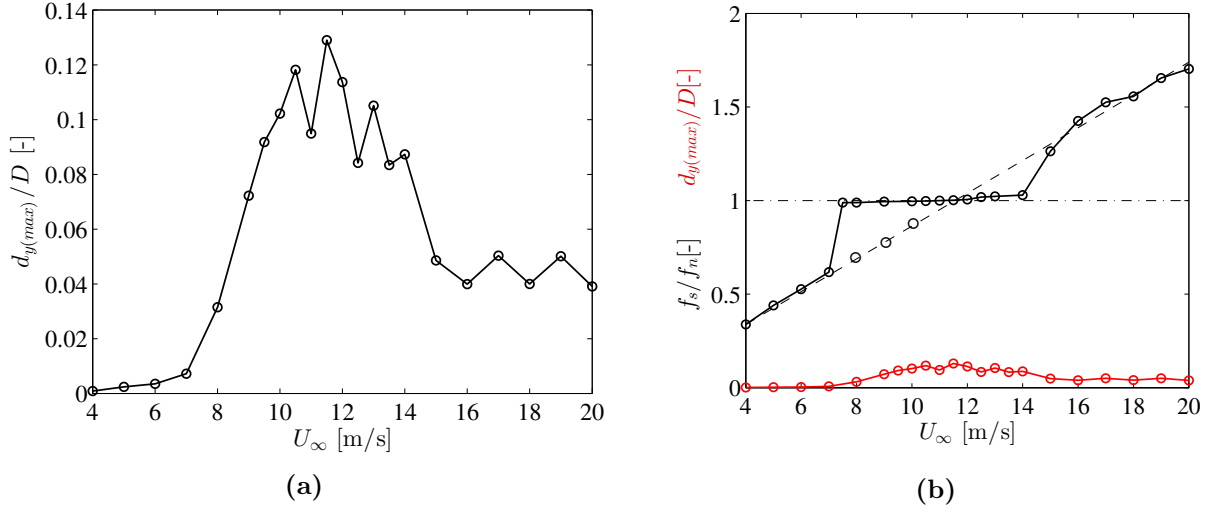


Figure 5.49: A 2D single-slice coupled FSI simulations of circular cylinder: (a) the peak vertical response and (b) vortex shedding frequencies at different flow velocities. The lock-in f_s is visible at $U_\infty = 8\text{--}13$ m/s. The dotted line (— · —) shows the resonance frequency whereas (— —) shows the linear relation of f_s with U_∞ .

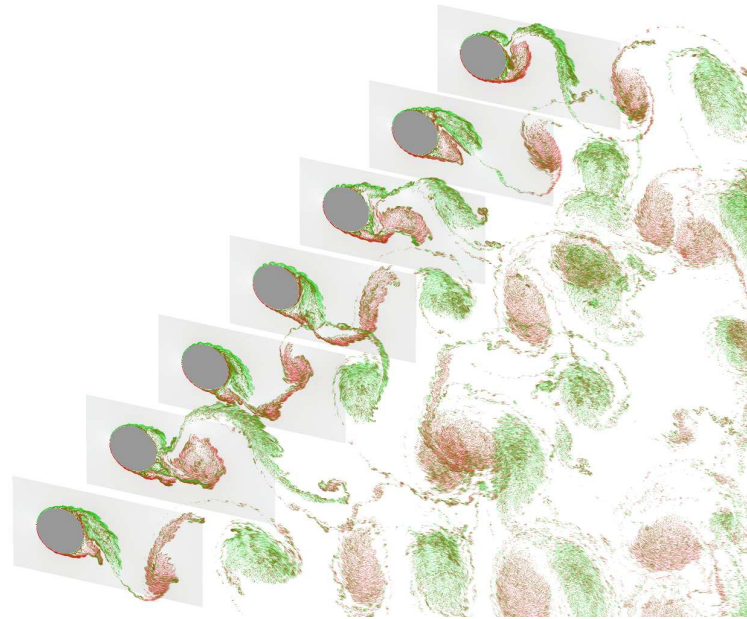
Solver	Numerical parameters		Value
Flow	Free-stream flow	U_∞	4–20 m/s
	Number of simulation slices	N_{slice}	7
	Position of simulation slices	$\xi_{z_i} = Z_i/L$ ($i = 1, \dots, 7$)	0.0714, 0.2143, 0.357 0.5, 0.6428, 0.7857, 1
	Number of panel per slice	$N_{pan(slice)}$	160
	Panel size per slice	$\Delta s_{(slice)}$	$\pi D/N_{pan(slice)}$
	Non-dimensional time step	$\Delta t_f^* = \Delta t_f U_\infty / \Delta s_{(slice)}$	2
	Number of particles (approx.)	$N_{particle}$	460,000 - 575,000
Structure	Number of shell elements	N_{elem}	2400
	Number of vibration modes	Φ_{num}	4
	Non-dimensional time step	$\Delta t_s^* = \Delta t_s U_\infty / \Delta s_{(slice)}$	2

Table 5.16: Vortex-induced vibration of clamped circular pipe: numerical parameters for pseudo-3D coupled VPM analysis.

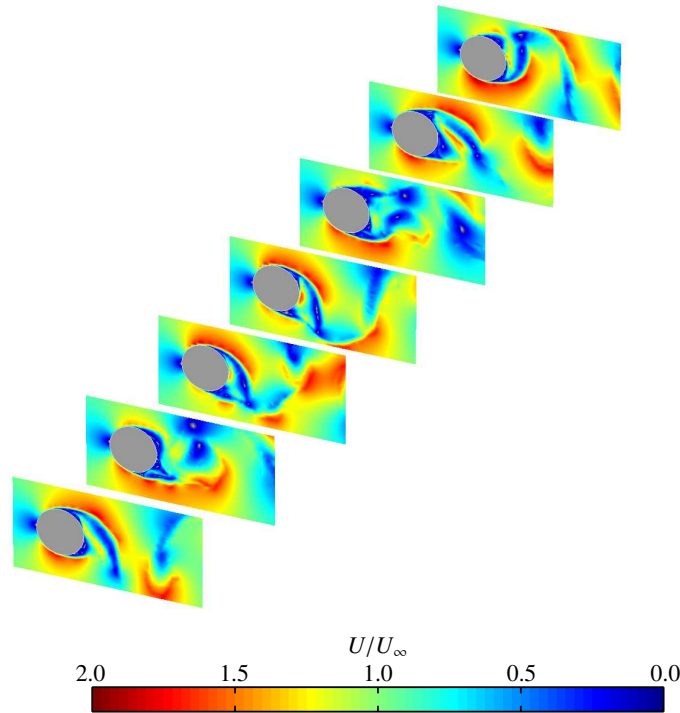
in a particular slice. Similarly, like the SDOF model, the response frequencies of the system mostly follow the lowest bending frequency of the circular pipe.

The significant response started from at or above 10 m/s in contrast to 9 m/s of SDOF model. The vertical displacement is reduced significantly above the wind speed of 13 m/s. The lock-in region is identified quite similar to the SDOF model; however, the response amplitudes are comparatively less. It is expected since the pseudo-3D model allows structural correlation along the longitudinal axis of the system; the differential displacement of the section in slices can influence the flow field. The phase differences of vortex shedding in slices allow the cancellation force. The SDOF is, therefore, may be a bit overestimation of the system responses.

Though the 2D SDOF model is simplistic, it gives a benchmark output for judging the prediction quality of the pseudo-3D VPM model. It is noteworthy that the buckling modes have a negligible contribution to the structural responses.



(a)



(b)

Figure 5.50: Pseudo-3D multi-slice simulation of a both-end clamped circular pipe: the instantaneous flow fields around the circular cylinders at each slices are shown in (a) and (b) for two sequential instances.

5.7.4 Owalling response of circular pipe at higher wind speeds

The aim here is to analyse the coupled simulation under high wind speed at which the vortex shedding has the potential to excite the system in higher vibration modes. Therefore, the wind speed is chosen approximately based on the buckling vibration mode ($f_3 = 9.37$ Hz). A target resonance wind speed according to f_3 is calculated approximately 45 m/s, which is based on St equal to 0.21 for the rigid circular section.

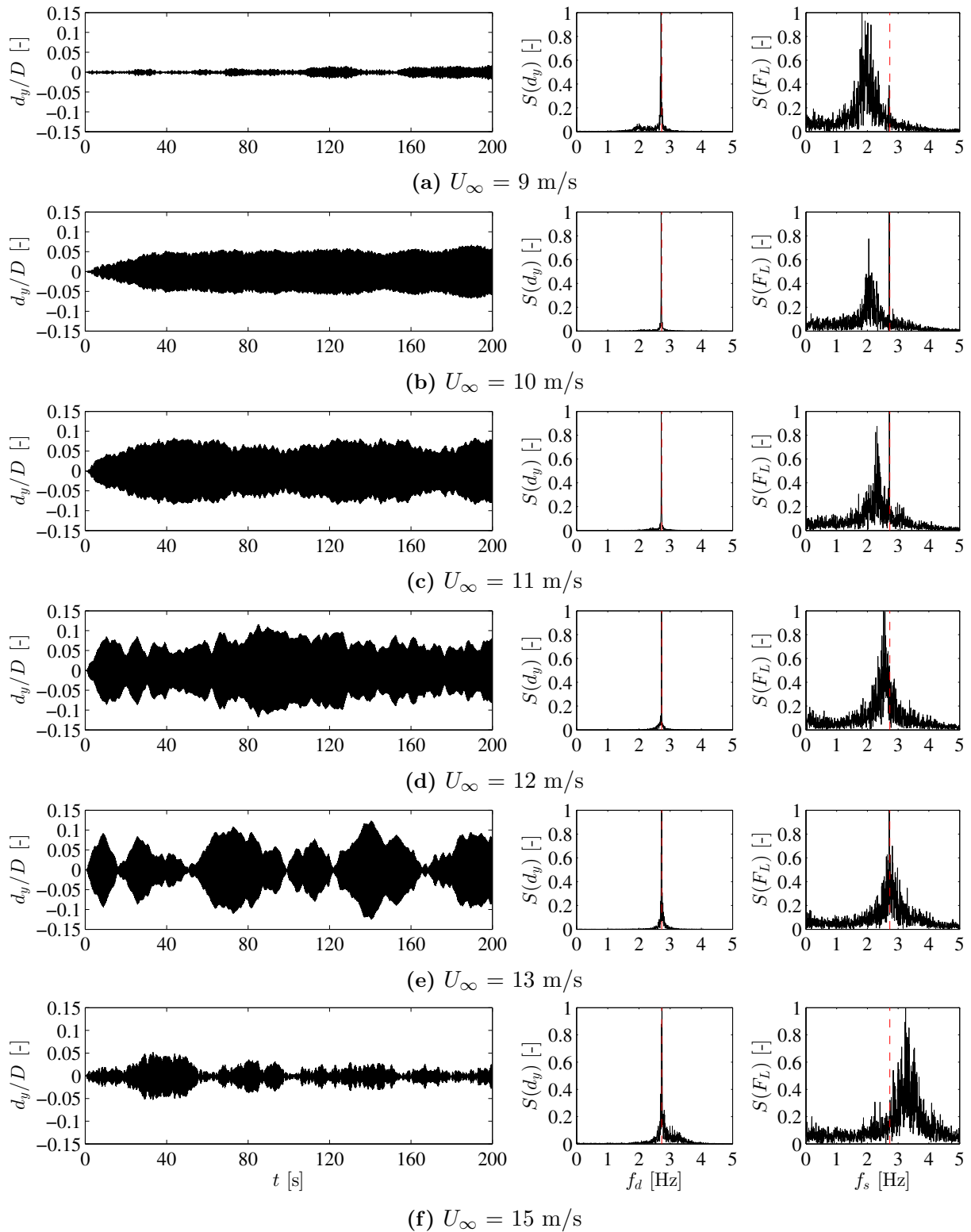


Figure 5.51: Multi-slice VIV analysis of flexible and long circular cylinder using pseudo-3D VPM with MDOF model: the normalized vertical displacement of the circular pipe (left), the response frequency f_d (middle), and the vortex shedding frequency f_s (right) are compared in (a-f) under different free stream flow of 9 m/s to 15 m/s. The dotted red lines show the first natural frequency of the system.

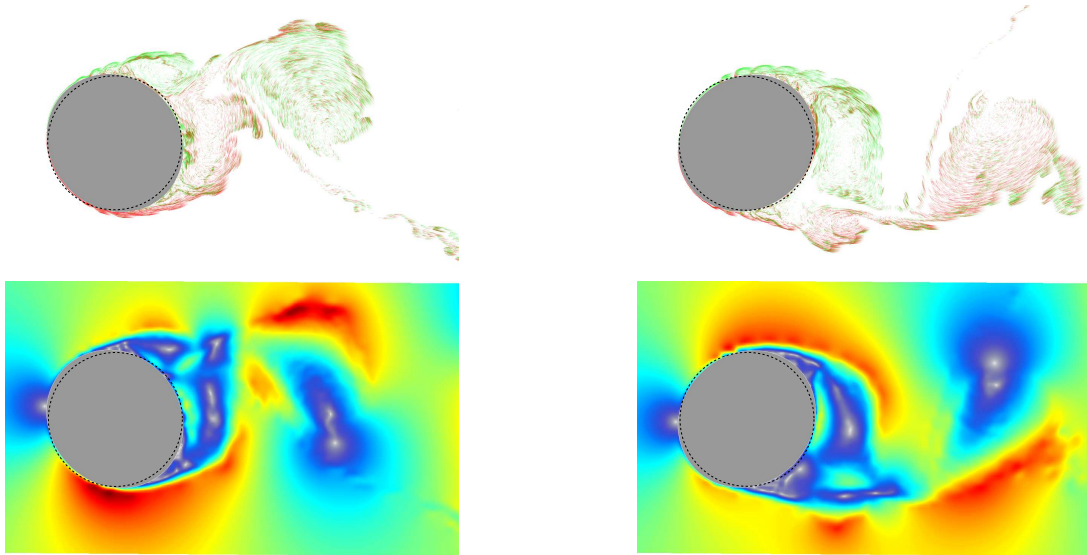


Figure 5.52: The shell buckling at the midspan of circular pipe is shown for two different phases under wind speed 45 m/s. The dotted line (- -) is the original circular section.

A significant amount of shell buckling is observed in the aeroelastic coupled responses, which is shown in Fig. 5.52 for the middle slice ($\xi_z = 0.5$) of the clamped circular pipe. The response of the circular section under the simulated wind velocity has shown a combination of different vibration modes; specifically, the coupling between the vertical and buckling vibration modes.

In order to visualize the ovaling response, a superposition of the responses at different times are compared in Fig. 5.53 for U_∞ of 11 m/s and 45 m/s. Clearly, the coupled responses are mainly vertical in case of 11 m/s, whereas the responses are buckled in case of 45 m/s.

Since the cross-section is continuously changing its shape, four specific points (P_1, \dots, P_4) are chosen around the periphery and monitored in order to inspect the response pattern (Fig. 5.54(a)). The local displacements are calculated based on the changes in position for the selected points with respect to their initial positions. These local displacements and corresponding response frequencies are compared to study the effect of different vibration modes. The local displacements of point P_1 in X and Y directions are shown in Fig. 5.54(left of (b)) and Fig. 5.54(left of (c)), respectively. Similarly, the local displacements of point P_2 along Y direction are shown in Fig. 5.54(left of (d)).

The relative and average displacements between points P_2 and P_4 along the Y direction are shown in Fig. 5.54(left of (e)) and Fig. 5.54(left of (f)), respectively. The closed views of the response time histories are shown in the middle, whereas the corresponding frequency spectrum is shown on the right side of Fig. 5.54(b-f).

It is important to mention again that the vibration modes corresponds to vertical bending are $f_1 = 2.73$ Hz and $f_2 = 7.53$ Hz, whereas corresponds to shell buckling are $f_3 = 9.37$ Hz and $f_4 = 9.51$ Hz (c.f. Fig. 5.47). The displacement of P_1 in X direction ($d_{X(P_1)}$) is observed expectedly based on the buckling modes since the vertical modes shouldn't contribute to the horizontal displacements. However, the displacement in Y direction ($d_{Y(P_1)}$) shows a mix of vertical and buckling vibration modes. Similarly, a combination of vertical and buckling vibration modes are observed in the case of $d_{Y(P_2)}$. The relative displacement of P_2 and P_4 in Y direction indicates the buckling modes, whereas the average displacements indicate the presence of lowest vertical bending mode.

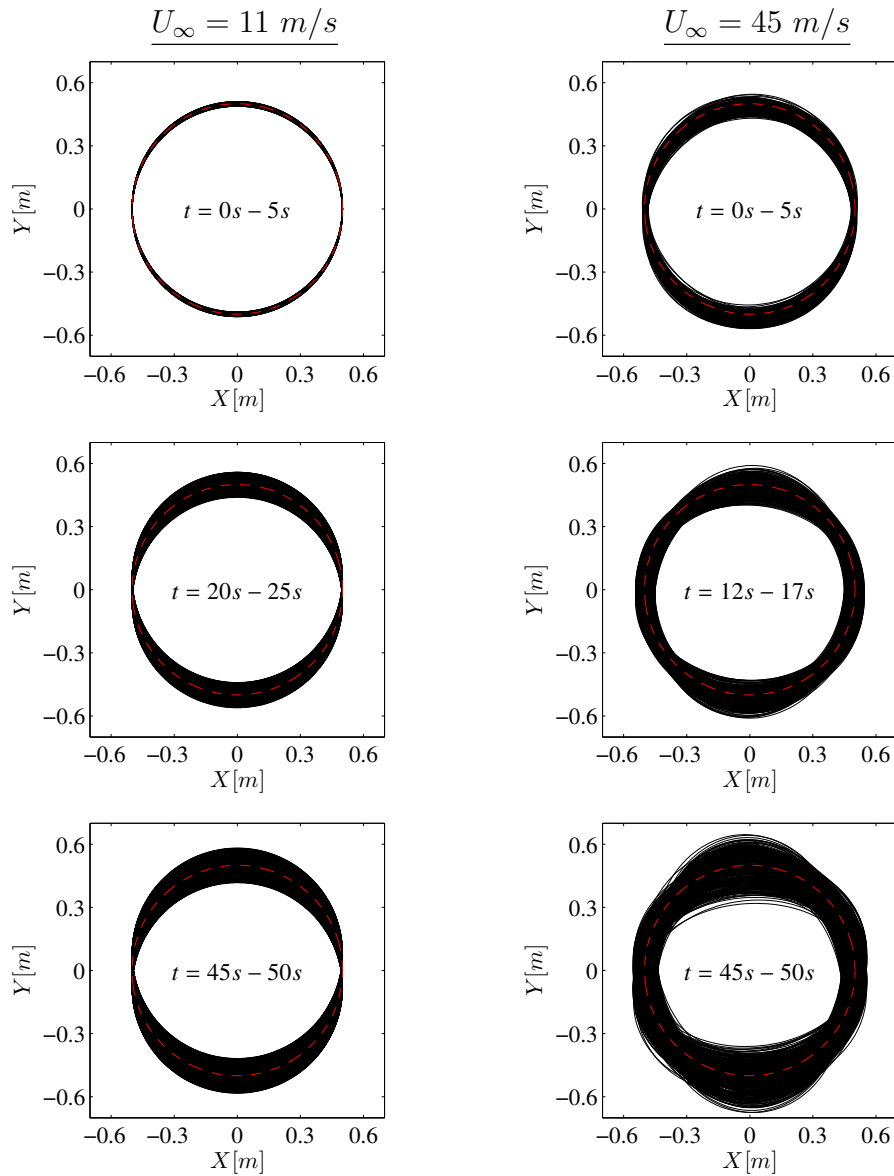


Figure 5.53: The superposition of the surface displacements at the midspan ($\xi_z = 0.5$) of the circular pipe under the free stream wind velocities of 11 m/s (left) and 45 m/s (right). In both cases, the development of coupled motion is shown for different time ranges of the coupled simulations. The dotted lines (- -) are plotted to show the original circular section.

Altogether, the section in the middle of the pipe experience buckling vibration while a vertical motion occurs simultaneously. The flow-induced buckling motion of a circular cylinder is a complex problem, and clearly, the model has been able to simulate the coupled motion.

5.8 Aeroelastic analysis of a thin-walled membrane roof

The membrane or thin-walled roof systems are getting increasingly popular since they are not only aesthetic but also provides more space and air. In the last years, the use of thin roofs in structural engineering became more and more common. However, it has also been reported recently about the collapse such roofs under wind action, such as the partial collapse of AFAS football stadium in Alkmaar, Netherlands (Fig. 5.55).

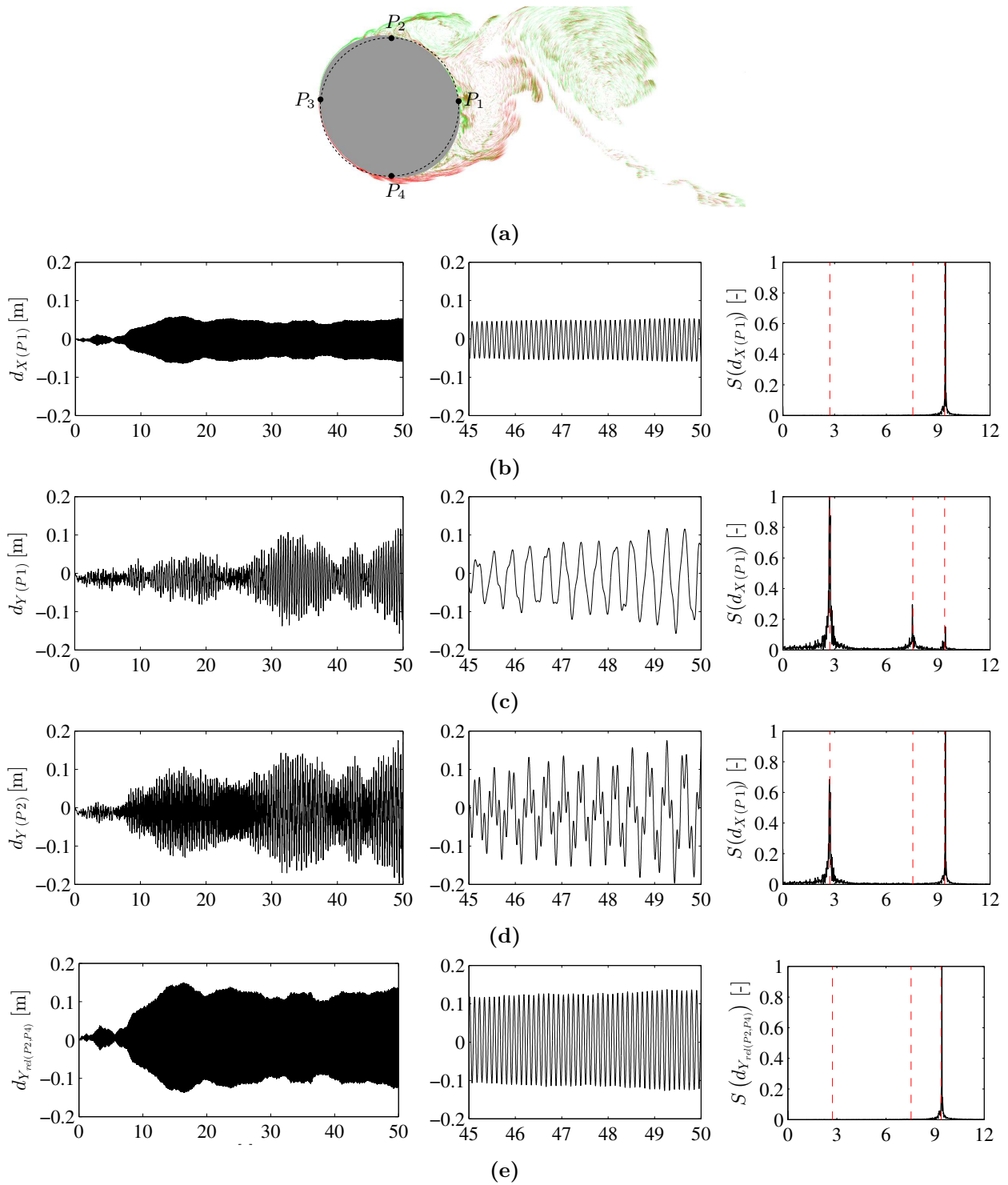


Figure 5.54: Pseudo-3D multi-slice VPM model for aeroelastic coupled simulation of the flexible and long circular pipe under 45 m/s: The local displacements are monitored at four points ($p_1 \dots p_4$) which are shown in (a). These local displacements and corresponding response frequencies are compared to study the effect of different vibration modes. The local displacements of point P_1 in X and Y directions are shown in (left of (b)) and (left of (c)), respectively. Similarly, the local displacements of point P_2 along Y direction are shown in (left of (d)). The relative and average displacements between points P_2 and P_4 are shown in (left of (e)) and (left of (f)), respectively. The closed view of the time histories are shown in middle, whereas the corresponding frequency spectrum is shown in the right of (b-f).

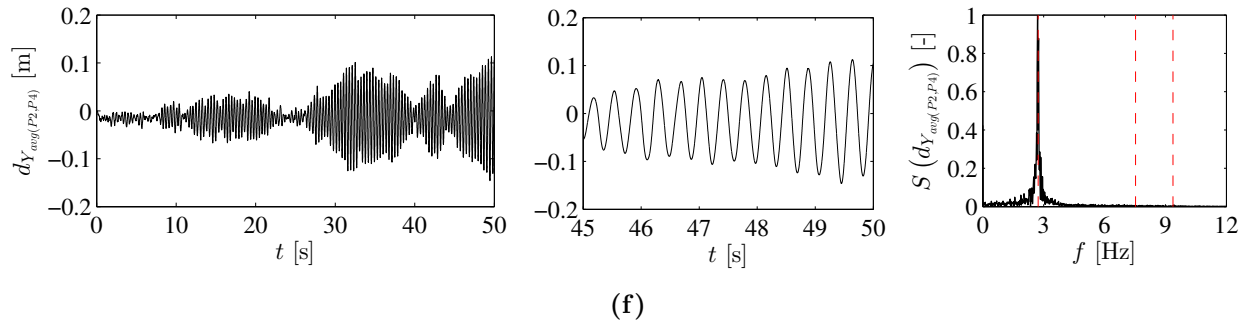


Figure 5.54: (continued)

A thin-walled curved roof system is simulated with the presented pseudo-3D multi-slice numerical model. The schematic configuration of the roof is shown in Fig. 5.56. From the top view, the front face of the roof is considered curved in a parabolic way. The thin membrane is supported by the frame of steel beams which are placed regularly along the length and width of the roof. The physical properties that are considered in this study for the numerical analyses are presented in Table 5.17. The numerical parameters associated with the 19-slice simulation is summarised in Table 5.18.



Figure 5.55: The collapse of AFAS football stadium in Alkmaar, Netherlands due to strong wind (Picture courtesy: BBC sports, 10th August, 2019).

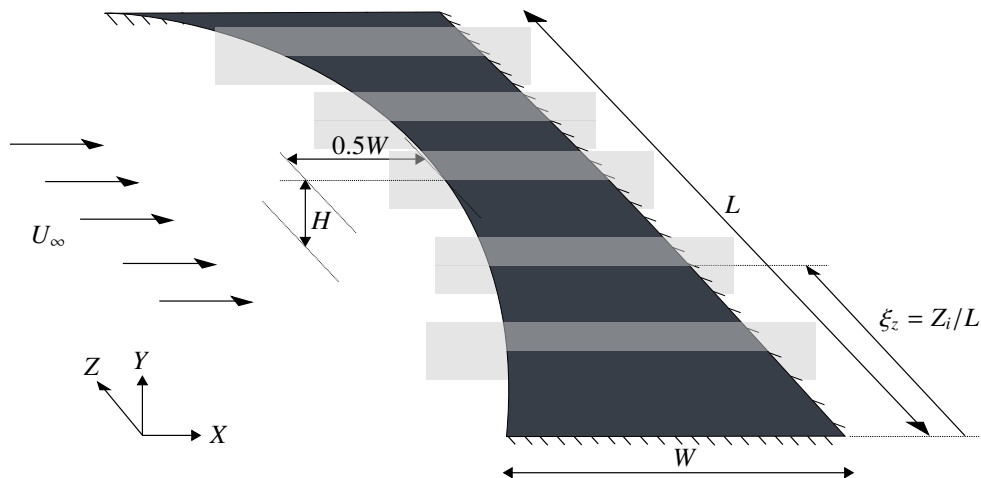


Figure 5.56: Schematic configuration of a membrane roof system under free stream flow U_∞ . The roof is considered curved in a parabolic way; the length, width and height are expressed as L , W , and H , respectively. The width is reduced by half at the centre along the length. The roof is fixed from three sides except the curved front face.

	Geometry and physical properties	Symbol	Value
Solid (membrane)	elastic modulus	E_m	2×10^9 Pa
	density	ρ_m	1000 kg/m ³
	thickness	h	20 mm
Solid (steel beams)	elastic modulus	E_{sb}	180 GPa
	density	ρ_{sb}	7950 kg m ⁻³
Fluid	air density	ρ_f	1.2 kg m ⁻³
	kinematic viscosity	ν_f	1.5×10^{-5} m ² s ⁻¹
Roof	length	L	20 m
	width	W	2 m
	height	H	0.4 m

Table 5.17: The physical properties and considered dimensions for the cantilever roof system.

Solver	Numerical parameters		Value
Flow	Free-stream flow	U_∞	30 and 40 m/s
	Number of simulation slices	N_{slice}	19
	Position of simulation slices	$\xi_{z_i} = Z_i/L$ ($i = 1, \dots, 19$)	0.05, 0.1,....., 0.9, 0.95
	Number of panel per slice	$N_{pan(slice)}$	160
	Non-dimensional time step	$\Delta t_f^* = \Delta t_f U_\infty / \Delta s_{slice(min)}$	2
	Number of particles (approx.)	$N_{particle}$	630,000 - 700,000
Structure	Number of shell elements	N_{elem}	1600
	Number of vibration modes	Φ_{num}	10
	Non-dimensional time step	$\Delta t_s^* = \Delta t_s U_\infty / \Delta s_{slice(min)}$	2

Table 5.18: Aeroelastic response analysis of a membrane roof: numerical parameters for pseudo-3D coupled VPM analysis.

The FE model of the described roof system is shown in Fig. 5.57(a-b). The roof is modelled using 80 and 20 shell elements along the length and width, respectively. The natural vibration modes and corresponding frequencies of the modelled roof are shown in Fig. 5.57(c-l).

The simulation of the roof system is performed under the wind speed of 30 and 40 m/s. The instantaneous vorticity around the roof system at different simulation slices are shown in Fig. 5.58 under the wind speed of 30 m/s. The displacement time histories of the tip of the roof system at different slices and response frequencies are compared in Fig. 5.59 and Fig. 5.60, respectively under the wind speed of 30 and 40 m/s.

The tip responses of different slices under 30 m/s are observed quite random (Fig. 5.59(a)) with contribution from different vibration modes (Fig. 5.59(b)). The responses are mainly upward due to the inclined shape of the roof which contributes to the increase in lift forces. The response amplitudes are quite small and the frequencies are observed mostly around the lowest vibration modes of the structure (e.g. $f_1 = 5.4$ Hz and $f_2 = 5.8$ Hz). However, the large amplitude LCOs are observed in tip responses under 40 m/s (Fig. 5.60(a)), which indicates strong aeroelastic interaction. In this case, the responses are dominantly periodic in all slices (Fig. 5.60(b)). Similarly, like the large-amplitude flapping of inverted cantilever plate, strong coupled responses are observed under the wind speed of 40 m/s. The coupled response frequency is observed 4.93 Hz, which is slightly lower than the first natural frequency of the roof.

The real time computation of such large scale analysis with the presented numerical model

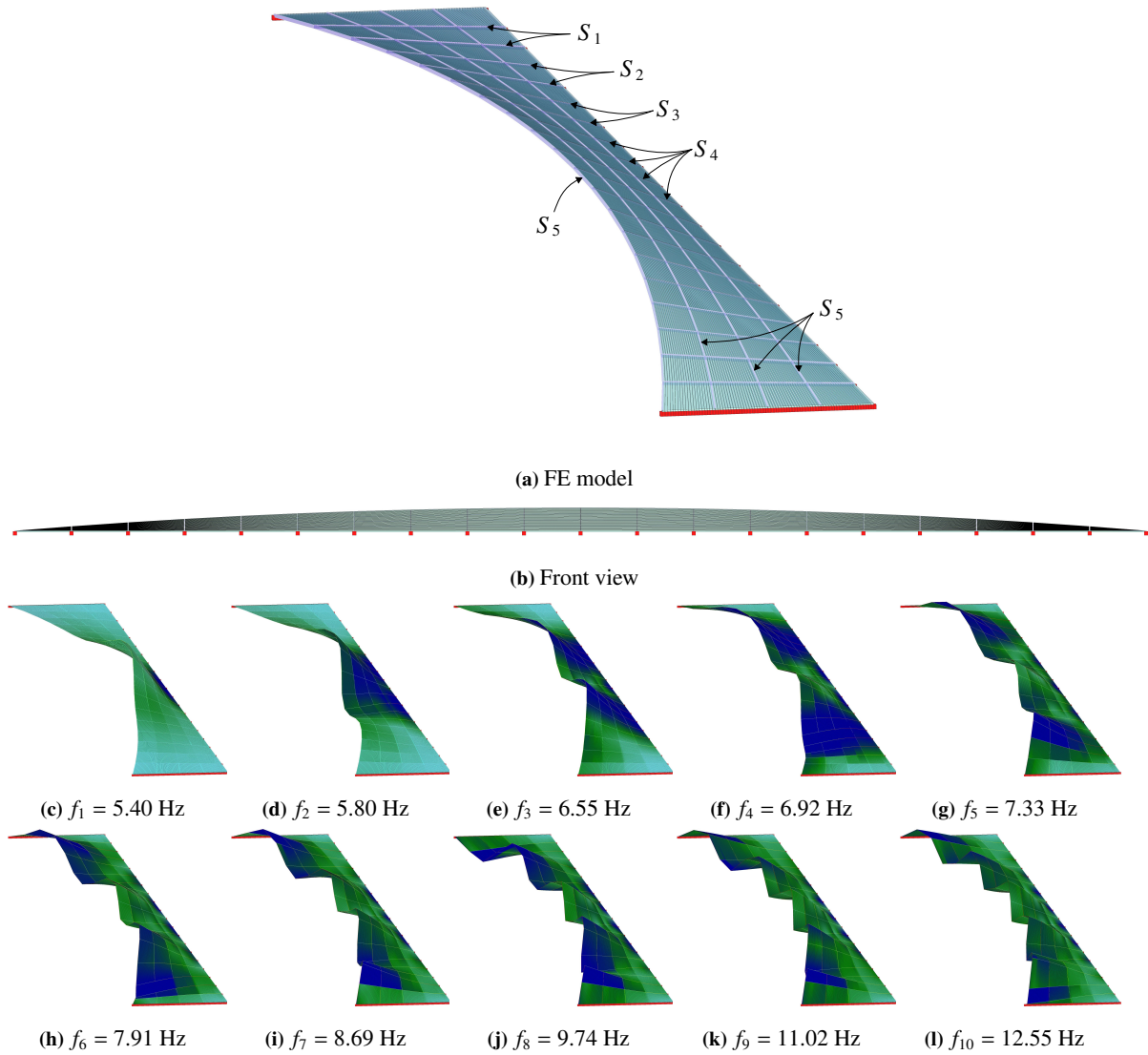


Figure 5.57: The FE model of the cantilever curved roof: (a) the thin roof is modelled by flexible membrane which is supported by a steel frame of different types of rectangular sections. Here, $S_1 = 3.5 \text{ cm} \times 1.5 \text{ cm}$, $S_2 = 2.5 \text{ cm} \times 1.5 \text{ cm}$, $S_3 = 2 \text{ cm} \times 1.5 \text{ cm}$, $S_4 = 1.5 \text{ cm} \times 1.5 \text{ cm}$, and $S_5 = 3 \text{ cm} \times 1.5 \text{ cm}$, (b) front view, (c-l) natural vibration modes and frequencies.

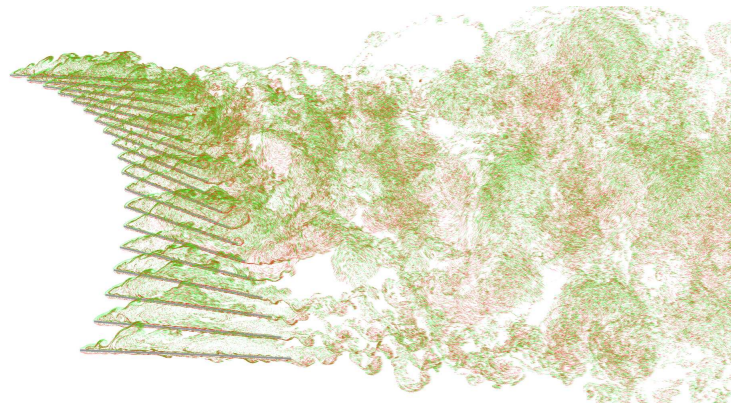


Figure 5.58: Instantaneous particle map of pseudo-3D roof system under laminar flow of 30 m/s.

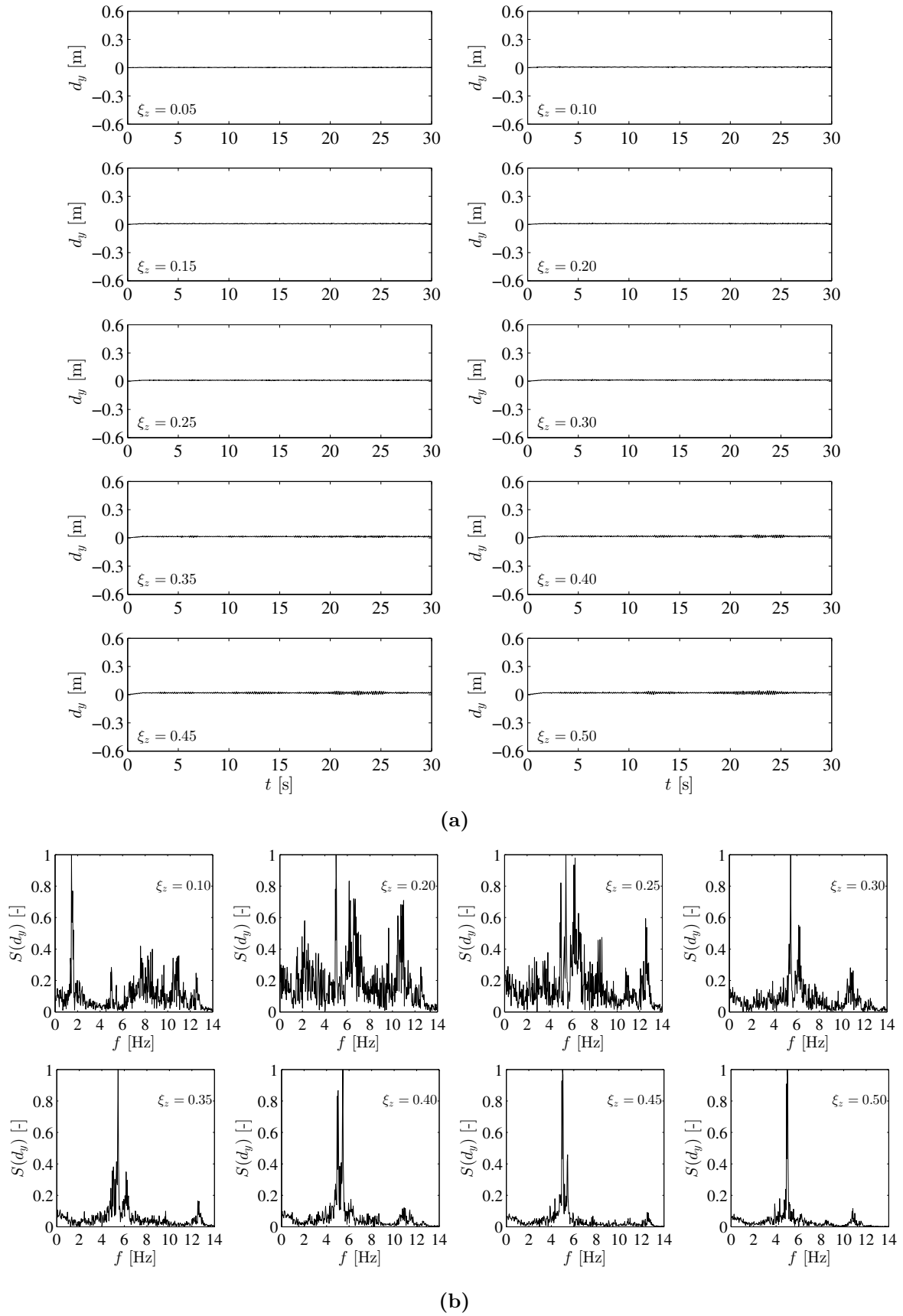


Figure 5.59: The pseudo-3D coupled simulation of the membrane roof: (a) the time histories of tip displacement at different slices of the roof under wind speed of 30 m/s, (b) the frequencies of tip responses at different slices.

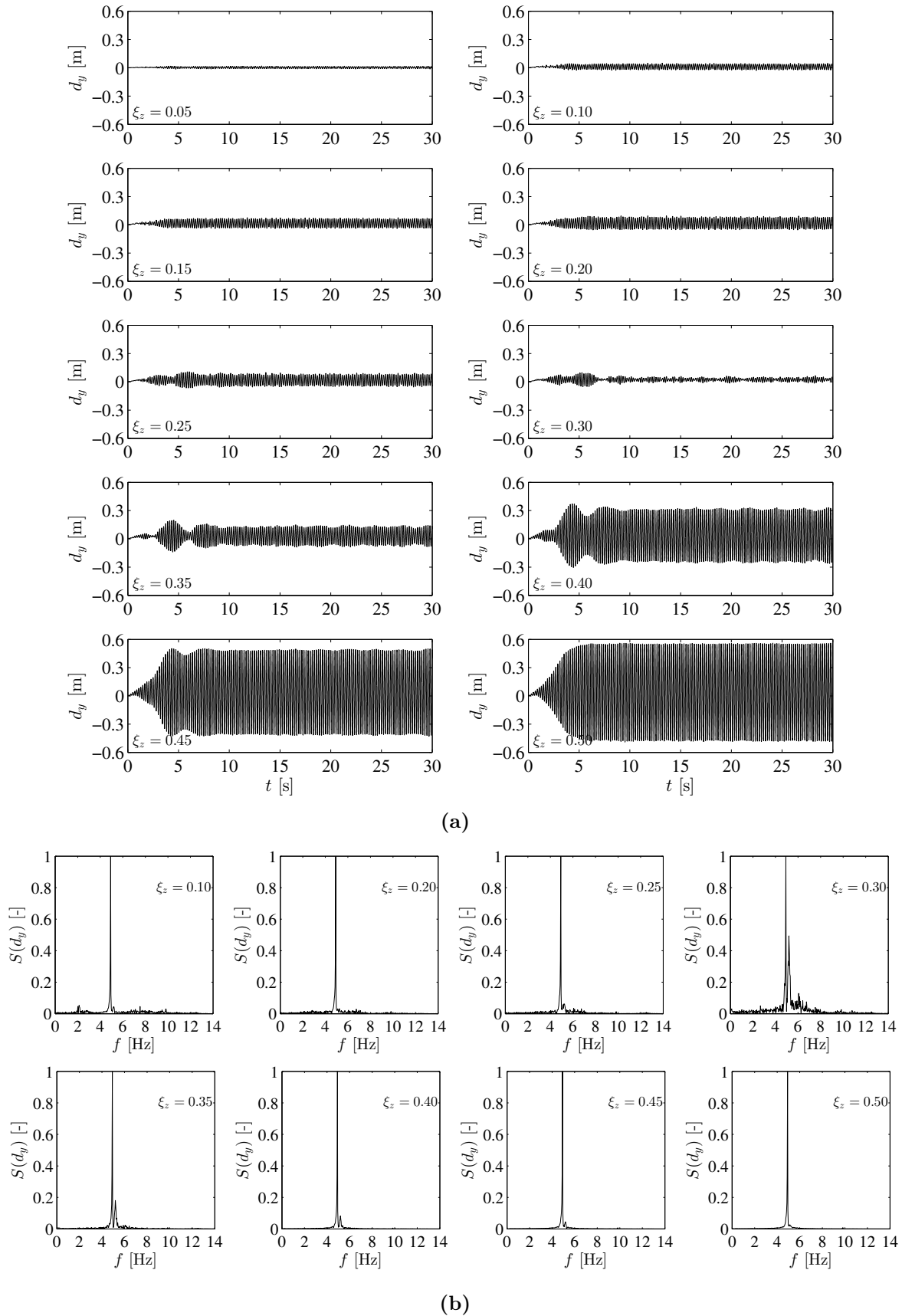


Figure 5.60: The pseudo-3D coupled simulation of the membrane roof: (a) the time histories of tip displacement at different slices of the roof under wind speed of 40 m/s, (b) the frequencies of tip responses at different slices.

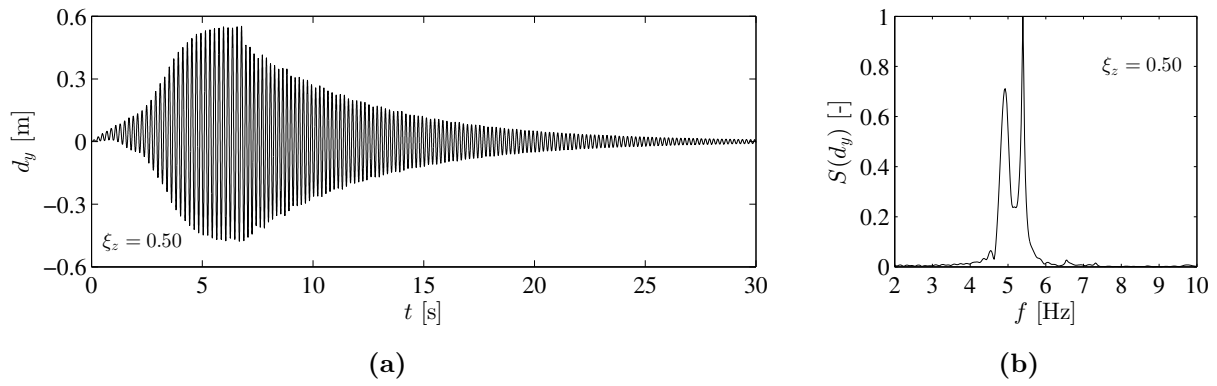


Figure 5.61: The free vibration analysis of the roof after the imitation of LCO at 40 m/s: (a) the time histories of tip displacement, and (b) the frequencies of tip responses at the mid-slice ($\xi_z = 0.50$) only.

took only around 16 hours and 20 hours, respectively. As for future scope, the interest exists to study the influence of bluff vertical plate at the tip of the roof on aeroelastic response. The influence of incoming turbulence can be considered also of particular study interest.

5.9 Pseudo-3D aeroelastic analysis of solar chimney

5.9.1 The solar chimney power plants

The demand for energy has been increasing day by day with the increase in population and industrial development. The fossil energy sources such as petroleum, coal, and natural gas are commonly used for energy consumption. The overexploitation of the mentioned energy sources has grown the global CO₂ emissions significantly. It has led to the global greenhouse effect, environmental pollution, increase of human diseases, altogether the deterioration of living conditions [169].

Various technologies concerning energy saving and renewable energy utilization are continually being reported. Solar chimney power plant (SCPP) provides technology for generation of solar-based electrical energy in the deserts and showing the potential to overcome the deficiencies of existing renewable energy technologies [113]. SCPPs are the most sustainable natural resources for electric power generation. They are entirely free of CO₂ emissions during the service since the solar radiation is used as fuel [241].

The SCPP is an energy form which combines the two most known types of alternative energies, wind and solar, into one single electric power generator [99]. It transforms solar radiation into heat, heat into wind and wind into electricity. A schematic of the SCPP is shown in Fig. 5.62. It combines three components: the collector area (CA), the power conversion unit (PCU) which includes one or several turbines with coupled generators, and the solar chimney (SC) at the centre of the collector. The airflow is produced inside the collector due to the buoyancy that results from the greenhouse effect. The air flows through the chimney and across the turbine, the kinetic energy of the air turns the turbine blades which in turn drive the generator.

The SCPP was first proposed in 1903 by the Spanish engineer Cabanyes [46], and further described in [111]. Professor J. Schlaich of Stuttgart later on in 1978 proposed on the issue again, and took the initiative of constructing a prototype SCPP in Manzanares/Spain, with

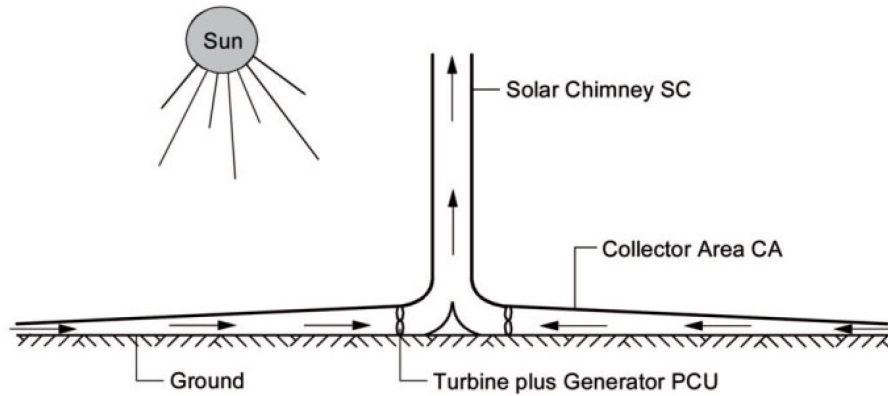


Figure 5.62: Schematic solar chimney power plant (picture courtesy: Von Backström et al. [241]).

a 200 m high SC and a maximum power output of 50 kW. Some further studies on this power plant can be found in [205, 206]. The description, basic mechanisms of fluid flow, heat transfer, power output, energy storage, and operation procedure of the turbine can be found in [169, 264]. Unlike conventional power stations, they do not have any adverse effect on the environment. In fact, it was reported in [265] that a commercial solar chimney power plant increases the chance of rainfall, especially for low-humidity air in the desert region.

5.9.2 Loads on solar chimneys and stability concerns

The solar chimneys are incredibly high, enlarged, over-dimensioned cooling tower shells. Load-response behaviour is very complex and can be governed by several key factors. Von Backström et al. [241] summarises the well-known problems to cooling tower designers from many years of experience with such shell structures such as high compression stresses under dead weight, wind action, temperature, shell buckling, wind-induced dynamic instabilities, soil-structure interaction, the fatigue of concrete, durability problems. Therefore, the structural design of a solar chimney is an optimisation process to compromise between several of these conflicting key points. Fig. 5.63 shows a series of such solar chimneys for SCPPs of different power capacity, pointing out its relationship to natural draft cooling towers. It emphasises the enormous differences in size, but also the similarities of optimally designed SCs in structural shape, compared to the world largest cooling tower in Niederaussem [45]. The details of 1000 m solar chimney are shown in Fig. 5.64.

Wind effects together with dead load dominate the design of solar chimney. Important to note that the power output and conversion efficiency of SCPP increase with a larger-scale power plant. However, with the increase of height, this thin-walled circular system become vulnerable to wind-induced vibrations. Wind attacks the chimney first statically, considered as constant in time, which is caused by the mean wind speed. Secondly, a broad-banded dynamic loading originates from wind turbulence. Thirdly, vortex-shedding induces on both sides of the chimney a narrow-banded dynamic excitation. All these loadings are well investigated in theory and in experiments for the lower parts of the atmospheric boundary layer (ABL). At tower heights, depending on the required Power plant capacity between 500 m and 1500 m, the scope of wind load standards is exceeded. Therefore, the existing code regulations need to be redeveloped mainly with regard to the characteristics of wind flow at high altitude, the resonance vibrations under gust or vortex excitation, the minimization of shell stresses.

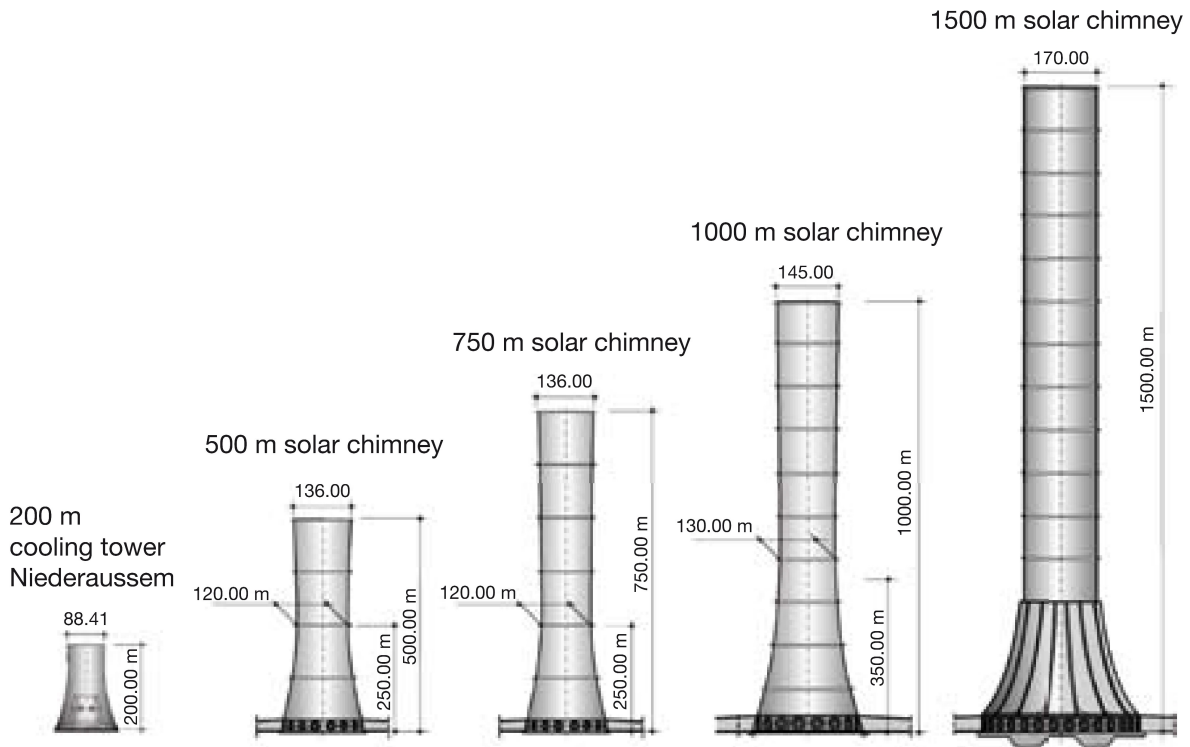


Figure 5.63: Variants of solar chimneys of different height (picture courtesy: Von Backström et al. [241]).

The use of ring stiffeners in SC allows the cross sections from shell-like deformations to beam-like ones. They increase the buckling stiffness of the chimney. A slight increase in stiffness by spokes removes the buckling vibration modes, and increases the buckling safety of the entire structure. It was discussed in Von Backström et al. [241] that the solar chimneys up to 500 m of height can clearly be executed without any ring stiffeners, however with disadvantages of stability issues and the maximum stresses. Chimneys of greater height require the application of strong ring stiffeners with or without internal spokes, such as shown in Fig. 5.64 for 1000 m tall SC. This is to ensure stability, stress safety and for economical reasons. Within the scope of this thesis, the vortex-induced vibration of the SC is of interest. The wind-structure interaction has been the main concern since it is one of the main component of reliable SC design. An extremely tall solar chimney which is 1500 m (see Fig. 5.63) is considered for aeroelastic response analysis using the newly proposed pseudo-3D multi-slice FSI model. Though the section details for 1500 m SC is not available, the dimensions are assumed based on the section details of 1000 m SC.

5.9.3 Analyses of aeroelastic response of 1500 m solar chimneys

In the following, the aeroelastic coupled responses of 1500 m SCs are analysed using the presented and validated pseudo-3D multi-slice VPM solver. In [113], it was discussed that the smallest critical wind speeds at which vortex resonance arises for SCs up to 1000 m (see Fig. 5.63) are far above the actual expected wind speed. The cause is the sufficiently high natural frequency. The third tower with 1500 m does not have sufficient natural frequency, and furthermore, it reaches in heights, in which larger speeds occur: vortex resonance can not be excluded any more. Therefore, the aeroelastic responses of the 1500 m is considered here VIV analyses.

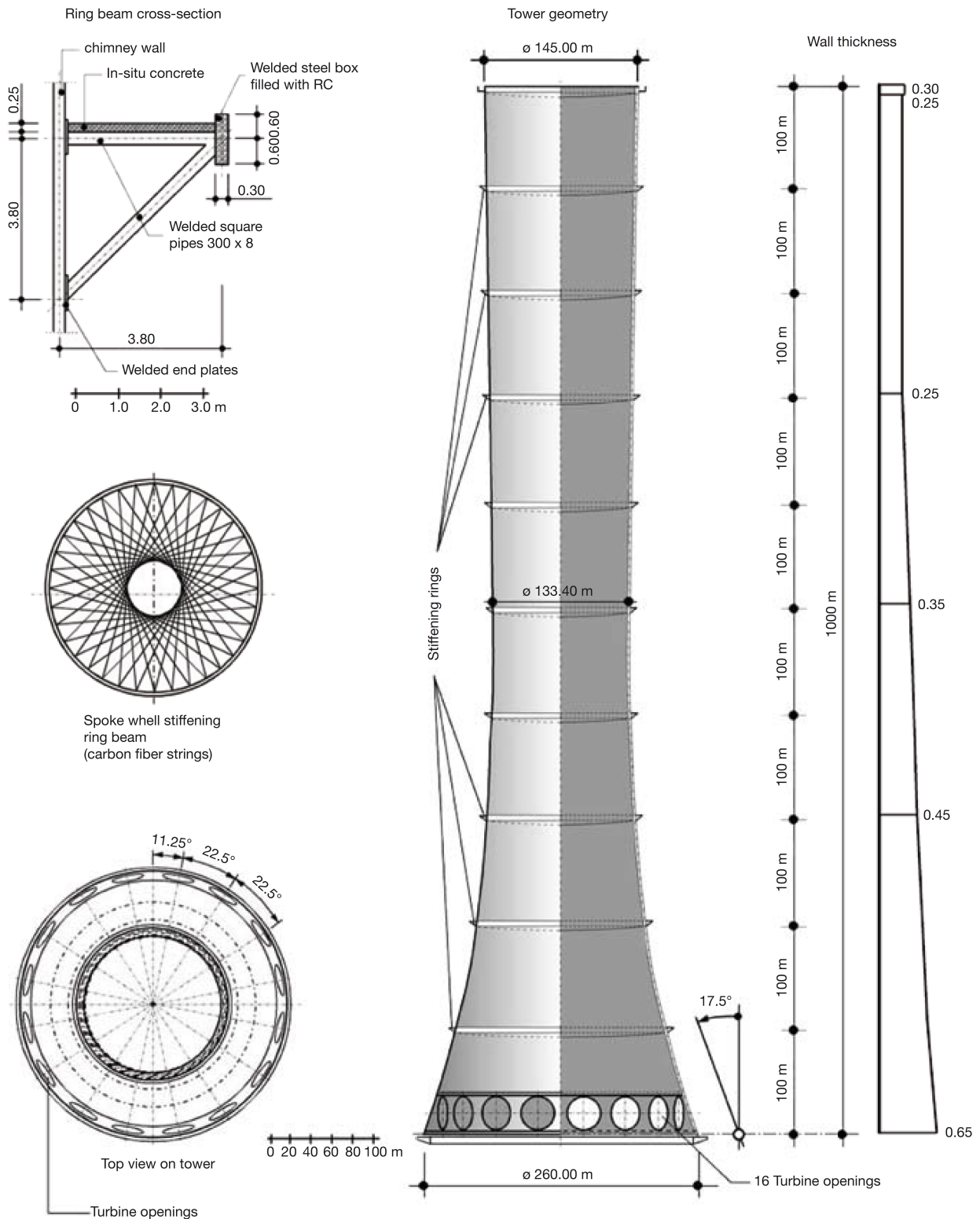


Figure 5.64: Details of a 1000 m solar chimney (picture courtesy: Von Backström et al. [241]).

Structural models of SC

The buckling stability of cylindrical shell structures, such as cooling towers, concerning the installation of intermediate ring stiffeners, was discussed in [113]. The installation of rings create nodal lines in the shell and increase the critical failure factor. The lowest natural

frequency of 500 m, 1000 m and 1500 m SC with ring stiffeners were mentioned to be 0.52 Hz, 0.18 Hz, and 0.08/0.10 Hz, respectively.

In this study, the physical dimensions of the 1500 m SC are considered based on the dimensions mentioned in Fig. 5.63. The diameter of the topmost plane is 170 m. The section details of 1500 m SC is not available, and therefore, the cross-section dimensions are assumed based on the details available for 1000 m SC in Fig. 5.64.

The intention of this study is limited to the aeroelastic analysis of VIV response. Two different structural configurations are considered for 1500 m SC:

- the basic SC with concrete shells only,
- the use of prestressing tendon (PT) at an interval of 150 m height as ring stiffener.

The finite element models for both systems are presented in Fig. 5.65. The concrete shells are modelled using 4000 shell elements (200×20). The PT steel is modelled using beam elements of circular cross-section (diameter = 55 mm). There are 200 PT beams, at each considered level (Fig. 5.65(right)), are considered to be connected from the perimeter shell nodes to the centre point of the plane. The tension force of 20 kN is applied at each PT beams. The diameter and thickness of the RC shell are summarized in Table 5.19 for a different level of the SC.

Position	Distance	Radius (R)	Thickness
Ground level	0–75 m	145–125 m	1.3 m
Intermediate level	75–150 m	125–105 m	1.21 m
Intermediate level	150–225 m	105–93 m	1.12 m
Intermediate level	225–300 m	93–85 m	1.06 m
Top level	300–1500 m	85–85 m	1.0–0.5 m

Table 5.19: The physical dimensions of 1500 m solar chimney

It is important to note that the SC with PT stiffener is modelled first by targeting the first natural frequency of 0.08 Hz, as a fact of validation. Once the lowest natural frequency is matched, the PT stiffeners are removed to model the chimney with RC shell only.

Aeroelastic coupled analysis of 1500 m chimney without stiffeners

In the following, the aeroelastic coupled simulation of the basic 1500 m SC, which is without any ring stiffeners, are performed under different wind speeds. The mean wind velocity profile along the height of the tall chimney is varying. However, for simplicity, the wind speed profile is considered uniform throughout the height. Since the diameter of the chimney is same for the major portion (300 m–1500 m), the consideration of uniform wind speed is the most critical scenario for VIV response. The study can be considered as a preliminary investigation to display the applicability of the pseudo-3D VPM. The natural vibration modes and corresponding frequencies are summarized in Fig. 5.66. Most of the dominant vibration modes are of the buckling of concrete shells.

The multi-slice aeroelastic coupled simulation of the solar chimney (without stiffeners) is performed using 21 slices. The numerical parameters are summarized in Table 5.20. The effective width of the slices are 75 m except 37.5 m at the ends.

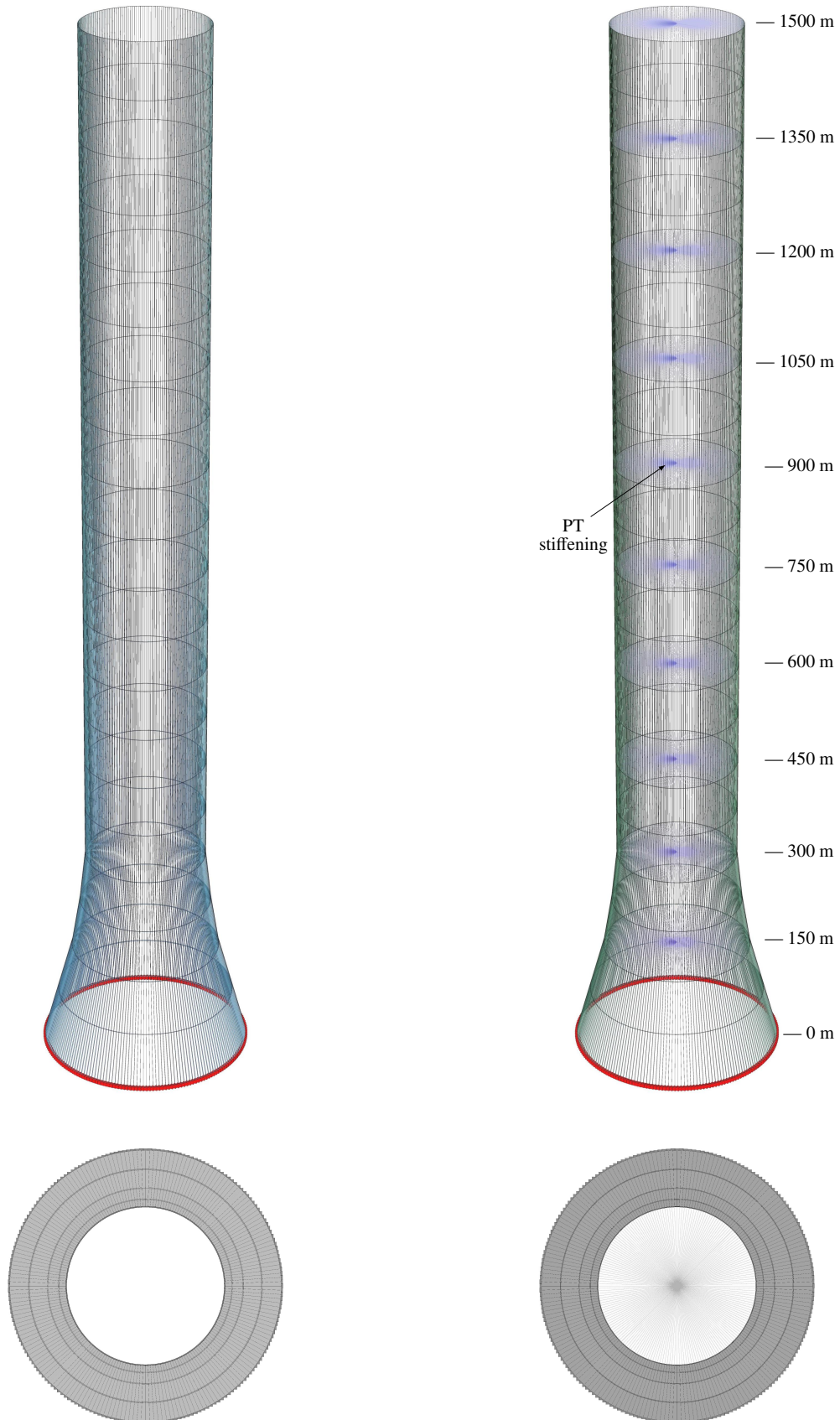


Figure 5.65: The finite element modelling of 1500 m tall solar chimneys with 3D and top views: (left) the system without any stiffening, (right) the stiffening of the system using prestressing tendons (PT).

It is difficult here to calculate the resonance VIV wind speed for this SC since the lowest vibration mode is of shell buckling. The buckling of the circular shell should change the vortex shedding pattern. However, in order to make an initial guess, considering that the

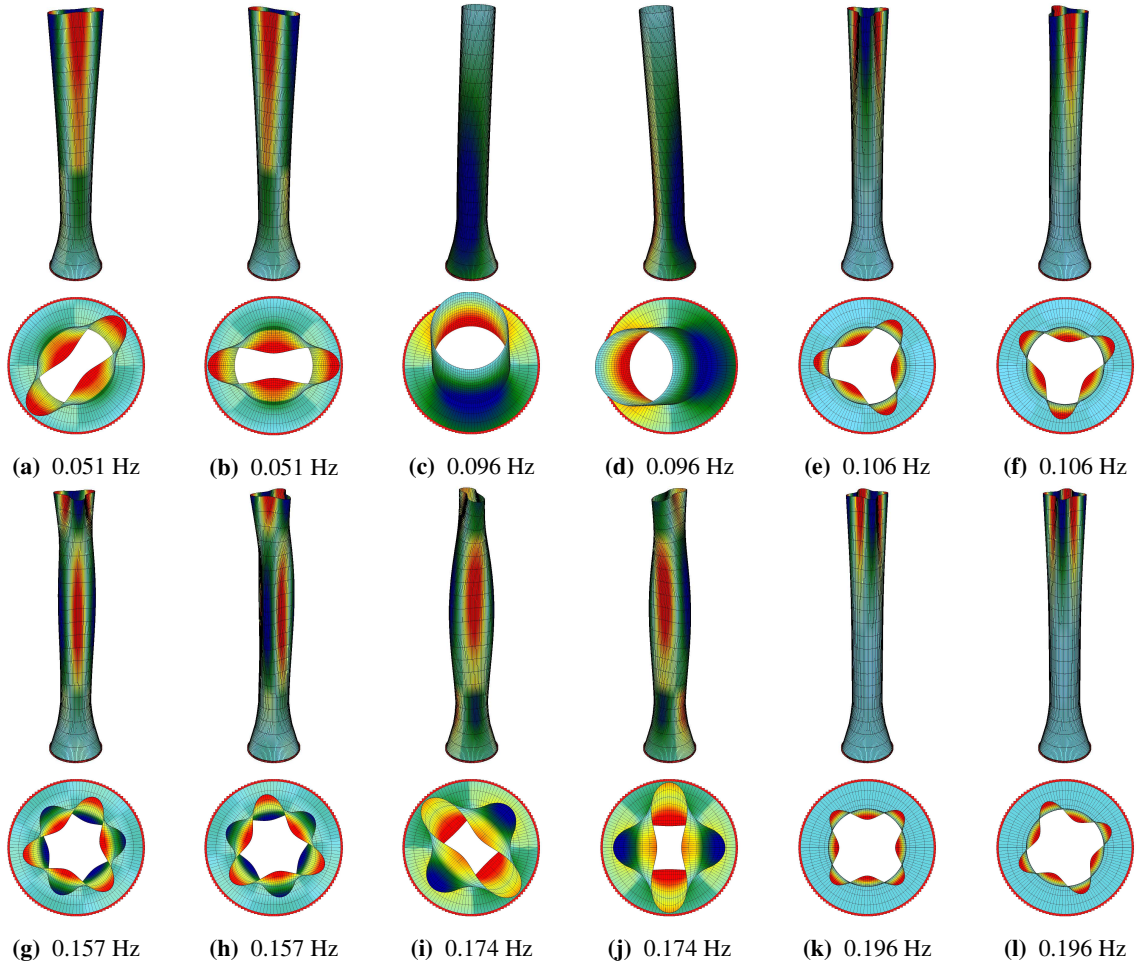


Figure 5.66: Analysis of the finite element model of 1500 m tall solar chimney (hollow configuration): the natural vibration modes and frequencies are shown in (a)-(l).

Solver	Numerical parameters	Symbol	Value
Flow	Free stream flows	U_∞	10–50 m/s
	Number of simulation slice	N_{slice}	21
	Length of the domain in slice	l_d	2000 m
	Width of the domain in slice	w_d	1000 m (approx.)
	Position of simulation slices	$\xi_{z_i} = Z_i/L$ ($i = 1, \dots, 21$)	0, 0.05, 0.1,,, 0.9, 0.95, 1
	Number of panel per slice	$N_{pan(slice)}$	200
	Non-dimensional time step	$\Delta t_f^* = \Delta t_f U_\infty / \Delta s_{slice(min)}$	2
	Poisson grid	$N_x \times N_y$	511 \times 255
	Number of particles (approx.)	$N_{particle}$	1,200,000 - 1,400,000
	Structure	Total number of shell element	N_{shell}
Number of peripheral shell			200
Number of shell along height			20
Number of vibration modes		Φ_{num}	12
Non-dimensional time step		$\Delta t_s^* = \Delta t_s U_\infty / \Delta s_{slice(min)}$	2

Table 5.20: Numerical parameters for aeroelastic response analyses of 1500 m tall solar chimneys.

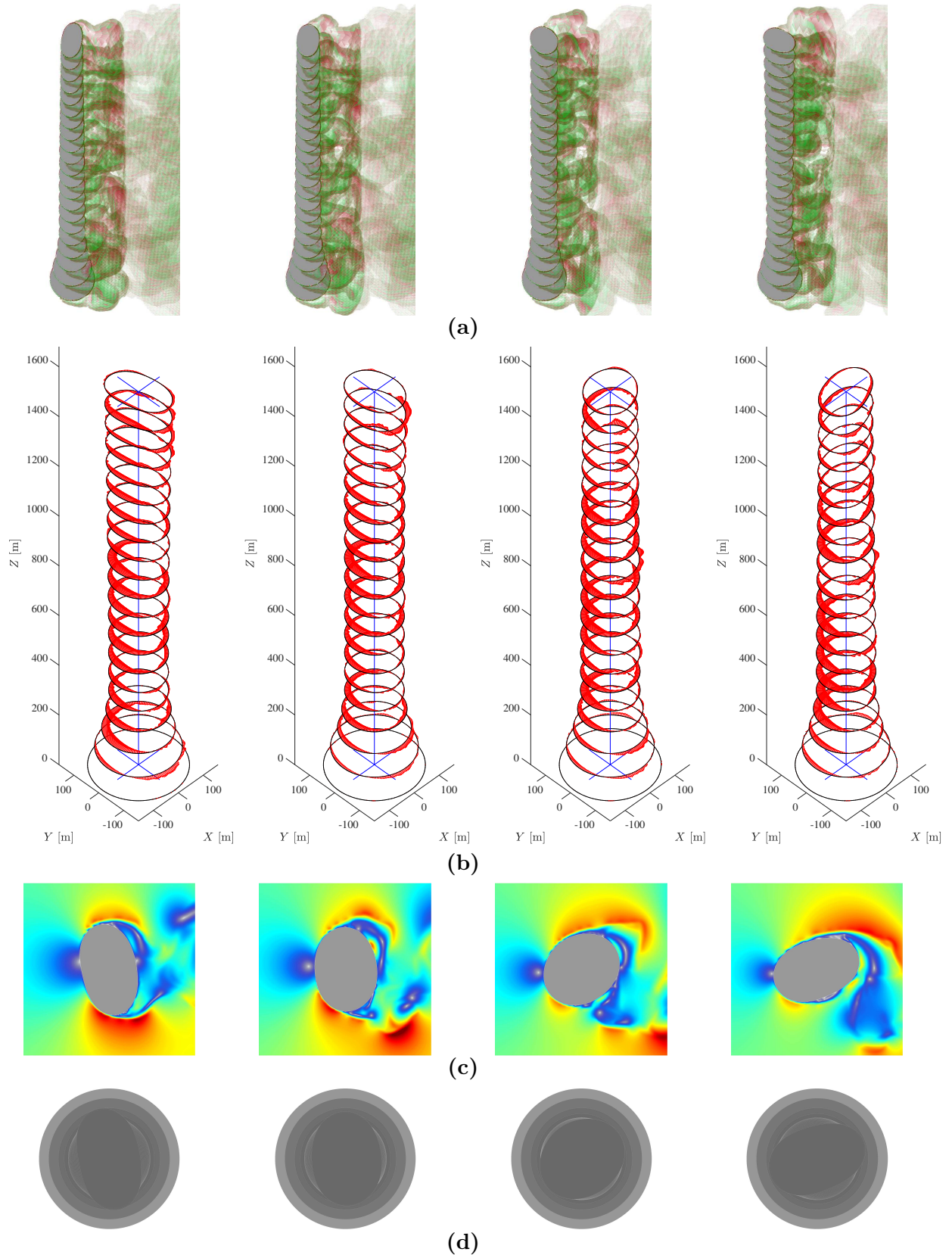


Figure 5.67: Pseudo-3D aeroelastic analysis of 1500 m tall solar chimney (hollow configuration) under the wind speed of 30 m/s: (a) instantaneous particle map, (b) slice-wise shell deformation and the distributed wind loads, (c) instantaneous velocity field around the top most slice, (d) instantaneous top view.

buckling response is very low as if shell is not deformed. An approximate resonance wind speed based on $\mathcal{S}t = 0.2$ and $f_n = 0.051$ Hz is calculated 43.35 m/s (c.f. Eq. (2.7)).

The multi-slice simulation of the chimney is performed under different wind speeds starting from 10 m/s. The outcome of the simulation for 30 m/s is displayed in Fig. 5.67. It is observed that the concrete shells experience significant amount of buckling at 30 m/s, which is lower than the estimated critical resonance wind speed.

The displacement of four nodes ($p_1 \dots p_4$) at the top slice are monitored to understand the buckling pattern of the chimney. The relative displacement along the X and Y axis are calculated and plotted in Fig. 5.68 under different wind speeds to understand the development of buckling motion. The relative displacement at the top slice at 20 m/s has almost reached up to 5 % of the diameter (170 m), which is quite large for such low wind speed.

The vibration of the chimney under wind speed 30 m/s is already quite large and therefore the responses under the wind speed 42 m/s or above are not presented. This model is not able to capture the nonlinear post-buckling response accurately. However, the fact is that for such an important large and tall structures, they are expected to behave linear.

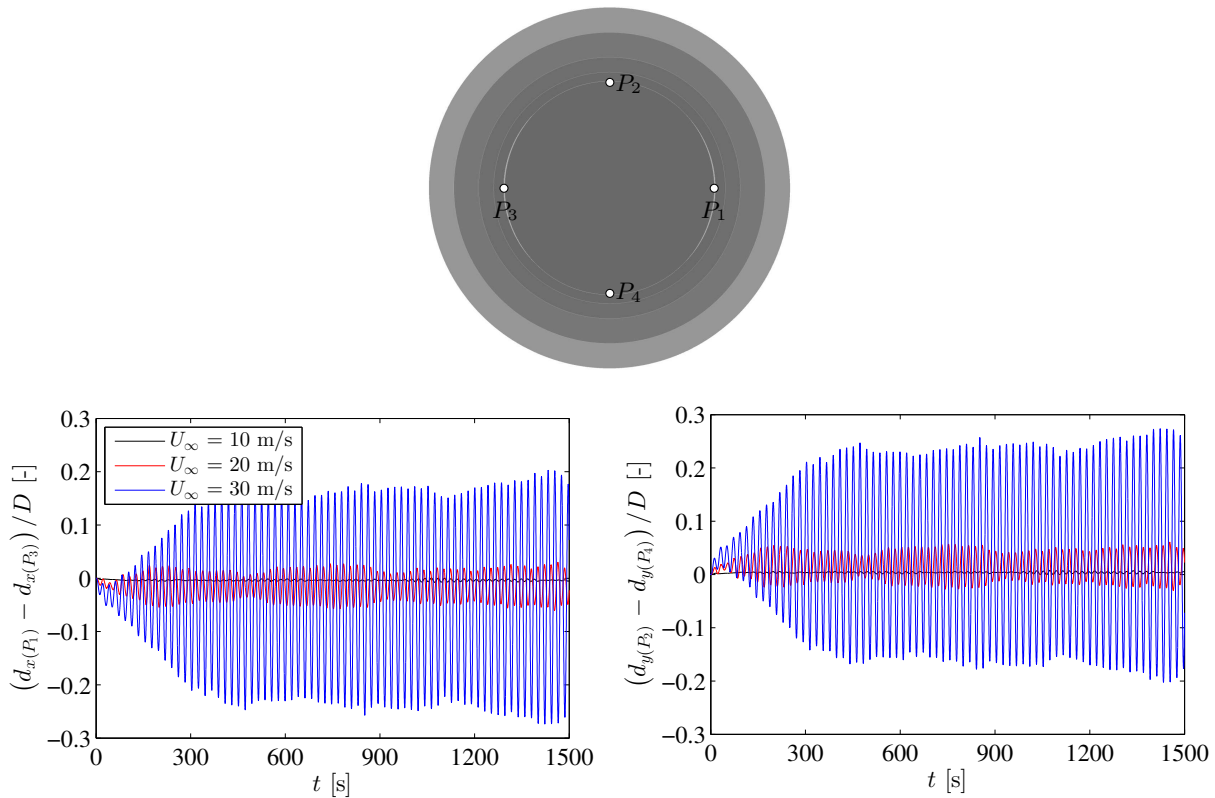


Figure 5.68: Comparison of relative horizontal and vertical displacements at the top slice considering the monitored nodes (top): (left) the normalized horizontal relative displacements, whereas in (right) vertical relative displacements.

Analysis of VIV response of 1500 m chimney with the stiffeners

In this section, the solar chimney, which is structurally improved by using PT stiffeners at regular interval (Fig. 5.65(right)), is considered for analysis of VIV response. The studies are performed similarly like the previous section. The numerical parameters are considered same as mentioned before in Table 5.20 and in relevant further discussions in Sec. 5.9.3. The

only difference is the use of 8 natural vibration modes from the FE model of stiffened SC, as shown in Fig. 5.69. The dominant vibration modes are like cantilever modes. Some higher modes show some buckling behaviour.

Here, the lowest vibration mode is without the shell buckling, like an bending mode of a vertical cantilever beam. It is therefore easy to approximate the resonance wind speed considering the diameter of the chimney at the top surface. An approximate calculation of the resonance wind speed based on $St = 0.2$ and $f_n = 0.08$ Hz is calculated 68 m/s.

The fully coupled aeroelastic analysis of the system is performed under 70 m/s, and the time histories of the horizontal and vertical displacement of four points (p_1, \dots, p_4) at the top slice are presented in Fig. 5.70. There is almost no differential displacement in between the points. The response resembles the bending of a vertical cantilever. The peak response along the flow direction is observed 12.3 m (0.82% of 1500 m) with a mean value of 4.9 m (0.33% of 1500 m).

The cross-wind response has been significantly larger with a peak value of 50.2 m (3.35% of 1500 m). This is a resonance phenomenon, and specifically, due to the vortex-induced from the circular sections. The motion of all the slices and acting uniformly distributed wind loads are shown in Fig. 5.71.

The system has been simulated under various wind speeds to understand the coupled motion

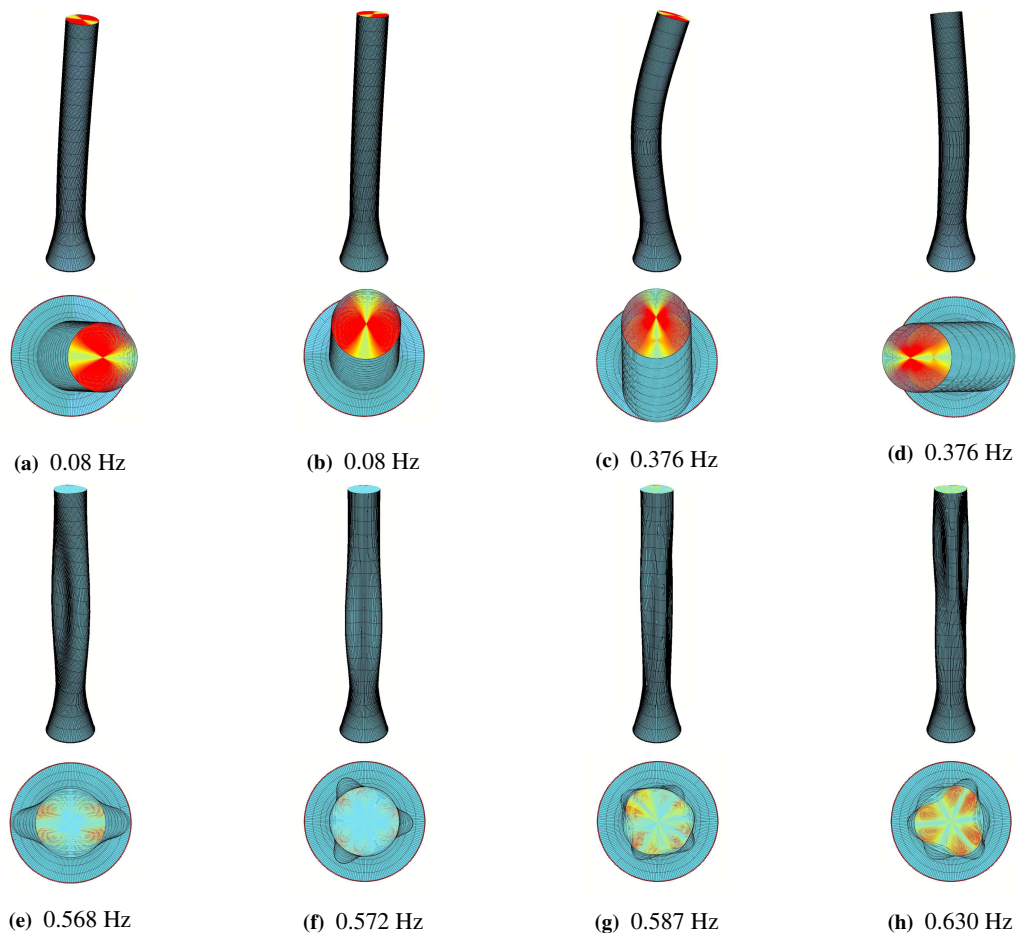


Figure 5.69: Analysis of the finite element model of 1500 m tall solar chimney (with PT tendon at regular interval): the natural vibration modes and frequencies are shown in (a)-(f).

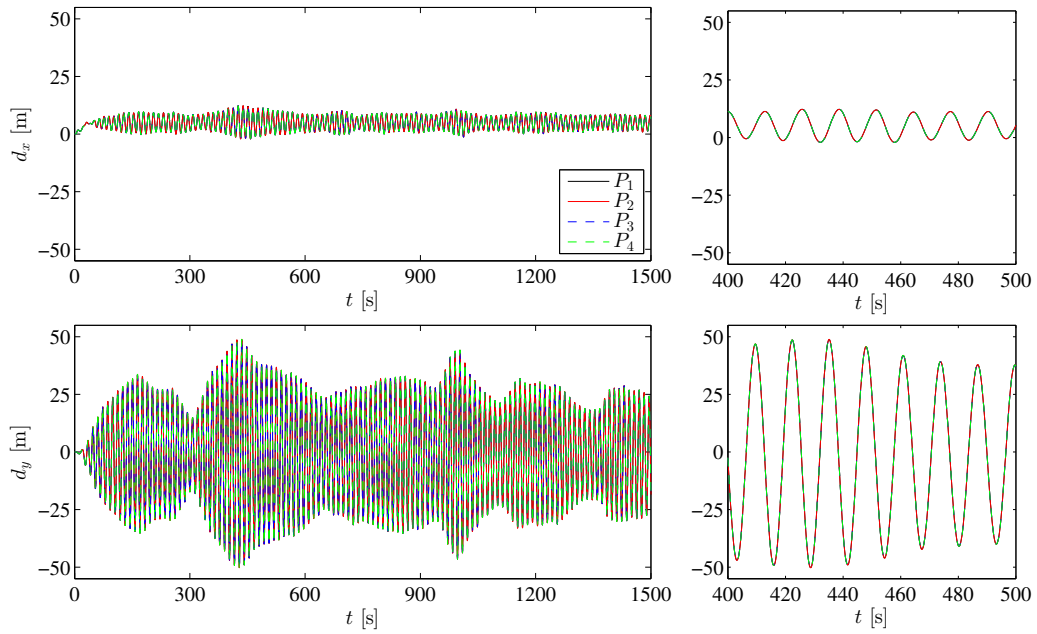


Figure 5.70: Aeroelastic response of a 1500 m tall solar chimney at wind speed of 70 m/s (stiffened SC): the time histories of horizontal (d_x) and vertical displacements (d_y) at 4 monitored points at the top plane of the tower (left), closed view of the plots (right).

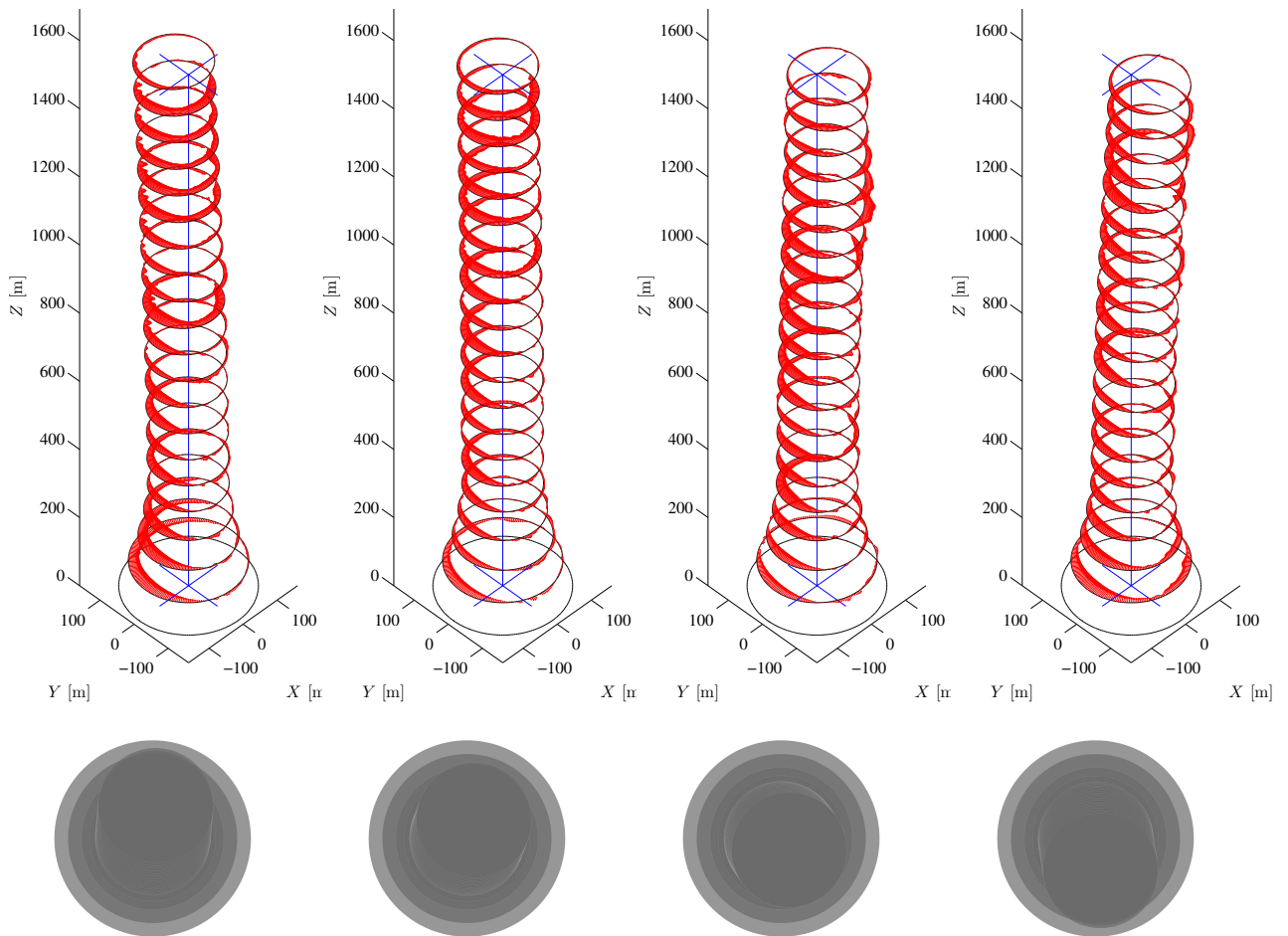


Figure 5.71: The aeroelastic response of 1500 m tall solar chimney under the wind speed of 70 m/s.

of the system before and after the resonance limit, and the comparison of the responses are shown in Fig. 5.72. Here, the nodal responses are compared only for p_2 since there has been little variation in response in the monitored points. It is observed that the system response is significantly large under wind speeds 70–80 m/s. Above these wind speeds, the along wind responses increase due to the increase in drag force; however, the cross-wind responses

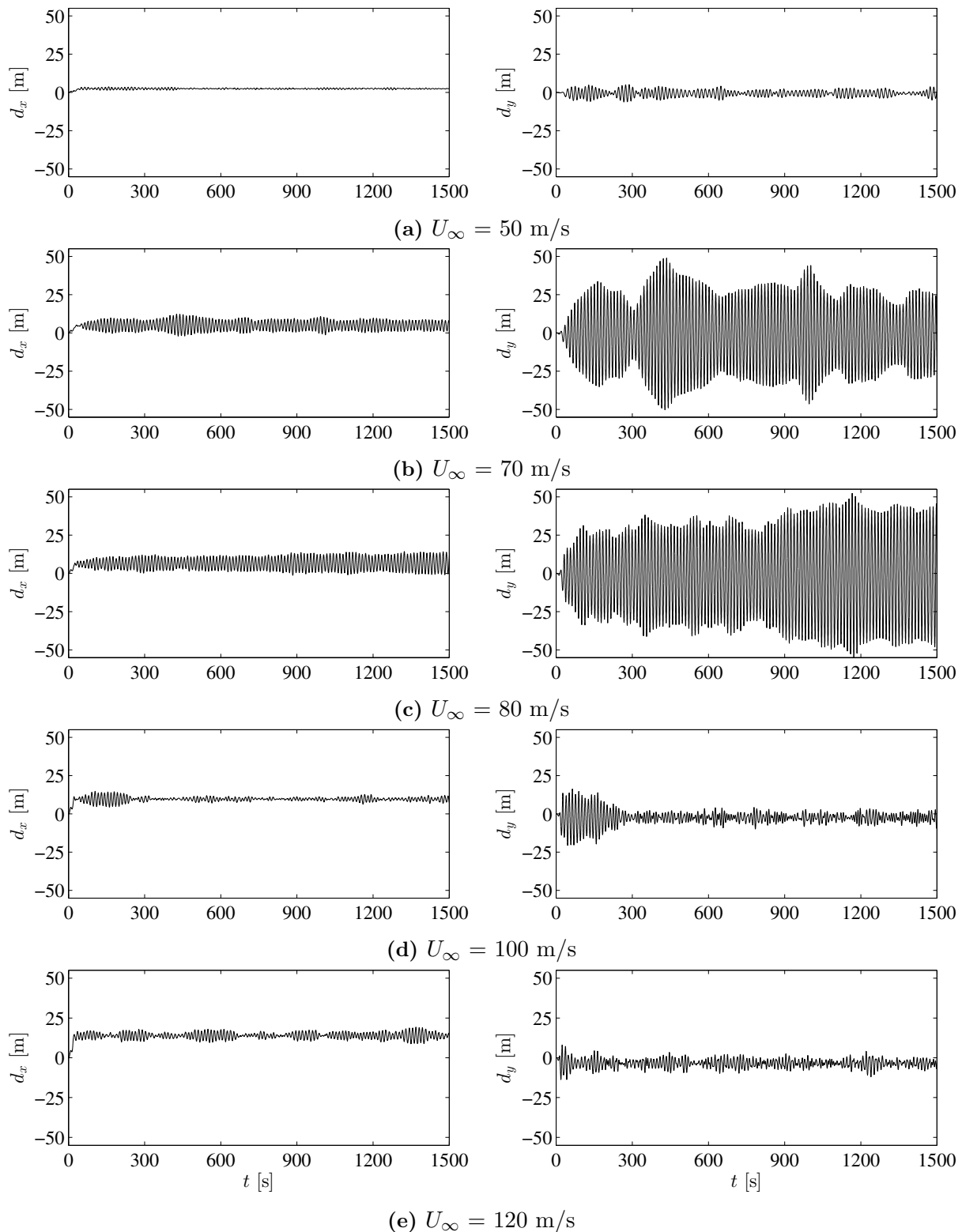


Figure 5.72: Aeroelastic analyses of 1500 m solar chimney at different wind speeds: comparison of horizontal and vertical response time histories at monitored point p_2 of top slice.

are reduced significantly since the forcing frequencies have been out of the resonance limit. Finally, the presented pseudo-3D VPM model shows its ability to handle aeroelastic coupled response of such large-scale mega structures.

5.10 Summary

This chapter has presented numerical analyses of several benchmark fluid–structure interaction (FSI) problems in the context of validating developed 2D and pseudo-3D extensions of VPM. The validated solvers have been utilised for analysing several FSI problems from the application point of view. It has been mentioned earlier that the 2D extension has been a coupling between 2D VPM with corotational finite element formulation to handle geometric nonlinearity of large-displacement FSI problems. On the other hand, the pseudo-3D VPM has been coupled with a linear structure model for small-displacement FSI problems.

The extended 2D coupled VPM is validated on benchmark large-displacement FSI problems such as the flapping of cantilever plates in axial flow and Kármán vortex street. The validated solver has been used further to investigate the large-amplitude aeroelastic interactions of several flexible cantilever plates. The changes in aeroelastic behaviour and flapping pattern of inverted and T-shaped cantilevers with/without tip mass has been investigated. The simulations are performed for increasing wind speeds until the permanent deflection mode occurs. The response amplitudes and oscillating frequencies have been compared. The reference and the T-shaped inverted cantilevers without tip mass have undergone VIV and shown large amplitude vibrations. The inverted cantilever with tip mass has exhibited stability in axial flow, and the large amplitude flapping has only been observed at very high wind speed. However, the same system with a mass-less vertical plate at the cantilever tip, i.e., T-shaped inverted cantilever with a tip mass, is susceptible to rotational flutter, as mentioned earlier. The T-shaped cantilever with tip mass vibrates mostly with the first natural frequency of the system whereas the reference cantilevers with the frequency of vortex shedding which has been much lower than the first natural frequency of the system. However, the inverted cantilevers, when the wind speed is much lower than the critical one, vibrate with their first natural frequency, since the no influences occur due to vortex shedding. A drop of response frequency has been observed in the case of the T-shaped cantilever as the wind speed increases. It has been discussed due to the geometric nonlinearity and negative aerodynamic stiffness. The flow around a rigid building with a flexible membrane roof has been analysed. The coupled behaviour of the membrane with the prestressing effects of gravity load is well modelled when compared to a reference study. The FSI model shows that it has the potential of modelling partially flexible system.

The new extension of pseudo-3D multi-slice VPM has been validated based on the identification of onset wind speed for the large-amplitude flapping of cantilever plates in axial flow and Kármán vortex street. Furthermore, the validated model has been employed for the analyses of VIV response of both-end clamped long circular pipe (42 m). The lock-in region is modelled using two coupled models: a single degree of freedom model based on rigid body and the proposed flexible multi-slice model. The method has been able to predict the ovaling oscillation of thin-walled circular shells. The solver has been applied further to simulate the aeroelastic coupled response of a large membrane roof and extremely tall solar chimneys. The studies have shown the efficiency and applicability of the pseudo-3D multi-slice VPM model for FSI analysis irrespective of the scale of shell structures.

Chapter 6

Aeroelastic energy harvesting

6.1 Introduction

In recent years, wireless sensor networks (WSNs) have gained increasing interest in structural health monitoring (SHM) due to rapid advancements in wireless technologies and low-power electronics. The speciality of WSNs is their ability to monitor structures and machines continuously without the need for associated installation costs of wiring. However, powering WSNs using the traditional limited-life batteries, which need regular replacement, can lead to substantial maintenance costs, particularly for extensive network systems. Due to continuous advancement, the power requirements of the sensors is in many cases in the range of a few milliwatts (mW). Therefore, the field of energy harvesting has experienced significant growth over the last few years due to the increasing demand of producing self-powered WSNs, micro-electromechanical systems (MEMS) technology, and portable low-power electronic devices with extended lifespans [3, 24, 36, 159].

Energy harvesting is the process of extracting energy from the surroundings of a system and converting it into usable electrical energy. A sustainable response of a mechanical system is desired for the generation of inexhaustible electric power to operate self-powered electronic devices. The aeroelastic interactions of several thin cantilever systems have been presented in the previous chapter (Chapter 5); some of them can be efficient sources of sustainable response.

This chapter presents the utilisation of the presented 2D coupled model of VPM in the context of performing aero-electromechanical coupled analysis. The suggested approach considers the damping effects of energy harvesters in a simplified manner. The proposed model is applied to analyse a flutter-based T-shaped electromagnetic energy harvester [186]. The prediction of the critical flutter wind speed and the energy output of the reference harvester for different electrical resistances are compared for validation of the method. The aim is to perform further comparative studies on different cantilever systems to understand aeroelastic interactions and to obtain guidelines for optimised design of experimental set-ups of prototype harvesters.

6.2 Vibration energy harvesting

6.2.1 Background

The vibration-based energy harvesters are typically inertial spring and mass systems. A very early phase review on vibration-based energy harvesting for wireless and self-powered microsystems was presented in Beeby et al. [36], Elvin et al. [93]. Piezoelectric and electromagnetic power conversions are the commonly used technique for energy harvesting. Piezoelectric generators use active materials with the ability to transform mechanical strain energy into electrical charge and, vice versa, to convert an applied electrical potential into the mechanical strain. Electromagnetic generators, on the other hand, employ electromagnetic induction arising from the relative motion between a magnetic flux gradient and a conductor. A schematic representation of the piezoelectric and electromagnetic energy harvesters is shown in Fig. 6.1. The power harvesting from vibration energy using piezoelectric materials was reviewed in Anton and Sodano [24], Daqaq et al. [68], Elahi et al. [88], Sodano et al. [220], Wei and Jing [250]. The applications of energy harvesting in commercial and residential buildings were presented in Matiko et al. [159].

6.2.2 Conversion mechanisms

Piezoelectric transduction

Piezoelectricity combines the electrical and mechanical behaviour of a material. Thus, the fundamental electrical and mechanical equations are combined to arrive at the constitutive equation. If the structural response of a slender piezo-beam (such as in Fig. 6.1 (a)) is modelled as a single degree of freedom (SDOF), two governing equations that include mechanical and electrical parts are:

$$m\ddot{y}_t + c\dot{y}_t + ky_t - \Theta V = f_y(t), \quad (6.1)$$

$$\Theta \dot{y}_t + C_p \dot{V} = -\frac{V}{R} = I, \quad (6.2)$$

where y_t is the tip deflection, V is the voltage, I is the current, $f_y(t)$ is the equivalent tip force, m is the mass, c is the damping coefficient, and k is the stiffness of the lumped mass model of the piezoelectric beam. Here, C_p is the piezoelectric capacitance and Θ is

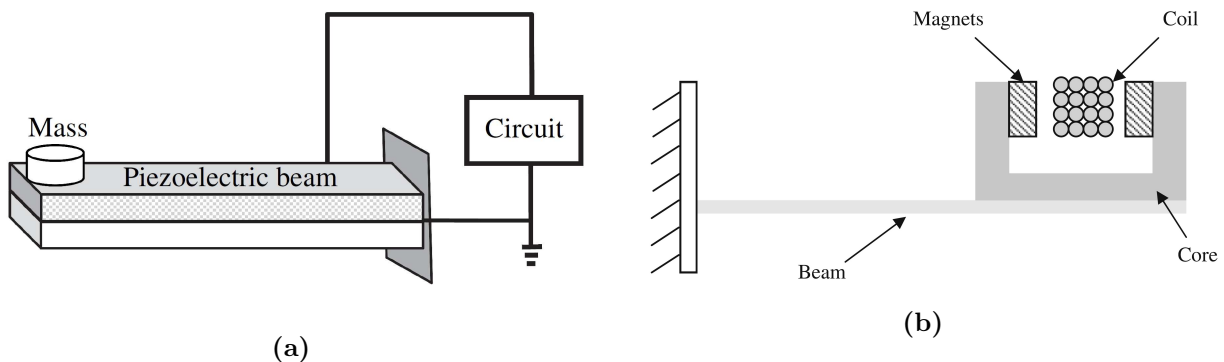


Figure 6.1: Schematic representation of the energy harvesting: (a) piezoelectric harvester [93], and (b) electromagnetic generator [87].

the electromechanical coupling coefficient of the piezoelectric beam. Eqs. (6.1) and (6.2) are known as the actuator and sensor equations, respectively. The power can be converted to power as V^2/R_L from the applied external electrical load resistance, R_L . The electrical energy E_p generated in a time interval can be expressed as follows

$$E_p = \int_0^t V I dt. \quad (6.3)$$

Electromagnetic induction

The conversion of kinetic or vibration energy into electricity using electromagnetic induction exploits the well-known Faraday's fundamental principle of electromagnetism. The relative movement between magnet and coil results in a varying amount of magnetic flux cutting through the coil which induces the voltage or electromotive force in a circuit [92]. According to Faraday's law of induction, the open-circuit voltage V_{oc} can be expressed as follows

$$V_{oc} = \oint_{l_{coil}} (v \times \beta) dl = Nl\beta v, \quad (6.4)$$

where β is the magnetic flux density at each coil segment, dl is the vector of each segment of the coil, l_{coil} is the total length of the coil, v is the relative velocity between the centre of the coil and the magnet, N is the number of coil turns. In general, $Nl\beta = \beta_{avg}l_{coil}$ is defined as electromagnetic coupling coefficient, in which β_{avg} is the average flux density across the coil range. The Voltage across the load resistance, V_L , can be calculated using the voltage divider rule as follows [131, 132]

$$V_L = V_{oc} \frac{R_L}{R_L + R_C}, \quad (6.5)$$

where R_L and R_C are the load resistance and coil resistance, respectively. The electrically generated damping C_e can be expressed as follows

$$C_e = \frac{(Nl\beta)^2}{R_L + R_C}, \quad (6.6)$$

where the influence of coil inductance is ignored. The use of Eq. (6.6) for the calculation of electrical damping is an approximation and only ideal for the case where the coil moves from a high field region β , to a zero field region [36]. It was shown in [47] for the case of a coil oscillating perpendicular to the surface of the magnet, that the instantaneous definition of coupling factor $Nl\beta$ is appropriate as long as only the radial component of the magnetic induction at the location of the coil is used for β . The electrical energy E_{emg} generated in a time interval can be expressed as follows

$$E_{emg} = \int_0^t c_e \dot{y}^2 dt. \quad (6.7)$$

The instantaneous power dissipation (P_e) in coil and load resistance from electromagnetic force can be expressed as follows

$$P_e = C_e v^2. \quad (6.8)$$

The governing equations for the theoretical energy harvester are given by the standard dynamic equations:

$$m\ddot{y} + (c_m + c_e)\dot{y} + ky = f_y(t), \quad (6.9)$$

where m is the vibrating mass, c_m is the mechanical damping, c_e is the equivalent electrical damping, k is the spring stiffness, y is the unknown displacement of the mass, and $f_y(t)$ is the external force at time t .

6.3 Brief review on aeroelastic energy harvesting

Aeroelastic energy harvesting from the motion of a structural system within a fluid flow involves the mutual interactions of (i) the fluid flow, (ii) the electromechanical structure, and (iii) the attached electrical circuit. The wind-induced excitations can be converted to electrical energy using piezoelectric or electromagnetic transducers. Intensive review on aeroelastic energy harvesters was presented in Abdelkefi [3], Wang et al. [248]. The intention of the author is, therefore, to present a very brief overview on aeroelastic energy harvesters.

6.3.1 Flutter/airfoil-based aeroelastic energy harvesters

Airfoil sections

A piezoelectric cantilever beam with an airfoil section attached to the end is susceptible to fluttering motion which can be used for energy harvesting. At a flow speed above the critical flutter limit, the self-excited movements can take place due to insufficient structural damping. The exploitation of aeroelastic vibrations for energy harvesting has been started since 2008. Erturk et al. [95] presented the results of preliminary experimental investigations and showed the possibility for piezoelectric energy harvesting from wind-induced vibration of morphing airfoil. It was followed by Anton and Inman [23] to supply energy to unmanned air vehicles (UAVs) applications. A novel aeroelastic energy harvesting device was proposed in Bryant and Garcia [41, 42] based on two-degree-of-freedom (2-DOF) model of typical airfoil. The possibility of energy harvesting from heaving and pitching motion of airfoil was investigated numerically and experimentally in several studies [43, 44, 73–75, 78–80, 96, 188, 267–269]. In order to be able to harvest from low wind speeds, Abdelkefi et al. [8] reported the importance of decreasing the linear flutter speed. Michelin and Doaré [164] investigated the possibility of harvesting energy from a flexible plate in an axial flow through flutter. The concept of nonlinear energy harvesting under a combination of base excitations and aerodynamic loadings for flutter-based energy harvesters was first introduced and studied in [38, 40].

Flutter in thin plate systems

The T-shaped flexible cantilever systems under wind loading may experience unstable vibration due to rotational flutter when the negative aerodynamic damping exceeds the mechanical damping of the system. An electromagnetic transducer was used in Park et al. [186] for the conversion of these mechanical vibrations into electrical energy. [54] analysed the T-shaped

harvesters numerically to optimize the performance. The channelization of the incoming flow by using a funnel [48, 148, 185] was found to be helpful to enhance the harvester performance. The efficiency of an inverted T-shaped cantilever for piezoelectric energy harvesting was shown in [149]. The unstable motion of thin cantilever plates under axial flow has recently been found effective for small-scale energy harvesting such as the use of flag fluttering [85, 97, 106, 165, 215, 224].

6.3.2 Energy harvesting from vortex-induced vibration

The formation of the von Kármán vortex street behind the bluff body to induce oscillations was first examined in Allen and Smits [19] for piezoelectric energy harvesting. The energy harvesting from ocean/river waves using piezoelectric polymers was investigated in [230]. The flow-induced vibration was exploited for energy harvesting in [202, 245–247]. The wakes behind the circular cylinders was shown in Akaydin et al. [14], Akaydin et al. [16] for energy harvesting using a flexible piezoelectric cantilever beam in the downstream. Xie et al. [256] proposed a new energy harvesting technique poled and electrode flexible ceramic cylinder. VIV-based energy harvesters were studied further in [4, 15, 32, 66, 67, 110, 251]. Studies in recent past [181, 183, 216, 263] presented efficient energy harvesting technique from VIV response of the inverted piezoelectric cantilever system.

6.3.3 Galloping-based energy harvesters

The transverse galloping is another aeroelastic phenomenon which has been used over the recent years for energy harvesting since it causes large oscillations amplitudes. When the wind speed exceeds a critical value at which an instability is initiated, the transverse galloping of elastic bluff bodies takes place and the prismatic structure starts to oscillate. Many studies have investigated the effects of various parameters on the behaviour of the galloping for different bluff body structures [20, 21, 33, 34]. The possibility of using transverse galloping to extract energy was investigated theoretically in [5, 6, 10, 11, 31, 39, 218, 219, 260, 262].

The concept of energy harvesting from galloping oscillation was presented in [218] for an equilateral triangle section, whereas using a D-shaped cross-section in [219]. The galloping of square cylinders was investigated in Abdelkefi et al. [6] for energy harvesting. Furthermore, the effects of the cross-section geometry (D-section, square, triangle, . . .) on the onset speed of galloping and the level of the output power was studied theoretically in [5, 12]. A coupled nonlinear electro-aeroelastic model was developed in Abdelkefi et al. [10] for galloping-based piezoelectric energy harvesters, which was validated experimentally in [218]. Yang et al. [260] investigated experimentally the influence of the cross-section geometry on the performance of a galloping-based energy harvesters. Zhao et al. [262] compared different methods that can be used to model the performance of galloping-based piezo-aeroelastic energy harvesters. A relationship between a dimensionless version of the harvested power and the wind speed for galloping-based energy harvesters was established in Bibo and Daqaq [39]. An equivalent circuit representation approach was proposed in Tang et al. [228] to predict the performance galloping-based energy harvesters. The concept of harvesting energy from hybrid vibrations which is from the base and galloping of a bluff body was theoretically investigated by Yan et al. [259]. The galloping-based electromagnetic energy harvesters were studied in [18, 65, 240].

6.3.4 Harvesters based on wake galloping

The response of a cylinder by the wakes of an upstream cylinder has attracted in last few years for aeroelastic energy harvesting. A wake galloping-based energy harvesting device using an electromagnetic transducer was designed and fabricated in [132, 133]. The effects of wake galloping on the range of flow speeds was investigated experimentally in [9] for piezoelectric energy harvesting. Furthermore, the turbulence effects on the performance of a galloping-based energy harvester were experimentally investigated in [7]. The piezoelectric energy harvesting from multiple elastic cylinders arranged in a line was investigated in [117, 118].

6.4 Torsional flutter-based T-shaped energy harvesters

6.4.1 Torsional flutter

Torsional flutter is SDOF aeroelastic instability with rotational motion. Figure 6.2 shows a schematic configuration of torsional flutter for a rigid bridge deck, where U_∞ is the free stream wind speed, B is the section width, and the section is supported by a linear rotational spring of stiffness $K_\alpha = M_\alpha/\alpha$. The governing equation of motion of the bridge deck for torsional flutter analysis can be expressed as [257]

$$M_\alpha(\ddot{\alpha} + 2\xi_\alpha\omega_\alpha\dot{\alpha} + \omega_\alpha^2\alpha) = \frac{1}{2}\rho U_\infty^2 B^2 \left[K A_2^* \frac{B\dot{\alpha}}{U_\infty} + K^2 A_3^* \alpha \right], \quad (6.10)$$

where M_α is the mass moment of inertia, ξ_α is the damping ratio, ω_α is the natural circular frequency of rotational motion, α is the rotational displacement. In the right side of Eq. (6.10), $K = B\omega/U_\infty$ is the non-dimensional reduced frequency, ρ is the air density, U_∞ is the free stream flow velocity, B is the section width, A_2^* and A_3^* are the non-dimensional function of K and known as aerodynamic or flutter derivatives which are associated with self-excited moment [204]. Since the derivatives are functions of frequency K , they can be measured only when the body is in the oscillatory state. Usually, they are measured in experimental wind tunnel tests; however, the CFD simulations are often used alternatively. For purely rotational system, the Eq. (6.10) may be expressed as following:

$$M_\alpha\ddot{\alpha} + \left\{ 2M_\alpha\xi_m\omega_\alpha - \frac{1}{2}\rho U_\infty B^3 K A_2^*(K) \right\} \dot{\alpha} + \left\{ M_\alpha\omega_\alpha^2 - \frac{1}{2}\rho U_\infty^2 B^2 K^2 A_3^*(K) \right\} \alpha = 0. \quad (6.11)$$

At a wind speed when A_2^* becomes positive, and the negative aerodynamic damping exceeds the total system damping, the system exhibits an increasing structural response. To express

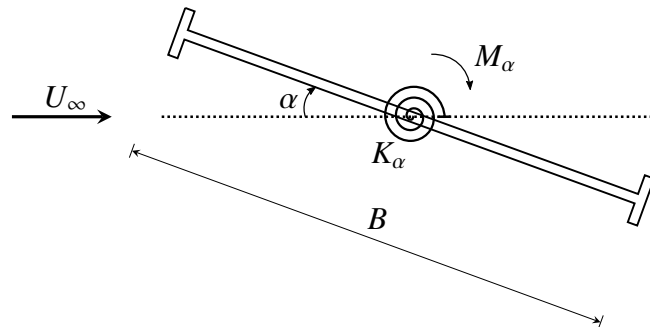


Figure 6.2: Schematic purely rotational motion of a bridge deck.

that the rotational damping is induced by the mechanical system, the term ζ_α in Eq. (6.11) is replaced by ζ_m . Here, this equation shows specifically that the total system damping is the sum of the mechanical damping and the aerodynamic damping, which may be expressed as

$$c_t = c_m + c_a = 2M_\alpha \xi_m \omega_\alpha - \frac{1}{2} \rho U_\infty B^3 K A_2^*(K) \quad (6.12)$$

where c_m , c_a and c_t represents the mechanical, aerodynamic and total damping of the system. It is noticeable from Eq. (6.11)-(6.12) that, at or above the critical wind speed the system experiences negative damping, starts vibrating in unstable way and exhibits the flutter phenomenon. Note, that the section shown in Figure 6.2 is similar to that of the original Tacoma Narrows Bridge which collapsed from torsional flutter and the failure of which has given rise to many studies into aerodynamic instabilities such as [176] and [162].

6.4.2 A reference T-shaped electromagnetic energy harvester

The susceptibility of the T-shaped cantilever system to torsional flutter was exploited advantageously in Park et al. [186] for electromagnetic power generation. The prototype T-shaped harvester and the energy extraction mechanism from such a system are presented schematically in Fig. 6.3. The configuration of the coils and magnets are shown here according to the reference harvester. The cantilever beam starts vibrating in an unstable fashion at or above the critical flutter wind speed. This allows the system to create a relative movement between the magnets and the coils and induces current flow through the circuit, cf. Fig. 6.3(e). The dimension and the dynamic properties of the reference harvester are summarised in Table 6.1.

Variables	Description	Value
W_h	harvester width	0.03 m
L_h	harvester length	0.042 m
H_{vp}	height of the vertical plate	0.02 m
t_h	harvester thickness	1.016×10^{-4} m
M	mass of the magnet	0.009 kg
E	elastic modulus of steel	180 GPa
I	moment of inertia	2.62×10^{-15} m ⁴
ζ_m	mechanical damping ratio	0.004
ω_h	circular frequency	46.1 rad/sec

Table 6.1: Physical dimensions and dynamic properties of the reference prototype T-shaped electromagnetic energy harvester.

6.4.3 Identification of flutter wind speed of T-shaped harvester

The use of a simplified rigid beam model

The rotational motion of flexible T-shaped reference harvester was numerically modelled and simulated in Park et al. [186] using a simplified SDOF rigid beam system. The flexible beam, cf. Fig. 6.4 (a), was idealized as a simplified SDOF system using an equivalent rigid beam element for flutter analysis, as shown in Fig. 6.4 (b). The length of the prototype harvester was reduced in the simplified model, which is denoted as L_r in Fig. 6.4 (b), and it was chosen 0.028 m. The equivalent modal mass M_α and stiffness K_α were calculated 2.35×10^{-4} kg m² and 0.499 N, respectively.

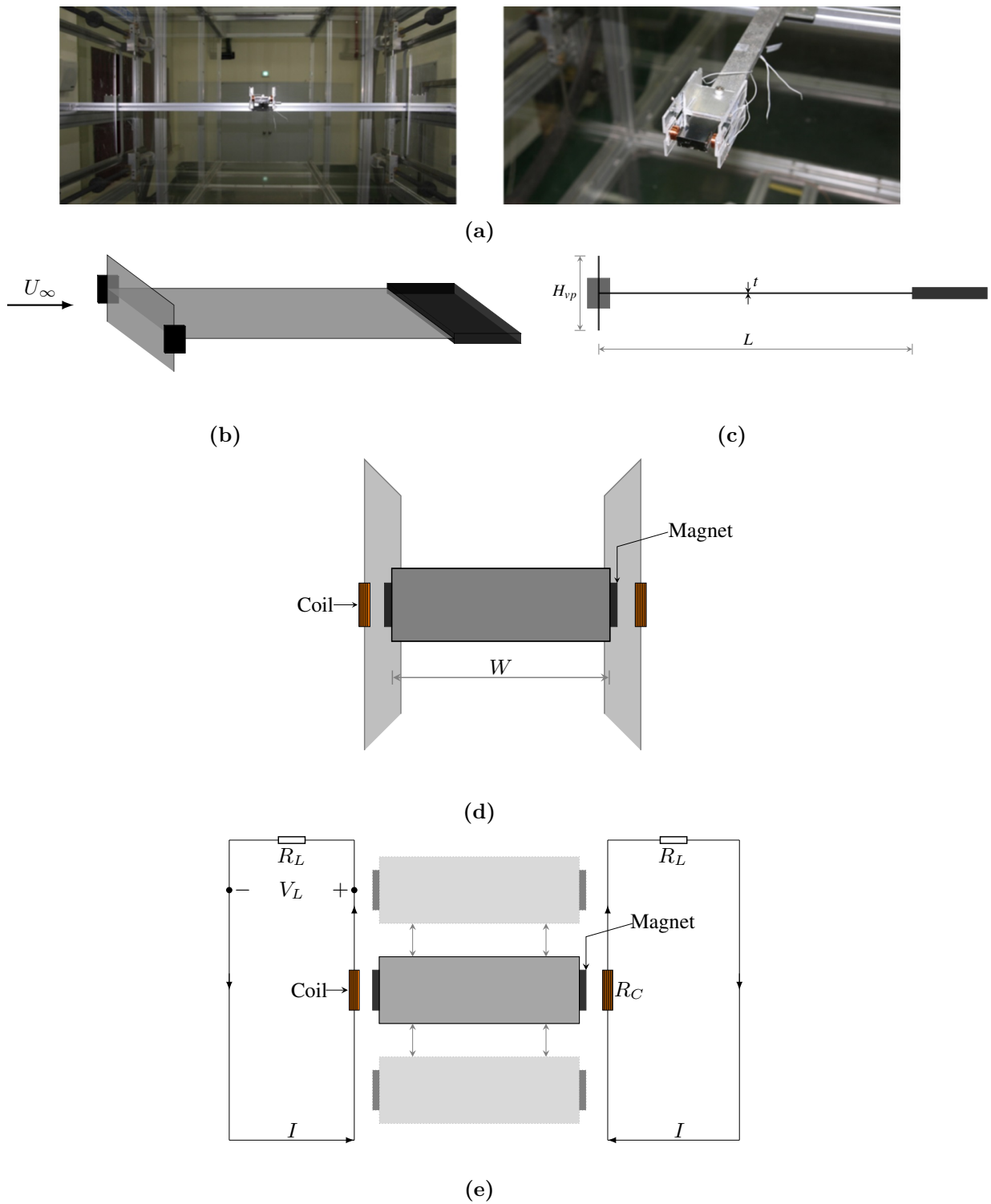


Figure 6.3: Electromagnetic energy harvesting from fluttering response of T-shaped cantilever systems: (a) the experimental wind tunnel set-up of a prototype T-shaped electromagnetic energy harvester [186]; (b) The schematic view of the harvester under free stream wind U_∞ ; (c) the side view of the cantilever harvester in which L , H and t indicate the length, height, and thickness, respectively. (d) The front view shows confined harvester in between walls; (e) the schematic conversion of mechanical vibration into electrical power using an electromagnetic transducer, in which I , R_L and R_C represents the current, electrical load resistance and coil resistance, respectively. V_L is the voltage across R_L .

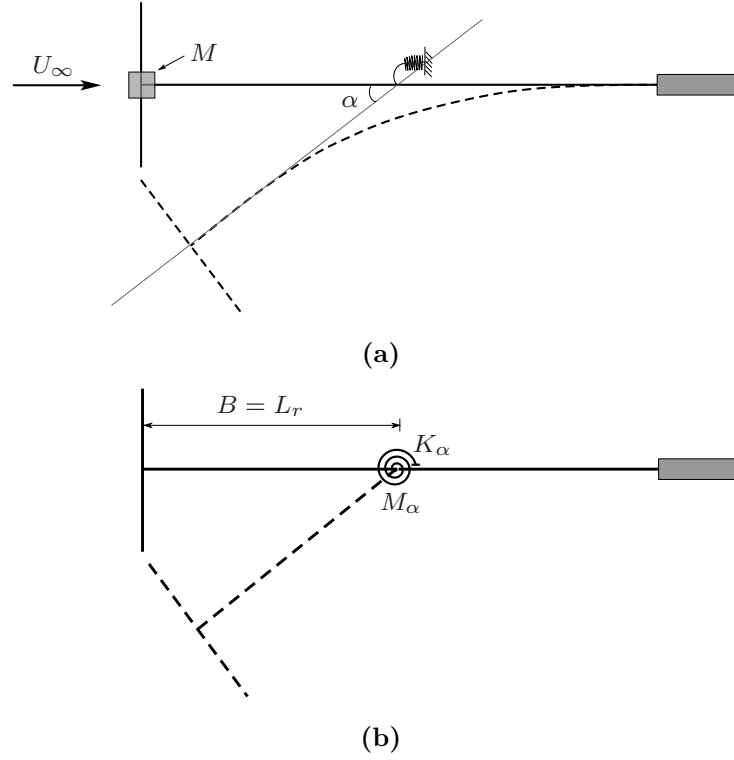


Figure 6.4: Modelling of T-shaped cantilever harvester: (a) the actual deformed shape of the flexible harvester whereas in (b) the simplified equivalent single degree of freedom model approximated using a rigid beam element [186].

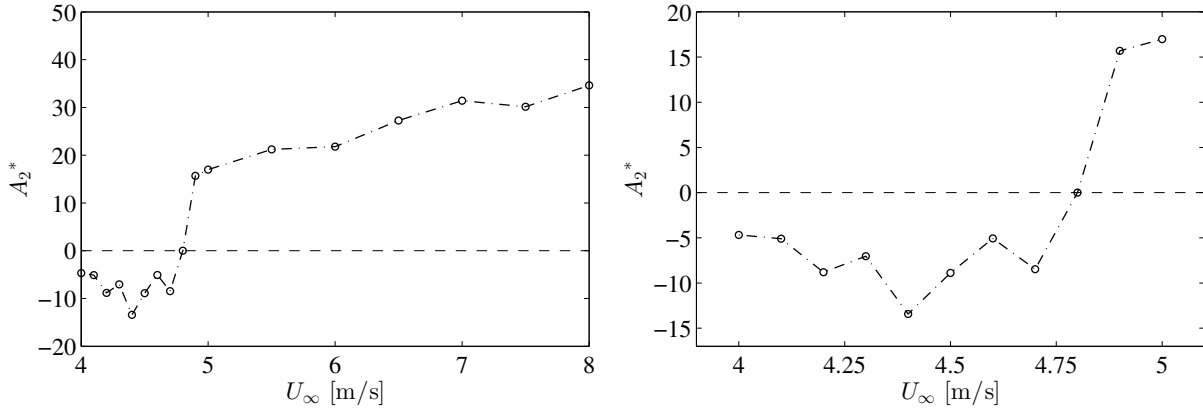


Figure 6.5: The flutter derivative A_2^* of the cantilever harvester obtained from forced vibration simulation using the simplified harvester model: estimated A_2^* (left) and the closed view in the critical region (right) [186].

The derivative-based flutter analysis was performed in Park et al. [186] to identify the critical flutter limit as well as to explain the phenomenon concerning the effect of negative aerodynamic damping, cf. Fig. 6.5. The critical onset flutter wind speed was identified to be 4.8 m/s. Fully coupled simulations were also performed to identify the critical flutter wind speed. In fully-coupled simulation of the harvester, the equation of motion concerning aero-electromechanical coupling for a SDOF model can be expressed as follows

$$M_\alpha \ddot{\alpha} + 2M_\alpha(\xi_m + \xi_e)\omega_\alpha \dot{\alpha} + k_\alpha \alpha = f_\alpha(t), \quad (6.13)$$

where, $(\xi_m + \xi_e)$ represents the sum of mechanical and electrical damping ratio of the harvester, $f_\alpha(t)$ represents the aerodynamic forces on the system.

The fully coupled simulations are performed again for the open circuit condition, which means that the mechanical damping is only considered ($\xi_e = 0$). The system starts vibrating in an unstable fashion at and above the wind speed of 4.8 m/s. The time histories of the vertical tip displacements for different wind speeds are compared in Fig. 6.6. The particle maps around the harvester at 5 m/s are shown in Fig. 6.7. The LCO is clearly observed at large displacements, as mentioned in [54, 186].

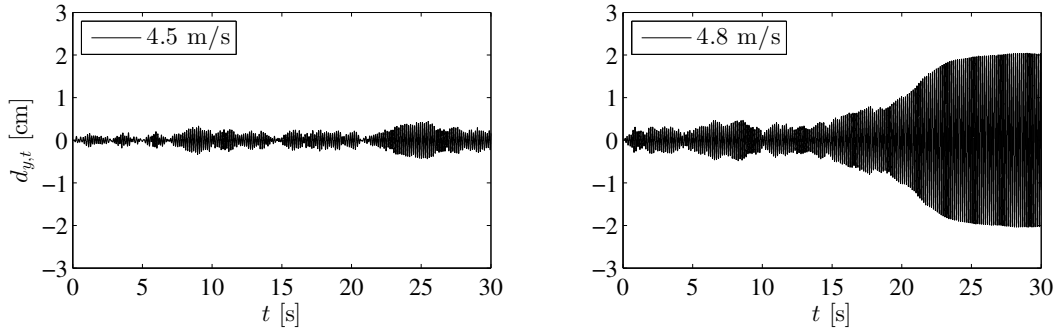


Figure 6.6: The use of simplified rigid beam model to identify the critical flutter wind speed based on the vertical tip displacement of the T-shaped harvester.

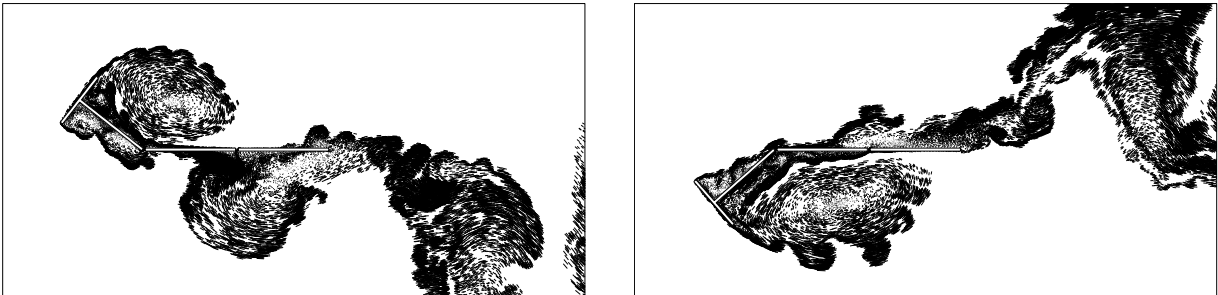


Figure 6.7: The particle maps at wind speed 5 m/s in case of simplified rigid beam model.

The actual flutter wind speed of the flexible harvester was observed at 4 m/s in the wind tunnel experiment under the open-circuit condition. The rigid beam model was found to be a reasonable approximation. However, it is not possible to predict the influences of system flexibility accurately on the global system response using such a simplified model. Furthermore, the prediction of the large displacements under wind speeds higher than the critical flutter limit are not found to be reliable. To evaluate the power output numerically, or to optimize the performance of such a harvester, it is crucial to model the system behaviour accurately.

Fully coupled flutter analysis of flexible T-shaped cantilever

This section presents the utilisation of the 2D coupled VPM solver for analysing the T-shaped cantilever system to identify the critical flutter wind speed. In this section, the proposed fully coupled VPM-based solver has been used to model the reference T-shaped cantilever harvester. The discretisation of the harvester within the framework of the flow and the

structural solver has been shown schematically in Figure 6.8. The physical dimensions and mechanical properties of the prototype harvester are considered according to Table 6.1. The numerical parameters are summarised in Table 6.2.

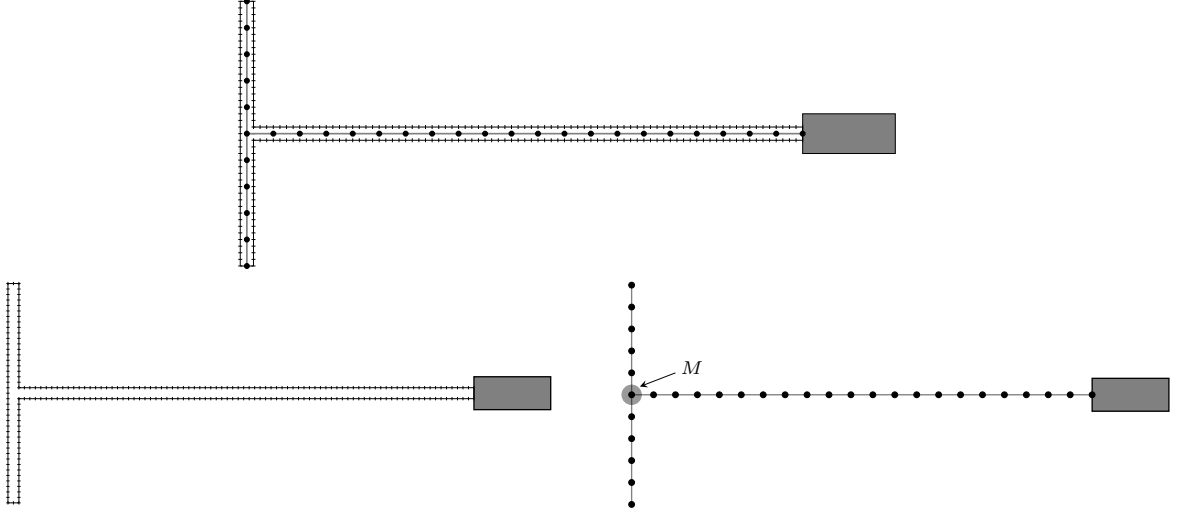


Figure 6.8: Discretisation of the T-shaped cantilever harvester: (top) the discretisation scheme of the cantilever system for the flow solver and structural solver together; (bottom-left) the discretisation of surface panels only for the flow solver; (bottom-right) the discretisation of the structural system into nodes and elements.

Solver	Numerical parameters		Value
Flow	Panel size	$\Delta s/H_{vp}$	0.05
	Non-dimensional time step	$\Delta t_f^* = \Delta t_f U_\infty / \Delta_s$	1.0
	Poisson grid	$N_x \times N_y$	511×255
	Number of particles	$N_{particle}$	105,000 - 115,000
Structure	Number of beam elements	N_{elem}	62
	Length of beam element	l_{elem}	0.001 m
	Time step of structural solver	$\Delta t_s^* = \Delta t_s U_\infty / \Delta_s$	1
	Number of sub-time steps		15

Table 6.2: Fully coupled simulation of the T-shaped cantilever harvester: numerical parameters.

Simulations are carried out at different wind speeds (2–8 m/s) to identify the critical flutter wind speed. Here, Figure 6.9 shows the numerically simulated harvester and the instantaneous flow fields. The vertical tip displacements of the cantilever harvester simulated at several wind speeds are compared in Figure 6.10. It is clearly observed that the system starts vibrating in an unstable manner from 4 m/s, which agrees with the identified onset flutter wind speed in the wind tunnel test.

6.5 Modelling and simulation of T-shaped electromagnetic energy harvesters

The EM transducer introduces additional electrical damping to the harvester system, which may influence the initiation of flutter-induced vibration significantly. In this section, the coupled solver is utilized to model the influences of EM transducer on the vibration of the prototype harvester. The objective is to estimate the energy outputs numerically under various wind speeds, precisely, according to the reference wind tunnel experiments.

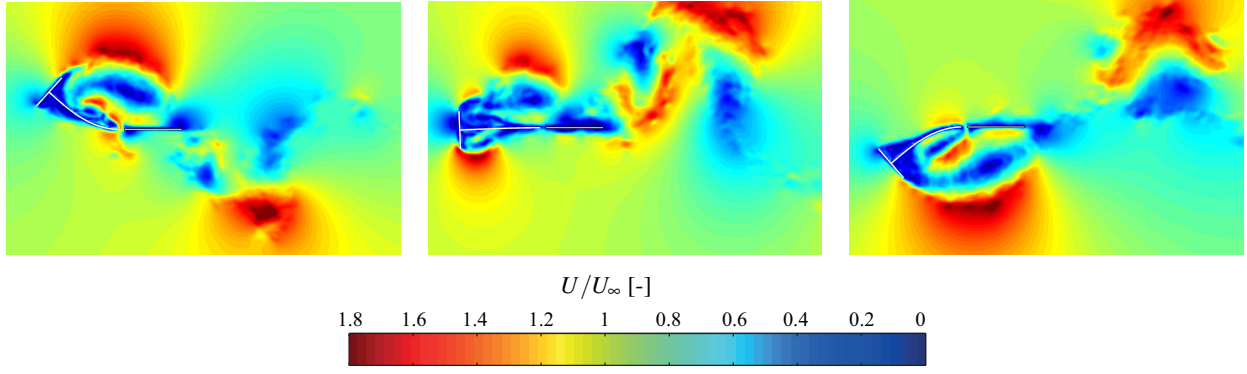


Figure 6.9: Coupled simulation of flexible T-shaped cantilever system: the flow fields around the deformed body are shown for sequential three vibration phases.

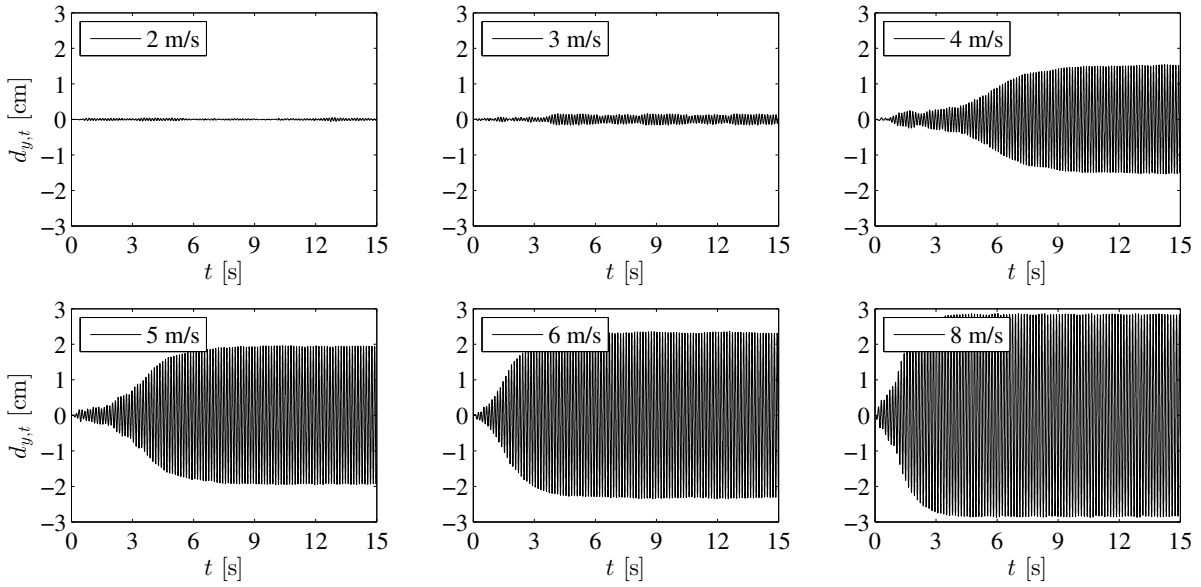


Figure 6.10: Fully coupled simulation of the T-shaped system under different wind speeds: Identification of critical onset flutter wind speed based on the aeroelastic coupled response; the vertical tip displacement of the mechanical system under different simulated wind speeds (2-8 m/s) are displayed.

6.5.1 Electrical damping effects in equation of motion

The relative movement between magnet and coil introduces electromagnetic force, which opposes the motion of the T-shaped harvester, due to the interaction between the field caused by the induced current and the magnetic fields. The equation of motion of the prototype harvester considering a MDOF model, the influence of electromagnetic transducer can be expressed as follows

$$\mathbf{M}\ddot{\mathbf{q}} + (\mathbf{C}_m + \mathbf{C}_e)\dot{\mathbf{q}} + \mathbf{K}\mathbf{q} = \mathbf{F}, \quad (6.14)$$

where $\mathbf{C}_m + \mathbf{C}_e$ represents the total system damping matrix, the sum of mechanical and electrical damping matrix, which is formulated within the framework of the structure solver based on Eq. (4.11). Considering the electrical damping added to the system damping, the proportional factors can be calculated using the first two vibration modes of the harvester

(ω_1 and ω_2) based on following equation

$$a_0 = \zeta_t \frac{2\omega_1\omega_2}{\omega_1 + \omega_2}, \quad a_1 = \zeta_t \frac{2}{\omega_1 + \omega_2}, \quad (6.15)$$

where ζ_t is the total system damping ratio. The electrical damping of the cantilever harvester can be expressed in terms of dynamic properties such that

$$C_e = 2m_\alpha \zeta_e \omega_\alpha, \quad (6.16)$$

where ζ_e and m_α are electrical damping ratio and modal mass of the harvester, respectively. For different electrical resistances, ζ_e can be obtained by performing experimental free vibration test. The total damping ratios ($\zeta_t = \zeta_m + \zeta_e(R_L)$) of the reference harvester for different electrical load resistances R_L (100–5000 Ω) were measured experimentally by performing free vibration tests [186]. The corresponding total system damping coefficients ($c_m + c_e(R_L)$) for various electrical load resistances were calculated using the following equation

$$c_m + c_e(R_L) = 2m_\alpha(\zeta_m + \zeta_e(R_L))\omega_\alpha. \quad (6.17)$$

For a cantilever beam with tip mass, the natural frequency and the rotational stiffness of the system can be calculated using $\omega_\alpha = \sqrt{3EI/mL^3}$ and $K_\alpha = 2EI/L^2$, respectively. The effective rotational mass can be calculated using $m_\alpha = K_\alpha/\omega_\alpha^2$. It is possible to express the total system damping of the harvester (c_t) in terms of the electromagnetic transformation factor $Nl\beta$ using Eq. (6.6) as follows

$$c_t = c_m + c_e(R_L) = 2m_\alpha\omega_\alpha\zeta_m + \frac{(Nl\beta)^2}{R_L + R_C}. \quad (6.18)$$

In this study, the term $R_L + R_C$ in Eq. (6.18) indicates the sum of the electrical load resistances and the coil resistances from two sets of closed circuits with magnets and coils, cf. Figure 6.3. The resistance of individual coil R_C was measured 130 Ω . In Figure 6.11(top), it shows the total system damping coefficients, which are calculated using Eq. (6.17), from the performed free vibration tests of the harvester [186] under different electrical load resistances. Additionally, the fitted damping coefficients of the prototype harvester according to Eq. (6.18) are plotted for comparison. The average transformation factor $Nl\beta$ is calculated approximately equal to 1.02 from the fitted damping coefficients in Figure 6.11(top). The approximation of average $Nl\beta$ is valid for cases where the relative movement between the coil and magnet produces a fluctuation of flow field from β to zero [36].

6.5.2 Modelling of energy outputs and validation

The reference harvester considering the effects of electromagnetic transducer is simulated using the coupled solver to model the energy outputs numerically. The dynamic motion of the harvester considering the additional electromagnetic damping effects has been modelled by solving the equation of motion for coupled electro-mechanical FSI problems, cf. Eq. (6.14). The additional electromagnetic damping for electrical resistances is addressed in the system damping matrix using the formulation of Rayleigh damping according to Eq. (6.15). The total system damping ratio ($\zeta_t = \zeta_m + \zeta_e(R_L)$) for any specific electrical resistance is calculated corresponding to Figure 6.11(top) using Eq. (6.17). For different electrical load resistances, the damping ratios are shown together in Figure 6.11 (bottom).

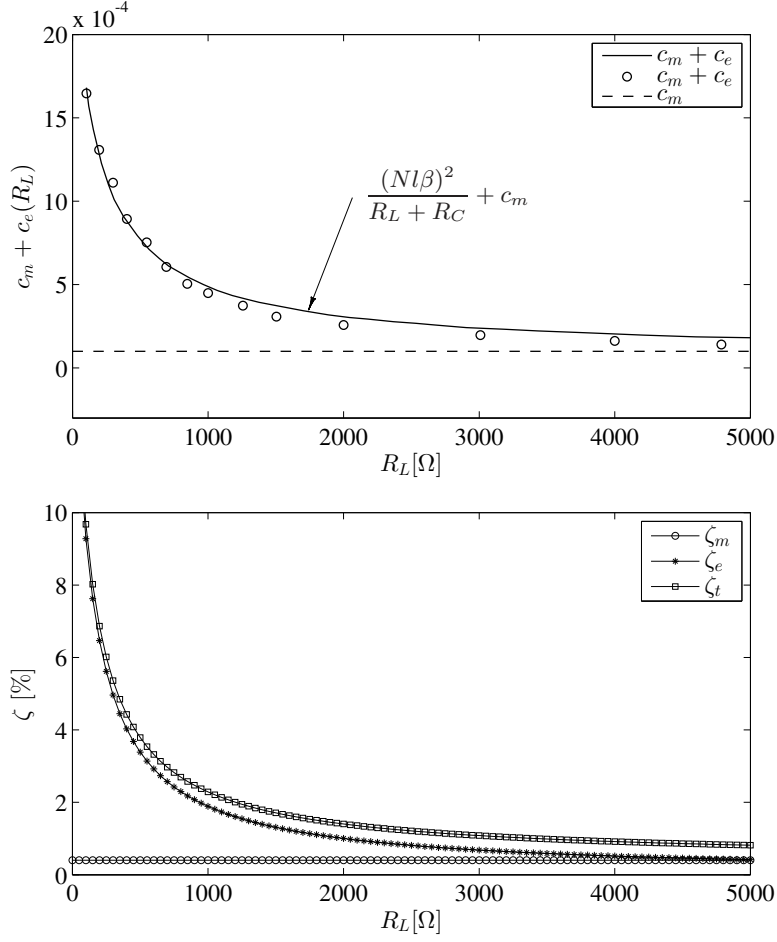


Figure 6.11: The damping of the prototype harvester: (top) total damping of the harvester estimated in reference study [186]. Here, the sum of the mechanical and electrical damping (o) indicates the experimentally measured damping, while (—) indicates the fitted total system damping. (— — —) represents the mechanical damping only. (bottom) Corresponding calculated mechanical, electrical and total damping ratios for different electrical load resistances to be used for the current numerical studies.

Simulations of the reference harvester are performed at different wind speeds (4–8 m/s) considering various electrical load resistances (100–5000 Ω). The electromotive voltage induced by the interaction between the coils and the magnets attached to the cantilever harvester is calculated using Eq. (6.5). Figure 6.12 shows the time history of the vertical tip displacements and the corresponding modelled voltage outputs for different wind speeds and electrical resistances. This figure shows the identified critical electrical resistances explicitly for different wind speeds, at which the system starts flutter-induced vibration and produces energy.

From the modelled voltage time histories at different wind speeds, the root mean square (RMS) voltage peaks (V_{rms}) for different electrical load resistances (R_L) are compared with the wind tunnel test results in Figure 6.13(a). The corresponding power outputs (P_{rms}) are computed from V_{rms} (i.e. V_{rms}^2/R_L), and compared with the wind tunnel test results in Figure 6.13(b). The modelled energy outputs, in comparison with the wind tunnel test results, are found quite satisfactory. Small differences are possibly due to the consideration of the rectangular magnet as a point magnet in the cantilever tip; the influences of the magnet shapes on the magnetic flux distribution are ignored in the presented numerical model.

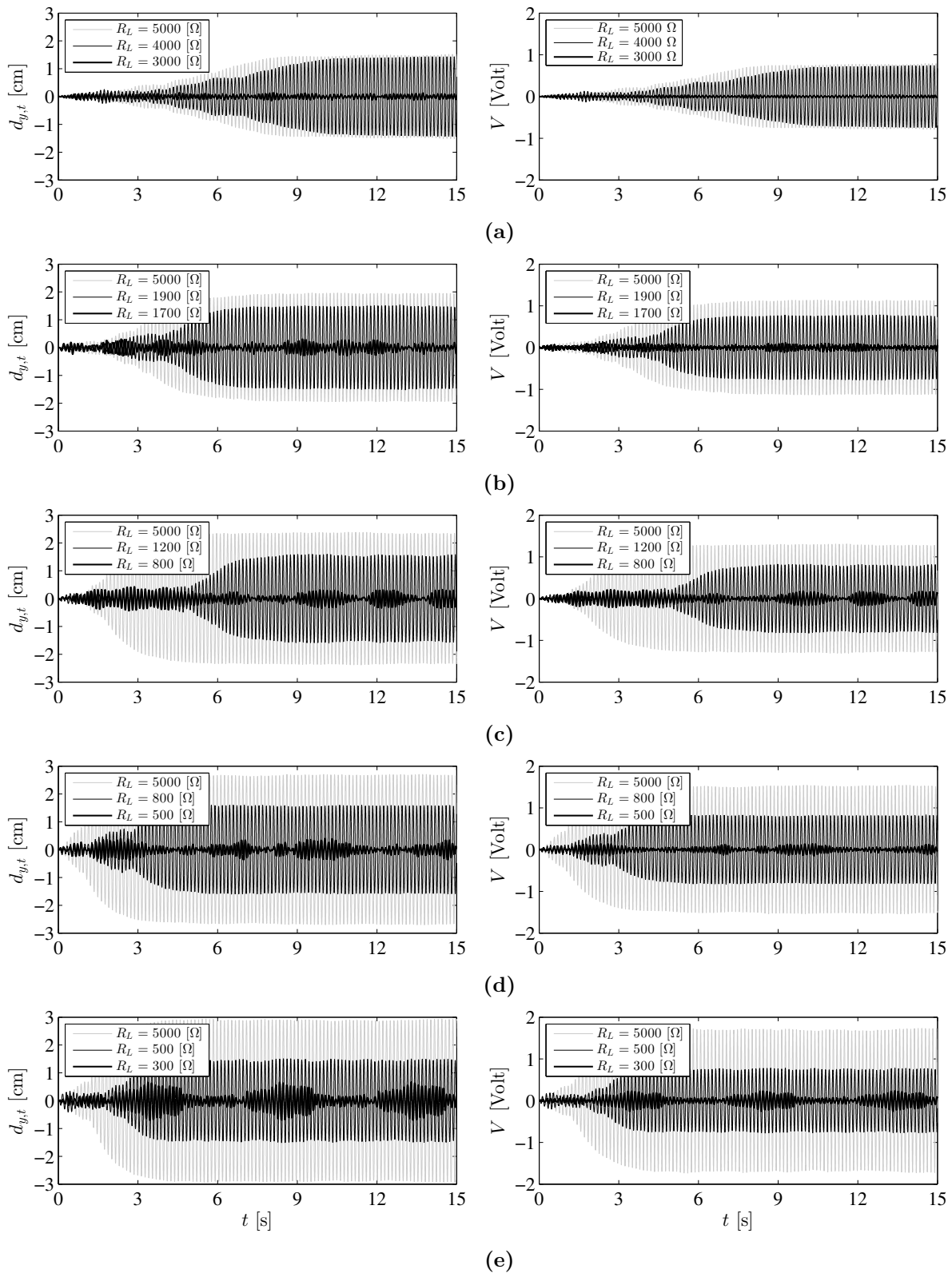


Figure 6.12: Comparison of the time histories of the tip responses (left) and predicted voltage outputs of the harvester considering different electrical resistances (R_L): the simulated under wind speeds are (a) 4 m/s, (b) 5 m/s, (c) 6 m/s, (d) 7 m/s, and (e) 8 m/s. For simulated wind speeds, the figures specifically show the identified critical R_L at which flutter vibration initiates. Additionally, the response and voltage time histories are shown for the maximum simulated R_L of 5000 Ω .

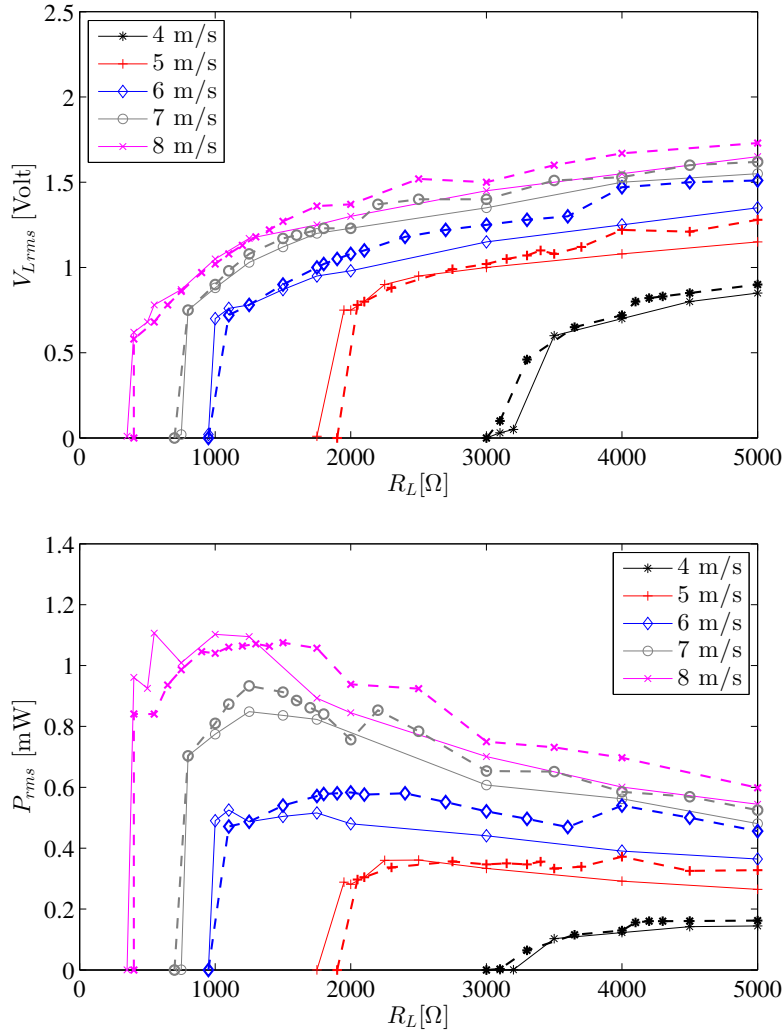


Figure 6.13: Comparison of the energy outputs of the reference prototype T-shaped harvester under different wind speeds and electrical resistances: (top) comparison of RMS voltages from CFD simulations (—) with the reference wind tunnel test results (- -), (bottom) comparison of RMS power outputs from CFD simulations (—) with the reference wind tunnel test results (- -).

The electrical power, the maximization of which is often the design goal of a harvester, is inversely proportional to the electrical resistance. It is observed for both cases, i.e. the experimental and the current numerical study results, in Figure 6.13(b) that the power outputs are decreasing after a critical point with the increase in electrical resistance. Though the modelled power outputs after the critical load resistances are found relatively lower than the experimental values, the identified critical flutter onset electrical resistances of the harvester for different wind speeds (4–8 m/s) are found satisfactory and presented in Figure 6.14.

6.6 Physical optimization of T-shaped energy harvesters

Electromagnetic power conversion from mechanical vibration is one of the most straightforward and robust techniques. The coupled simulations are performed to investigate the influences of the physical shape of the harvester on the energy outputs. The intention is to optimize the physical configuration of the harvester to maximize the power output, however,

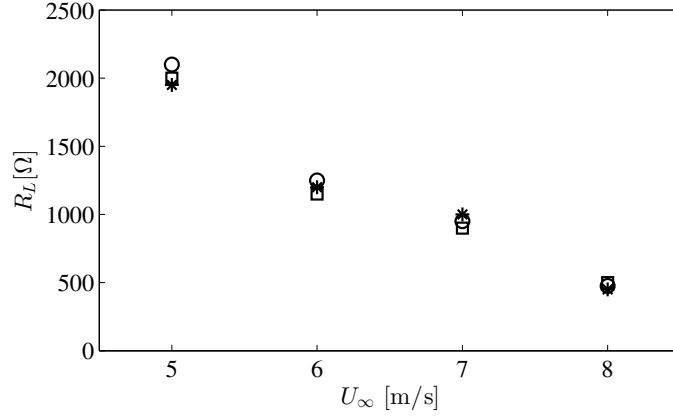


Figure 6.14: Identification of critical flutter onset load resistance (R_L) of the prototype harvester: critical R_L identified based on derivative based analysis (□) and based on the energy outputs in wind tunnel experiments (○) [186]; critical R_L identified based on estimated energy outputs numerically using coupled solver (*), c.f. Figure 6.12.

considering the range of wind speeds (4–8 m/s) used in wind tunnel experiments [186].

6.6.1 Influential electrical parameters

The optimization of power output from an electromagnetic energy harvester requires the prior understanding of influential parameters involving with the power conversion. Two key parameters that can increase the power output are

- EM damping (cf. Eq. (6.8)),
- the velocity of the relative movement between magnet and coil [194].

The velocity of the oscillating motion of the cantilever tip is a function of the tip displacement ($d_{y,t}$) and response frequency (f_r), and therefore, the dependency of the power output of an electromagnetic harvester can be expressed as follows

$$P_e \propto \zeta_e d_{y,t}^2 f_r^2. \quad (6.19)$$

The increase in EM damping may be achieved by increasing the number of coil turns; however, the corresponding increase in coil resistance reduces the power output. The reduction in electrical load resistance is another option to enhance the EM damping.

It is important to note that the flutter-based harvesters with the increase in EM damping would demand for higher wind speeds for power generation. On the other hand, the decrease in EM damping allows the system to vibrate and to extract power at low wind speed.

The other option is to increase the relative velocity between the magnet and coil for the enhancement of the power output. If electrical components such as the configuration of the coil and magnet are already optimized or fixed, the increase of system frequency can enhance the response velocity. However, the increase in system frequency results in the reduction in the vibration amplitude, which can reduce the power output. A comprehensive study is necessary to understand all these aspects, which needs the modification of the geometrical configuration of the reference harvester.

6.6.2 Effect of physical shape on flutter-based T-shaped harvesters

Three physical parameters of the reference T-shaped harvester, which are: the (a) tip plate height, (b) length and (c) thickness, have been considered for the intended optimization study. The intention is to identify optimized harvester geometry concerning the maximization of the extracted power output.

The influence of tip plate height on energy output

The self-exciting forces which govern the flutter phenomenon depend on this tip height of the cantilever harvester. Therefore, the influences of the tip height on power output are investigated initially. The reference harvester is simulated at wind speed 5 m/s using the corresponding flutter onset load resistance R_L of 1900 Ω , however, considering different modified cantilever tip height H_m . The simulated modified harvesters and the corresponding modelled RMS power outputs are compared in Figure 6.15. The power output increases with the increase in the height of cantilever tip, however, up to a critical height H_{cr} .

Study on harvester geometry for optimization of energy output

The objective is to find an optimized harvester configuration without changing the range of target wind speeds. Therefore, the attention is given to increase the velocity of relative movement between the coil and the magnet to maximize the harvested energy outputs.

The enhancement of relative velocity may be achieved by increasing the vibration frequency and/or the displacement amplitude. The increase in harvester thickness enhances the system

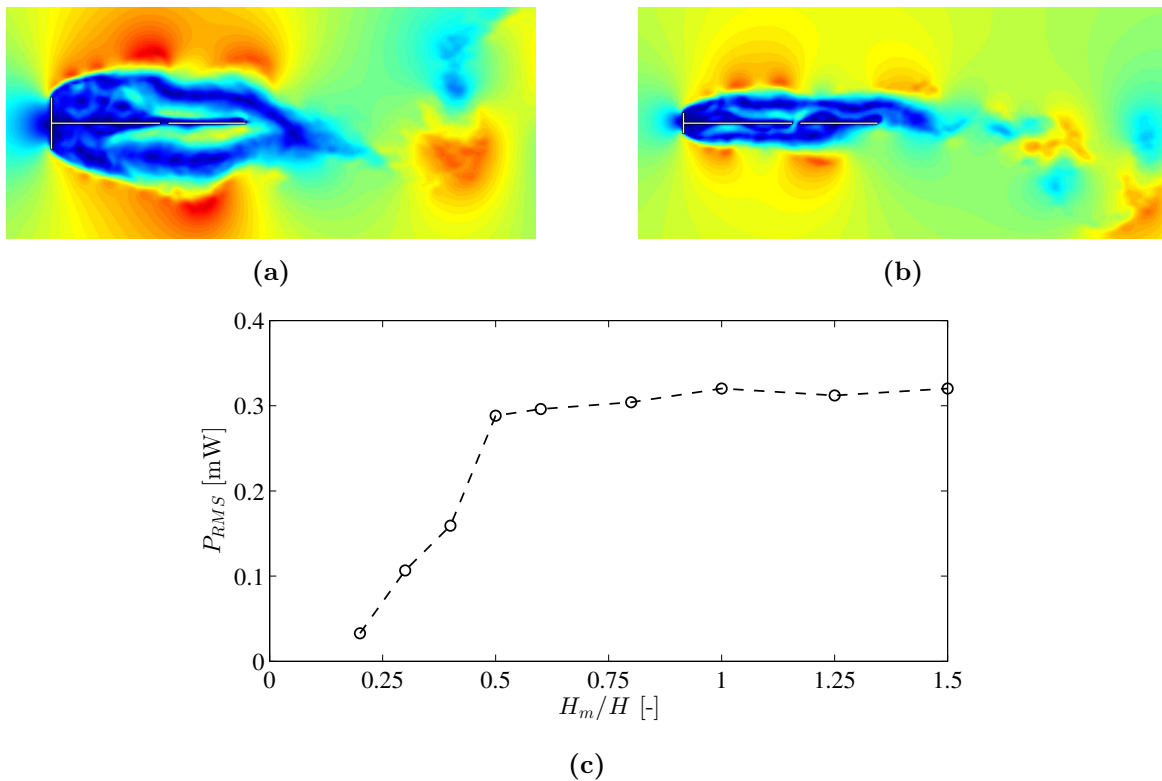


Figure 6.15: The influence of vertical plate height H_{vp} on power output of reference T-shaped harvester: (a) the reference harvester, (b) the modified harvester with tip height $H_m = 0.2H_{vp}$, and (c) the RMS power outputs for different height of vertical plate.

frequency, however, with a reduction in displacement amplitude. In contrast, the increase in harvester length allows the system to vibrate large amplitudes with a decrease in the frequency of vibration. Therefore, the length and the thickness of the harvester are investigated together for some modified configurations.

The reference harvester is modified and studied for three additional cases with the increased length of 0.05 m, 0.06 m, and 0.07 m, and three other cases with the increased thickness of 0.125 mm, 0.15 mm and 0.175 mm. Altogether, 16 number of harvesters have been investigated to understand the system behaviour in terms of modelled power output.

Importantly, the cantilever tip mass, which means the attached magnet, and the transformation factor $Nl\beta$ are considered same as the reference harvester. The height of the cantilever tip H for all the modified harvesters is chosen 0.02 m according to the reference harvester. For each modified harvester, using the system natural frequency and rotational mass, the electrical damping ratio for any particular electrical resistance is calculated using Eq. (6.20),

$$\zeta_e(R_L) = \frac{c_e(R_L)}{2m_\alpha\omega_\alpha}. \quad (6.20)$$

The modified harvesters are also simulated at 8 m/s considering the R_L of 750 Ω . For chosen combinations of harvester lengths and thicknesses, the comparison of physical shapes, the natural frequencies of the systems and corresponding electrical damping ratios of the modified harvesters are shown in Figure 6.16. Importantly, in this study the mechanical damping ratio ζ_m for all the modified harvesters are considered same as the reference harvester, which is 0.4%. This assumption may be acceptable since the associated errors in the assumed mechanical damping ratios of different modified harvesters are less significant in comparison with corresponding electrical damping ratios ζ_e .

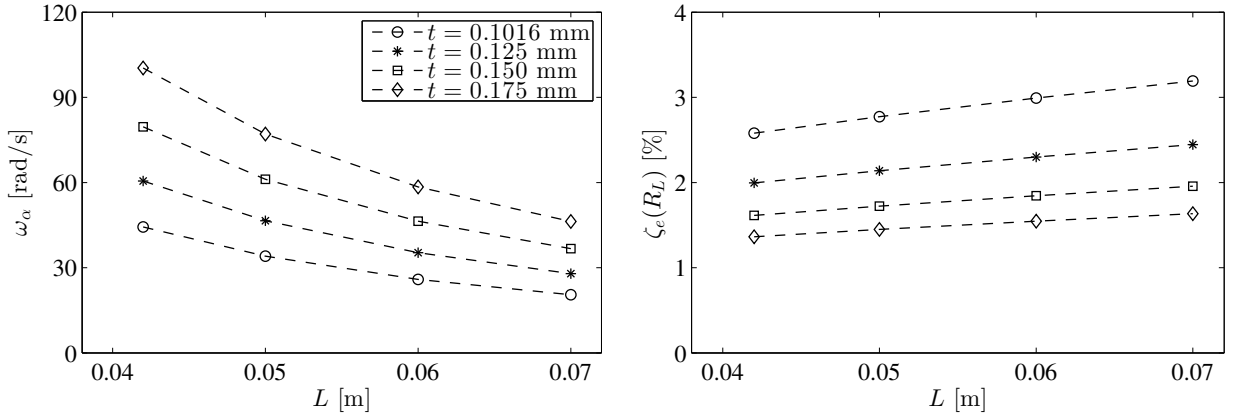


Figure 6.16: Modification in length and thickness of the reference T-shaped harvester, and corresponding changes in dynamic properties and electrical damping ratios: (left) natural frequencies, (right) corresponding electrical damping ratios for $R_L = 750 \Omega$.

The modelled power output for modified harvesters at 8 m/s considering $R_L = 750 \Omega$ are compared in Figure 6.17. The frequency of extracted power output of individual harvester is found nearly equal to its first natural frequency. The maximum power output is modelled from the harvester that has the length and thickness of 0.07 m and 0.175 mm thickness, respectively. The maximum power output is found to be 5.3 mW which is approximately five times that of the reference harvester in the wind tunnel experiment at 8m/s.

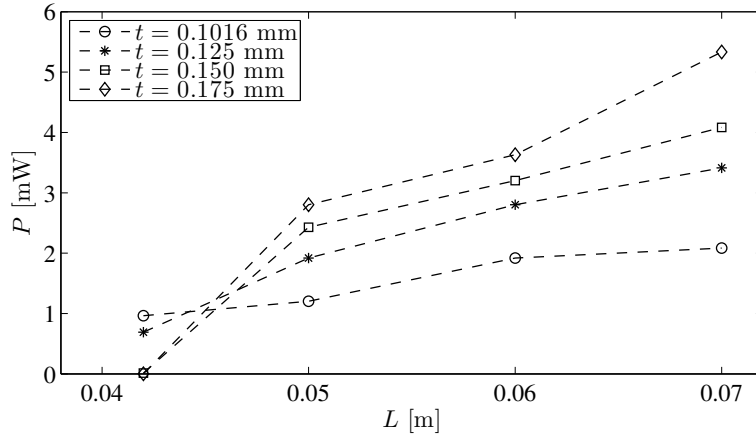


Figure 6.17: Comparison of the modelled power output of the studied harvesters along with the reference harvester under the wind speed of 8 m/s and load resistance $R_L = 750 \Omega$.

Importantly, the natural frequencies of the harvesters having same thickness are observed decreasing with the increase in harvester length, cf. Figure 6.16(left), whereas the electrical damping ratios are increasing, cf. Figure 6.16(right). However, the power outputs are observed increasing in contrast to the increase in electrical damping, cf. Figure 6.17. This is specifically due to the increase in vibration velocity which is due to the increase in vibration amplitudes with the increase in harvester length.

It is observed that the short harvesters having higher natural frequencies produce almost no power output due to the reduction in vibration amplitude, which is the case of the harvester having length and thickness of 0.042 m and 0.175 mm thickness, respectively. The study results in Figure 6.17 shows that the increase in the length and the thickness of the harvester, however, with an optimized combination the performance of the harvester may be enhanced significantly without changing the target inflow wind speed. Moreover, for cases where the restriction in the harvester size is less, such numerical investigations may be helpful to find optimized harvester configuration for the maximization of the harvested energy.

6.7 A framework for optimisation of electrical parameters as preliminary study

A comparative study on different cantilever systems is performed to obtain guidelines for the design of experimental set-ups of prototype harvesters. The aim is to perform a multi-objective optimization based on aeroelastic interactions of different cantilever systems, the conversion mechanisms, identification of critical electrical parameters.

The changes in aerodynamic behaviour and flapping pattern of inverted and T-shaped cantilever harvesters with/without tip mass have been presented in Sec. 5.4. The influences of damping ratios are analysed as preliminary studies to investigate the electrical damping effects of energy harvesters. The influential parameters such as response amplitude and oscillating frequency are compared to identify not only efficient cantilever harvesters but also an appropriate combination of physical and electrical parameters depending on target wind speeds.

6.7.1 Preliminary analysis of electromagnetic energy harvesters

The maximization of power output for a target wind speed within a limit of envelope volume of harvesters has been shown in Sec. 6.6.2. However, the optimization of R_L has not been studied for the geometrically optimized harvester. Moreover, the performance of the geometrically optimized harvester has not been investigated further under higher wind speeds. The present study aims to avoid many optimization processes related to different variables from the mechanical and electrical point of views.

The study presents a framework to perform an investigation in a backward way through coupled numerical simulation to identify initially the optimised mechanical system based on FSI simulations. It follows by identifying optimum damping for maximum power output for a target wind speed, and then the selection of electrical parameters such that they provide the identified optimum damping effects.

The studies on different cantilever systems in Sec. 5.4 shows that the inverted cantilever with tip mass has low potential of electromagnetic energy harvesting (Fig. 5.15) since the LCO is observed only at very high wind speed of 30 m/s. However, the inverted T-shaped cantilever with tip mass has been found promising for energy harvesting considering its LCO for a wide range of wind speeds.

The influential response parameters of an electromagnetic energy harvester (c.f. Eq. (6.19)) are compared in Fig. 6.18 for different wind speeds. The maximum harvesting potential is observed at wind speed of 20.5 m/s. However, the presented result in Fig. 6.18 is from T-shaped system considering mechanical damping only and, it does not reflect the effect of electromagnetic damping.

The initiation of fluttering of the system can be influenced significantly by the inclusion of electrical damping [186]. Therefore, the aim here is to utilize the coupled simulations to identify critical electrical damping for a target wind speed, and to estimate potential power output by considering the system as an electromagnetic energy harvester. The electrical parameters can be calculated later based on the identified critical electrical damping.

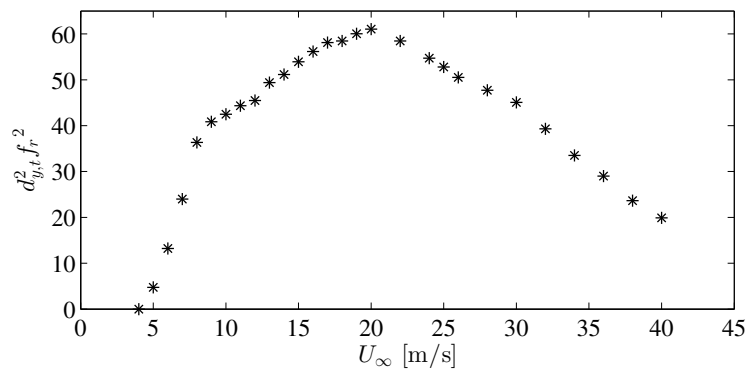


Figure 6.18: Comparison of influential response parameters of T-shaped cantilever with tip mass under different incoming flow (from Fig. 5.15).

Investigation on inverted cantilevers as EM harvesters

The T-shaped cantilever with tip mass ($L \times W \times H_{vp} = 5.1 \text{ cm} \times 6.4 \text{ cm} \times 1 \text{ cm}$) is considered as a prototype harvester and simulated under the target wind speeds of 10 m/s

and 15 m/s. The aeroelectromechanical coupled simulations are performed by solving the equation of motion of the harvester (Eq. (6.14)). The aim is to simulate the system under different total harvester damping ratios $\zeta_t = \zeta_m + \zeta_e$, in which ζ_m and ζ_e are the mechanical and electrical damping ratios, respectively. Here, ζ_m is considered 0.5%. Fig. 6.19 shows the average peak response and frequency of the cantilever tip for different ζ_e .

It is observed that the flutter response of the cantilever harvester reduces with the increase in ζ_e . Furthermore, the system is vibrating at higher frequencies at large ζ_e . It may be due to the increase in aerodynamic stiffness since the response amplitude is comparatively small at large ζ_e . Fig. 6.20 shows calculated power output of the system under different electrical damping using Eqs. (6.8, 6.16). The critical electrical damping coefficients $C_{e(crit)}$ are identified approximately 0.002372 N.s/m and 0.00178 N.s/m for wind speeds 10 m/s and 15 m/s, respectively. The corresponding maximum power outputs are found to be 4.58 mW and 5.14 mW.

Now, the optimized R_L for this T-shaped harvester can be calculated using Eq. (6.6), in a backward way for known or chosen $Nl\beta$ and R_C , such that the electrical damping become close to $C_{e(crit)}$. Based on $R_C = 300 \Omega$, Fig. 6.21 shows the electrical damping coefficients for different combination of $Nl\beta$ and R_L (using Eq. (6.6)). This plot can be prepared for different R_C . In present study, the design of T-shaped harvester is based on two set of magnet and coil (Fig. 6.3), as was shown in [186]. This means the values of $C_{e(crit)}$ for one set of magnet and coil are 0.001186 N.s/m and 0.00089 N.s/m for wind speeds 10 m/s and 15 m/s,

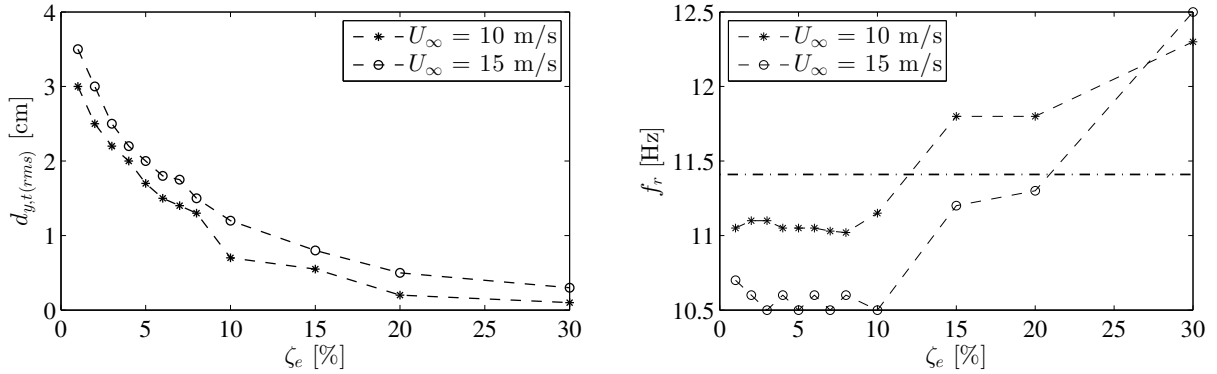


Figure 6.19: The average peak vertical tip displacements (a) and response frequency (b) of the T-shaped cantilever with tip mass. Simulations are performed for different electrical damping under U_∞ of 10 m/s and 15 m/s.

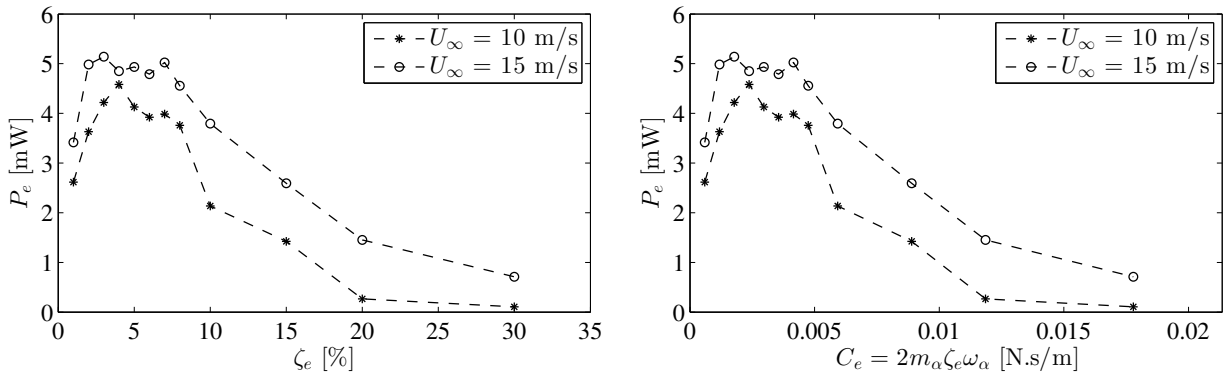


Figure 6.20: The predicted power outputs of T-shaped cantilever harvester are compared in (left) and (right) for different electrical damping under U_∞ of 10 m/s and 15 m/s.

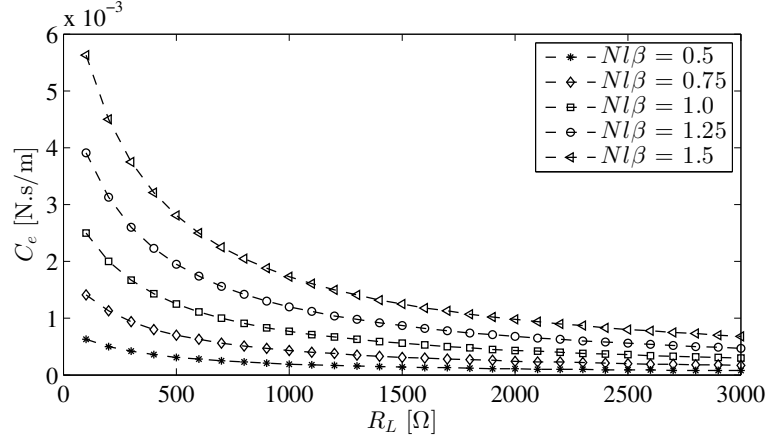


Figure 6.21: The electrical damping for different coupling coefficients $NI\beta$ and load resistances R_L considering $R_C = 300 \Omega$.

respectively. If the value of $NI\beta$ is considered 1.0, the critical R_L are identified 545 Ω and 825 Ω from Fig. 6.21 for wind speeds 10 m/s and 15 m/s, respectively. In case of $NI\beta$ equal 1.5, the critical R_L are identified 1600 Ω and 2230 Ω , respectively.

This presented backward procedure shows that it is efficient to utilize coupled FSI simulations to find the aeroelectromechanically optimized system for a target wind speed for a target harvester volume. It helps to obtain an idea about the critical damping as well as the maximum potential energy output for the target wind speed.

The value of $NI\beta$ depends on experimental setups such as the distance between the magnet and coil [47]. From a practical point of view, the value of $NI\beta$ for a T-shaped cantilever harvester for defined resistances can be calculated by performing free vibration tests. Once the value of $NI\beta$ is known, the electrical resistance can be calculated based on the identified $C_{e(crit)}$ for a target wind speed. This simplified optimization framework for the selection of electrical parameters based on the critical damping can save time and effort of numerical and experimental testing the prototype harvesters.

Application of the framework on geometrically optimized T-shaped harvester

In the following, the geometrically optimized T-shaped harvester, which has been shown in Sec. 6.6.2 under the wind speed of 8 m/s, is considered here to study the performance in higher wind speeds as well as for identifying critical electrical parameters.

The coupled simulations are performed under wind speeds 8 m/s, 12 m/s, 15 m/s, and 20 m/s for different electrical damping ratios ζ_e . The predicted average peak displacement, response frequency, and power outputs are displayed in Fig. 6.22 for different electrical damping. The maximum power outputs are predicted 5.41 mW, 8.7 mW, 16.3 mW, and 34.7 mW under wind speeds 8 m/s, 12 m/s, 15 m/s, and 20 m/s, respectively. The electrical parameters can be selected as mentioned in previous section by preparing a reference plot like Fig. 6.20(c) with the help of Eq. (6.6).

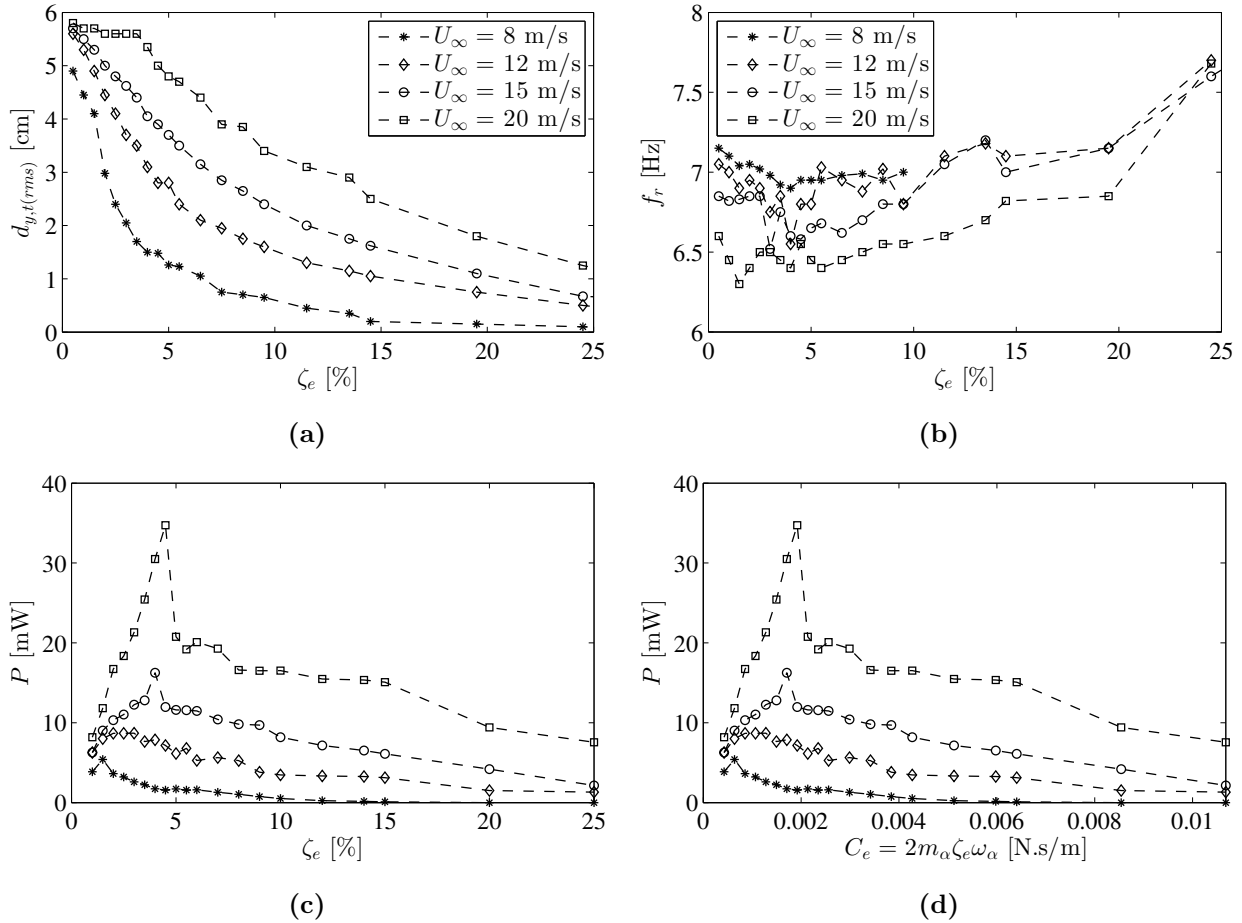


Figure 6.22: Coupled analysis of a geometrically optimized T-shaped harvester under different wind speeds: (a) vertical tip displacements, (b) response frequency, (c) and (d) power outputs for different electrical damping.

6.7.2 Studies on different cantilevers for preliminary assessment of piezoelectric harvesting

This section discusses on the governing equations of piezoelectric energy harvesters with a focus on critical parameters that are responsible for the performance of the harvesters. The aeroelectromechanical coupled simulations are performed on inverted and T-shaped cantilever systems, schematically shown in Fig. 6.23, to perform a preliminary investigation on their potential for piezoelectric energy harvesting.

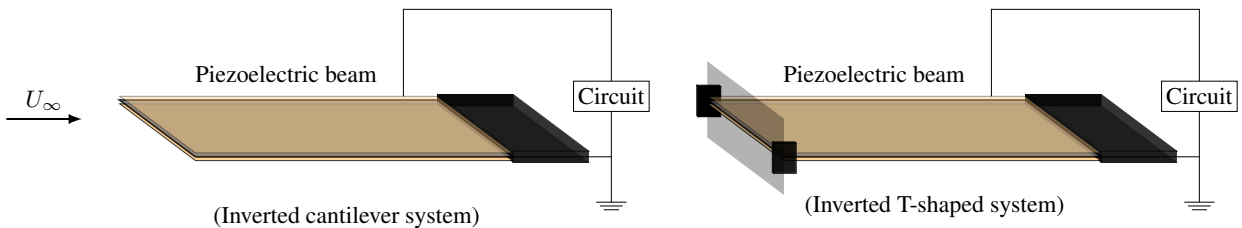


Figure 6.23: Schematic representation of piezoelectric energy harvesting from the vibration of cantilever beams under wind flow: inverted cantilever beam (left), and inverted T-shaped cantilever with tip mass (right).

The single-degree-of-freedom (SDOF) modelling of the harvester beam is a frequently used modelling approach since it allows simple expressions for the electrical outputs. Two governing equations those include the mechanical and electrical parts are repeated again

$$m\ddot{d}_{y,t} + c\dot{d}_{y,t} + kd_{y,t} - \Theta V = F_t, \quad (6.21)$$

$$\Theta \dot{d}_{y,t} + C\dot{V} = -\frac{V}{R} = I. \quad (6.22)$$

The harvested power (P_p) for an inertial piezoelectric harvester was found to be proportional to the vibration amplitude and to the cube of the operation frequency [16, 171] such that

$$P_p \propto d_{y,t} f_r^3, \quad (6.23)$$

where f_r is the frequency of vibration of the cantilever harvester. It is clear that the increase in operational frequency increases the power output more than the tip displacement $d_{y,t}$.

The response comparison in Fig. 5.15 shows that the inverted cantilever plate among the studied systems vibrates with maximum tip displacement. It is found comparatively less in case of inverted T-shaped cantilever; however, the response frequency of the T-shaped system shows its higher potential for piezoelectric energy harvesting. Therefore, the values of $(d_{y,t}/L)f_r^3$ are compared in Fig. 6.24 for different cantilever systems under different wind speeds. The comparison is declared qualitative since the FSI simulations are performed based on the mechanical system only; the piezoelectric effects haven't been included. The tip displacements ($d_{y,t}$) in Fig. 6.24 are normalized here by the length (L) of the cantilever to represent the displacement type whether they are small or large in amplitude.

The values of $(d_{y,t}/L)f_r^3$ for inverted T-shaped cantilever are found approximately in between 770 and 850 for wind speeds 7-20 m/s. In case of the harvesters studied in [183] and [149], the values of $(d_{y,t}/L)f_r^3$ of the harvesters for the maximum power output are found approximately 400 and 60, respectively. Even though the electrical damping hasn't been account, the study shows the necessity of performing a preliminary investigation on different cantilever systems to understand their potential for energy harvesting. The FSI simulations can be particularly

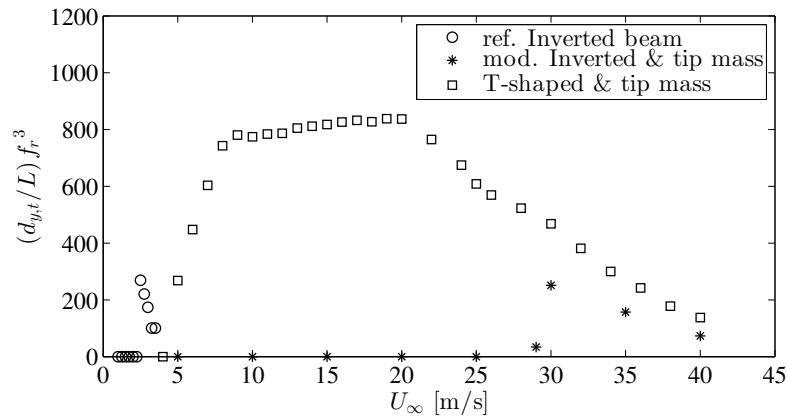


Figure 6.24: Analysing the potential of piezoelectric energy harvesting of different cantilever systems for a wide range of wind speeds: a qualitative comparison is shown with respect to influential parameters to optimize power output. Here, the higher value of $(d_{y,t}/L)f_r^3$ shows higher potential of energy harvesting from the system response under the simulated wind speed.

helpful not only to find appropriate system but also to find the optimum system dimensions to achieve the maximum value of $(d_{y,t}/L)f_r^3$ for a particular target wind speed.

A comparative study is performed on the inverted cantilever and T-shaped cantilever with tip mass for piezoelectric energy harvesting. The reference inverted cantilever (Sec. 5.2.3) and the modified T-shaped cantilever with tip mass (Sec. 5.3) are considered here. The assessment here is qualitative since the simulations are not properly aeroelectromechanical coupled. The governing equations (Eqs. (6.21) and (6.22)) are not solved in coupled manner. Different electrical damping ratios are considered as a representation of the electrical damping effects. If the cantilevers are of same length and width, and with the same amount of piezoelectric patches on both surface it may be assumed for a specific electrical configuration that the damping effects in terms of ζ_e are in a similar range (e.g., the cantilevers of same length and width in Fig. 6.23). The aim is to investigate the coupled behaviour of the systems under different ζ_e qualitatively.

The values of $(d_{y,t}/L)f_r^3$ are compared in Fig. 6.25. It is important to note that the studied wind speeds are different based on the type of cantilever system. The inverted cantilevers are found promising for under very low wind speeds like 2.5 m/s, at which the T-shaped cantilever with tip mass shows no flutter response. Importantly, the inverted cantilevers shows less influence by the increase in electrical damping, particularly in terms of $(d_{y,t}/L)f_r^3$ for ζ_e up to 10 %. This is due to the low bending stiffness (D) and modal mass of the inverted

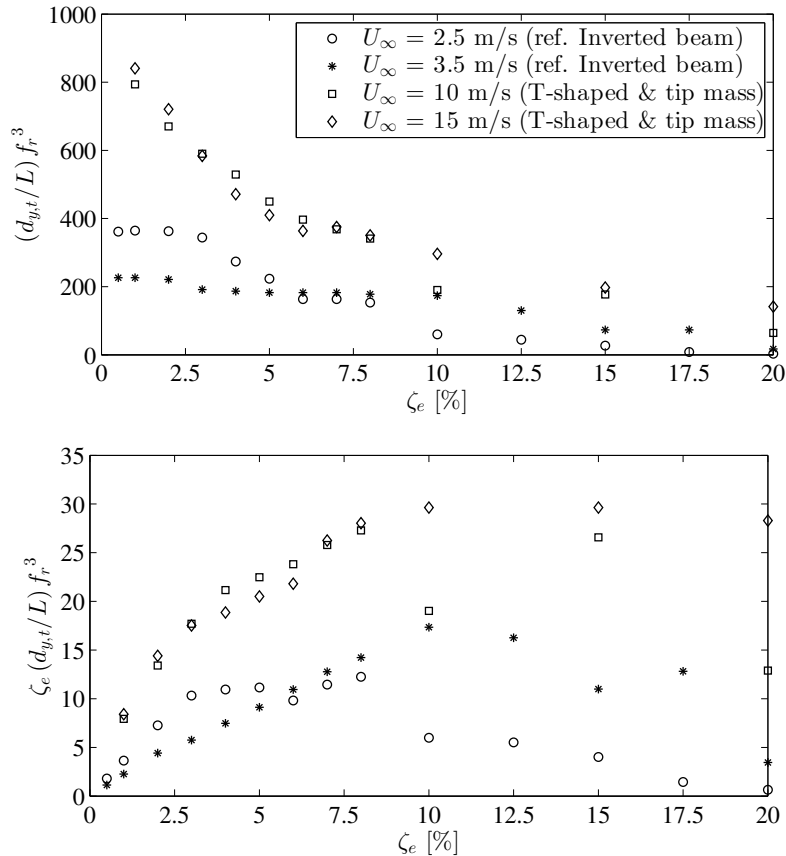


Figure 6.25: Preliminary investigation on the potential of piezoelectric energy harvesting of different cantilever systems: a qualitative comparison is shown with respect to influential parameters. Here, the value of $(d_{y,t}/L)f_r^3$ in (top) shows the potential of energy harvesting under the simulated wind speed. The influence of damping is portrayed in (bottom), qualitatively.

cantilever system.

The values of $(d_{y,t}/L)f_r^3$ for T-shaped cantilever are found greater than those of inverted cantilever when compared for same damping ratio, however, for higher wind speeds of 10 m/s and 15 m/s. Considering that the power output is linearly proportional to electrical damping. The values of $\zeta(d_{y,t}/L)f_r^3$ are compared in Fig. 6.25(b) to identify the optimum electrical damping ratio.

This study shows that the inverted cantilevers are more promising when the target wind speed is low. Moreover, what makes inverted cantilever promising is its predictability of critical wind speed based on the bending stiffness (Eq. 5.3) in order to exploit the range of low wind speeds by using several different harvesters. The T-shaped cantilever with tip mass, which is sensitive to damping, is more preferable for higher wind speeds. The benefit of T-shaped cantilever is that one harvester is able to harvest energy for wide range of wind speeds.

6.8 Summary

This chapter has presented a 2D aeroelectromechanical coupled model for simulation of thin-plate flexible systems to evaluate and optimise the performance of aeroelastic energy harvesters. The electrical damping effects, which are associated with the resistances of the electromagnetic transducer, are modelled in a simplified manner by using the Rayleigh damping model. As a validation of the presented coupled solver, the onset flutter wind speed, energy output and the critical onset flutter electrical resistances under different wind speeds (4–8 m/s) have been modelled and estimated satisfactorily in comparison with the reference results from wind tunnel experiment.

The optimization of harvester performances depends on many parameters such as the geometry, the mechanical system, its interaction with incoming wind, the electrical damping, and its effect on aeroelastic interactions. Therefore, it is necessary to understand the influence of different parameters individually. Overall, the two most influential parameters that influence the power outputs have been discussed to be electromagnetic damping and relative velocity movement between coil and magnet. The increase in electromagnetic damping enhances the power output; however, it damped the flutter response down. The other option is to increase the velocity of vibration, which may be achieved by increasing the system frequency and/or by allowing the system to vibrate at large amplitudes. Hence, keeping this information into consideration, the geometric modification has been performed over the reference T-shaped system by changing the length and thickness to find an optimized harvester configuration. The predicted power output of the optimized harvester (maximum envelope volume of 42 cm³) at wind speed 8 m/s is found as 5.3 mW, which is five times the power output extracted from the reference harvester (envelope volume of 25.2 cm³) at the same wind speed.

A comparative study on different cantilever systems is performed to obtain guidelines for the preliminary design of experimental set-ups of prototype harvesters. The aim is to deliver a multi-objective optimisation based on aeroelastic interactions of different cantilever systems, the conversion mechanisms, identification of critical electrical parameters, etc. The changes in aerodynamic behaviour and flapping pattern of inverted and T-shaped cantilever harvesters with/without tip mass are investigated. The simulations are performed for increasing wind speeds until the permanent deflection mode occurs. The electromagnetic and piezoelectric conversion approaches are considered only. The influences of damping ratios are analysed as

preliminary studies to investigate the electrical damping effects of energy harvesters. The influential parameters such as response amplitude and oscillating frequency are compared to identify not only efficient cantilever harvesters but also an appropriate combination of physical and electrical parameters depending on target wind speeds. The study results show that the inverted cantilever plate is excellent for piezoelectric energy harvesting from very low wind speed, however, for a narrow range of wind speeds. On the other hand, the T-shaped cantilever with tip mass is very good for electromagnetic and piezoelectric energy harvesting, however at high wind speeds. The benefit of this system is that it can harvest for a wide range of wind speeds.

Chapter 7

Modelling the effect of free stream fluctuations on aeroelastic interactions

7.1 Introduction

In this chapter, the vorticity carrying particles are utilized for the simulation of inflow fluctuations within the framework of two-dimensional (2D) vortex particle methods (VPM). Two new extensions of VPM are presented using the concept of seeding vortex particles in the free stream velocity. The first approach allows for simulating pulsating or periodic incoming flow. In contrast, the second approach models inflow fluctuations as a reproduction of an original simulation of turbulent wakes or vortex shedding from upstream bodies. The extensions are proposed to be used to model inflow fluctuations for FSI simulation of flexible systems, however, of rigid systems too.

The concept of seeding particles for VPM was introduced in Prendergast and McRobie [192] and Prendergast [193] for modelling of 2D unsteady wind. The particles were pre-calculated from statistically generated target turbulent wind field. The method was further employed in Hejlesen et al. [115], Rasmussen et al. [197] for the simulation and estimation of the aerodynamic admittance in bridge aerodynamics. The particle seeding techniques within the context of presented VPM-based solver was presented in Kavrakov and Morgenthal [140, 141], Tolba and Morgenthal [234, 235, 236] to simulate turbulent flow in multiple 2D slices for pseudo-3D buffeting analysis of long-span bridges.

The pulsating flow fluctuation is modelled by seeding pre-calculated particles from two seeding points near the upstream boundary. The seeding mechanism and the orientation of the particles are handled such that they induce only horizontal velocity components around the centre of the domain. In contrast, the vertical velocity components are nearly cancelled out. In the second numerical extension, the particles are seeded for the reproduction of a simulated wake flows from upstream bluff bodies. The method is referred to as flow reproduction method (FRM). The vorticity calculation and the seeding techniques of the vortex particles are quite similar to the approached mentioned in Prendergast and McRobie [192] and Prendergast [193].

7.2 Pulsating incoming flow

7.2.1 Background

In fluid dynamics, a flow with periodic variations is known as pulsating flow. The pulsations are characterised by the form of the upstream flow velocity as follows

$$U(t) = \bar{U} + u_m \sin(2\pi ft + \phi) = \bar{U} + u(t), \quad (7.1)$$

where \bar{U} is the mean flow velocity, u_m is the amplitude of the maximum deviation of the flow fluctuations, f is the signal frequency, ϕ is the phase angle at time $t = 0$, and $u(t)$ is the fluctuating velocity component along the flow direction.

The study of unsteady pulsating flow is of practical engineering importance especially in the field of turbo-machinery [13, 101, 102, 157, 158], blood flow in the circulatory system [155, 207, 213, 239], design of total artificial lung to provide better gas exchange [195]. With an assumption of flow parallel to the pipe axis, Uchida [237] presented an exact solution of pulsating laminar flow superposed on the steady fluid motion in a circular pipe. The understanding of the characteristics of vibrations induced by the vortex shedding is of great importance in the design of marine risers [109, 172]. The pulsating flow has a significant influence on the vortex shedding and lock-on of cylindrical sections [17, 29, 128, 143, 222]. Furthermore, it was shown experimentally in [130] that the heat transfer from a square cylinder can be enhanced substantially by keeping the pulsating frequency within the lock-on regime.

7.2.2 A New Numerical Technique in VPM for Pulsating Flow

The proposed numerical scheme

The proposed numerical technique is presented in Fig. 7.1 for a particular time instance. The particles are released from two seeding points (top and bottom) near the upstream, and they are convecting downstream in the free stream flow U_∞ . The particles that exist in between the seeding section and the downstream border are only responsible for the external influence on the velocity field. The intention is to induce target periodic flow fluctuations around the centre of the simulation domain.

The generated fluctuating flow may be confronted by a downstream structural system, e.g., a small-scale energy harvester, as shown in Fig. 7.1. It is essential to investigate the particles, particularly, the way they influence on the velocity field around the centre of the simulation domain when the strength and the orientation of the particles are varied periodically. However, it is convenient to study first the influences of the convecting particles of constant strength before imposing the variation for the simulation of pulsating flow.

The velocity field from vortex particles

The velocity contributions of a few particles in the centre of the simulation domain are displayed schematically in Fig. 7.1. Here, some equidistant particle pairs are convecting forward, and the absolute strength of the particles in each pair are equal. Since the rotational direction of the particles in each pair is opposite, the particles allow cancellation of vertical velocity components u_y at the centre of the domain in contrast to imposing the horizontal veloc-

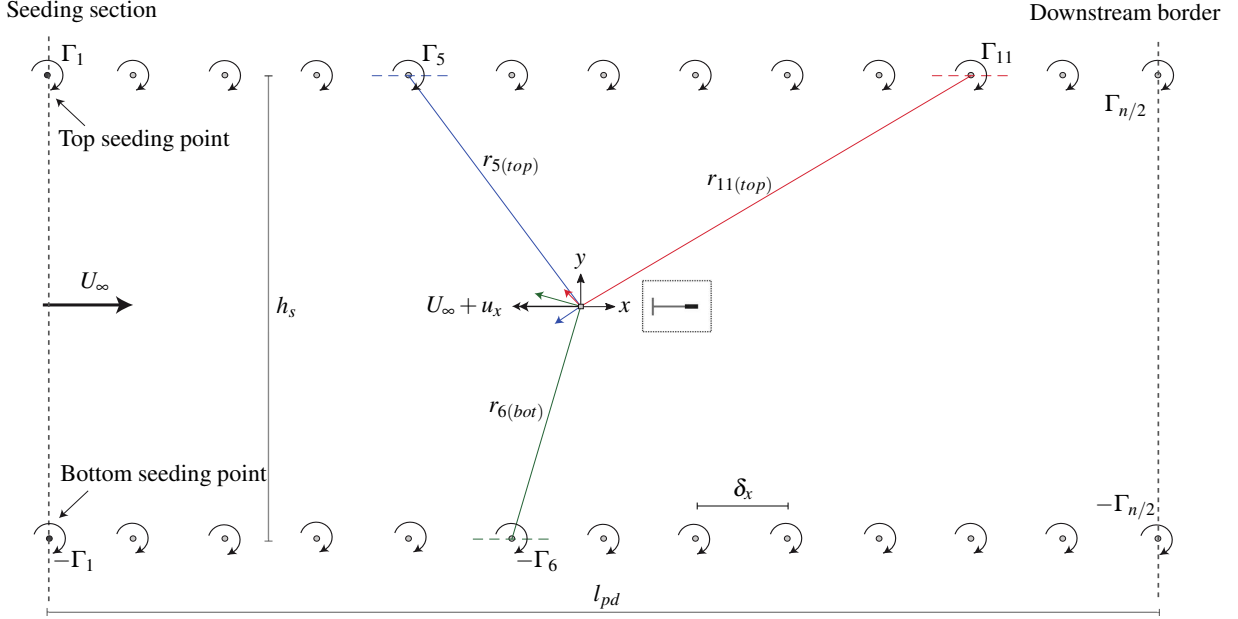


Figure 7.1: The schematic of a proposed numerical scheme for the simulation of pulsating incoming flow within the framework of 2D VPM: the particles are regularly released from the upstream two seeding points which are separated by a distance of h_s . The particles are convecting downstream in the free stream flow U_∞ . Here, l_{pd} is the effective length of the domain for the particles. The centre of the simulation domain is the target location for the simulation of pulsating flow. The induced resultant velocity components are shown in the domain centre from the convecting particles in the top and bottom layers. A small-scale structural system such as the energy harvester is shown just after the centre of the domain to indicate that the performance of the harvester under the periodic fluctuation is of particular study interest.

ity component u_x . Therefore, the calculation of the particle strengths and their rotational direction is a prerequisite.

Some assumptions are applied to make the pre-calculation process practicable. For example, the particles are considered convecting straight in the free stream flow, as shown in Fig. 7.1; the interaction among the particles are ignored in the calculation process. Therefore, the distance between the consecutive particles along the flow direction is assumed to equal and denoted as δ_x . Now, considering that roughly n number of particles exist in the defined simulation domain for a particular time instant. The particles are convecting in two layers, which is separated by a distance of h_s . The number of particles in the domain for a specific layer is assumed to be $n/2$. In the case of random particles convecting in two layers, the amount of fluctuation in the flow field from the contribution of all the convecting particles can be expressed as follows

$$u(\mathbf{x}) = -\frac{1}{2\pi} \sum_{p=1}^{n/2} \frac{\Gamma_{p(top)} \times (\mathbf{x}_p - \mathbf{x})}{|\mathbf{x}_p - \mathbf{x}|^2} - \frac{1}{2\pi} \sum_{p=1}^{n/2} \frac{\Gamma_{p(bot)} \times (\mathbf{x}_p - \mathbf{x})}{|\mathbf{x}_p - \mathbf{x}|^2}, \quad (7.2)$$

where $\Gamma_{p(top)}$ and $\Gamma_{p(bot)}$ represents the p^{th} pair of vortex particles convecting in top and bottom particle layers, respectively. Now, considering that the particles in a pair for each release step are of same absolute strength such that $|\Gamma_{p(top)}| = |\Gamma_{p(bot)}| = \Gamma_p$; however, the rotational direction is opposite as shown in Fig. 7.1. Since the magnitude and the rotational

direction of the particles are predefined, the pattern of particle contributions in the domain centre is obvious. Therefore, the term $(\mathbf{x}_p - \mathbf{x})$ is replaced by r in Eq. (7.2), and the velocity contribution of the particles in between the layers of convecting particles can be expressed as follows

$$u(\mathbf{x}) = -\frac{1}{2\pi} \sum_{p=1}^{n/2} \Gamma_p \left(\frac{1}{r_{p(top)}} + \frac{1}{r_{p(bot)}} \right), \quad (7.3)$$

$$u(\mathbf{x}) < 0, \text{ if } \Gamma_{p(top)} > 0 \text{ and } \Gamma_{p(bot)} < 0 \text{ and, vice-versa.}$$

Note that the particle map is symmetric concerning the horizontal axis x based on the applied assumptions. Therefore, the vertical velocity component in the centre of the domain, $u_y(x_c)$, induced by the released vortex particles can be neglected due to the cancellation of the contribution from the particles from the top and bottom particle layers. However, the total horizontal velocity component in the centre of the domain from Eq. (7.3) can be expressed as follows

$$u_x(\mathbf{x}_c) = -\frac{1}{2\pi} \sum_{p=1}^{n/2} \Gamma_p \left(\frac{1}{r_{p(top)}} \frac{h_s/2}{r_{p(top)}} + \frac{1}{r_{p(bot)}} \frac{h_s/2}{r_{p(bot)}} \right). \quad (7.4)$$

If the absolute strength of the released particles are considered equal such as Γ , the induced velocity component in the centre of the domain can be expressed as follows

$$u_x(\mathbf{x}_c) = -\frac{\Gamma h_s}{4\pi} \sum_{p=1}^{n/2} \left(\frac{1}{r_{p(top)}^2} + \frac{1}{r_{p(bot)}^2} \right) = -\frac{\Gamma h_s}{4\pi} F_r, \quad (7.5)$$

if $\Gamma_{p(top)} = \Gamma$ and $\Gamma_{p(bot)} = -\Gamma$,

where F_r is the factor that counts the influence of the distance of the particles from the centre of the domain. The Eq. (7.5) shows that the amount of velocity component, which can be induced at the centre of the domain, depends on the strength of the particles Γ , the distance between the particle seeding points h_s . The Eq. (7.5) particularly shows that a constant horizontal velocity component can be induced in the centre of the domain if the absolute strength of all the released particles are same while the rotation directions are maintained opposite, as discussed. Now, to induce a constant target velocity component $u_x(\mathbf{x}_c)$, when the parameters U_∞ , h_s , δ_x and n are already selected, the strength and the rotation of the particles for top and bottom layer can be calculated from the following equations

$$\Gamma_{p(top)} = -\Gamma_{p(bot)} = \begin{cases} \frac{4\pi |u_x(\mathbf{x}_c)|}{h_s F_r}, & \text{if } u_x(\mathbf{x}_c) \leq 0, \\ -\frac{4\pi |u_x(\mathbf{x}_c)|}{h_s F_r}, & \text{otherwise.} \end{cases} \quad (7.6)$$

Variation of vorticity to simulate periodic flow fluctuations

It is shown in Eq. (7.6) that an additional constant velocity component can be induced in the centre of the simulation domain as long as the particles are seeded in the free stream flow by keeping their strength and orientation unchanged. Now, if the strength of the predefined vortex particles is varied gradually while seeded from the upstream two points, it is expected to have time-dependent fluctuations in the centre of the domain.

The aim is to model the target periodic flow in the centre and its surrounding of the simulation domain. To calculate the attribute of the particles conveniently, the Eq. (7.6) has been used by replacing $u_x(\mathbf{x}_c)$ with $u(t)$. Note that the particular attention in this study is the simulation of very low-frequency periodic flow. In such a case, the wavelength of the periodic flow $\lambda = U_\infty/f$ is much larger than the domain length L such that $\lambda \gg L$, and the changes in the strength of the particles those exist in the simulation domain due to the required variation in strength is negligible. Hence, the Eq. (7.6) can be used piecewise for calculating the periodic time history of the particle strengths. Now, to simulate the periodic fluctuation shown in Eq. (7.1), the average velocity of the periodic flow \bar{U} is modelled by the free stream flow U_∞ whereas the fluctuating components $u(t)$ are modelled by releasing the pre-calculated particles. If the particles are assumed to be released in every Δt_r step, the piecewise time history of the particles for top and bottom particle release points are calculated using the following equations

$$\Gamma_{top}(t_i) = -\Gamma(u_m) \frac{u(t_i)}{u_m}, \quad (7.7)$$

$$\Gamma_{bot}(t_i) = \Gamma(u_m) \frac{u(t_i)}{u_m}, \quad (7.8)$$

where t_i is the discrete time at which the i^{th} particles have to be released, $\Gamma(u_m)$ is the particle strength to induce a velocity component of u_m using Eq. (7.6), and $u(t_i)$ is the fluctuating component at discrete time t_i .

7.2.3 Flow fluctuations using vorticity carrying particles

The aim is to simulate specific flow fluctuations within a target smaller domain around the domain centre, in which a structural system like energy harvester may be tested under the modelled periodic flow. Therefore, the size of the simulation domain and the vertical distance between the particle layers should be large enough to minimize the mutual interactions of the particles.

Flow field influenced by constant strength particles

In this study, the absolute strength of the particles is kept constant to induce constant velocity components ($\pm u_m$). The particles are calculated based on the Eq. (7.6), and clearly, they depend on the known positions of the particles and the distance between particle layers (h_s). A rectangular simulation domain of length L and height H is chosen, such that $L/H = 2$. The height of the particle seeding points h_s is chosen such that $h_s/L = 0.4$, c.f. Fig. 7.1.

The simulations are performed for non-dimensional time (tU_∞/L) of 20 with a time step $\Delta t U_\infty/L = 0.00096$. The particles are seeded with a release time step of Δt_r such that $\Delta t_r/\Delta t = 4$. It is assumed that all the seeded particles will convect with the velocity of free stream flow U_∞ . Based on this assumption, the particle distance δ_x can be calculated ($\delta_x = U_\infty \Delta t_r$). Now, the approximate number of particles at each particle layer using Eq. (7.9),

$$N_{P_{cpl}} \approx l_{pd}/(U_\infty \Delta t_r) + 1 \approx l_{pd}/\delta_x + 1, \quad (7.9)$$

is found to be 260. The constant strength and the orientation of the particles are calculated to induce a constant velocity component (u_m/U_∞) of 0.15 along the flow direction. The strength time histories of the seeded particle are shown in Fig. 7.2 (a). The numerical parameters are summarized in Table 7.1.

Numerical parameters		Value
Peak amplitudes of longitudinal velocity fluctuation	u_m/U_∞	± 0.15
Length/height of the domain	L/H	2
Distance between seeding and downstream section	l_{pd}/L	0.998
Height of particle seeding points	h_s/L	0.4
Simulation time step	$\Delta t U_\infty/L$	0.00096
Particle release step	$\Delta t_r/\Delta t$	4
Number of particles calculated for each particle layer	$N_{P_{cpl}}$	260

Table 7.1: Simulation to induce additional constant velocity component to the free stream flow: numerical parameters.

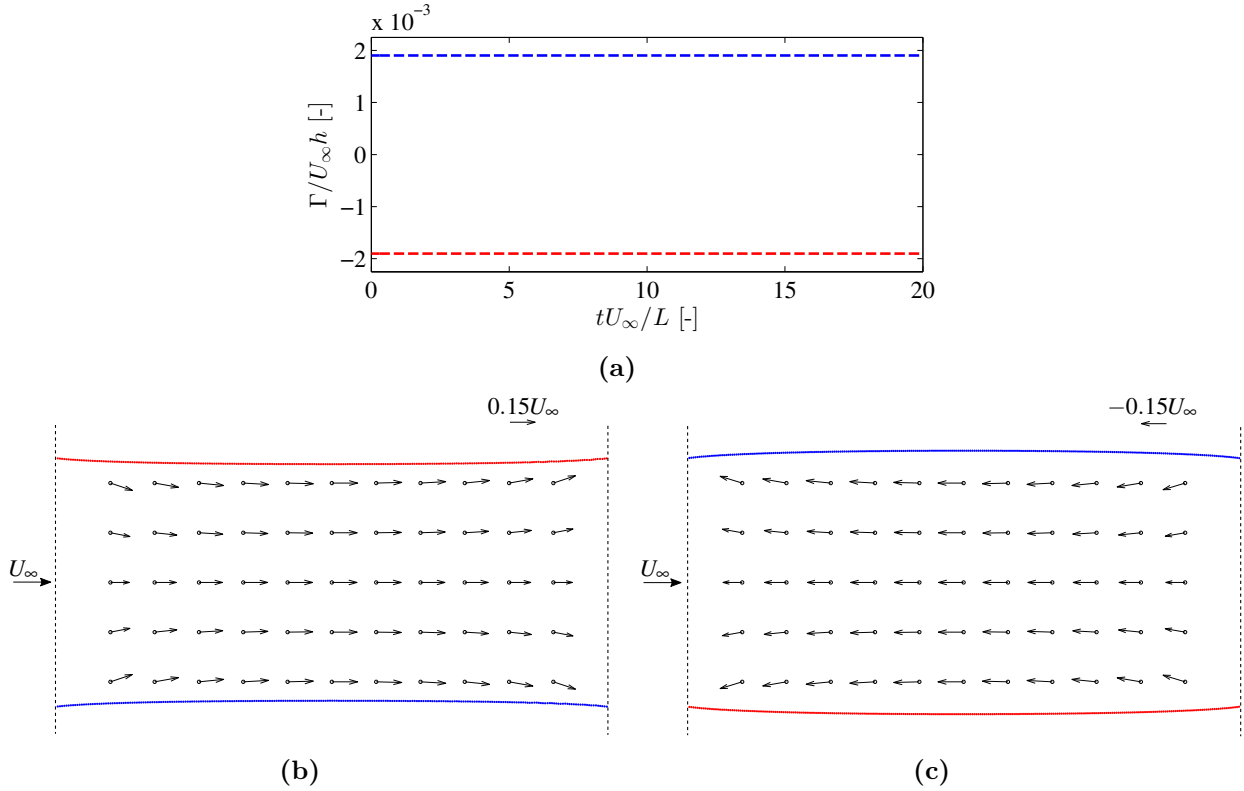


Figure 7.2: Study on the induced velocity field due to the regular seeding of the particles: (a) the discrete-time histories of the particles for the top and bottom seeding points. The time histories show that the particles are of same absolute strength and they are opposite in rotational direction. In (b)–(c), the constant flow fields are induced by the continual convection of the particles. The velocity components are shown influenced based on the choice of seeding points.

Two simulations are performed by releasing the particles, however, by alternating their seeding points. The flow field under the released particles are monitored, and the induced velocity components in the monitored positions are presented in Fig. 7.2 (b)–(c) for a particular time instant. Since the strengths of the particles are constant, the field vectors remain constant throughout the simulation. The induced velocity components around the domain centre are achieved with an error less than 0.25%. Expectedly, the induced velocity vectors are found quite uniform regarding the magnitudes along the flow direction. In contrast, the vertical components around the central portion of the simulation domain are almost zero (see Fig. 7.2 (b–c)). It is because of the opposite orientation of the particles, which allows the cancellation of the vertical velocity components.

Clearly, the interaction among the particle layers is observed in Fig. 7.2 (b–c). The particles are found convecting with velocities slightly different from U_∞ . The particles are observed moving faster in the study case of Fig. 7.2 (b) while moving slower in the study case of Fig. 7.2 (c). However, the particle velocities and the mutual interaction among the particles between two layers are so synchronized that the quality of the modelled flow fields for different target u is found within the satisfactory level.

Sinusoidal flow fluctuation along the flow direction

It is evident from the study results presented in Fig. 7.2 that the method has the potential to model periodic flow fluctuations, which may be performed by changing the strength of the vortex particles correspondingly, as explained in section 7.2.2.

Here, the periodic sinusoidal flow velocity $U(t)$ as shown in Eq. (7.1) is simulated; the non-dimensional peak velocity amplitude u_m/U_∞ and the non-dimensional frequency of the signal fL/U_∞ are chosen 0.15 and 0.1042, respectively. The time history of the particles for two particle release points are calculated based on Eq. (7.7) and Eq. (7.8). Importantly, the value of non-dimensional wavelength λ/L is 9.6 which satisfies the requirement of much larger wavelength than the length of the simulation domain.

The numerical parameters for this simulation is considered same as before in Table 7.1 except $tU_\infty/L = 96$. The free stream flows U_∞ is considered equal to the mean flow velocity \bar{U} of the target periodic signal whereas the fluctuations are intended to model from the contributions of the released particles. In this simulation case, the vortex particles which are changing in time are regularly released from the particle seeding points with a release time step of Δt_r such that $\Delta t_r/\Delta t = 4$.

The snapshots of the instantaneous absolute velocity field $U = \bar{U} + \sqrt{u^2 + w^2}$, as computed from the instantaneous fluctuating velocity components u and w , are shown in the left side of Fig. 7.3 (b–f). The non-dimensional colour-bar is provided to visualize the change of the velocity field with respect to the targeted flow fluctuations. The particle maps corresponding to the flow fields are shown on the right side of Fig. 7.3 (b–f). The associated changes in the strength of the vortex particles are also shown using colour-bar in terms of non-dimensional parameter $(\Gamma/U_\infty h)$ for corresponding time steps. The periodic behaviour of the flow field is visible in Fig. 7.3 and the quality of the modelled flow field is found satisfactory, particularly within the target small domain.

7.2.4 Quality assessment

This section presents the quantitative quality of the modelled periodic flow fluctuation in Sec. 7.2.3. Several sampling points are used in the central portion of the simulation domain to perform the flow monitoring, c.f. Fig. 7.4 (a). The sampling points are organized in a grid pattern to perform a profile-based quality assessment using statistical measures. The position of the sampling profiles along the flow direction (x) is shown to the coordinate system. Nine sampling profiles have been used at a non-dimensional spacing dx/h of 0.2.

The variation of the average flow velocity of the modelled flow in different sampling profiles are shown on the left side of Fig. 7.4 (b). The average error induced in the modelled average flow velocity from all the sampling points is found to be around 0.2 %. The variation of the modelled peak velocity amplitude for the sampling profiles are shown on the right side of Fig. 7.4 (b). The average of the peak velocity amplitudes (\bar{u}_m) in the central sampling

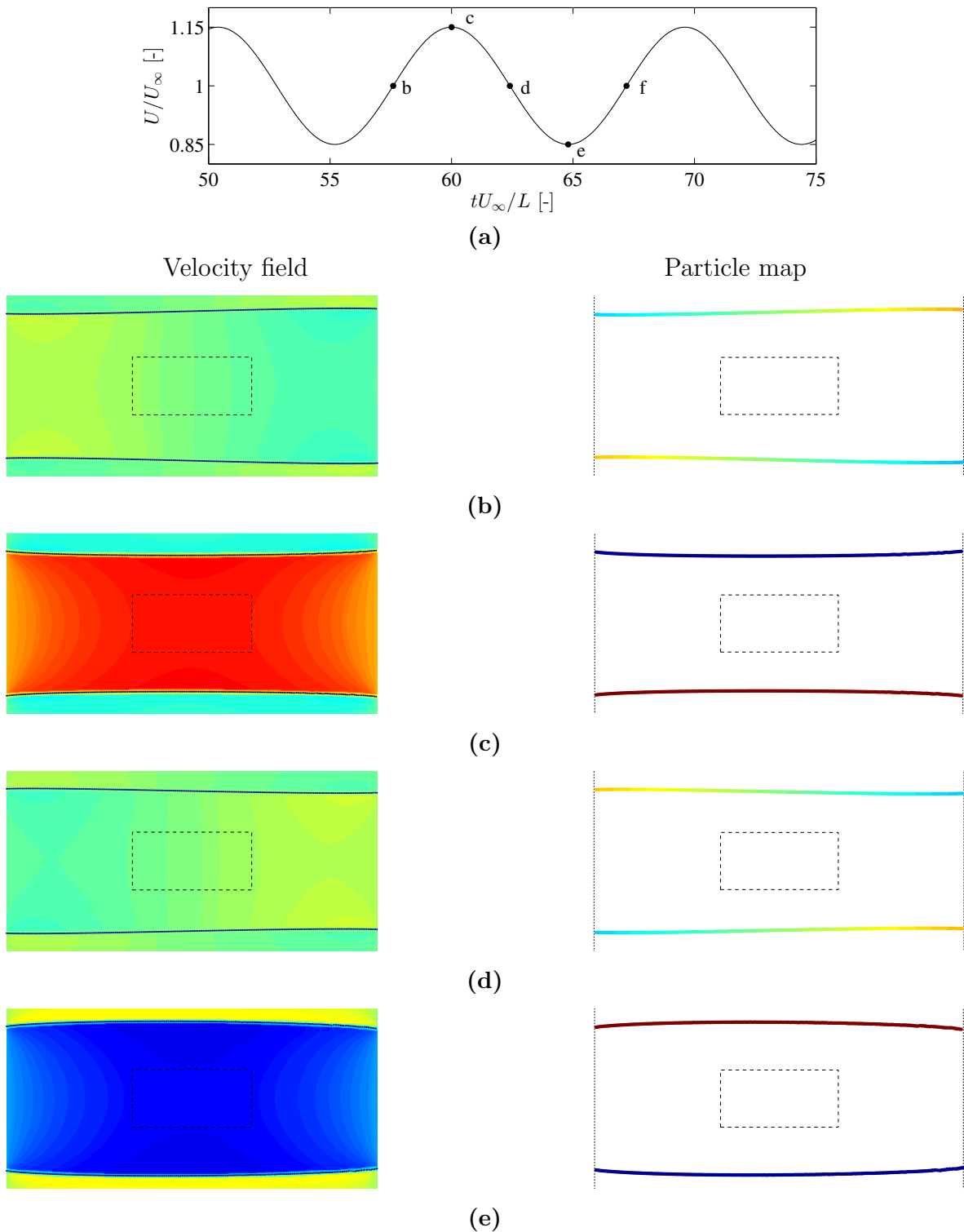


Figure 7.3: Periodic flow fluctuations by releasing predefined vortex particles ($u_m/U_\infty = 0.15$, $fL/U_\infty = 0.1042$): (a) the target sinusoidal flow fluctuations. The modelled instantaneous velocity field and corresponding particle maps are shown in (b-d) for different phases of the target flow such that (b) nT , (c) $(n+1/4)T$, (d) $(n+1/2)T$, (e) $(n+3/4)T$, and (f) $(n+1)T$. Here, T is the period of the target flow. The $\Gamma/U_\infty h$ shows non-dimensional particle strength. The dotted rectangle in the domain centre is to show the domain of interest for the target periodic flow (figure continued).

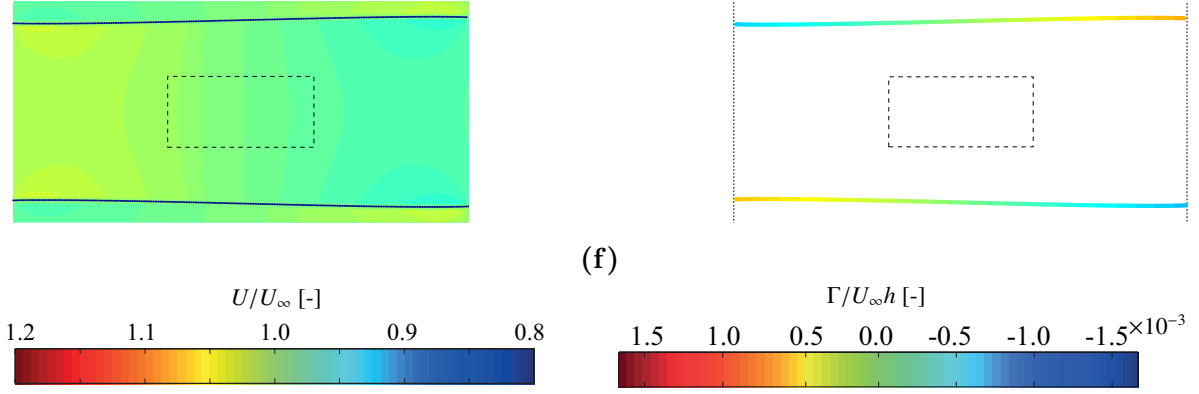


Figure 7.3: (continued)

profile has been observed deviated approximately around 1 % from the target value. The distribution of \bar{u}_m is found 2–4 % less for the five sampling profiles within the target smaller domain, which is shown using dotted lines in Fig. 7.4 (a). The error in \bar{u}_m is found increasing in the sampling profiles outside of the small target domain; however, the aim is to achieve the targeted periodic flow within the mentioned small domain in good quality. The necessity of having a sufficiently large domain that has been discussed earlier is particularly based on the quality of modelled flow within the target small domain.

In Fig. 7.4 (c), the instantaneous resultant flow field at the domain centre is compared with the target signal. The discussed reduction is found within the mentioned percentage in every studied case of fluctuating amplitudes; however, up to a maximum fluctuation frequency of $L/\lambda \leq 0.25$. Above this value, the wavelength of the flow is not sufficiently large compared to the length of the domain, and the quality of the flow decreases drastically, which is shown in Sec. 7.2.6.

7.2.5 Convergence of the proposed numerical scheme

The convergence of the proposed numerical scheme is studied for the employed number of particles within the simulation domain. It is, however, depends mainly on the release time step of the particles in the simulation. On the contrary, it is also possible to find the particle release time step based on a selected number of particles to be used.

The same periodic target flow is simulated in four different simulations in which the particles are seeded with the non-dimensional released time step $\Delta t_r/\Delta t$ of 1, 15, 50, and 100. The corresponding total number of vortex particles N_P is calculated 2080, 140, 42 and 22, respectively. The non-dimensional peak velocity amplitude u_m/U_∞ is targeted here 0.125. The non-dimensional frequency of the signal fL/U_∞ is chosen 0.1042, as before.

Fig. 7.5 compares the instantaneous flow fields for a specific time to observe the convergence of the flow field. The flow field converges with an increased number of particle. The time histories of the vortex particles which are calculated based on Eq. (7.7) and Eq. (7.8) are presented in Fig. 7.6 (a). The convergence of the flow field in the domain centre for the mentioned time instant is shown in Fig. 7.6 (b) depending on N_P . The simulations which are performed are entirely different for the particle map and the strength time histories. However, the modelled flow fields are observed quite similar when the modelled flow fields are compared, e.g. in Fig. 7.5 (c-d).

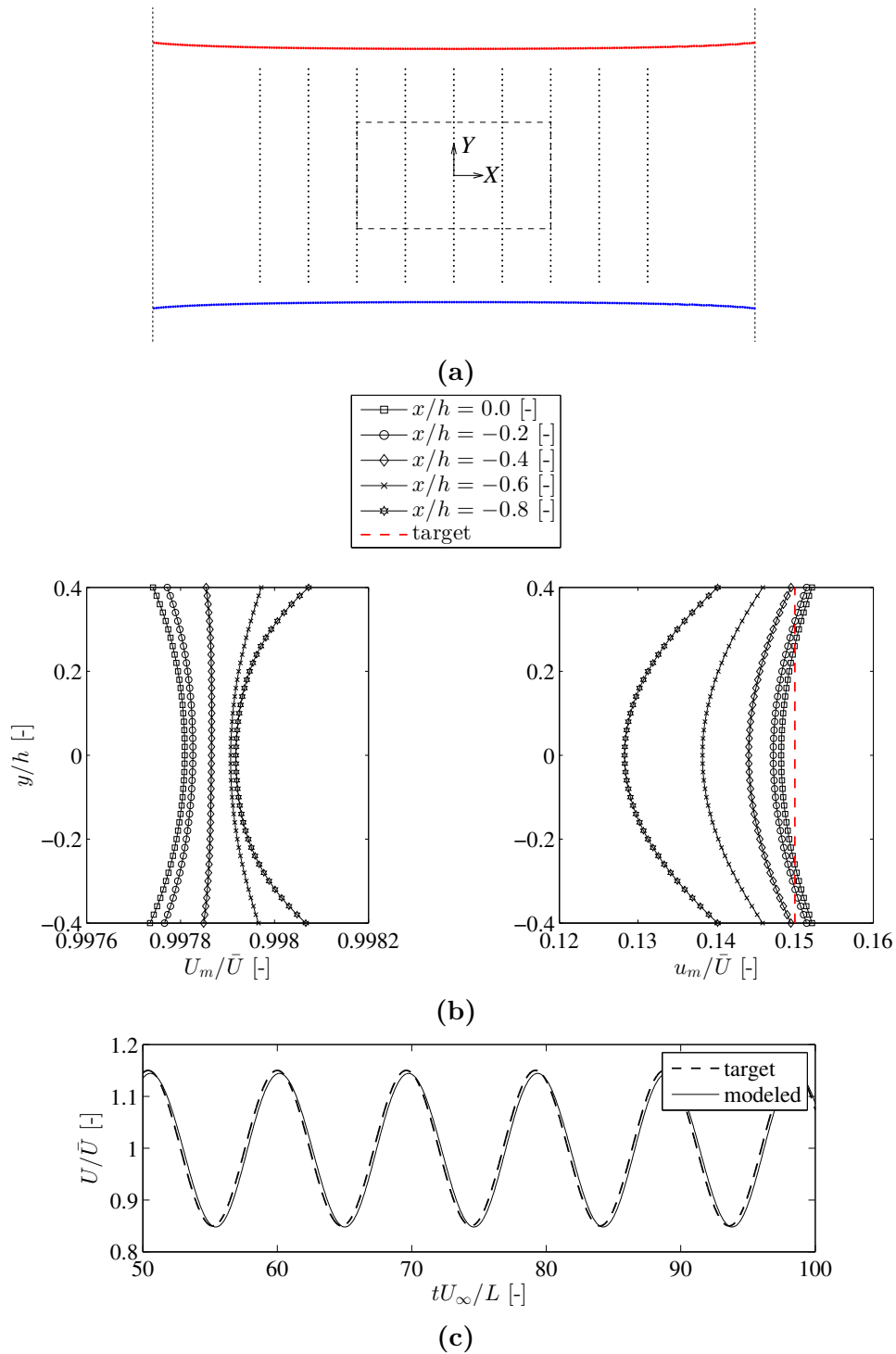


Figure 7.4: Quality assessment of the modelled periodic flow that has been presented in Fig. 7.3: the location of the velocity sampling points are shown in the simulation domain (a). The comparison of profiles for modelled mean flow and non-dimensional peak velocity u_m/\bar{U} are shown in the left and right side of (b), respectively. The location of the motoring profiles is presented in the legend with respect to their positions in the domain. The time history of the resultant velocity field of the modelled flow in the centre of the simulation domain is presented in (c).

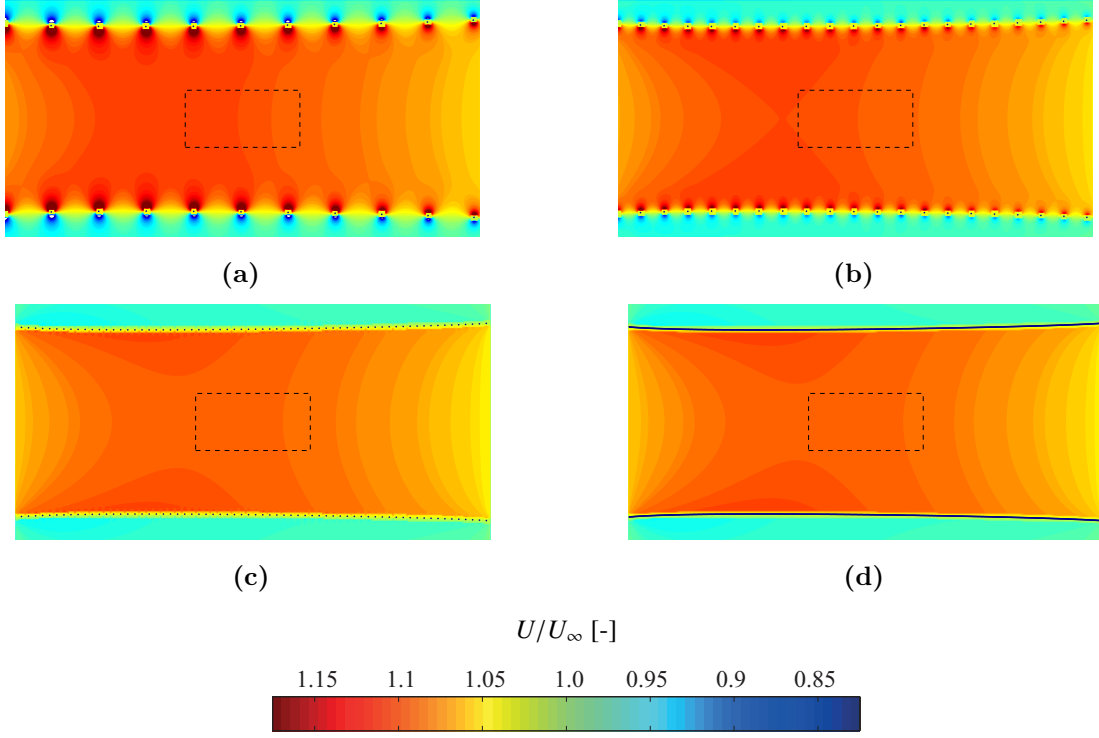


Figure 7.5: Convergence study to validate the proposed numerical scheme by simulating a target sinusoidal flow ($u_m/U_\infty = 0.125$, $fL/U_\infty = 0.1042$): the target flow is simulated in four ways for different number of seeded particles, and corresponding instantaneous velocity fields are compared in (a-d). Here, the simulations are performed for different particles seeding step ($\Delta t_r/\Delta t$) and total number of particles (N_P) such that (a) $\Delta t_r/\Delta t = 100$, $N_P = 22$, (a) $\Delta t_r/\Delta t = 50$, $N_P = 42$, (a) $\Delta t_r/\Delta t = 15$, $N_P = 140$, (a) $\Delta t_r/\Delta t = 1$, $N_P = 2080$, respectively.

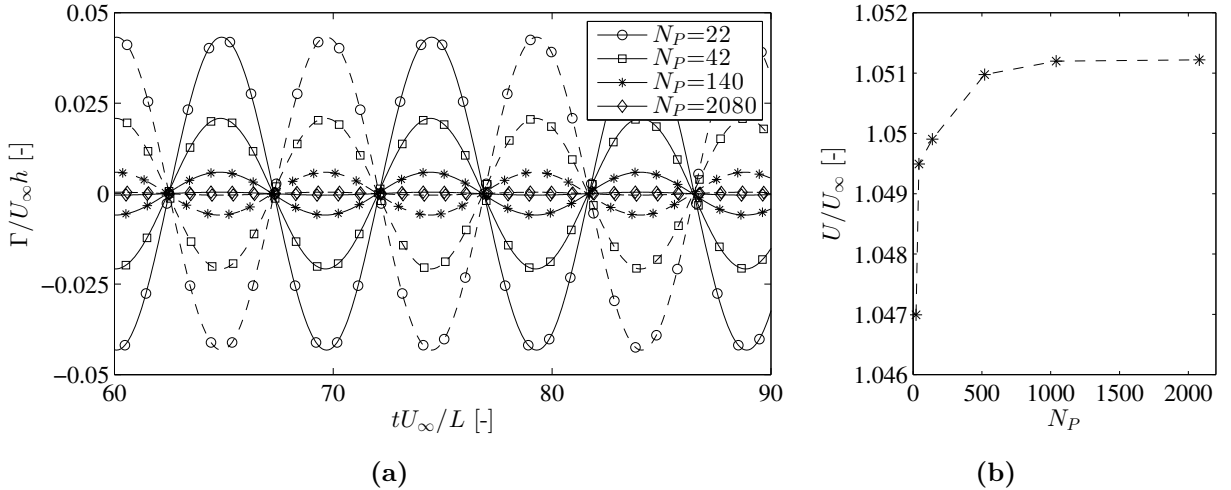


Figure 7.6: The influence of the number of particles (N_P) on the time histories of particle strength, and on the modelled flow fields (the simulation of the periodic flow in Sec. 7.2.5): (a) the periodic and discrete time histories of the particle strength for two seeding points depending on N_P , c.f. Fig. 7.5. Here, the solid lines (—) and dashed lines (- - -) show the discrete particle time histories for the top and bottom particle seeding points, respectively. (b) The convergence of the flow field in the domain centre for a particular time instant depending on N_P .

7.2.6 The influence of flow characteristics

In the following, the influence of the characteristic flow parameters such as the peak fluctuating velocity amplitude (u_m) and the frequency of the targeted sinusoidal flow signal are studied to estimate their influence on the performance of the numerical scheme. If the frequency of the periodic flow increases such that the wavelength becomes smaller than the length of the simulation domain, the assumption that neglects the slight variation of the particle strength is not valid any more. Therefore, it is expected to have a limiting frequency condition for a chosen domain size and flow characteristics.

Simulations are performed by targeting a range of peak velocity amplitude (u_m) and flow-frequency (f). The time step and domain parameters are chosen as before, c.f. Table 7.1. It means that the particle release step $\Delta t_r/\Delta t = 4$, and corresponding $N_P = 520$.

The modelled peak velocity amplitudes ($u_{m(mod)}$), the induced errors, and the modelled mean flow velocities are compared in Fig. 7.7 for different frequencies of the periodic flow. It is observed in Fig. 7.7 (a–b) that the quality of the modelled flow reduces drastically after a non-dimensional frequency limit value L/λ of 0.25. It is the upper frequency limit of periodic target fluctuation for the presented numerical scheme. The average velocity of the modelled flow, c.f. Fig. 7.7 (c), has been found sufficiently accurate for all frequency ranges. The observations show that the increase in u_m is not reducing the quality of the modelled periodic flow as long as the value of L/λ is far smaller than 0.25, c.f. Fig. 7.7 (a).

The accuracy of the numerical scheme is very high for the cases where the frequency of the flow fluctuation is very low. It has also been observed earlier in the case study of Fig. 7.2, in which the frequency is zero, and the quality of the induced fluctuations has been excellent. Therefore, it may be concluded that the method has the required potential to simulate a periodic flow signal, which is composed of several low frequencies ($\bar{U} + \sum_{i=1}^n u_{m_i} \sin(2\pi f_i t)$, for $i=1, 2, \dots, n$) such that $L/\lambda_i < 0.25$.

7.2.7 Influence of periodic fluctuations on T-shaped harvesters

This section presents the influence of inflow fluctuations on the aeroelastic motion and performance of T-shaped energy harvesters. The energy harvesters based on aeroelastic instability phenomena are analysed most commonly under steady wind speeds. The low-frequency periodic incoming flow is modelled here as a representation of the large eddies of atmospheric wind, especially to investigate their influences on the performance of flutter-based harvesters.

The channelization of the incoming flow using a funnel reduces the effects of the vertical fluctuations and the angle of attack of mean flow [48, 148, 185]. However, the variations of the wind speeds along the flow direction are unavoidable. The influences of the magnitude of the fluctuating flow and the fluctuating frequency on onset flutter wind speed of the harvester have been investigated.

The T-shaped system under periodic incoming flows

The simplified rigid beam model (c.f. Sec. 6.4.3) of the T-shaped harvester is used here to analyse the motion of the system under low-frequency periodic incoming flows. The energy output of the T-shaped electromagnetic harvester, apart from the electrical parameters, depends on the maximization of the vibration of the cantilever tip. Therefore, the study focuses particularly on the initiation and pattern of LCO of the harvesters.

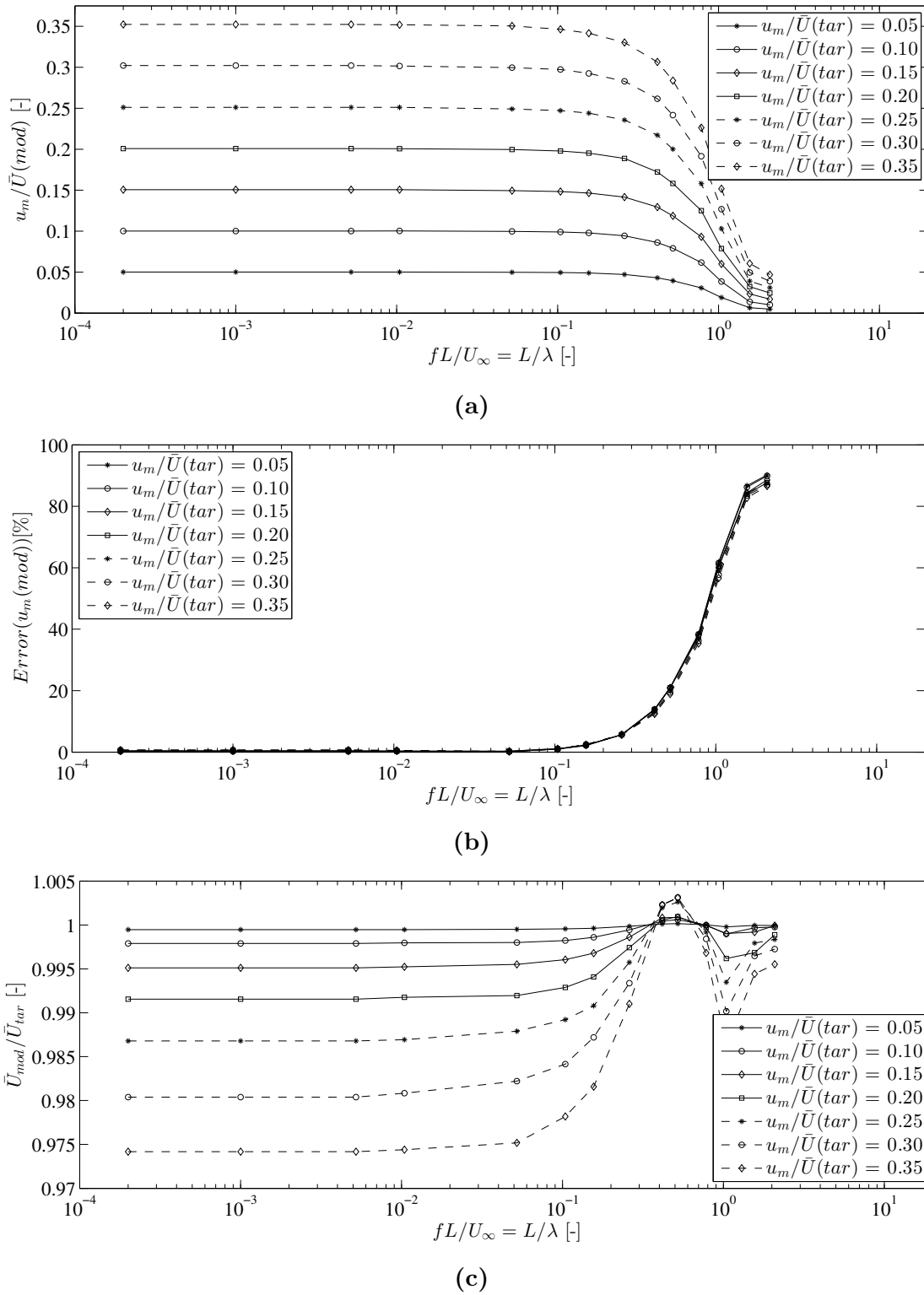


Figure 7.7: The quality of the modelled flow is presented with respect to the targeted peak velocity amplitude and the frequency of flow fluctuations. Here, the centre of the simulation domain is monitored only to compare the quality of the modelled flow. The modelled peak velocities ($u_m/\bar{U}(mod)$) are compared in (a) with respect to the targeted peaks for different ranges of targeted frequencies. The corresponding error percentages in modelled peak velocity amplitudes are shown in (b). The ratios of modelled and the target mean velocities are compared in (c).

The critical onset flutter wind speed $U_{\infty(cr)}$ of the T-shaped cantilever has been shown 4.8 m/s when the simplified SDOF rigid beam model is used (c.f. Sec. 6.4.3). In current studies, the simulation domain ($L = H = 2$ m) is chosen square, and very large when compared to the size of the harvester. It is to reduce the influence of its motion on the convecting particles for pulsating flow.

The modelled harvester is simulated under the periodic flows with mean wind speed of 4, 4.5, 4.8, 5, and 5.5 m/s. For all of the chosen study cases, the values of $u_m/U_{\infty(cr)}$ are chosen 0.1, 0.15, 0.2, 0.25, and 0.3. The frequency of the flow fluctuation f_u is selected 0.2 Hz which satisfies the requirement of $L/\lambda_u < 0.25$ to model the periodic target flow with sufficient quality. The numerical parameters are summarized in Table 7.2.

Numerical parameters		Value/Values
Free stream flows	U_{∞}	4, 4.5, 4.8, 5, 5.5 m/s
Mean flow velocities (Pulsating flow)	\bar{U}	4, 4.5, 4.8, 5, 5.5 m/s
Peak amplitudes of longitudinal velocity fluctuation	u_m	0.48, 0.72, 0.96, 1.2, 1.44 m/s
Frequency of flow fluctuation	f_u	0.2 Hz
Length and height of the domain	$L = H$	2 m
Height of particle seeding points	h_s/L	1.2 m
Total simulation time	tU_{∞}/L	40

Table 7.2: Study on the harvester motion depending on the mean flow and the fluctuation amplitude: numerical parameters.

The dynamic motion of the T-shaped system and the surrounding flow fields are presented in Fig. 7.8 under U_{∞} of 5 m/s with and without imposed fluctuations in the incoming flow. The envelope of the vertical tip displacement of the modelled harvester under different steady and periodic incoming flows are compared in Fig. 7.9.

It is observed in Fig. 7.9 (a) that the harvester starts vibrating gradually large amplitudes under the periodic incoming flows, especially in the cases of large amplitude flow fluctuations. In Fig. 7.9 (b), the unstable flutter vibration is clearly observed for, almost, all the studied cases of u_m under the average wind speed \bar{U} of 4.5 m/s which is less than the critical steady wind speed $U_{\infty(cr)}$ of 4.8 m/s. The envelopes of the LCO under the periodic flow are observed expectedly in periodic fashion with the frequency of the incoming flow.

In case of Fig. 7.9 (c), when \bar{U} and $U_{\infty(cr)}$ is equal to 4.8 m/s, the unstable flutter vibration initiates earlier for periodic incoming flows; particularly for strong fluctuations. Similar vibration patterns are observed under the periodic flows at higher wind speeds, such as the case shown in Fig. 7.9 (d-e). However, the peak amplitudes of the envelopes are comparatively small when compared the same under the steady incoming flow. Fig. 7.9 (b-e) shows that the increase in the amplitude of fluctuation (u_m) helps in earlier initiation of flutter vibration; however, the influence on the peak vibration amplitude is comparatively less.

The harvester vibration in such fashion may be explained comparing the aerodynamic derivative A_2^* under different wind speeds, which have been shown earlier in Fig. 6.5. The aerodynamic damping becomes negative when A_2^* is positive, and vice versa. In case of periodic inflow cases, when the instantaneous velocity becomes more than $U_{\infty(cr)}$ and the negative aerodynamic damping exceeds the system damping, and the harvester experiences large amplitude vibration. It is also true that when the instantaneous velocity becomes less than the $U_{\infty(cr)}$, positive aerodynamic damping added to the system damping and allows the system to stabilize. However, Fig. 6.5 has shown that the values of A_2^* for wind speeds above the critical flutter limit ($U_{\infty(cr)} = 4.8$ m/s) are quite high in comparison with the values for wind

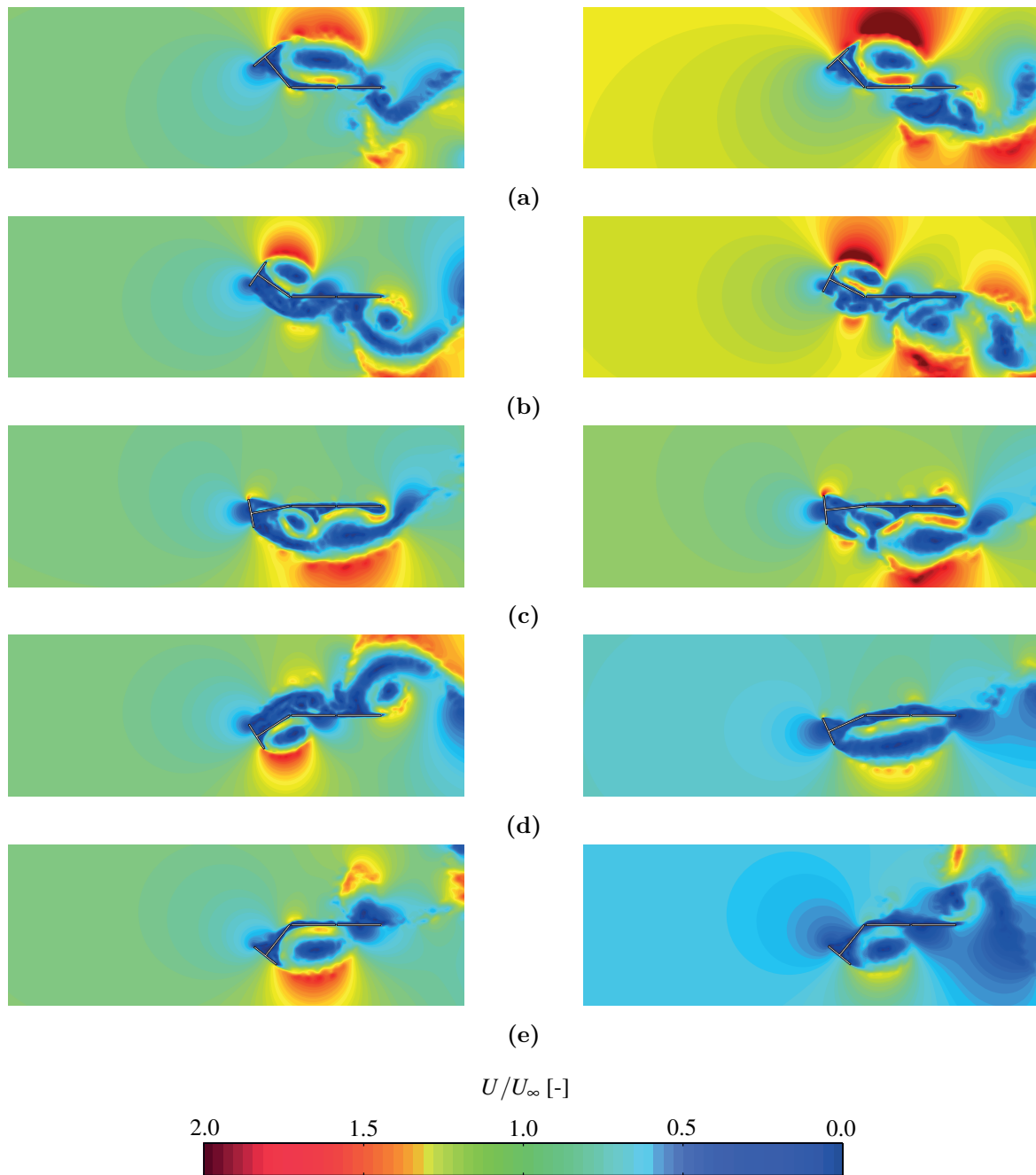


Figure 7.8: Dynamic motion of the harvester under steady and periodic incoming flow: comparison of the incoming field and the flow field around the harvester at different vibration phases. The simulations are performed under U_∞ of 5 m/s; the left figures of (a–e) show the steady incoming flow whereas the right figures show the periodic fluctuations imposed in the incoming flow. The amplitude of fluctuating velocity $u_m/U_{\infty(cr)}$ is chosen 0.3 for a frequency of 0.2 Hz. The non-dimensional colour bar is shown for the comparison of the flow fields.

speeds below the limit. The fact is that the amount of negative aerodynamic damping that induces, when the inflow speed crosses the critical flutter limit, is larger than the amount of positive aerodynamic damping in inflow speed lower than the critical one. Therefore, the harvester is found in unstable flutter vibration in case of Fig. 7.9 (b) even though the average wind speed \bar{U} is lower than $U_{\infty(cr)}$. Moreover, flutter-induced vibration initiates much earlier than the same under $U_{\infty(cr)}$, c.f. Fig. 7.9 (c).

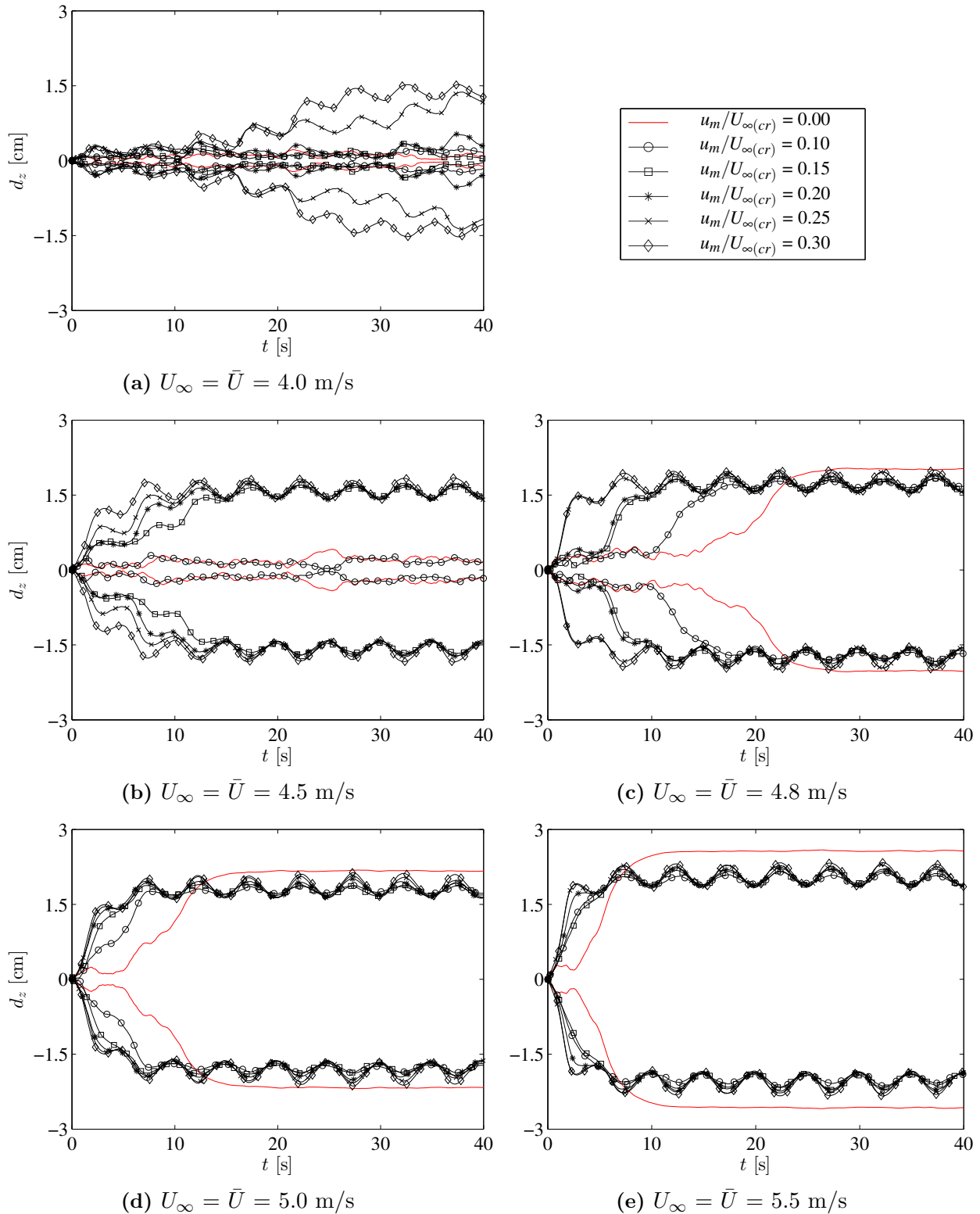


Figure 7.9: Study on the dynamic motion of the harvester under steady U_∞ and periodic incoming flow $U(t)$: the envelope of the vertical displacements of the harvester are compared in (a–e). The frequency of the flow fluctuation is chosen 0.2 Hz. Here, \bar{U} shows the average of the target incoming flow $U(t)$. The non-dimensional values of the selected peak amplitude of the velocity fluctuations $u_m/U_{\infty(cr)}$ are shown in the legend. The red continuous lines (—) show the displacement envelopes of the modelled harvester under the steady inflow condition.

The maximum and the root mean square (RMS) of vertical displacements of the modelled harvester are presented in Fig. 7.10. The result shows that the T-shaped flutter-based harvester may perform the energy production in case of wind speeds slightly less than $U_{\infty(cr)}$ if there are sufficient fluctuations along the flow direction. The studied scenarios show that the possibility of energy conversion from the T-shaped harvester under periodic flow reduces in case of wind speeds above $U_{\infty(cr)}$. However, the earlier initiation of fluttering response under the periodic incoming flow shows the harvesting potential in sub-critical wind speeds.

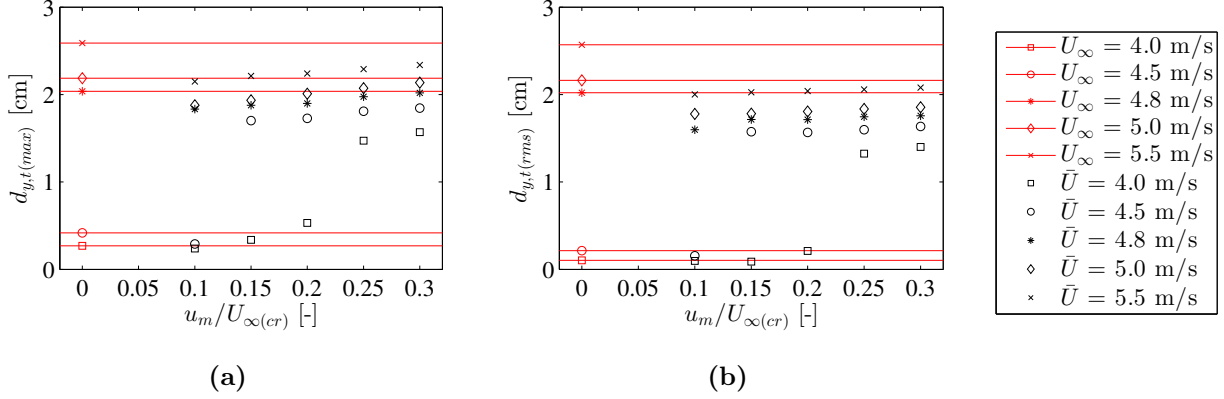


Figure 7.10: Comparison of the vertical displacements of the harvester under steady U_{∞} and periodic incoming flows $U(t)$; the displacement time histories of which are already shown in Fig. 7.9: (a) the maximum of the peak displacements, and (b) the root mean square of the peak displacements. Here, \bar{U} represents the average of the fluctuating flow field $U(t)$. The frequency of the periodic incoming flows is 0.2 Hz.

The influence of fluctuation frequency

The dynamic motion of the modelled harvester is investigated here for different frequency of periodic incoming flow. The simulations, which have been shown in Fig. 7.9 (b and e), are performed again under U_{∞} and \bar{U} of 4.5 m/s and 5.5 m/s; however, the frequencies of the periodic fluctuation f_u are considered 0.04 Hz, 0.1 Hz, 0.2 Hz, 0.5 Hz, 0.8 Hz, and 1.0 Hz, while u_m/U_{∞} is chosen 0.2.

The envelopes of the vertical displacement are compared in Fig. 7.11. In case of the displacement envelopes under U_{∞} and \bar{U} of 4.5 m/s, which are shown in Fig. 7.11 (a), the flutter initiates very early under very-low-frequency f_u of 0.04 Hz. It is due to the instantaneous flow velocity that increases and stays for a longer duration above $U_{\infty(cr)}$. Exactly for the same reason, when the instantaneous flow velocity that stays for the longer duration under $U_{\infty(cr)}$, the harvester vibration stabilizes faster. However, the average responses under all the studied frequencies are observed very close to each other.

A similar vibration pattern is observed in Fig. 7.11 (b) under 5.5 m/s. The periodic wind fluctuates in between 4.54 – 6.46 m/s. Important to note that the peak displacement is found less compare to the steady flow. It is due to the dissipation of the input energy of the harvester by the positive aerodynamic damping, especially the duration when the harvester is under the wind speed less than $U_{\infty(cr)}$. The periodic positive and negative aerodynamic damping effect reduces the harvester response. Because of this same reason, the responses of the harvester in Fig. 7.9 (e) are much lower than the same under steady flow. The changes in the aerodynamic damping with respect to the flow duration displays a significant role in the response pattern of the harvester under cyclic loading.

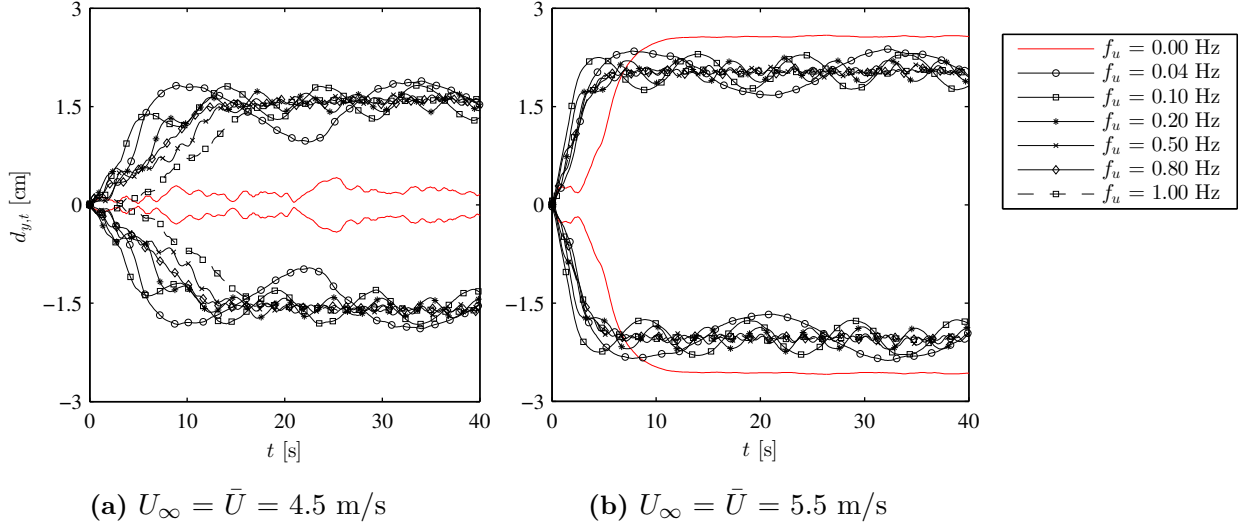


Figure 7.11: The effect of the fluctuation frequency on the motion of modelled harvester: the envelopes are compared for vertical displacement under U_∞ and \bar{U} of 5.5 m/s. The peak amplitude $u_m/U_{\infty(cr)}$ is chosen 0.2.

The harvester under large velocity fluctuation at very low frequency

The modelled harvester is simulated again under the periodic incoming flow, however, under large velocity fluctuation at very-low-frequency. Here, the analyses are performed for the studied cases of Fig. 7.9 (c), which means $U_{\infty(cr)}$ and \bar{U} are 4.8 m/s. The frequency of the periodic fluctuation f_u is considered 0.02 Hz only; the corresponding value of L/λ is 0.0083, which is far smaller than the upper limit value of 0.25. The non-dimensional amplitudes of the imposed fluctuation u_m/U_∞ are chosen 0.2, 0.4 and 0.6.

The variation of the wind velocities according to the chosen conditions and the envelopes of the vertical tip displacement are compared in Fig. 7.12. The initiation of flutter is not only earlier, but also the displacement envelopes quite more substantial than the same under the steady flows. As mentioned earlier, it is due to the instantaneous flow velocity that increases and stays for a longer duration with wind speeds much larger than $U_{\infty(cr)}$. The stabilization of the harvester response under the periodic flow because of the incoming wind speed less than $U_{\infty(cr)}$ for a longer duration. The displacement plateau in case of $u_m/U_\infty = 0.6$ is the limiting value of the vertical displacement since it becomes equal to the length of the simplified harvester, which is 0.028 m.

7.2.8 Application of pulsating flow on flexible T-shaped harvester

Here, the fully coupled flexible model of the T-shaped harvester (c.f. Sec 6.4.3) is simulated under the periodic incoming flow, which is composed of multiple low frequencies. The target flow is composed of three different frequencies which is shown in Fig. 7.13(a) based on the following equation

$$U = \bar{U} + \sum_{i=1}^3 u_{m_i} \sin(2\pi f_{u_i} t), \quad (7.10)$$

where $\bar{U} = 4 \text{ m/s}$, $u_{m_1} = 0.6 \text{ m/s}$, $u_{m_2} = 0.5 \text{ m/s}$, and $u_{m_3} = 0.2 \text{ m/s}$, $f_{u_1} = 0.02 \text{ Hz}$, $f_{u_2} = 0.05 \text{ Hz}$, $f_{u_3} = 0.1 \text{ Hz}$. The modelled flow (without harvester) is compared in Fig. 7.13(a), which is quite satisfactory.

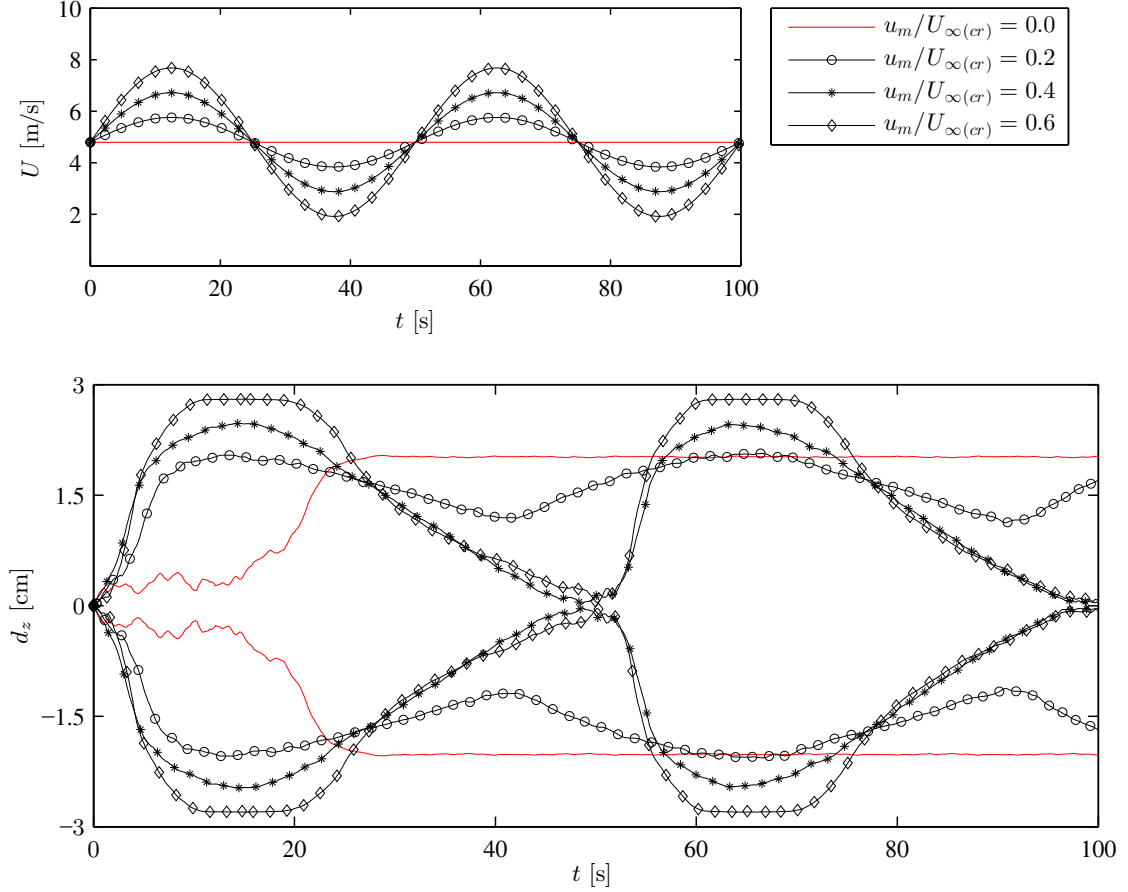


Figure 7.12: The dynamic motion of the harvester under periodic flow of high fluctuations at very low frequency: (top) the time histories of the studied incoming wind speeds, (bottom) corresponding envelopes of the vertical displacements of the modelled harvester.

The flexible T-shaped harvester is placed in the centre of the simulation domain for coupled analysis. In addition to the structural parameters of the harvester in Table 6.2, the numerical parameters related to the periodic flow are summarised in Table 7.3.

The tip displacements and response frequencies are compared in Fig. 7.13(b) and (c), respectively. Clearly the fluttering of the T-shaped cantilever strongly influenced by the incoming periodic flow as discussed earlier for the rigid model. The coupled response frequency is almost uninfluenced by the fluctuations in the incoming flow.

Numerical parameters		Value/Values
Free stream flows	U_∞	4 m/s
Mean flow velocities (Pulsating flow)	\bar{U}	4 m/s
Peak amplitudes of longitudinal velocity fluctuation	u_{m1}, u_{m2}, u_{m3}	0.6 m/s, 0.6 m/s, 0.2 m/s
Frequencies of longitudinal flow fluctuation	f_{u1}, f_{u2}, f_{u3}	0.02 Hz, 0.05 Hz, 0.1 Hz,
Length and height of the domain	$L = H$	2.5 m
Height of particle seeding points	h_s/L	1.8 m
Simulation time step	Δt	0.0009827 s
Particle release step	$\Delta t_r/\Delta t$	4

Table 7.3: Study on the harvester motion depending on the mean flow and the fluctuation amplitude: numerical parameters.

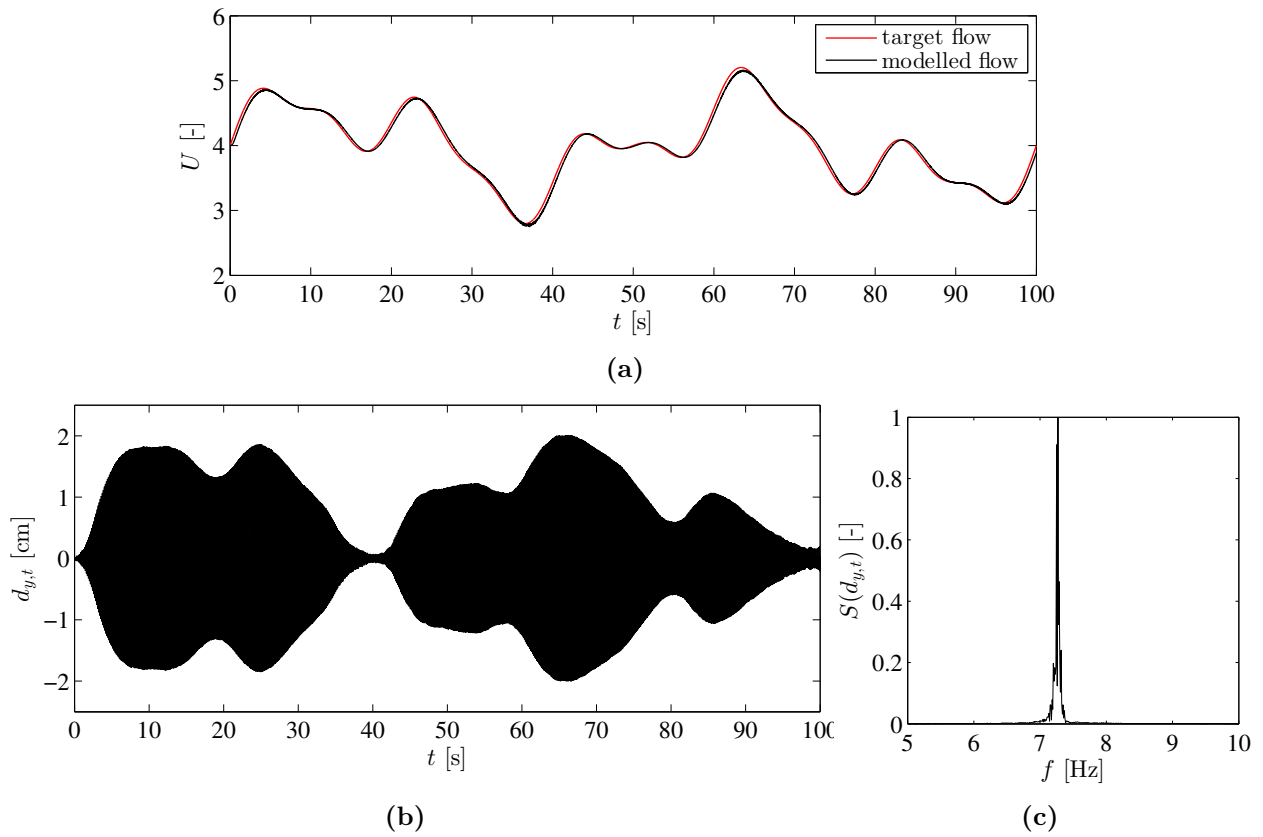


Figure 7.13: The study on flexible T-shaped harvester under pulsating flow, which is composed of three different low frequencies: (a) comparison of target and modelled flow, (b) tip displacement of the flexible harvester, and (c) response frequencies of tip displacement.

7.2.9 Pulsating flow on flexible cantilever in Kármán vortex street

In the following, the low frequency periodic incoming flow is applied to the 2D large-displacement aeroelastic interaction problems. In this context, the reference 2D FSI problem in which a thin elastic cantilever structure is immersed in the wake of a rigid square body (c.f. Sec. 5.2.1) is simulated again under the low frequency periodic incoming flow. Instead of free stream flow U_∞ of 0.513 5m/s, the sinusoidal fluctuation is added to the free stream. The fluctuation amplitude is chosen such that $u_m = 30\%U_\infty$. The value of f_u is chosen 0.05 Hz. The system under periodic incoming flow is shown schematically shown in Fig. 7.14(a). With the added 30 % fluctuations, the target time history of the sinusoidal flow is displayed in Fig. 7.14(b).

Fig. 7.15 compares the time history of the tip response and the response frequencies. Clearly, the periodic incoming flow has shown significant influence in the response pattern. The envelope of the tip responses is following the time history of the cyclic incoming flow. The maximum tip response hasn't increased much when the incoming velocity increases; however, the decrease of response is observed when the velocity of incoming flow reduces. The system under the free stream flow has vibrated with a dominant coupled frequency of 3.12 Hz; however, Fig. 7.15(b-c) shows several frequencies which are due to the influence of periodic flow on the vortex shedding of rigid square section. The increase in incoming flow velocity increases the vortex shedding frequency of a square section, and vice-versa. Therefore, the coupled responses have reflected the change of incoming flow frequencies.

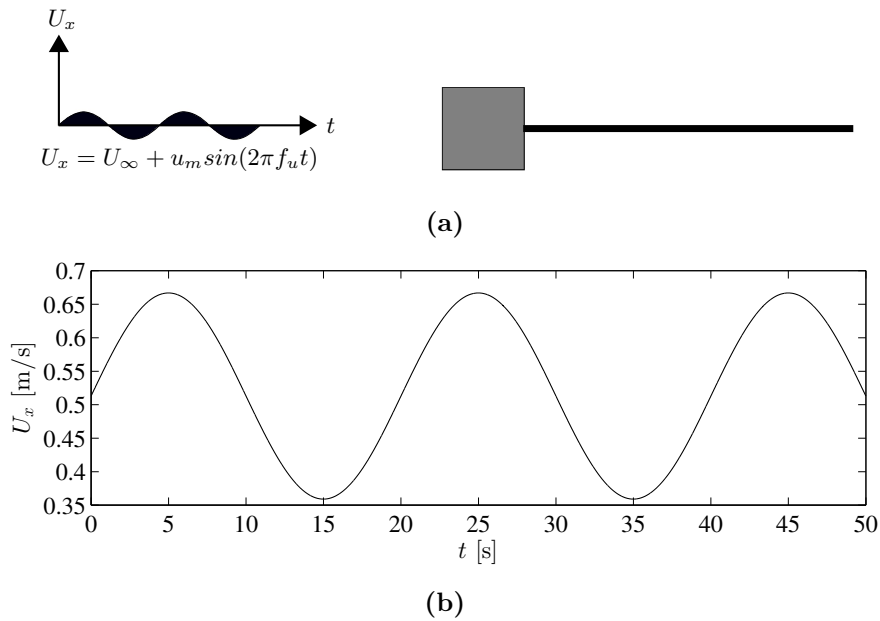


Figure 7.14: Study on the influence of pulsating flow on Kármán vortex street and further on coupled response of flexible cantilever: (a) schematic problem; (b) the time history of target incoming flow.

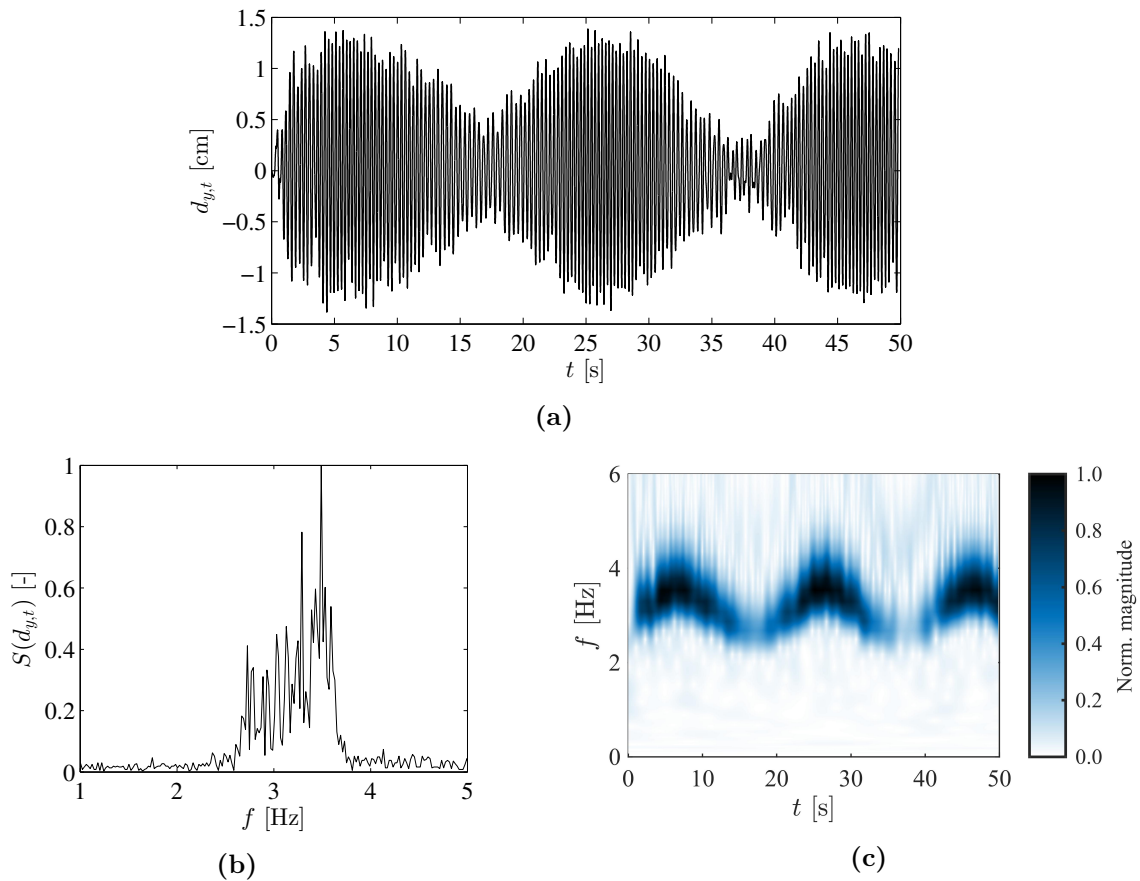


Figure 7.15: Flexible cantilever response in Kármán vortex street influenced by low frequency periodic flow: (a) the time history of tip response, (b) normalised frequency spectrum of response time history, and (c) corresponding normalised wavelet transformation.

7.2.10 Summary

The section has presented a numerical technique within the framework of 2D VPM to simulate periodic incoming flow ($U(t) = \bar{U} + u_m \sin(\omega t)$) by seeding pre-calculated vortex particles into the free stream velocity. Periodic variation of particle strength while convecting downstream allows inducing the desired periodic flow around the centre of the simulation domain. In brief, the average velocity of the periodic flow (\bar{U}) has been modelled by the free stream flow (U_∞) while the periodic fluctuations ($u_m \sin(\omega t)$) by the seeded particles.

The sinusoidal incoming flows have been modelled as the target flow to investigate the accuracy, validate the method, and to show the limitation of the proposed scheme. The domain length is a critical parameter because of the assumption that the particles that exist within the domain in each time step are approximate of equal strength, even though they are changing. Therefore, the wavelength (λ) of the periodic target flow should be sufficiently larger than the length of the domain. It has been shown through several studies that the quality of the modelled flow shows little influence due to the increase in the amplitude of flow fluctuations; however, the quality drops drastically if L/λ is higher than 0.25.

The coupled motion of a reference T-shaped harvester has been investigated under steady and periodic incoming flows of several fluctuation amplitudes and frequencies. The changes in the aerodynamic damping with respect to the flow duration displays a significant role in the response pattern of the harvester under cyclic loading. The benchmark case of a flexible cantilever in Kármán vortex street has been reinvestigated under low frequency pulsating incoming flow to show the effects on the coupled dynamic motion.

7.3 The flow reproduction method

7.3.1 Introduction

This section presents a novel 2D extension of the VPM which allows complex transient flow features computed by an original simulation to be recreated for use as inflow conditions in other simulations. This is facilitated by recording velocity time signals of the original simulation and computing time traces of vortex particles to be seeded into the secondary simulation near its upstream domain boundary.

The proposed Flow Reproduction Method (FRM) allows to re-create the flow field, without the need to simulate the underlying physics responsible for the flow features. A natural field of application is the re-creation of wakes from flows past bluff bodies of arbitrarily complex geometry, the resolution of which is computationally expensive.

The recording is performed on a sampling system of the velocity field. Reproduction of the sampled simulation is then performed by inserting vortex particles in defined positions and time intervals into the secondary simulation. This proceeds in a smaller domain with the advantage of significantly reduced computational cost.

In the simulations presented here, wake flows of upstream cylinders are reproduced. Convergence studies are performed to validate the FRM. The quality of flow reproduction is assessed and quantified. The computational efficiency of the reproduction simulation is enhanced additionally by using different adaptive numerical techniques. The method is then applied to fluid-structure interaction simulations of a wake buffeting problem.

7.3.2 A new numerical method for reproduction of flow simulation

Numerical technique and approximation of vortex particles

A complete overview of FRM, quality assessment, and its application concerns are presented schematically in Fig. 7.16, which shows an upstream square section ($B_1/D_1 = 1$), the complete velocity sampling system, and the flow monitoring points. The downstream rectangular section is shown here as a representation of wake buffeting analysis.

The turbulent feature of oncoming wakes from upstream sections depends on free stream velocity, number of sections, their shapes and positions. In case of highly complex geometries, a substantial amount of computational efforts may be required in terms of the number of particles for the convergence of the flow fields [177]. The speciality of FRM is that the numerical approach is independent of the upstream conditions of the flow simulation; it reproduces the flow fields based on how they have been simulated initially. However, for simplicity, a square cylinder at Reynolds number Re of 500 is chosen to present the method in the following.

The principal aim of the method is to model specific simulated oncoming wake flows from upstream bodies only by seeding vorticity carrying particles (Γ) into a VPM simulation, thereby reproducing the effect of the original flow. To obtain the particles of an original simulation of flows past upstream bodies, it is necessary to perform velocity sampling initially using a predefined sampling system in the downstream vortex shedding. For each sampling step, the corresponding particles are approximated from the sampled velocity components.

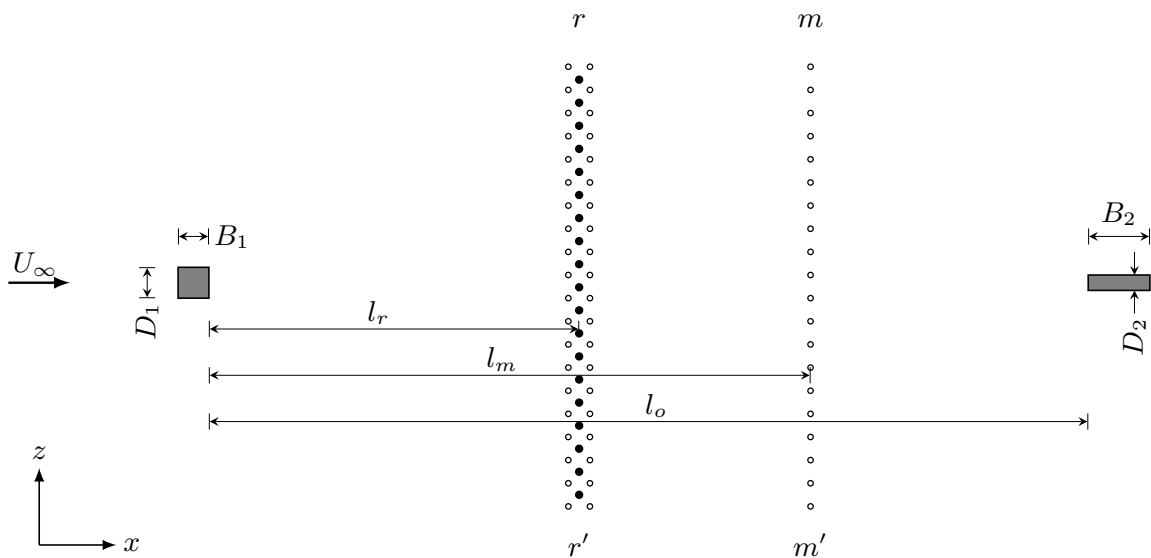


Figure 7.16: Schematic of flow reproduction method: An upstream section ($B_1 \times D_1$) in free stream flow U_∞ , a downstream section ($B_2 \times D_2$) for wake buffeting analysis. The velocity sampling points (\circ) are shown around the section rr' . Each combination of the closest four sampling points (\circ) is referred as sampling-cell. Here, (\bullet) indicates approximated vortex particles of each square sampling-cell for flow reproduction. l_o is clear distance between the sections. l_r and l_m indicate the distance of the sampling system and the flow monitoring profile respectively from the downstream edge of upstream section. The section rr' shows the position of the approximated vortex particles and the section mm' is the flow monitoring profile showing the velocity sampling points for quality assessment.

In a 2D flow field, for a cell shown in Fig. 7.17, the circulation may be expressed as follows:

$$\Gamma = \iint_A \omega \cdot dA = \left(\frac{\partial u}{\partial z} - \frac{\partial w}{\partial x} \right) dx dz. \quad (7.11)$$

For every sampling step, it is necessary to transform the sampled velocity components of the sampling-cells into vortex particles or circulations. A typical sampling-cell is shown in the right side of Fig. 7.17 that has four corner velocity sampling points containing altogether eight fluctuating velocity components. For such a sampling-cell of size $(dx \times dz)$, the strength of the vortex particle can be approximated from Eq. (7.11) using Eq. (7.12) [193],

$$\Gamma_a = \left(\left[\frac{\left(\frac{u_2 + u_4}{2} \right) - \left(\frac{u_1 + u_3}{2} \right)}{\partial z} \right] - \left[\frac{\left(\frac{w_4 + w_3}{2} \right) - \left(\frac{w_1 + w_2}{2} \right)}{\partial x} \right] \right) dz dx. \quad (7.12)$$

It was observed in [193] Eq. (7.12) approximates the particle strength stronger than the actual. Therefore, a strength reduction factor α_{rf} is considered in present studies, and the modified strength of the vortex particle Γ_m can be expressed as:

$$\Gamma_m = \alpha_{rf} \Gamma_a. \quad (7.13)$$

The strength reduction factor α_{rf} within the range of 0.8 to 0.9 is found helpful for improving the quality of flow reproduction. All the simulation results presented further are based on the consideration that $\alpha_{rf} = 0.85$. Necessarily, the validation of α_{rf} is explained later.

The approximated vortex particles are located at the centre of corresponding square sampling-cells. To execute flow reproduction, for every sampling step the position coordinates of the approximated vortex particles along the particle release position (rr' in Fig. 7.16) and their magnitudes need to be calculated and stored.

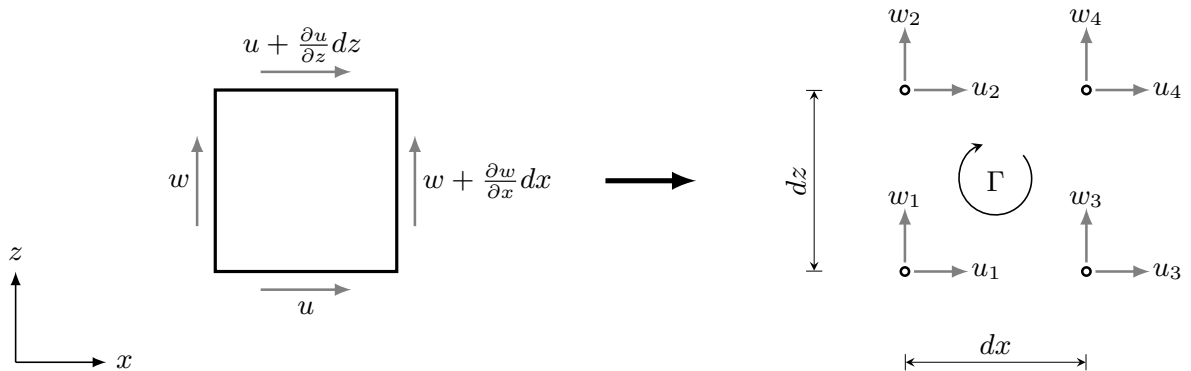


Figure 7.17: Circulation around a typical square sampling-cell from the velocity sampling system in Fig. 7.16: The sampled fluctuating velocity components in the four corner velocity sampling points (\circ) and the corresponding vortex particle (Γ) is located at the centre of the sampling-cell.

Velocity sampling system and important parameter concerns

The first step is to perform sampling velocity signals from the original flow simulation using a predefined sampling system. The velocity sampling points in the original flow domain should be arranged such that it consists of a series of square sampling-cells arranged vertically across the flow direction, as shown in Fig. 7.16. The height of the sampling system should be high enough to capture the vortices in the vortex shedding.

Two parameters must be equal to keep consistency between original and reproduction simulation which are the rate of velocity sampling from original flow simulation and the rate of particle seeding in the reproduction of flow simulation.

The number of the velocity sampling points in the sampling system and their positions are governed by the choice of dx . Therefore, the selection of the sampling-cell size (dx) is the earliest concern before defining the sampling system. The parameter dx depends on the free-stream velocity, the time-step of the original simulation and the number of time-step at which the velocity should be sampled. The relation can be expressed as follows

$$dx = dt_s U_\infty = n_s \Delta t U_\infty, \quad (7.14)$$

where U_∞ and dt_s are respectively the free stream velocity and the time step of velocity sampling, Δt is the time step of the original flow simulation, and $n_s = dt_s / \Delta t = 1, 2, \dots, n$ indicates the number of simulation time steps considered within the time step of velocity sampling. Clearly, dx determines the number of particles in section rr' , and therefore, it is a matter of computational efficiency of the reproduction simulation.

Now, as an example, $n_s = 1$ refers $dt_s = \Delta t$, which indicates the velocity sampling for each time step of the original flow simulation. If the velocities are sampled differently such that $n_s > 1$ or $dt_s > \Delta t$, it is necessary to choose corresponding sampling-cell size (dx) based on Eq. (7.14).

Once the sampling-cell size dx is calculated based on the chosen n_s , it is necessary to define the sampling points to perform the velocity sampling from the original simulation, and importantly, at every dt_s step. The rate of inclusion of vortex particles in reproduction simulation should be equal to the rate of velocity sampling such that the particle release step

$$dt_r = dt_s = n_s \Delta t. \quad (7.15)$$

Reproduction of vortex shedding from a square cylinder

The vortex shedding of a square cylinder immersed in free stream flow is considered the flow reproduction. The methodological steps to perform the reproduction of a simulated flow are summarized in the following:

- selection of sampling time step n_s ($= n_s \Delta t$) of velocity sampling in original simulation
- calculation of the sampling-cell size dx using Eq. (7.14) and the identification of sampling points in the original flow domain (see Fig. 7.16)
- a complete sampling of velocity components from original flow simulation at the location of sampling points

- approximation of vortex particles for each sampling-cell using Eq. 7.13 and storing them with the release location for each release step
- seeding of the predefined particles into the free stream flow of reproduction simulation.

The flows past an upstream square cylinder ($B_1/D_1=1$) at $Re = 500$ is considered as an example for flow reproduction. The numerical parameters regarding the original simulation and the reproduction simulation are summarized in Table 7.4. The original and reproduction simulation has the same time step ($\Delta t_{orig} = \Delta t_{rep}$). The velocity sampling is performed at every 5th simulation time step. Necessarily, the vortex particles are released in reproduction simulation with a time step equal to the sampling time step ($dt_s = dt_r$). The simulation results are shown in Fig. 7.18, where the flows are shown reproduced step by step with the convection of the the released particles in the free stream. The comparison of the instantaneous flow fields between the original and reproduced flow fields shows good qualitative agreement, however, the quantitative quality assessments are presented in Sec. 7.3.3–7.3.4.

Original flow			Reproduction flow		
Numerical parameters		Value	Numerical parameters		Value
Number of panels	N_{panel}	200	Number of panels	N_{panel}	0
Panel size	$\Delta s/B_1$	0.02	Panel size	$\Delta s/B_1$	-
Simulation time step	$\Delta t_{orig}U_\infty/B_1$	0.2	Simulation time step	$\Delta t_{rep}U_\infty/B_1$	0.2
Release distance	l_r/B_1	20	Strength reduction factor	α_{rf}	0.85
Sampling interval	n_s	5	Particle release step	dt_rU_∞/B_1	0.1
Sampling cell-size	dx/B_1	0.1			
Sampling time step	dt_sU_∞/B_1	0.1			

Table 7.4: Numerical parameters for an original and corresponding reproduction simulation of flow past a square cylinder at $Re = 500$.

7.3.3 Validation study and efficiency of flow reproduction

Convergence study

The convergence study is performed based on the number of particles released in the flow stream of reproduction simulation. In VPM the accuracy in the flow field can be enhanced by increasing the number of particles; however, doing such may be computationally very expensive. Therefore, in convergence study, it is attempted to observe the ability and quality of FRM to reproduce an original simulation using less number of particles, which is possible by sampling original simulation using bigger sampling-cells. Therefore, a number of reproduction simulations with respect to the number of released particles was carried out for the selected original simulation of flows around the upstream square cylinder. The reproduction simulations were performed by releasing N_{rp} number of particles at every dt_r step which can be calculated using Eq. (7.16),

$$N_{rp} = \frac{h_{ss}}{dx} - 1, \quad (7.16)$$

where h_{ss} is height of the velocity sampling system. For convergence study, the original flow simulation in Sec. 7.3.2 is performed and sampled again in four different scenarios based on the number of sampling step $n_s = 1, 5, 10$ and 20 . The height of the sampling system (h_{ss}) is considered same for all scenario. The numerical parameters for the studied flow reproduction cases are summarized in Table 7.5.

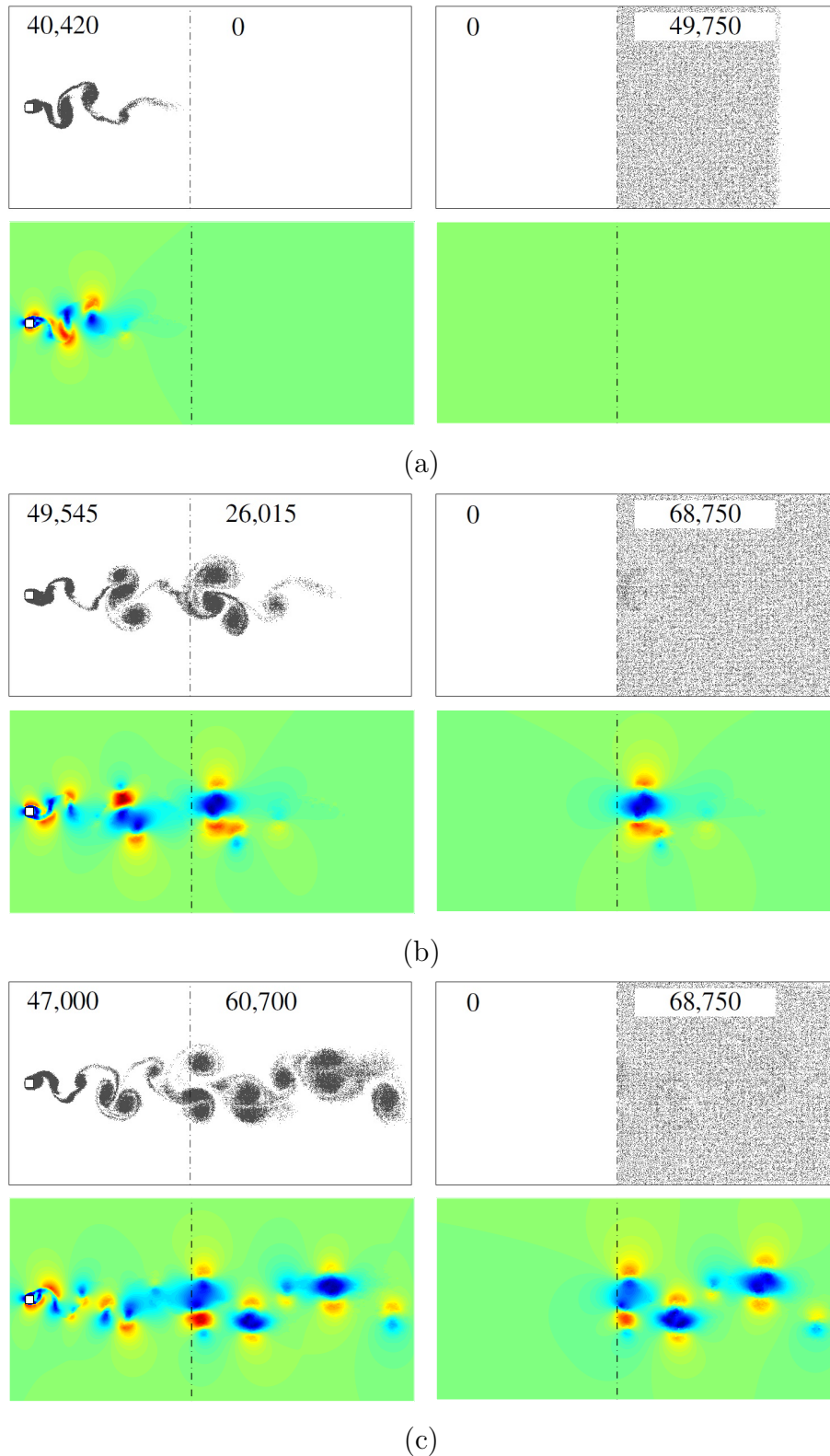


Figure 7.18: The reproduction simulation of flow past a square section by sequential seeding of precalculated vortex particles into the free stream flow: The comparison of particle and flow fields for both simulations are shown at non-dimensional time $tU_\infty/B_1 =$ (a) 20, (b) 40, and (c) 60. For each case of (a-c), the left figures show the convecting particles (top) and flow fields (bottom) of original flow simulation, whereas the right figures show the corresponding particle maps (top) and flow fields (bottom) of reproduction simulation. $(-\cdot-\cdot-)$ lines refer to the location of the sampling system in case of original flow, whereas refer to the particle release section in case of reproduced flow. The approximate instantaneous number of vortex particles in the selected domains are shown for both flows.

	Reproduction (1)	Reproduction (2)	Reproduction (3)	Reproduction (4)
Parameters	Value	Value	Value	Value
$\Delta t_{rep} U_\infty / B_1$	0.2	0.2	0.2	0.2
n_s	1	5	10	20
dx / B_1	0.02	0.1	0.2	0.4
h_{ss} / B_1	25	25	25	25
N_{rp}	1250	250	125	65
$dt_r U_\infty / B_1$	0.02	0.1	0.2	0.4
$t U_\infty / B_1$	200	200	200	200

Table 7.5: Convergence study: numerical parameters associated with reproduction simulations performed by seeding different number of particles.

The results of the convergence study are presented in Fig. 7.19. It shows the comparison of instantaneous absolute velocity field $U = \sqrt{u^2 + w^2}$ as computed from the instantaneous velocity components u and w . It is observed from Fig. 7.19(b-e) that the reproduced flow fields are clearly converging to a specific reproduction flow field. The corresponding instantaneous particle maps and the number of particles in the domains are also presented. The contour plots of the reproduction field errors are found reducing with the increment in released number of particles. The field errors (U_{err}) induced in reproduction are calculated based on Eq. (7.17) where U_{orig} and U_{rep} indicates original and reproduced velocity fields respectively.

$$U_{err} = U_{rep} - U_{orig} \quad (7.17)$$

The alternating vortex shedding of the original simulation is reproduced quite satisfactory, c.f. Fig. 7.19(b-e), which indicates good approximation of the vortex particles from original simulation. However, the flow field errors that are calculated based on direct deduction of the flow fields using Eq. (7.17), are mainly due to the relative shifting of the vortex shedding in position in reproduction simulations.

Adaptive numerical techniques in flow reproduction

Large sampling step increases the sampling-cell size and hence reduces the number of particles. VPM simulations with less number of particles become computationally faster due to the reduction in the computational effort that requires counting the mutual interaction between the particles and their velocity calculations. Though a sufficient number of particles are often needed for higher flow resolution, the reproduction of the flow fields in Fig. 7.19(c-e) are found satisfactory without having significant influences from the reduction in the number of released particles. However, using very few numbers of particles can change reproduced flow fields drastically from original simulation either locally, such as in Fig. 7.19(b), or globally.

The reproduction of original simulation presented in Fig. 7.19(e) is performed by releasing 1250 number of particles at every simulation step which is eventually ended up with 22 times more numbers of particles in the flow domain than original simulation. This particular flow reproduction case, therefore, becomes computationally highly ineffective since the simulation contains a lot of zero-circulation vortex particles.

The application of particle remeshing (PR) allows replacing irregularly spaced and insignificant particles by a new set of particles on the particle mesh. The technique was shown in Morgenthal and Walther [177] to be computationally efficient for simulations with a huge number of particles. Here, Fig. 7.20(a) shows the reproduced flow field of Fig. 7.19(e) with the implementation of PR.

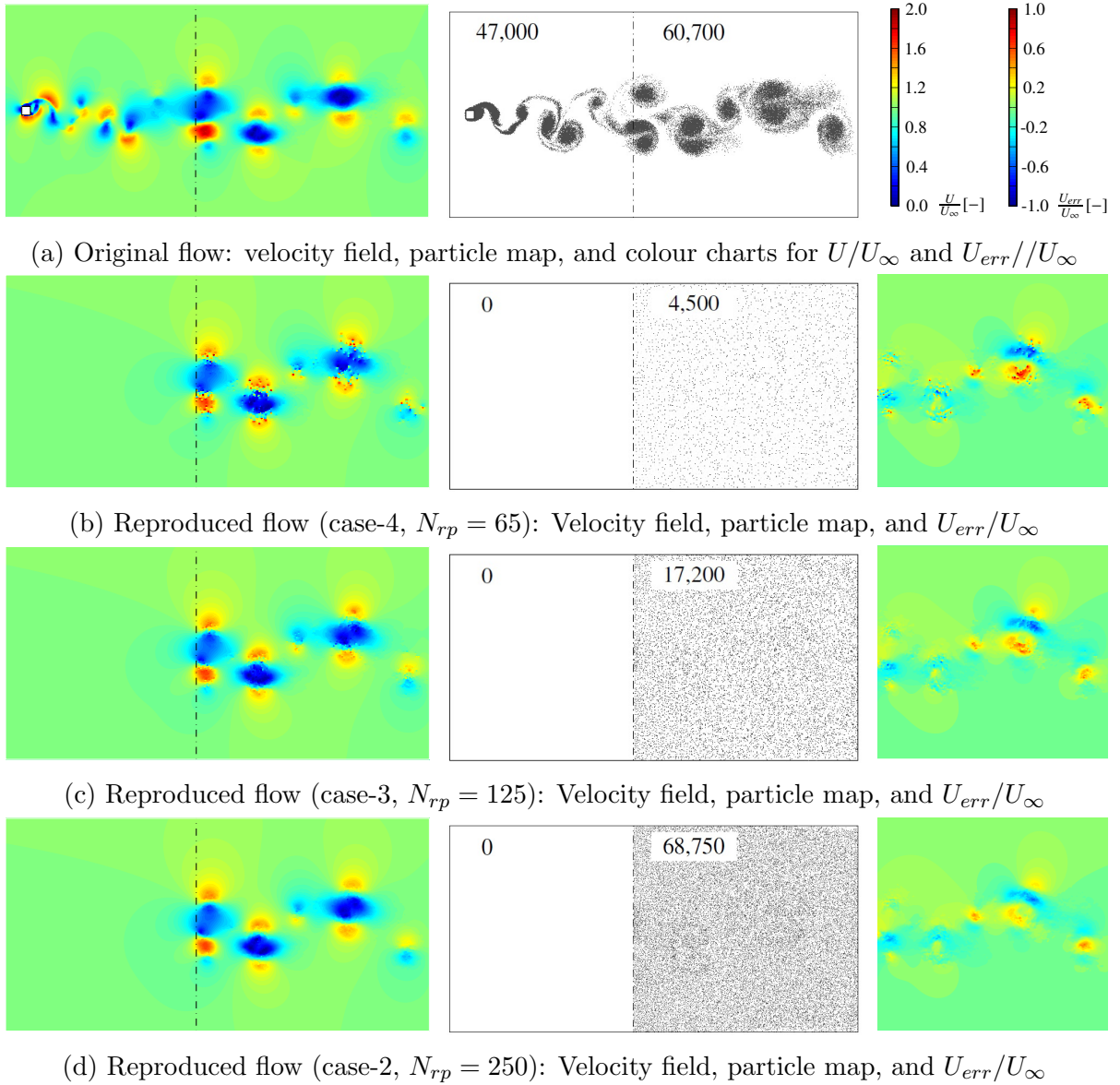
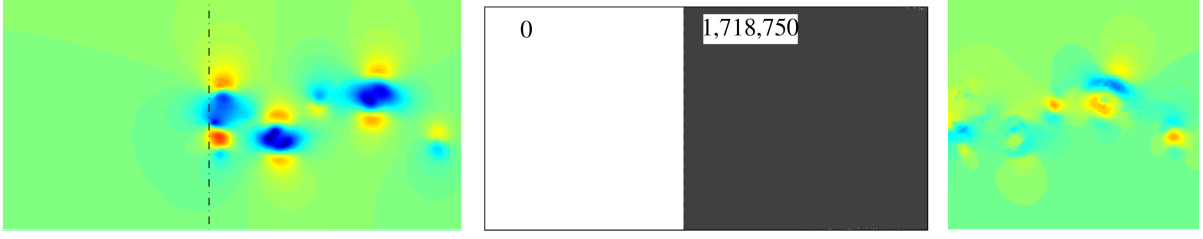
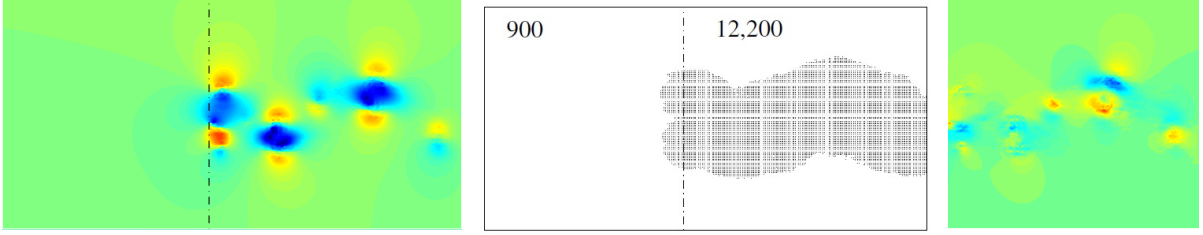


Figure 7.19: Convergence study of FRM: The original flow field (a) is reproduced in four different scenarios by releasing $N_{rp} = 65, 125, 250$ and 1250 (b-e) number of particles, respectively into the reproduction simulations. $(-\cdot-\cdot-\cdot)$ lines drawn over the plots in (left of (a)) refer to the location of the sampling system whereas in the plots (left and middle of (b-e)) refer to the particle release section. The snapshot of absolute flow fields U of original (left of (a)) and reproduced simulations (left of (b-e)) are shown for time $tU_\infty/B_1 = 60$. Accordingly, the particle maps (middle of (a-e)) and the reproduction flow field errors U_{err} (right of (b-e)) are presented. For the reproduction errors, only the comparable flow domain are compared, which is after the release section $(-\cdot-\cdot-\cdot)$. The instantaneous total number of particles in the selected domain are shown. The reproduced flow fields and also the flow errors are clearly converging to a specific solution field which is (e). The non-dimensional magnitudes of flow fields and reproduction errors are shown by colour-bar (right of (a)). (figure continued . . .)

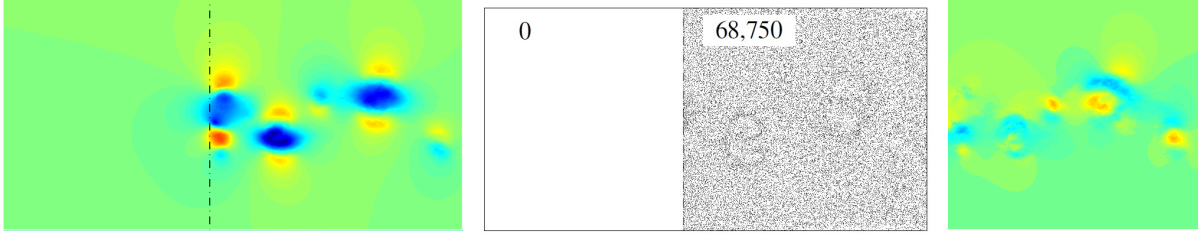


(e) Reproduced flow (case-1, $N_{rp} = 1250$): Velocity field, particle map with, and U_{err}/U_{∞}

Figure 7.19: (continued)



(a) Reproduced flow (case-5, use of particle remeshing): U_{rep}/U_{∞} , particle map, and U_{err}/U_{∞}



(b) Reproduced flow (case-6, adaptive time step using $\Delta t_{rep} = dt_s$): U_{rep}/U_{∞} , particle map, and U_{err}/U_{∞}

Figure 7.20: Computationally effective techniques in flow reproductions: Implementation of particle remeshing in flow reproduction: (a) shows the snapshot of the reproduced flow field U (left) by releasing $N_{rp} = 1250$ particles with the implementation of PR, c.f. Fig. 7.19(e), corresponding particle map (middle) and flow field errors U_{err} (right). Adaptive flow reproduction using the reproduction simulation time step (Δt_{rep}) equal to the velocity sampling step (dt_s): (b) shows the snapshot of the reproduced flow fields U (left) using $\Delta t_{rep} = dt_s$ for the case in Fig. 7.19(d), corresponding particle map (middle) and flow field errors U_{err} (right).

Additionally, an adaptive time step of reproduction simulation is proposed for cases $n_s > 1$. The aim is to use large time step using the simulation time step equal to the sampling step, i.e. $\Delta t_{rep} = dt_s = n_s \Delta t_{orig}$, which allows the simulation to be faster by reducing the number of simulation time step to NT/n_s . For example, Fig. 7.20(b) shows reproduction case in Fig. 7.19(d) where $\Delta t_{rep} = 5\Delta t_{orig}$ and $NT = 2,000$.

The numerical parameters for the two studied flow reproductions with adaptive numerical techniques are summarized in Table 7.6.

Run-time comparison

A study of Run-Time (RT) comparison is performed for better visualization of efficiency of the computationally effective techniques applied in FRM. Here, the original simulation and the reproduction simulations, which are presented in Sec. 7.3.3 and Sec. 7.3.3, are performed for

Parameters	Reproduction (5)	Reproduction (6)
	Value	Value
$\Delta t_{rep} U_\infty / B_1$	0.2	1
n_s	1	5
dx / B_1	0.02	0.1
h_{ss} / B_1	25	25
N_{rp}	1250	250
$dt_r U_\infty / B_1$	0.02	0.1
$t U_\infty / B_1$	200	200

Table 7.6: Adaptive numerical techniques in FRM: Numerical parameters associated with reproduction simulations.

$NT = 10,000$ using GPU-accelerated (Graphics Processing Unit) CFD solver VXflow [175]. Simulations are performed separately one after another using a computer having windows 7 operating system, 8 cores, 3.5 GHz processor, 16 GB RAM and NVIDIA GeForce GTX 770 graphics card. The relative Run-Time (RT_{rep}/RT_{orig}) and the relative average number of particles between original and reproduced flow simulations (NP_{rep}/NP_{orig}) are presented in Table. 7.7.

Though the number of particles NP_{rep} are reduced significantly in some cases, the reproduction simulations are not found correspondingly faster. Firstly, this is due to the simple geometry of original simulation; the discretisation of the square section needs relatively less panels. FRM should be more effective when the original simulation contains complex or multiple bodies. Secondly, the reproduction simulations needs additional computational effort for acquiring stored particle information.

The implementation of PR takes same time for cases $n_s = 1$ and $n_s = 5$ since the number of particles are same after the implementation of PR. The adaptive reproduction, which considers $\Delta t_{rep} = n_s \Delta t_{orig}$, appears as the most effective in this study. However, PR or choice of higher n_s can also be effective depending on the simulation scenarios. Choice of higher n_s or bigger sampling-cell size (dx) may be effective where the number of particles are enough to avoid the local errors. PR should be helpful where huge number of particles are required to capture original flow field due to complex upstream conditions. The adaptive reproductions are always effective since they reduce the number of simulation time step.

$\frac{\Delta t_{rep}}{\Delta t_{orig}}$ [-]	n_s [-]	$\frac{dx}{B_1}$ [-]	System	Particle remeshing	$\frac{NP_{rep}}{NP_{orig}}$ [-]	$\frac{RT_{rep}}{RT_{orig}}$ [-]
1	1	0.02	GPU	No	22	Memory restriction
1	1	0.02	CPU	No	22	106
1	1	0.02	GPU	Yes	0.25	≈ 1
1	5	0.1	GPU	No	0.90	1.80
5	5	0.1	GPU	No	0.90	0.55
1	5	0.1	GPU	Yes	0.25	≈ 1
1	10	0.2	GPU	No	0.24	≈ 1
1	20	0.4	GPU	No	0.06	0.70

Table 7.7: Run-time comparison of simulations using different FRM techniques. Here, NP represents the average number of particles in simulation domain

Study on strength reduction factor

It was explained in Prendergast [193] that the strength of the approximated particle (Γ_a) of a sampling-cell using Eq. (7.12) was determined less by a factor of $\frac{2}{\Pi}$ to the original circulation (Γ_o) alongside the sampling-cell. It was explained further that the use of sampling-grid of higher dimension ($n \times n$) minimized this reduction in particle strength and helped to conserve almost the total circulation of the modelled flow field. However, while modelling the large scale unsteady boundary layer by inserting approximated particles in VPM simulation, the turbulence intensity of the longitudinal velocity components of the modelled flow was found around 30% less than the target while the vertical component achieved almost the target.

The turbulence intensity of an arbitrary chosen point in reproduction simulation is found always comparatively higher in magnitude than that of original simulation, when the vortex particles are approximated using Eq. (7.12). A number of reproduction simulations are performed therefore for the presented original simulation for different α_{rf} . The vortex particles are approximated using Eq. (7.13) instead of Eq. (7.12). The influences of the factor α_{rf} in flow reproduction are presented in Fig. 7.21, that is based on the profile comparison of mean flow velocity \bar{U} and the turbulence intensity of fluctuating velocity components I_u and I_w .

The flow reproduction quality is observed better with the use of $\alpha_{rf} = 0.85$ (see Fig. 7.21). To observe the influences of α_{rf} more closely, the fluctuating velocity components at the centre sampling point of the flow monitoring profile are presented in Fig. 7.22.

For both cases α_{rf} , which are 0.85 and 1, the correlation factors of u and w in between the original and reproduction simulations are similar, which show that the global characteristics like the contained frequencies of the signal are replicated well in both scenarios. The spectrum of the signals in Fig. 7.22 are presented in Fig. 7.23, which also validates the same argument. However, the comparison of the peaks of the signals shows that the standard deviation of the fluctuations are found higher in case of $\alpha_{rf} = 1$. The use of the factor $\alpha_{rf} = 0.85$ in the approximation of the strength of vortex particles therefore helps to capture reasonably well original flow fields in flow reproduction.

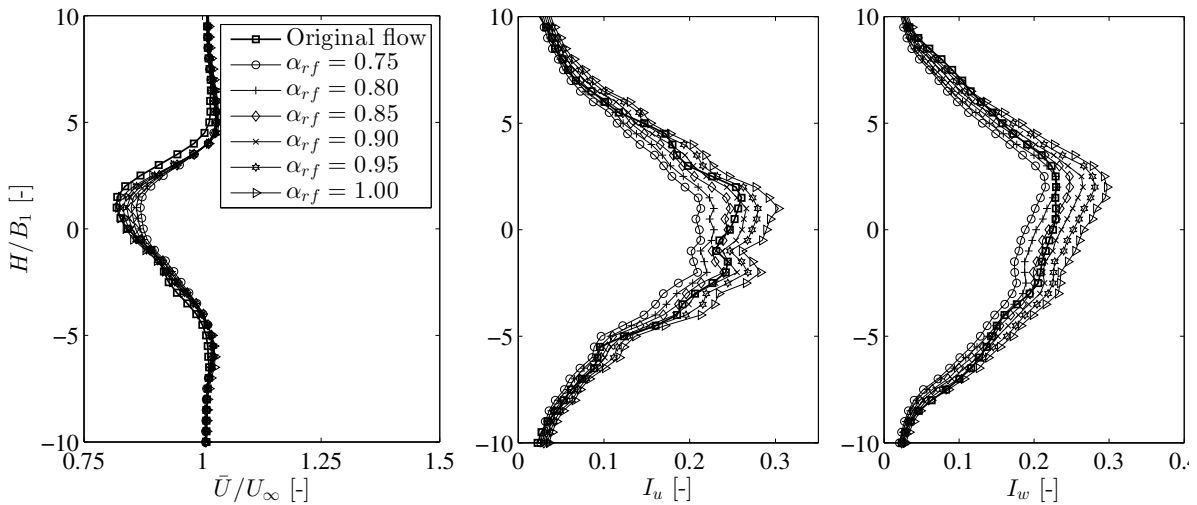


Figure 7.21: The influences of strength reduction factor (α_{rf}) on the quality of flow reproduction based on the comparison of characteristic flow profiles ($l_r = 17B_1$ and $l_m = 22B_1$): \bar{U} (left), I_u (middle), and I_w (right).

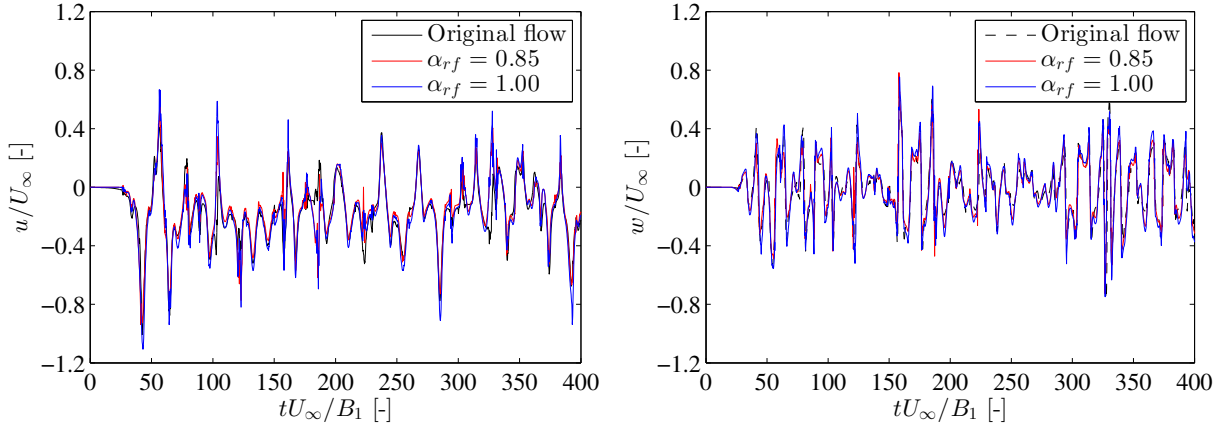


Figure 7.22: The comparison of instantaneous fluctuating velocity components $u(t)$ and $w(t)$: The flows are monitored at the centre sampling point of the flow monitoring profile, i.e. at $(l_m, 0)$ cf. Figs. 7.16, 7.21. Top: The comparison of $u(t)$ and statistical quantities: $\sigma(u_{orig}/U_\infty)$ (- - -) = 0.2065, $\sigma(u_{rep}/U_\infty)$ (- - -) = 0.2058, $\sigma(u_{rep}/U_\infty)$ (—) = 0.2386, $corr(u_{orig}/U_\infty, u_{rep}/U_\infty)$ (- - -, - -) = 0.9416, $corr(u_{orig}/U_\infty, u_{rep}/U_\infty)$ (- - -, —) = 0.9441. Bottom: The comparison of $w(t)$ and statistical quantities: $\sigma(w_{orig}/U_\infty)$ (- - -) = 0.2088, $\sigma(w_{rep}/U_\infty)$ (- - -) = 0.2220, $\sigma(w_{rep}/U_\infty)$ (—) = 0.2589, $corr(w_{orig}/U_\infty, w_{rep}/U_\infty)$ (- - -, - -) = 0.9346, $corr(w_{orig}/U_\infty, w_{rep}/U_\infty)$ (- - -, —) = 0.9379.

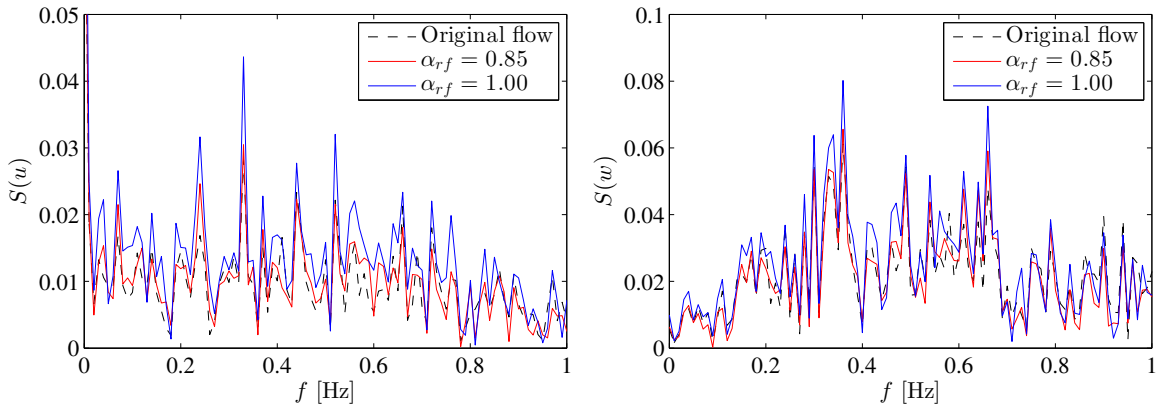


Figure 7.23: Spectrum of time history of fluctuating velocity components $u(t)$ (left) and $w(t)$ (right) from the signals shown in Fig. 7.22.

Reproduction of different wake flows

The numerical technique FRM is presented relatively general in terms of inflow condition of flow simulation around bluff sections. It has been mentioned that the method in terms of sampling and seeding doesn't change on the complexity of inflow condition. As example, the method is applied here to model a special phenomena such as von Kármán vortex street at very low Re . A qualitatively quality comparison is made for reproduced flow fields in Fig. 7.24(a) and shows good agreement with the original fields. In another example case, the reproduced flow fields for an original simulation of two upstream square sections are shown in Fig. 7.24(b) and found to be satisfactory. Importantly, it many not be possible to reproduce every single turbulent eddies in the original flow field since the interaction among the particles, especially of those, before the sampling system are missing. However, it is intended here to asses the quality in terms of statistical properties, which are presented in the following section.

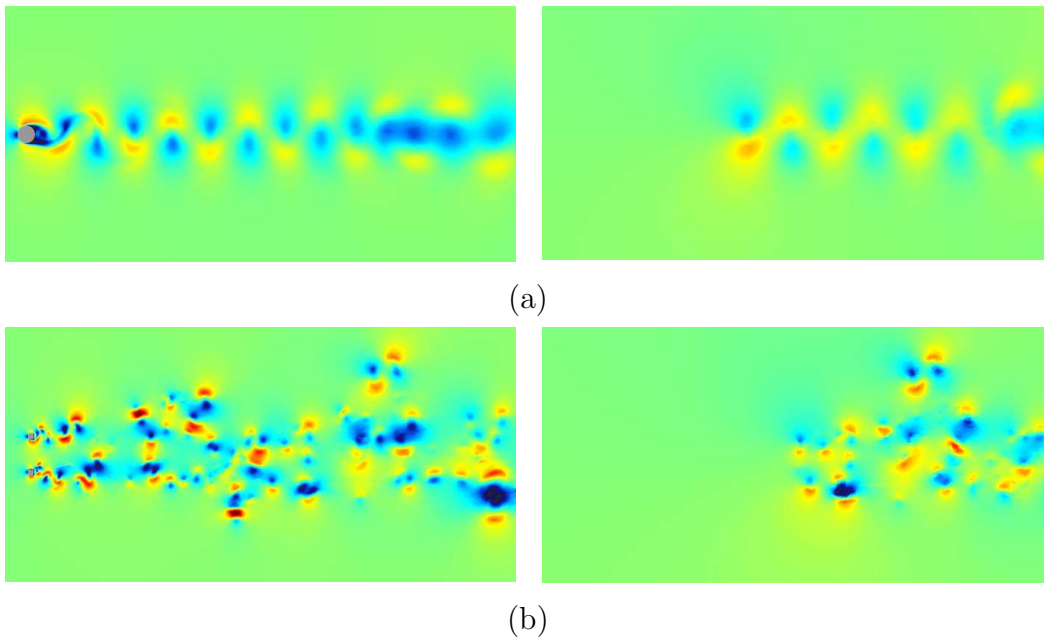


Figure 7.24: Reproduction of simulations of different flow phenomena: Reproduction of (a) von Kármán vortex street from a circular cylinder at $Re = 200$, and (b) vortex shedding from two upstream square sections at $Re = 500$.

7.3.4 Quality assessment

This section presents the quality of flow reproduction. The earlier discussions on quality in Sec. 7.3.3 has been qualitative and based on the flow fields for a particular time instant. The aim of this section here is to consider the reproduction of flow over the entire simulation time and to estimate the quality using some commonly used statistical measures. The velocity sampling points which has been shown in the downstream flow monitoring section in Fig. 7.16 are employed for implementing profile based quality assessments. While assessing the quality of flow reproduction, the influence of different variables of the presented technique are also studied. For example, the influences of location of sampling system in original flow simulation is studied. Furthermore, the quality is assessed for reproduction cases with different number of released particles including the computationally effective techniques.

Effects of position of sampling system

It is necessary to study the influence of the position of sampling system to know about the dependency of FRM on this parameter. Hence, the original simulation is simulated considering different location of the sampling system.

Original simulation is performed and sampled in four different scenarios by locating the sampling system in the simulation cf. Fig. 7.16, such that l_r are chosen $11B_1$, $14B_1$, $17B_1$ and $20B_1$. The simulations are monitored using flow monitoring profile (mm') such that $l_m = 25B_1$.

Importantly, the choice of different l_r relocates the complete sampling systems, and therefore, the corresponding set of vortex particles should be completely different. However, the reproduced fields from different set of vortex particles are expected not to change a lot. The results are presented in Fig. 7.25 which shows good reproduction quality up to some extent.

From several studies (not presented here), the quality of reproduced flow reduces if the

velocities are sampled in the original simulation very close to the upstream geometry. This is because the fluctuations near the upstream section are very much oscillatory. In such flow reproduction cases, the influences of the missing alternating particles just before the particles released in section (rr') are comparatively higher and hence the reproduced flow field may not be the expected one. In addition, the oscillatory flow near the upstream section may reduce the strength of approximated vortex particles while using Eq. (7.13) due to the possibility of different order of magnitudes for u and w . The influence of the particle strength reduction is visible in Fig. 7.25 for case $l_r = 11B_1$, where the \bar{U} profile is approaching to U_∞ profile due to this effect. The reduction of the particle strength for case $l_r = 11B_1$ is also visible in I_u profile. However, with the increase in l_r this particular effects are reduced, and hence, using $l_r = 20B_1$ the reproduction quality is found to be quite satisfactory. Therefore, the sampling system should be located such that the vortex shedding in the original simulation is clear and separated enough before reaching the sampling system.

Quality of computationally effective techniques

The use of particle remeshing (PR) and the adaptive reproduction technique in FRM have already been presented in Sec. 7.3.3 as computationally effective technique. However, the qualities are explained only in terms of the snapshots of flow fields and reproduction errors. To evaluate the reproduction quality of the computationally effective techniques, the original simulation is sampled such that $l_r = 20B_1$ and monitored at $l_m = 25B_1$. The computationally effective reproductions are performed based on the number of released particles that are $N_{rp}=1250$, 250 (adaptive reproduction), 125 and 65. Particle remeshing is employed only for the case of $N_{rp} = 1250$. The profile based comparison of the reproduction quality is presented in Fig. 7.26. Clearly, all the reproduction simulations are showing almost the same reproduction quality. It is also visible that after a converged reproduction solution the quality can not be increased significantly by increasing the number of particles or by reducing the sampling-cell size. That also suggests to use computationally effective techniques of FRM in wake buffeting analysis without having significant errors.

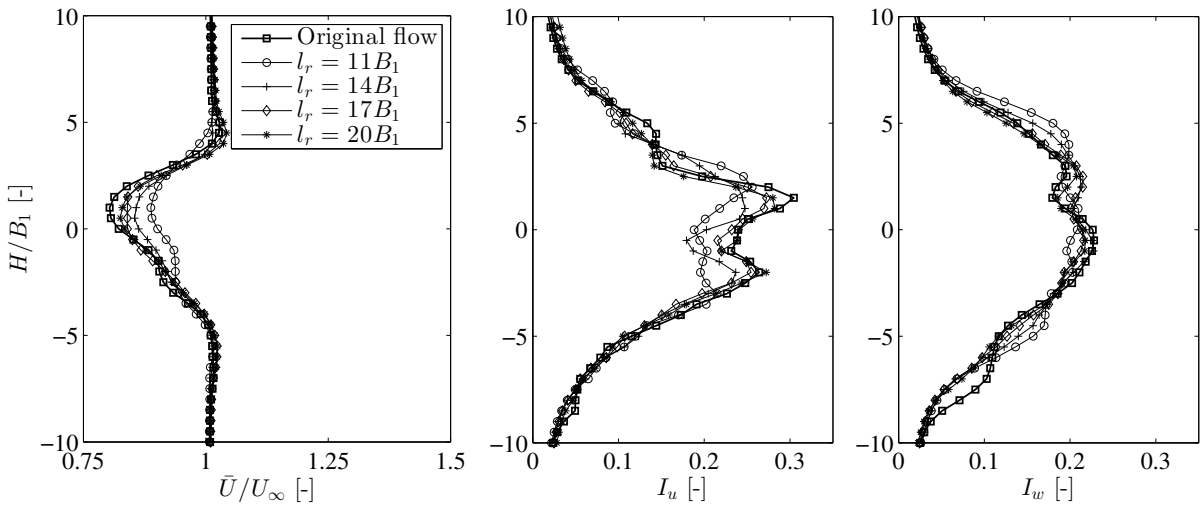


Figure 7.25: The reproduced flow quality influenced by the location of the velocity sampling system or the particle release location (l_r) based on characteristic flow profiles: \bar{U} (left), I_u (middle), and I_w (right).

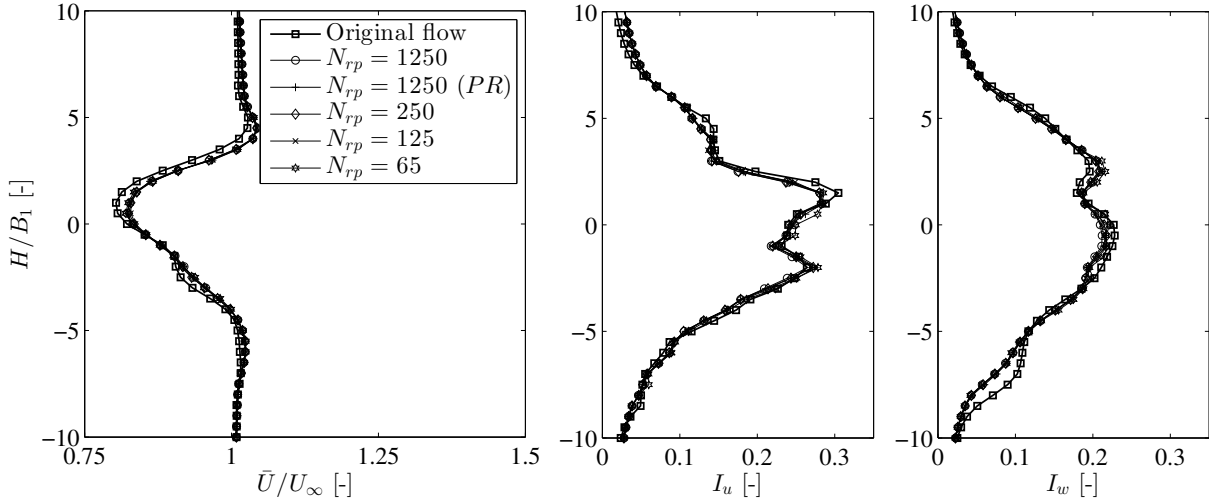


Figure 7.26: The quality assessment of different flow reproduction techniques using characteristic flow profiles: \bar{U} (left), I_u (middle), and I_w (right).

7.3.5 Wake buffeting analysis

The structures immersed in wind fields can be subjected to static and dynamic forces caused by mean and fluctuating wind velocities, respectively, which in turn oscillate the structures [217, 223]. The vibration of a structure induced by the fluctuating wakes coming from upstream often governs the design criteria [58, 229, 261]. In nature, aerodynamic behaviours are three-dimensional under the fluctuating drag, lift and moment loads on the structure; however, the focus of the study is limited to the analysis of the transverse response, e.g. [187, 214], of a downstream rectangular section under the turbulent wakes.

An elastically supported rectangular section in turbulent wakes

The vibration of an elastically supported rectangular section ($B_2/D_2 = 4$), cf. Fig. 7.16, is analysed under the inflow conditions of upstream wakes from square cylinder. The intention is to compare the vibration of the system under original wakes as well as under the reproduced wakes. The critical response is expected to happen especially when the system natural frequency will be equal to the frequency of the vortex shedding from upstream section.

The upstream square section is simulated at $Re = 500$ to find the vortex shedding frequency which is shown in Fig. 7.27. The Strouhal number $St = f_s B_1 / U_\infty$, where f_s is the frequency of the vortex shedding, is found approximately 0.137 which is reasonable with experimental and numerical results for a square section at $Re = 500$ [156]. The vortex shedding frequency $f_s \simeq 0.7$ is considered the natural frequency (f_n) of the downstream section for wake buffeting analysis. The non-dimensional structural mass-damping parameters of the downstream section are chosen such that the Scruton number $Sc = m\zeta / \rho D_2^2 = 83.33$.

A number of simulations are performed for response analysis of the downstream section under different inflow conditions, which are steady flows, wakes from upstream square section, and reproduced wakes, and the results are shown in Fig. 7.28. The displacement time history under the reproduced wakes in Fig. 7.28(c) is not expected to be the same under the original wakes in Fig. 7.28(b). Because, the particles released in the simulation of Fig. 7.28(c) are calculated from the original simulation without having the downstream section like in Fig. 7.19(a). The existence and also the dynamic vibration of the downstream section, cf.

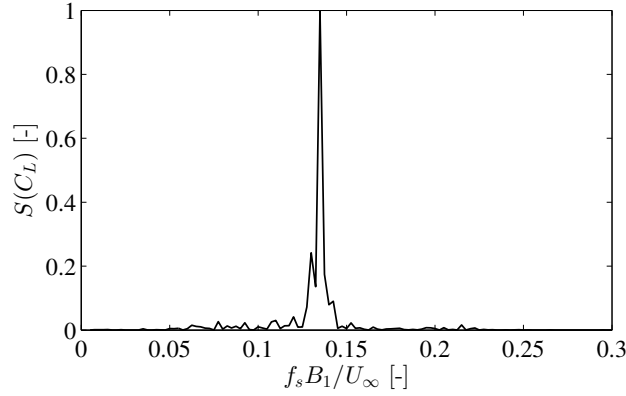


Figure 7.27: Normalized spectrum of the lift coefficient time history: the upstream square section in the original simulation at Reynolds number $Re = 500$.

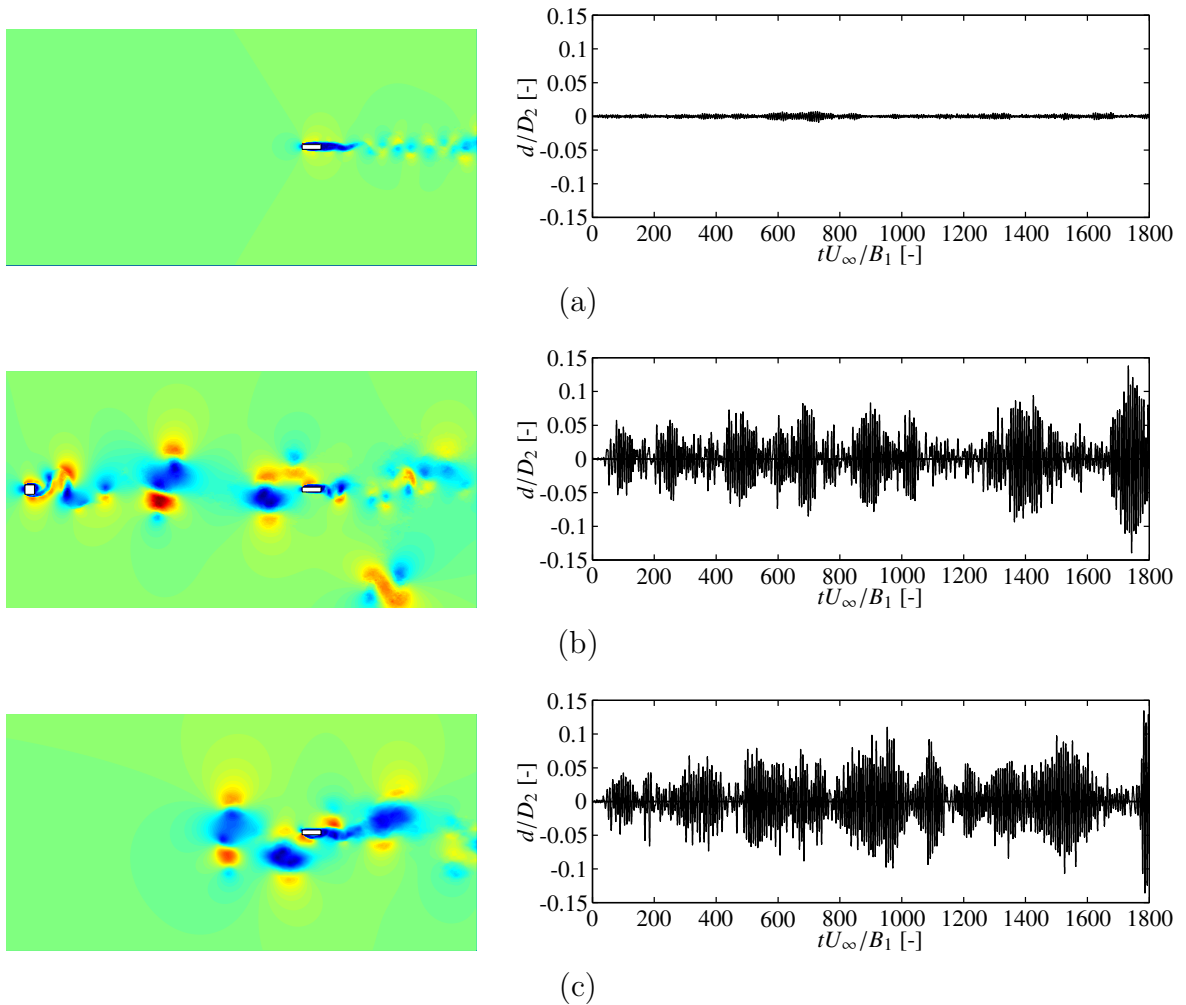


Figure 7.28: Dynamic simulations of the downstream section under different inflow conditions ($f_n B_1 / U_\infty = 0.137$, $Sc = 20.83$): (a) Steady flow U_∞ : snapshot of the flow field (top), vertical vibration, $d_{max}/D_2 = 0.0044$ and $d_{rms}/D_2 = 0.0046$ (bottom), (b) original wakes from upstream square: snapshot of the flow field (top), vertical vibration, $d_{max}/D_2 = 0.138$ and $d_{rms}/D_2 = 0.085$ (bottom), and (c) reproduced wakes ($n_s = 5$, $N_{rp} = 250$, $l_r = 20B_1$): snapshot of the flow field (top), vertical vibration, $d_{max}/D_2 = 0.136$ and $d_{rms}/D_2 = 0.086$ (bottom).

Fig. 7.28(b), has influences on the upstream wakes. The comparison of maximum and RMS displacements of the downstream section under original and reproduce wakes in Fig. 7.28 shows good agreement.

Comparison of different reproduction techniques in wake buffeting analysis

A Run-Time (RT) analysis is performed to evaluate the efficiency of the computationally effective techniques of FRM in wake buffeting analysis and the results are presented in Table. 7.8. Clearly, all the cases are found computationally effective with respect to RT taken by the wake buffeting simulation under original wakes. Particularly, the wake buffeting analysis under reproduced wakes using adaptive reproduction technique allows the simulation to be performed five times faster than original wake buffeting analysis. In current study, the upstream condition has been used very simple, which is only a small square section. The wake buffeting simulations should be more effective for cases where the upstream wakes come from multiple sections or a section of complex geometry. In those cases, significant amount of vortex particles are required to achieve converged wake flow fields from upstream bodies.

$\frac{\Delta t_{rep}}{\Delta t_{orig}}$ [-]	n_s [-]	NT [-]	$\frac{dx}{B_1}$ [-]	Applied Strategy	$\frac{RT_{rep}}{RT_{orig}}$ [-]	RT_{rep} [hr]
1	1	90,000	0.02	Particle Remeshing	0.70	14
5	5	18,000	0.10	Adaptive Reproduction	0.20	4
1	10	90,000	0.20	Bigger track-cell size (dx)	0.75	15

Table 7.8: Comparison of Run-time of the wake buffeting simulations using different computationally effective techniques in FRM.

7.3.6 Aeroelastic interaction of T-shaped harvester in fluctuating wind

In the following, the coupled motion of the T-shaped flexible harvester (c.f. Sec 6.4.3) is simulated under the fluctuating incoming flows. The flow fluctuations are imposed using two different approach: (a) reproduction of turbulent wakes from upstream bodies, and (b) random free-stream turbulence, c.f. Kavrakov and Morgenthal [141].

The motion of harvester in reproduced wakes from upstream bodies

The wake flow is reproduced from three upstream bodies considering free stream velocity of $U_\infty = 4$ m/s, which is the critical flutter wind speed of the T-shaped harvester. Fig. 7.29 shows the fluctuating flow components of the reproduced flow at the centre of the simulation domain, where the harvester will be placed. The turbulence intensities are calculated $I_u = 0.213$ and $I_w = 0.23$. Now, the coupled analysis of the harvester is performed under the seeded particles in free stream flow $U_\infty = 4$ m/s. The results of the coupled analysis in turbulent wakes are summarised in Fig. 7.30. The vertical tip displacement of the T-shaped system reduces significantly. It is due to the high fluctuations in the flow that never allowed the system to develop flutter. In another way, it is due to the continuous change of positive and negative aerodynamic damping. The initiation of flutter motion is continuously interrupted by the reduction in negative aerodynamic damping.

It is important to note that the turbulence in the flow is significantly high, and the frequencies of flow fluctuations are different and lower than the frequency of the harvester (see Fig. 7.29). However, they impose almost no influence on the coupled response frequency, which are observed very close to the natural frequency of the T-shaped system. It is because the coupled rotational motion of the T-shaped harvester is governed mainly by the motion-induced forces.

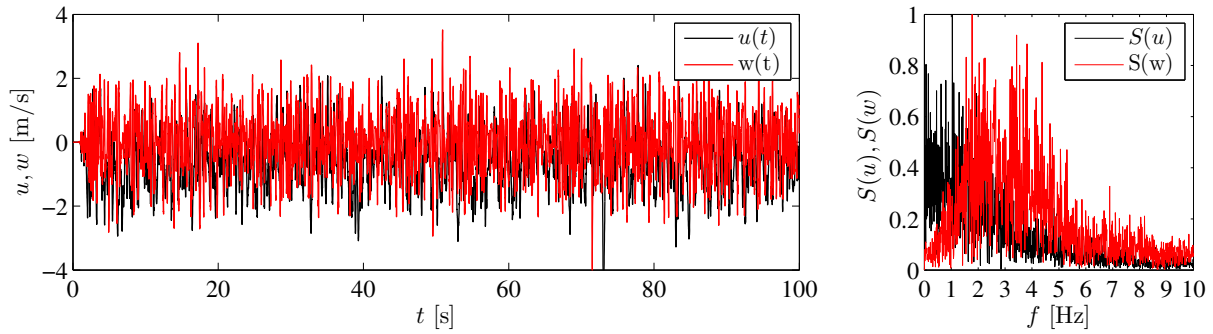


Figure 7.29: Fluctuating velocity components of reproduced wakes from upstream bodies: (left) velocity time history, and (right) frequency spectrum.

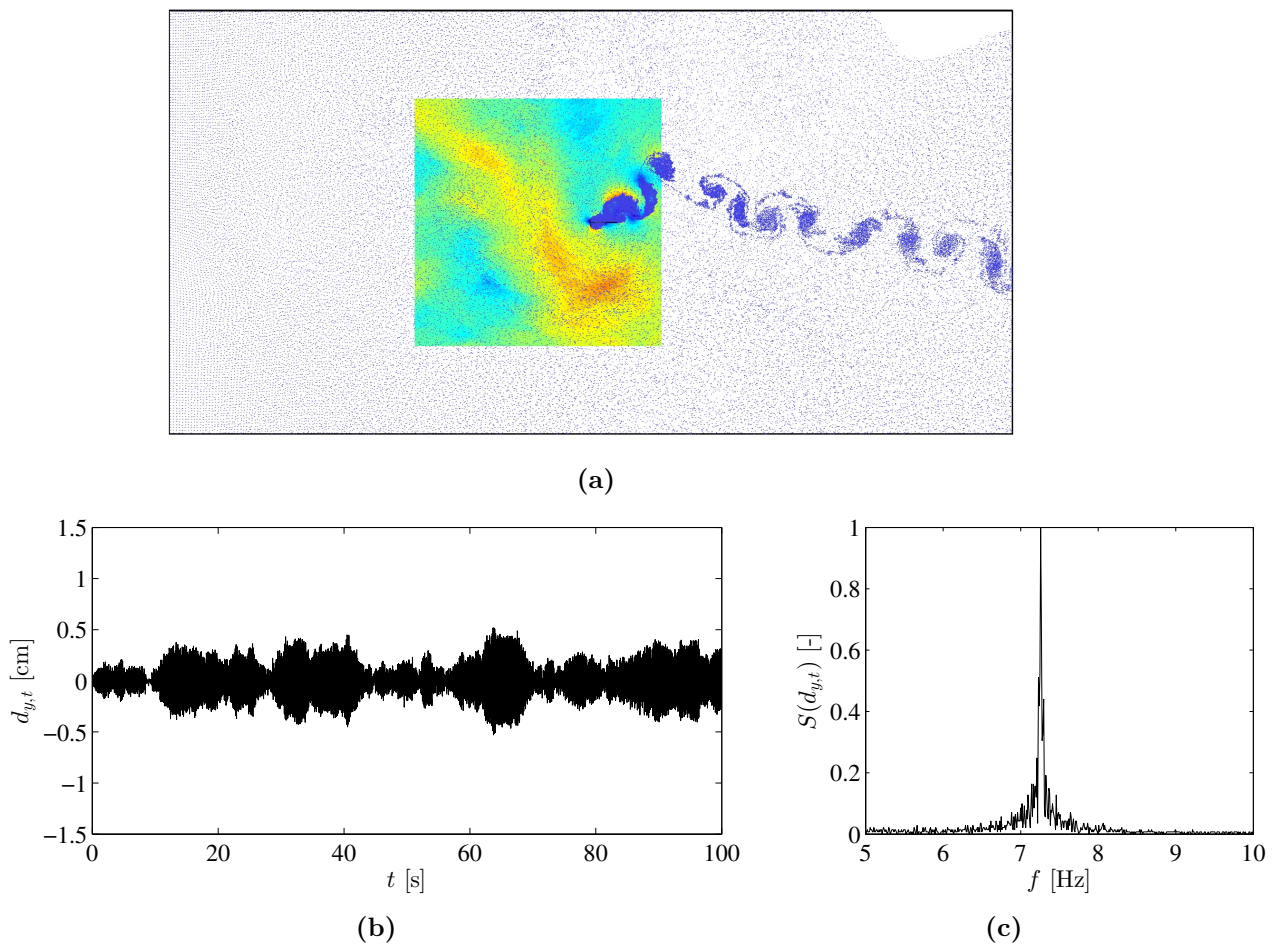


Figure 7.30: Coupled simulation of flexible harvester in the reproduced wakes: (a) instantaneous particle map and flow field around oscillating harvester, (b) tip displacement, and (c) response frequency.

The flexible harvester in 2D random free-stream turbulence

Similarly, as in the previous section, the flexible harvester is analysed under random turbulence. The isometric turbulence is produced using the method developed in Kavrakov and Morgenthal [141]. The target parameters of isometric turbulence are chosen: $I_u = 0.1$, and $I_w = 0.1$, $L_u=10$ m, $L_w=10$ m, $\bar{U}=4$ m/s. Fig. 7.29 shows the fluctuating flow components of the reproduced flow at the centre of the domain, where the harvester will be placed. The turbulence intensities are obtained $I_u = 0.06$, and $I_w = 0.04$. It is due to the use of small simulation domain (2.5 m \times 2.5 m) which is not enough to capture the effects of eddies of different length scales. The simulation domain is significantly large for the harvester, however, not for modelling of atmospheric turbulence of different eddies. The algorithm in Kavrakov and Morgenthal [141] was used for bridge aerodynamics, and it was shown that the method could model target flow fluctuations with satisfactory accuracy. The present study, however, is not concerned with the accuracy of the modelled flow fluctuations. Instead, the interest is to analyse the coupled motion of the harvester under the modelled mild turbulence.

Similarly, as before, the analysis is performed with the seeded particles in the free stream flow $U_\infty = 4$ m/s. The results of the coupled analysis are summarised in Fig. 7.32. Now, the T-shaped system is fluttering; however, the effect of the turbulence is evident in the response envelope. The fluttering motion of the T-shaped harvester is due to the sustainable negative aerodynamic damping though influenced slightly by the inflow fluctuations.

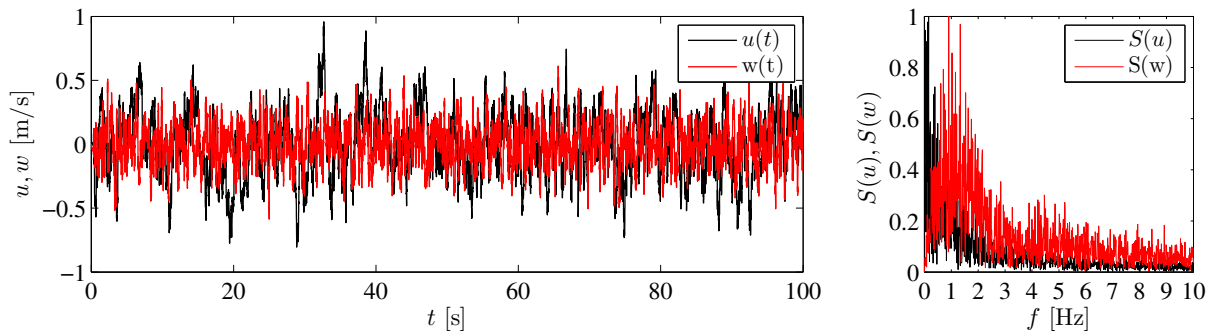


Figure 7.31: Fluctuating velocity components of random free-stream turbulence: (left) velocity time history, and (right) frequency spectrum.

7.3.7 Summary

The flow reproduction method (FRM) has been presented as a new extension of the 2D VPM to simulate complicated transient flow features analysed by an original simulation to be recreated for use as inflow conditions in other simulations. The general methodology of flow reproduction has been presented sequentially, which contains the discussion on velocity sampling from an original simulation, the approximation of vortex particles, and the seeding of the particles for the reproduction of the target wakes. The convergence study has shown that the target wake flows can be simulated not only using a different number of particles but also with adaptive numerical strategies such as particle remeshing.

The dynamic motion of a rectangular section have been analysed under original and reproduced wakes. The maximum and mean displacements of the section and their good agreement between the results confirm the applicability of FRM for modelling the inflow wakes in dynamic simulations. The FRM has been found to be an effective means for performing

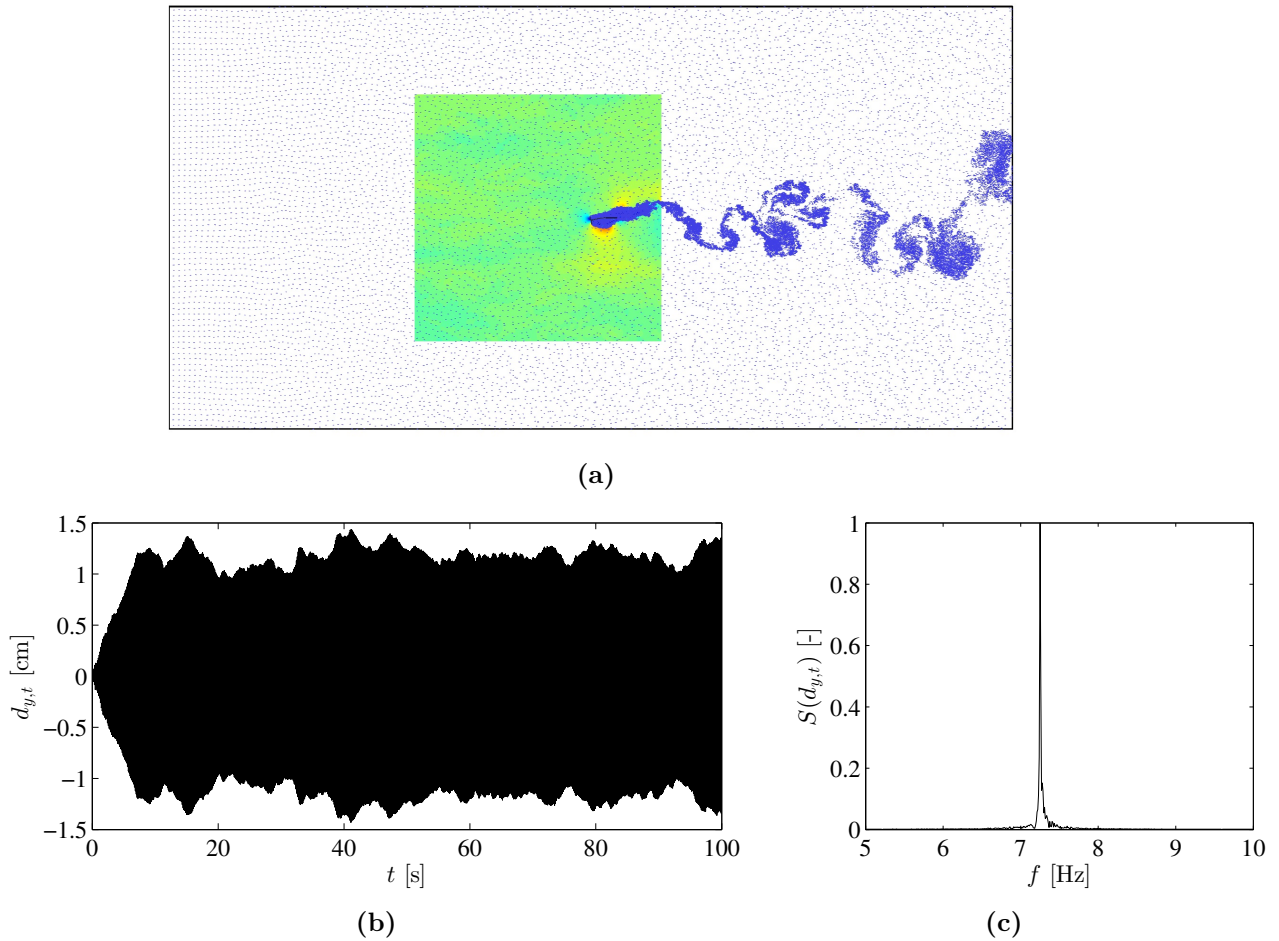


Figure 7.32: Coupled simulation of flexible harvester in the free-stream random turbulent flow: (a) instantaneous particle map and flow field around oscillating harvester, (b) tip displacement, and (c) response frequency.

simulations where particular inflow conditions need to be re-used in multiple dynamic simulations, e.g. for shape optimization, reliability or sensitivity based analyses, wake buffeting analyses in which the inflow wakes originate from multiple complex sections.

Finally, the coupled motion of a reference flexible T-shaped harvester has been investigated under reproduced wakes and random free-stream turbulence to study its performance for energy harvesting. The outcome shows that the T-shaped system can display flutter response even in turbulent flow if the turbulence is mild. However, in wake flows with high turbulence intensity the T-shaped cantilever has not been able to initiate large response. The use of funnel in the incoming wakes can improve the energy harvesting potential from wakes.

Chapter 8

Conclusions

8.1 Summary

This research is intended to extend the applicability of Vortex Particle Methods (VPM) for complex fluid–structure interactions (FSI) of thin-walled flexible structural systems under steady and fluctuating incoming flows. Previous frameworks of the VPM, within two-dimensional (2D) and pseudo-three-dimensional (pseudo-3D) multi-slice formulations, had been employed for performing FSI simulations of line-like flexible structures, such as long-span cable-supported bridges and towers. Many fundamental studies and aerodynamic problems in long-span bridges were analysed. Attractive analysis features, successfully validated outcome, and the ability of the in-house VPM-based solver to simulate efficiently sophisticated flow features with high-resolution motivated the author for further extensions towards FSI simulations flexible systems. Other authors developed several advancements to this VPM-based flow solver in recent past such as the adaptive solution strategies and the modelling of statistical turbulent incoming flows. However, the analysis of the system from the cross-section point of view was always limited to bluff bodies only. The extension of the VPM to handle with deformable bodies had been a demand to be able to use the VPM-based solver for analysing aeroelastic interaction problems.

In this context, two new coupled extensions were developed using the partitioned numerical approach for 2D and pseudo-3D VPM for analysing FSI problems. The 2D extension of VPM was developed for large-displacement FSI simulation of thin plate systems. On the other hand, the pseudo-3D VPM was extended within the multi-slice formulations for thin-walled shell-type structures. The fluctuations in the incoming flow can impose significant influence in the coupled dynamic response. Apart from the extensions of VPM for coupled FSI simulations, two further novel extensions were implemented within the framework of 2D VPM for modelling of inflow fluctuations. These extensions were designed such that they could apply to the coupled FSI algorithms for analysing aeroelastic interactions in fluctuating incoming flows.

The partitioned approach was used because of its flexibility of using different existing solvers for fluid and structure models. The immersed boundary element method (BEM) was utilised in both extensions of VPM for analysing the complex flow dynamics around deformable boundaries. The surface of the flexible body was discretized in each slice by introducing

elements on its boundary. The surface vorticity was discretized as sheets of linearly varying vorticity along the surface panels. The flexible beam or thin plate undergoing large vibrations requires a more advanced structural modelling to predict the system vibrations accurately. A structural solver based on a corotational finite element formulation was coupled with the mentioned 2D VPM solver to model the large deformation effects. In another coupled extension, the pseudo-3D VPM was extended for analysing complex aeroelastic interactions of thin-walled shell-type structures in a multi-slice manner. The novelty of this extension was the inclusion of 3D natural vibration modes within the existing framework which allowed modelling of deformable geometry through the use of multiple 2D VPM analysis. In both extensions, the structural equations were formulated at the mid-surface of the thin elements. The structural analysis, in case of 2D coupled VPM extension, included the effects of geometrical nonlinearity of beam elements. On the other hand, the structural analysis in pseudo-3D coupled VPM was performed in a modal coordinate system using the superposition of linear vibration modes.

Chapter 2 presented earlier some fundamental issues of fluid dynamics, different aerodynamics phenomena, and nonlinear aeroelasticity. Chapter 3 described several vital aspects of FSI simulations, as part of the literature review of numerical methods, which usually governs to the choice of fluid and structure solver, and the coupling approaches. The chapter presented further the governing equations of VPM, and the existing analysis features for analysing bluff-body aerodynamics.

Chapter 4 has presented different modifications in details that were introduced or implemented additionally to the existing formulations of VPM solver for coupling with a structural solver. The chapter was mainly devoted to explaining the discretization of the system in fluid and structure solver and their interaction procedures. Several schematic explanations included the projection of the fluid pressures from the surface panels to the structure nodes, the solution of the nodal displacements, the feedback projection of structural solution to the boundary panels, and update of boundary conditions.

The validation studies for the coupled FSI algorithms of VPM were presented in Chapter 5, which were based on several benchmark aeroelastic problems. Several application cases were studied further for a deeper understanding of aeroelastic coupled behaviour. The 2D coupled solver was validated on benchmark large-displacement FSI problems such as the aeroelastic flapping of inverted and T-shape cantilever plates, the flag-type flapping of cantilever plates in axial flow and Kármán vortex street. The validated solver was utilised to study the changes in aeroelastic behaviour and flapping pattern of inverted and T-shaped cantilevers with/without tip mass. Furthermore, the coupled response of a prestressed flexible membrane roof was performed as a further validation study of such applications. In case of pseudo-3D formulation of the VPM, the method was developed for two types of system: Thin plate-type system in which the flow passes over both surface and the circular cylinders in which fluid passes over the outer surface only. The first model was validated by identifying the critical flapping wind speed of several cantilever plates. The model was applied to the analysis of an extensive cantilever roof system. On the other hand, the second model was used for analysing the vortex-induced vibration (VIV) of a long clamped circular pipe. The method was utilised to simulate ovaling effects of the thin-walled circular section due to cross-wind effects. The solver was utilised further to analyse the VIV of the solar chimney, an extremely tall vertical tube-like structure which is vulnerable against lateral buckling of the shells.

The Chapter 6 presented a simplified model for complex aero-electromechanical coupled analysis to study on aeroelastic energy harvesters. The study intended to identify potentially

efficient cantilever systems in terms of sustainable limit cycle oscillations (LCO) for small-scale vibration energy harvesting while the target wind speed was of particular interest. The coupled model was proposed within the framework of 2D VPM for large-displacement FSI problems. The electrical damping effects added to the mechanical damping were modelled using the Rayleigh damping approach. The critical flutter wind speed and the energy output of a reference prototype electromagnetic energy harvester were modelled for validation of the method. The study presented further the optimisation of physical and electrical parameters of energy harvester to maximise the power output for a range of target wind speeds. The study focused on further modelling of different cantilever systems with/without tip mass for electrical damping effects to find optimised and the sustainable response of the aeroelastic system. The aim was to provide useful guidelines for the preliminary design of aeroelastic energy harvesters.

In Chapter 7, two new extensions of 2D VPM, which were developed based on the technique of seeding vortex particles in the free stream flow, were presented for the simulation of inflow fluctuations. The first extension was proposed for the simulation of the periodic incoming flow. The method utilized the natural convection of the particles, which were regularly seeded from two distant seeding points near the upstream boundary. The seeding mechanism and the orientation of the particles were handled such that they induced only horizontal velocity components around the domain centre. In contrast, the vertical components were nearly cancelled out. The sinusoidal periodic flow was modelled by seeding the particles of varied strength and orientation, correspondingly. Convergence studies were performed to validate the scheme. The quality of the modelled periodic flows was assessed and quantified. The method was applied for T-shaped energy harvester to study the effects on the performance. The other numerical extension, which was introduced as the flow reproduction method (FRM), was implemented to simulate the sophisticated transient flow features computed by an original simulation to use as inflow conditions in other simulations. This was facilitated by recording the velocity-time signals of the original simulation and computing time traces of vortex particles to be seeded into the secondary simulation near its upstream domain boundary. The developed method thus allows re-creating the flow field, without the need to simulate the underlying physics responsible for the flow features. A natural area of application is the re-creation of wakes from flows past bluff bodies of arbitrarily complex geometry, the resolution of which is computationally expensive. The recording of the velocity field of an original flow simulation was performed on a sampling system. Reproduction of the sampled simulation was performed by inserting vortex particles in defined positions and time intervals into the secondary simulation. The computational efficiency was achieved through the use of a smaller simulation domain and different adaptive numerical techniques. The method was applied further to FSI simulations of wake buffeting problems.

The developed numerical extensions which were presented in this thesis for 2D and pseudo-3D VPM relied on several assumptions and contained application limit to some extent. First of all, the flow analysis of VPM is purely 2D, and therefore, the 3D across-flow effects were ignored. It was similarly valid for the pseudo-3D multi-slice approach since each slice was an independent 2D flow simulation. The slice-wise correlations were achieved through structural vibration modes and FSI effects. Therefore, the thesis presented the benchmark cases which were treated as 2D in literature or test cases in which 3D effects could be ignored. Another critical issue for the 2D coupled solver was the disregarding of added mass effects. Several studies in literature showed that the aeroelastic coupled problems are less affected by added mass effects. Among the simulated test cases in this thesis, the flapping flag suffered numerical instability due to added mass effects when the material

thickness was considered significantly less. Strong coupling between fluid and structure solver is necessary to enhance the applicability. The pseudo-3D extension of the VPM solver is limited to the application of thin-walled linear structures only. The thin-walled large systems around us are most commonly of varying shapes; the disregarding of 3D flow effects can influence the outcome significantly. In the numerical extension of pulsating incoming flow, the pre-calculation of particle strength was based on several assumptions. One of them was disregarding of interaction between the particles; however, the interaction did exist when they were seeded in the free stream velocity.

The studies in the thesis were mostly based on numerical analysis; however, some of them were directly compared with wind tunnel test results as part of model validation. Although experimental wind tunnel tests are always considered a standard approach, such tests are expensive, time-consuming, and have scaling limitations. The numerical methods are impressive to predict the full-scale aerodynamic behaviour, modelling of complex shapes, and clear visualization of interesting flow phenomena around bluff or moving flexible bodies. The visualization of complex aeroelastic coupled behaviour of several test cases in the thesis justified the previous statement. Furthermore, the easy controlling of the input parameters for fluid and structural models allows for aerodynamic optimization.

8.2 Conclusions

The numerical extensions of VPM proposed in this study have shown the ability to perform aeroelastic FSI problems of thin-walled flexible structures, including different inflow conditions. The comparisons of the results with several experimental and benchmark FSI problems have shown good agreement. It has to emphasise that the type of analysed aeroelastic interaction problems are based on one of the main limitations of the coupled solver, which is the flow analysis is purely two-dimensional. However, several analysis outcomes within the applicability have shown new insights of aeroelastic coupled interactions. The study has demonstrated the applicability of the 2D coupled solver not only for analysing large-displacement FSI problems but also predicting the motion and energy output of aeroelastic energy harvesters.

The numerical model to analyse the interaction between the fluid and moving deformed body depends on accurate representation of the geometry and vortex sheet on the moving deformed body. Thanks to the boundary element method (BEM) that allows the discretisation of complex geometry and arbitrarily large deformation. The treatment of the interface mesh in FSI simulations is of significant concerns, mainly when the displacement is large. The grid-less nature of VPM removes the requirement of mesh refinement at the fluid–structure interface. The finite element formulation of structural motion at the mid-surface is found helpful. For such FSI models of non-conforming mesh, the challenges exist in the requirement of projecting information from one interface to another, and it requires particular attention since they act independently. Furthermore, accurate prediction of surface vorticity is a critical concern, and therefore, the influence matrix of boundary panels has been calculated at every simulation step. The enforcement of the velocity boundary conditions is satisfied in addition to the continuity equations. Excellent prediction of the boundary layer of an oscillating flat plate shows the ability of the mid-surface approach of the coupled model. It validates not only the enforcement of the velocity boundary conditions for BEM but also the projection of information at the fluid–structure interface.

The validated 2D coupled VPM model has shown its ability to investigate complex aeroelastic

interactions of large-displacement problems. The flapping of a simple thin cantilever plate can show significantly different aeroelastic interactions based on the boundary condition and inflow conditions. The method has been able to predict such complex aeroelastic interactions with satisfaction when compared with the literature. This fact has allowed studying on aeroelastic coupled behaviour and flapping pattern of different inverted and T-shaped cantilevers with/without tip mass. The analyses have been performed for increasing wind speeds until the permanent deflection mode occurs, and the results has displayed significant differences in coupled mechanisms and LCO. The extension of the coupled scheme with a 3D flow solver would allow including the across-flow effects, such as for the oscillating thin plates for different aspect ratios.

The pseudo-3D coupled extension of VPM has been excellent for predicting the critical wind speed at which a linear thin-walled structure can experience large-amplitude unstable vibration or LCO behaviour. In reality, the interactions can be catastrophic. The method has shown its ability of predicting ovaling motion in case of closed circular shells. For roof type systems, it has been able to predict the differential response of the deformed bodies in between the slices including the critical interactions. Even though the coupled method has neglected the 3D across-flow effects, it is still applicable to analyse many essential structures such as large-scale solar chimneys.

The aeroelectromechanical coupled analysis using the 2D coupled extension of VPM has been successful, considering very good predictions of flutter limit and energy output of a reference harvester in the wind tunnel under different electrical resistances. Comparative study on different cantilever systems using the validated solver helps to obtain several useful guidelines for the preliminary design of experimental set-ups of prototype harvesters. The influential parameters, such as the response amplitude and oscillating frequency, are compared to identify not only efficient cantilever harvesters but also an appropriate combination of physical and electrical parameters depending on target wind speeds. There is always critical or optimal damping to achieve maximum power output from a harvester for specific wind speed. The inverted cantilever has been found very effective for piezoelectric energy harvesting in low wind speeds. The system has been found less sensitive to the increasing damping due to less bending stiffness and system mass. The LCO for a narrow range of wind speeds has been the only limitation. However, it is possible to use multiple inverted cantilever systems of different bending stiffness to exploit a variety of low wind speeds. The flutter-induced LCO of the T-shaped cantilever with tip mass has been suitable for electromagnetic and piezoelectric energy harvesting for a wide range of wind speeds. The damping sensitive T-shaped cantilever with tip mass produces energy when the wind speed is above the critical flutter limit. Therefore, it has been suggested for higher wind speeds.

The aeroelastic coupled behaviour small-scale energy harvester has been found governed by the large scale eddies which can be represented as a sum of the periodic incoming flow of very low frequencies. The studies of cyclic incoming flow on the performance of T-shaped harvester have shown that the fluctuations can be useful to induce the initiation of flutter when the mean flow is less or around the critical flutter limit. However, when the incoming wind is far above the critical limit, the effect is only visible through the periodic shaped of the LCO envelope. The FRM is found to be an effective means for performing simulations where particular inflow conditions need to be re-used in multiple dynamic simulations, e.g. for shape optimization, reliability or sensitivity based analyses. Concluding, the FRM has the potential to significantly improve the computational efficiency in wake buffeting analyses or similar problems where the inflow wakes originate from sections of complex geometry.

8.3 Recommendations for future studies

The presented numerical extensions of VPM and their application of a wide range of FSI problems of thin-walled structures show the path towards further improvement and new scopes for future study.

Excellent modelling quality of the 2D coupled VPM for large-amplitude aeroelastic interactions indicates the need for extension of the flow solver to 3D, which would enhance the applicability of the solver with the inclusion of the across-flow effects. The aeroelastic interactions of conventional and inverted cantilever plates with the impact of aspect ratio is a very challenging study. A more comprehensive parametric study of plate aspect ratio would allow improving the general understanding of aeroelastic behaviour. A similar statement also goes for the membrane roof system in which the modelling of 3D flow field would allow predicting realistic coupled behaviour.

The 2D coupled solver allows the analysis of motion-induced forces such as the validation studies has been shown for the enforcement of velocity boundary condition. Excellent modelling of the boundary layer around the oscillating flat plate indicates several promising possibilities for future studies. For example, the aerodynamic derivatives can be obtained from motion-induced forces of flexible plates to identify the critical flutter wind velocity. In the same context, another fascinating study field would be the application of the artificial neural network (ANN) for FSI simulations. The modelling of aerodynamic forces for various motions of deformed thin bodies can be trained with ANN to eliminate the need for the flow solver in FSI analysis.

The limitation of the partitioned extension of 2D VPM lies in its loosely coupled algorithm. When the coupled interaction is significant, a strong coupling is necessary between the fluid and structure solver in terms of additional loops until a convergence criterion is satisfied. However, it is as good as strongly coupled solvers in the field of aeroelastic coupled problems due to less influence of added mass effect from the air.

The coupled model of 2D VPM has been very good for predicting the aeroelectromechanical coupled behaviour of prototype harvesters. The studies on different flexible cantilever systems suggest using inverted cantilever in low wind speed for piezoelectric energy harvesting, whereas the T-shaped inverted cantilever with tip mass for electromagnetic and piezoelectric energy harvesting in higher wind speeds. It would be an attractive study to prepare different energy harvesters based on the numerical result and measuring the energy output experimentally in the wind tunnel.

The extension of the pseudo-3D VPM using geometrically nonlinear beam model remains to be developed. With the increasing flexibility of structures such as tall towers, very long-span cable-supported bridges, this extension would allow analysing the nonlinear aeroelastic behaviour of line-like structures.

The extension pseudo-3D VPM for thin-shell structures shows the need for 3D extension of the flow solver strongly. The inclusion of nonlinearity in the structural analysis is necessary for reliable prediction of aeroelastic failure mechanisms. The interest exists to study on the tall chimneys in the turbulent wind for varying free stream velocity along with the height of the structure.

Bibliography

- [1] Abbas, T. (2016). *Assessment of Numerical Prediction Models for Aeroelastic Instabilities of Bridges*. PhD thesis.
- [2] Abbas, T. and Morgenthal, G. (2016). Framework for sensitivity and uncertainty quantification in the flutter assessment of bridges. *Probabilistic Engineering Mechanics*, 43:91–105.
- [3] Abdelkefi, A. (2016). Aeroelastic energy harvesting: A review. *International Journal of Engineering Science*, 100:112–135.
- [4] Abdelkefi, A., Hajj, M., and Nayfeh, A. (2012a). Phenomena and modeling of piezoelectric energy harvesting from freely oscillating cylinders. *Nonlinear Dynamics*, 70(2):1377–1388.
- [5] Abdelkefi, A., Hajj, M., and Nayfeh, A. (2012b). Piezoelectric energy harvesting from transverse galloping of bluff bodies. *Smart Materials and Structures*, 22(1):015014.
- [6] Abdelkefi, A., Hajj, M. R., and Nayfeh, A. H. (2012c). Power harvesting from transverse galloping of square cylinder. *Nonlinear Dynamics*, 70(2):1355–1363.
- [7] Abdelkefi, A., Hasanyan, A., Montgomery, J., Hall, D., and Hajj, M. R. (2014a). Incident flow effects on the performance of piezoelectric energy harvesters from galloping vibrations. *Theor. Appl. Mech. Lett*, 4:022002.
- [8] Abdelkefi, A., Nayfeh, A. H., and Hajj, M. (2012d). Modeling and analysis of piezoaeroelastic energy harvesters. *Nonlinear Dynamics*, 67(2):925–939.
- [9] Abdelkefi, A., Scanlon, J., McDowell, E., and Hajj, M. R. (2013a). Performance enhancement of piezoelectric energy harvesters from wake galloping. *Applied Physics Letters*, 103(3):033903.
- [10] Abdelkefi, A., Yan, Z., and Hajj, M. (2013b). Nonlinear dynamics of galloping-based piezoaeroelastic energy harvesters. *The European Physical Journal Special Topics*, 222(7):1483–1501.
- [11] Abdelkefi, A., Yan, Z., and Hajj, M. R. (2013c). Modeling and nonlinear analysis of piezoelectric energy harvesting from transverse galloping. *Smart Materials and Structures*, 22(2):025016.
- [12] Abdelkefi, A., Yan, Z., and Hajj, M. R. (2014b). Performance analysis of galloping-based piezoaeroelastic energy harvesters with different cross-section geometries. *Journal of Intelligent Material Systems and Structures*, 25(2):246–256.

- [13] Abidat, M., Hachemi, M., Hamidou, M., and Baines, N. (1998). Prediction of the steady and non-steady flow performance of a highly loaded mixed flow turbine. *Proceedings of the Institution of Mechanical Engineers, Part A: Journal of Power and Energy*, 212(3):173–184.
- [14] Akaydin, H., Elvin, N., and Andreopoulos, Y. (2010). Wake of a cylinder: A paradigm for energy harvesting with piezoelectric materials. *Experiments in Fluids*, 49(1):291–304.
- [15] Akaydin, H., Elvin, N., and Andreopoulos, Y. (2012). The performance of a self-excited fluidic energy harvester. *Smart Materials and Structures*, 21(2):025007.
- [16] Akaydin, H. D., Elvin, N., and Andreopoulos, Y. (2010). Energy harvesting from highly unsteady fluid flows using piezoelectric materials. *Journal of Intelligent Material Systems and Structures*, 21(13):1263–1278.
- [17] Al-Asmi, K. and Castro, I. (1992). Vortex shedding in oscillatory flow: Geometrical effects. *Flow Measurement and Instrumentation*, 3(3):187–202.
- [18] Ali, M., Arafa, M., and Elaraby, M. (2013). Harvesting energy from galloping oscillations. In *Proceedings of the world Congress on Engineering*, volume 3, pages 2053–205. WCE.
- [19] Allen, J. and Smits, A. (2001). Energy harvesting Eel. *Journal of Fluids and Structures*, 15(3-4):629–640.
- [20] Alonso, G. and Meseguer, J. (2006). A parametric study of the galloping stability of two-dimensional triangular cross-section bodies. *Journal of Wind Engineering and Industrial Aerodynamics*, 94(4):241–253.
- [21] Alonso, G., Meseguer, J., and Pérez-Grande, I. (2007). Galloping stability of triangular cross-sectional bodies: A systematic approach. *Journal of Wind Engineering and Industrial Aerodynamics*, 95(9-11):928–940.
- [22] Anderson, J. D. and Wendt, J. (1995). *Computational fluid dynamics*, volume 206. Springer.
- [23] Anton, S. R. and Inman, D. J. (2008). Vibration energy harvesting for unmanned aerial vehicles. In *Active and Passive Smart Structures and Integrated Systems 2008*, volume 6928, page 692824. International Society for Optics and Photonics.
- [24] Anton, S. R. and Sodano, H. A. (2007). A review of power harvesting using piezoelectric materials (2003–2006). *Smart Materials and Structures*, 16(3):R1.
- [25] Argentina, M. and Mahadevan, L. (2005). Fluid-flow-induced flutter of a flag. *Proceedings of the National academy of Sciences of the United States of America*, 102(6):1829–1834.
- [26] Baek, H. and Karniadakis, G. E. (2012). A convergence study of a new partitioned fluid–structure interaction algorithm based on fictitious mass and damping. *Journal of Computational Physics*, 231(2):629–652.
- [27] Baker, C. (2003). Some complex applications of the “wind loading chain”. *Journal of Wind Engineering and Industrial Aerodynamics*, 91(12-15):1791–1811.
- [28] Balint, T. and Lucey, A. (2005). Instability of a cantilevered flexible plate in viscous channel flow. *Journal of Fluids and Structures*, 20(7):893–912.

-
- [29] Barbi, C., Favier, D., Maresca, C., and Telionis, D. (1986). Vortex shedding and lock-on of a circular cylinder in oscillatory flow. *Journal of Fluid Mechanics*, 170:527–544.
- [30] Barone, M. F. and Payne, J. L. (2005). Methods for simulation-based analysis of fluid-structure interaction. Technical report, Sandia National Laboratories.
- [31] Barrero-Gil, A., Alonso, G., and Sanz-Andres, A. (2010). Energy harvesting from transverse galloping. *Journal of Sound and Vibration*, 329(14):2873–2883.
- [32] Barrero-Gil, A., Pindado, S., and Avila, S. (2012). Extracting energy from vortex-induced vibrations: A parametric study. *Applied Mathematical Modelling*, 36(7):3153–3160.
- [33] Barrero-Gil, A., Sanz-Andrés, A., and Alonso, G. (2009a). Hysteresis in transverse galloping: the role of the inflection points. *Journal of Fluids and Structures*, 25(6):1007–1020.
- [34] Barrero-Gil, A., Sanz-Andres, A., and Roura, M. (2009b). Transverse galloping at low reynolds numbers. *Journal of Fluids and Structures*, 25(7):1236–1242.
- [35] Bathe, K.-J. (2006). *Finite element procedures*. Klaus-Jurgen Bathe.
- [36] Beeby, S. P., Tudor, M. J., and White, N. (2006). Energy harvesting vibration sources for microsystems applications. *Measurement Science and Technology*, 17(12):R175.
- [37] Behdinan, K., Stylianou, M., and Tabarrok, B. (1998). Co-rotational dynamic analysis of flexible beams. *Computer Methods in Applied Mechanics and Engineering*, 154(3-4):151–161.
- [38] Bibo, A. and Daqaq, M. (2013a). Investigation of concurrent energy harvesting from ambient vibrations and wind using a single piezoelectric generator. *Applied Physics Letters*, 102(24):243904.
- [39] Bibo, A. and Daqaq, M. (2014). On the optimal performance and universal design curves of galloping energy harvesters. *Applied Physics Letters*, 104(2):023901.
- [40] Bibo, A. and Daqaq, M. F. (2013b). Energy harvesting under combined aerodynamic and base excitations. *Journal of Sound and Vibration*, 332(20):5086–5102.
- [41] Bryant, M. and Garcia, E. (2009a). Development of an aeroelastic vibration power harvester. In *Active and Passive Smart Structures and Integrated Systems 2009*, volume 7288, page 728812. International Society for Optics and Photonics.
- [42] Bryant, M. and Garcia, E. (2009b). Energy harvesting: a key to wireless sensor nodes. In *Second International Conference on Smart Materials and Nanotechnology in Engineering*, volume 7493, page 74931W. International Society for Optics and Photonics.
- [43] Bryant, M. and Garcia, E. (2011). Modeling and testing of a novel aeroelastic flutter energy harvester. *Journal of Vibration and Acoustics*, 133(1):011010.
- [44] Bryant, M., Wolff, E., and Garcia, E. (2011). Aeroelastic flutter energy harvester design: the sensitivity of the driving instability to system parameters. *Smart Materials and Structures*, 20(12):125017.

- [45] Busch, D., Harte, R., Krätzig, W. B., and Montag, U. (2002). New natural draft cooling tower of 200 m of height. *Engineering Structures*, 24(12):1509–1521.
- [46] Cabanyes, I. (1903). Las chimeneas solares (solar chimneys). *La energia eléctrica*.
- [47] Cannarella, J., Selvaggi, J., Salon, S., Tichy, J., and Borca-Tasciuc, D.-A. (2011). Coupling factor between the magnetic and mechanical energy domains in electromagnetic power harvesting applications. *IEEE Transactions on Magnetics*, 47(8):2076–2080.
- [48] Capatina, O., Grosan, T., Vadan, I., Trimbitas, R., Ignat, S., and Calarasu, A. (2010). The funnel effect and its practical benefits in wind applications. In *Automation Quality and Testing Robotics (AQTR), 2010 IEEE International Conference on*, volume 3, pages 1–5. IEEE.
- [49] Causin, P., Gerbeau, J.-F., and Nobile, F. (2005). Added-mass effect in the design of partitioned algorithms for fluid–structure problems. *Computer Methods in Applied Mechanics and Engineering*, 194(42-44):4506–4527.
- [50] Çengel, Y. A., Turner, R. H., and Cimbala, J. M. (2001). *Fundamentals of thermal-fluid sciences*, volume 703. McGraw-Hill New York.
- [51] Chang, C.-C. and Chern, R.-L. (1991). A numerical study of flow around an impulsively started circular cylinder by a deterministic vortex method. *Journal of Fluid Mechanics*, 233:243–263.
- [52] Chawdhury, S. and Morgenthal, G. (2016). Flow reproduction using vortex particle methods for simulating wake buffeting response of bluff structures. *Journal of Wind Engineering and Industrial Aerodynamics*, 151:122–136.
- [53] Chawdhury, S. and Morgenthal, G. (2017). Numerical simulations of aeroelastic instabilities to optimize the performance of flutter-based electromagnetic energy harvesters. *Journal of Intelligent Material Systems and Structures*, page 1045389X17711784.
- [54] Chawdhury, S. and Morgenthal, G. (2018). Numerical simulations of aeroelastic instabilities to optimize the performance of flutter-based electromagnetic energy harvesters. *Journal of Intelligent Material Systems and Structures*, 29(4):479–495.
- [55] Chawdhury, S. and Morgenthal, G. (2019). A partitioned solver to simulate large-displacement fluid–structure interaction of thin plate systems for vibration energy harvesting. *Computers & Structures*, 224:106110.
- [56] Chopra, A. K. (1995). *Dynamics of structures theory and*.
- [57] Chopra, A. K. (2007). *Dynamics of structures: theory and applications to earthquake engineering*, volume 3. Pearson/Prentice Hall Upper Saddle River, NJ.
- [58] Cigada, A., Diana, G., Falco, M., Fossati, F., and Manenti, A. (1997). Vortex shedding and wake-induced vibrations in single and bundle cables. *Journal of Wind Engineering and Industrial Aerodynamics*, 72:253–263.
- [59] Clough, R. W. and Penzien, J. (1995). *Dynamics of Structures*. Computers & Structures, Inc., 3 edition.
- [60] Clough, R. W. and Penzien, J. (2003). Dynamics of structures, (revised). *Computers and Structures, Inc., Berkeley, Calif.*

-
- [61] Connell, B. S. and Yue, D. K. (2007). Flapping dynamics of a flag in a uniform stream. *Journal of Fluid Mechanics*, 581:33–67.
- [62] Cottet, G.-H. (1996). Artificial viscosity models for vortex and particle methods. *Journal of Computational Physics*, 127(2):299–308.
- [63] Cottet, G.-H., Koumoutsakos, P., and Salihi, M. L. O. (2000a). Vortex methods with spatially varying cores. *Journal of Computational Physics*, 162(1):164–185.
- [64] Cottet, G.-H., Koumoutsakos, P. D., et al. (2000b). *Vortex methods: Theory and practice*. Cambridge university press.
- [65] Dai, H., Abdelkefi, A., Javed, U., and Wang, L. (2015). Modeling and performance of electromagnetic energy harvesting from galloping oscillations. *Smart Materials and Structures*, 24(4):045012.
- [66] Dai, H., Abdelkefi, A., and Wang, L. (2014a). Piezoelectric energy harvesting from concurrent vortex-induced vibrations and base excitations. *Nonlinear Dynamics*, 77(3):967–981.
- [67] Dai, H., Abdelkefi, A., and Wang, L. (2014b). Theoretical modeling and nonlinear analysis of piezoelectric energy harvesting from vortex-induced vibrations. *Journal of Intelligent Material Systems and Structures*, 25(14):1861–1874.
- [68] Daqaq, M. F., Masana, R., Erturk, A., and Quinn, D. D. (2014). On the role of nonlinearities in vibratory energy harvesting: A critical review and discussion. *Applied Mechanics Reviews*, 66(4):040801.
- [69] Davenport, A. G. (1993). The generalization and simplification of wind loads and implications for computational methods. In *Computational Wind Engineering 1*, pages 409–417. Elsevier.
- [70] Davenport, A. G. (2002). Past, present and future of wind engineering. *Journal of Wind Engineering and Industrial Aerodynamics*, 90(12-15):1371–1380.
- [71] de Boer, A., Van Zuijlen, A., and Bijl, H. (2007). Review of coupling methods for non-matching meshes. *Computer methods in applied mechanics and engineering*, 196(8):1515–1525.
- [72] de Langre, E. (2008). Effects of wind on plants. *Annu. Rev. Fluid Mech.*, 40:141–168.
- [73] de Marqui, C., Vieira, W. G., Erturk, A., and Inman, D. J. (2011). Modeling and analysis of piezoelectric energy harvesting from aeroelastic vibrations using the doublet-lattice method. *Journal of Vibration and Acoustics*, 133(1):011003.
- [74] de Marqui Jr, C. and Erturk, A. (2013). Electroaeroelastic analysis of airfoil-based wind energy harvesting using piezoelectric transduction and electromagnetic induction. *Journal of Intelligent Material Systems and Structures*, 24(7):846–854.
- [75] de Marqui Jr, C., Erturk, A., and Inman, D. J. (2010). Piezoaeroelastic modeling and analysis of a generator wing with continuous and segmented electrodes. *Journal of Intelligent Material Systems and Structures*, 21(10):983–993.
- [76] Denavit, M. D. and Hajjar, J. F. (2013). Description of geometric nonlinearity for beam-column analysis in OpenSees.

- [77] Dettmer, W. and Perić, D. (2006). A computational framework for fluid–structure interaction: Finite element formulation and applications. *Computer Methods in Applied Mechanics and Engineering*, 195(41-43):5754–5779.
- [78] Dias, J., de Marqui Jr, C., and Erturk, A. (2013). Hybrid piezoelectric-inductive flow energy harvesting and dimensionless electroaeroelastic analysis for scaling. *Applied Physics Letters*, 102(4):044101.
- [79] Dias, J., de Marqui Jr, C., and Erturk, A. (2014). Three-degree-of-freedom hybrid piezoelectric-inductive aeroelastic energy harvester exploiting a control surface. *AIAA Journal*, 53(2):394–404.
- [80] Doaré, O. and Michelin, S. (2011). Piezoelectric coupling in energy-harvesting fluttering flexible plates: linear stability analysis and conversion efficiency. *Journal of Fluids and Structures*, 27(8):1357–1375.
- [81] Donea, J., Giuliani, S., and Halleux, J.-P. (1982). An arbitrary Lagrangian-Eulerian finite element method for transient dynamic fluid–structure interactions. *Computer Methods in Applied Mechanics and Engineering*, 33(1-3):689–723.
- [82] Dowell, E. H. (2015). *A modern course in aeroelasticity*, volume 217. Springer.
- [83] Dowell, E. H. and Ilgamov, M. (1988). *Studies in nonlinear aeroelasticity*. Springer-Verlag New York Inc.
- [84] Dunnmon, J., Stanton, S., Mann, B., and Dowell, E. (2011a). Power extraction from aeroelastic limit cycle oscillations. *Journal of Fluids and Structures*, 27(8):1182–1198.
- [85] Dunnmon, J., Stanton, S., Mann, B., and Dowell, E. (2011b). Power extraction from aeroelastic limit cycle oscillations. *Journal of Fluids and Structures*, 27(8):1182–1198.
- [86] Dyrbye, C. and Hansen, S. O. (1997). *Wind loads on structures*.
- [87] El-Hami, M., Glynne-Jones, P., White, N., Hill, M., Beeby, S., James, E., Brown, A., and Ross, J. (2001). Design and fabrication of a new vibration-based electromechanical power generator. *Sensors and Actuators A: Physical*, 92(1-3):335–342.
- [88] Elahi, H., Eugeni, M., and Gaudenzi, P. (2018). A review on mechanisms for piezoelectric-based energy harvesters. *Energies (19961073)*, 11(7).
- [89] Eldredge, J. D. (2010). A reconciliation of viscous and inviscid approaches to computing locomotion of deforming bodies. *Experimental Mechanics*, 50(9):1349–1353.
- [90] Eldredge, J. D., Colonius, T., and Leonard, A. (2002). A vortex particle method for two-dimensional compressible flow. *Journal of Computational Physics*, 179(2):371–399.
- [91] Eloy, C., Lagrange, R., Souilliez, C., and Schouveiler, L. (2008). Aeroelastic instability of cantilevered flexible plates in uniform flow. *Journal of Fluid Mechanics*, 611:97–106.
- [92] Elvin, N. and Erturk, A. (2013). *Advances in energy harvesting methods*. Springer Science & Business Media.
- [93] Elvin, N. G., Lajnef, N., and Elvin, A. A. (2006). Feasibility of structural monitoring with vibration powered sensors. *Smart Materials and Structures*, 15(4):977.

-
- [94] Engels, T., Kolomenskiy, D., Schneider, K., and Sesterhenn, J. (2013). Two-dimensional simulation of the fluttering instability using a pseudospectral method with volume penalization. *Computers & Structures*, 122:101–112.
- [95] Erturk, A., Bilgen, O., Fontenille, M., and Inman, D. J. (2008). Piezoelectric energy harvesting from macro-fiber composites with an application to morphing-wing aircrafts. In *Proceedings of the 19th International Conference on Adaptive Structures and Technologies, Ascona, Switzerland, Oct*, pages 6–9. Citeseer.
- [96] Erturk, A., Vieira, W., de Marqui Jr, C., and Inman, D. J. (2010). On the energy harvesting potential of piezoaeroelastic systems. *Applied Physics Letters*, 96(18):184103.
- [97] Eugeni, M., Elahi, H., Fune, F., Lampani, L., Mastroddi, F., Romano, G. P., and Gaudenzi, P. (2020). Numerical and experimental investigation of piezoelectric energy harvester based on flag-flutter. *Aerospace Science and Technology*, 97:105634.
- [98] Ferziger, J. H., Perić, M., and Street, R. L. (2002). *Computational methods for fluid dynamics*, volume 3. Springer.
- [99] Francke, W., de Richter, R., Petersen, O., and Petersen, J. (2013). A realistic growth path for solar wind power. In *Applied Mechanics and Materials*, volume 283, pages 57–64. Trans Tech Publ.
- [100] Fujino, Y. and Siringoringo, D. (2013). Vibration mechanisms and controls of long-span bridges: A review. *Structural Engineering International*, 23(3):248–268.
- [101] Galindo, J., Climent, H., Guardiola, C., and Tiseira, A. (2009). On the effect of pulsating flow on surge margin of small centrifugal compressors for automotive engines. *Experimental Thermal and Fluid Science*, 33(8):1163–1171.
- [102] Galindo, J., Fajardo, P., Navarro, R., and García-Cuevas, L. (2013). Characterization of a radial turbocharger turbine in pulsating flow by means of CFD and its application to engine modeling. *Applied Energy*, 103:116–127.
- [103] Gatzhammer, B. (2014). *Efficient and flexible partitioned simulation of fluid–structure interactions*. PhD thesis, Technische Universität München.
- [104] Gharakhani, A. and Stock, M. (2005). 3-D vortex simulation of flow over a circular disk at an angle of attack. In *17th AIAA Computational Fluid Dynamics Conference*, page 4624.
- [105] Giacomello, A. and Porfiri, M. (2011a). Underwater energy harvesting from a heavy flag hosting ionic polymer metal composites. *Journal of Applied Physics*, 109(8):084903.
- [106] Giacomello, A. and Porfiri, M. (2011b). Underwater energy harvesting from a heavy flag hosting ionic polymer metal composites. *Journal of Applied Physics*, 109(8):084903.
- [107] Gilmanov, A., Le, T. B., and Sotiropoulos, F. (2015). A numerical approach for simulating fluid structure interaction of flexible thin shells undergoing arbitrarily large deformations in complex domains. *Journal of Computational Physics*, 300:814–843.
- [108] Gilmanov, A. and Sotiropoulos, F. (2005). A hybrid cartesian/immersed boundary method for simulating flows with 3d, geometrically complex, moving bodies. *Journal of computational physics*, 207(2):457–492.

- [109] Gorman, D., Reese, J., and Zhang, Y. (2000). Vibration of a flexible pipe conveying viscous pulsating fluid flow. *Journal of Sound and Vibration*, 230(2):379–392.
- [110] Grouthier, C., Michelin, S., Bourguet, R., Modarres-Sadeghi, Y., and de Langre, E. (2014). On the efficiency of energy harvesting using vortex-induced vibrations of cables. *Journal of Fluids and Structures*, 49:427–440.
- [111] Günther, H. (1931). In hundred years-future energy supply of the world. *Stuttgart: Kosmos, Franckh'sche Verlagshandlung*.
- [112] Habchi, C., Russeil, S., Bougeard, D., Harion, J.-L., Lemenand, T., Ghanem, A., Della Valle, D., and Peerhossaini, H. (2013). Partitioned solver for strongly coupled fluid–structure interaction. *Computers & Fluids*, 71:306–319.
- [113] Harte, R., Höffer, R., Krätzig, W. B., Mark, P., and Niemann, H.-J. (2012). Solare aufwindkraftwerke: Ein beitrag der bautechnik zur nachhaltigen und wirtschaftlichen energieerzeugung. *Bautechnik*, 89(3):173–181.
- [114] Heil, M., Hazel, A. L., and Boyle, J. (2008). Solvers for large-displacement fluid–structure interaction problems: segregated versus monolithic approaches. *Computational Mechanics*, 43(1):91–101.
- [115] Hejlesen, M. M., Rasmussen, J. T., Larsen, A., and Walther, J. H. (2015). On estimating the aerodynamic admittance of bridge sections by a mesh-free vortex method. *Journal of Wind Engineering and Industrial Aerodynamics*, 146:117–127.
- [116] Hirt, C. W., Amsden, A. A., and Cook, J. (1974). An arbitrary Lagrangian-Eulerian computing method for all flow speeds. *Journal of Computational Physics*, 14(3):227–253.
- [117] Hobbs, W. B. (2010). *Piezoelectric energy harvesting: vortex induced vibrations in plants, soap films, and arrays of cylinders*. PhD thesis, Georgia Institute of Technology.
- [118] Hobbs, W. B. and Hu, D. L. (2012). Tree-inspired piezoelectric energy harvesting. *Journal of Fluids and Structures*, 28:103–114.
- [119] Holmes, J. D. (2015). *Wind Loading of Structures*. CRC press.
- [120] Hou, G., Wang, J., and Layton, A. (2012). Numerical methods for fluid–structure interaction — A review. *Communications in Computational Physics*, 12(2):337–377.
- [121] Hron, J. and Turek, S. (2006). A monolithic FEM/multigrid solver for an ALE formulation of fluid–structure interaction with applications in biomechanics. In *Fluid-structure interaction*, pages 146–170. Springer.
- [122] Hsiao, K. M. and Yang, R. T. (1995). A co-rotational formulation for nonlinear dynamic analysis of curved Euler beam. *Computers & Structures*, 54(6):1091–1097.
- [123] Huang, L. (1995). Flutter of cantilevered plates in axial flow. *Journal of Fluids and Structures*, 9(2):127–147.
- [124] Hübner, B., Walhorn, E., and Dinkler, D. (2001). Strongly coupled analysis of fluid–structure interaction using space–time finite elements. In *2nd European Conference on Computational Mechanics*, pages 546–547.

-
- [125] Hübner, B., Walhorn, E., and Dinkler, D. (2004). A monolithic approach to fluid–structure interaction using space–time finite elements. *Computer Methods in Applied Mechanics and Engineering*, 193(23-26):2087–2104.
- [126] Huera-Huarte, F. and Bearman, P. (2009). Wake structures and vortex-induced vibrations of a long flexible cylinder—part 1: dynamic response. *Journal of Fluids and Structures*, 25(6):969–990.
- [127] Hughes, T. J., Liu, W. K., and Zimmermann, T. K. (1981). Lagrangian-Eulerian finite element formulation for incompressible viscous flows. *Computer methods in applied mechanics and engineering*, 29(3):329–349.
- [128] Hwang, K., Sung, H., and Hyun, J. (2001). An experimental study of large-scale vortices over a blunt-faced flat plate in pulsating flow. *Experiments in Fluids*, 30(2):202–213.
- [129] Isyumov, N. (2012). Alan G. davenport’s mark on wind engineering. *Journal of Wind Engineering and Industrial Aerodynamics*, 104:12–24.
- [130] Ji, T. H., Kim, S. Y., and Hyun, J. M. (2008). Experiments on heat transfer enhancement from a heated square cylinder in a pulsating channel flow. *International Journal of Heat and Mass Transfer*, 51(5):1130–1138.
- [131] Jung, H.-J., Kim, I.-H., and Jang, S.-J. (2011). An energy harvesting system using the wind-induced vibration of a stay cable for powering a wireless sensor node. *Smart Materials and Structures*, 20(7):075001.
- [132] Jung, H.-J. and Lee, S.-W. (2011). The experimental validation of a new energy harvesting system based on the wake galloping phenomenon. *Smart Materials and Structures*, 20(5):055022.
- [133] Jung, H.-J., Lee, S.-W., and Jang, D.-D. (2009). Feasibility study on a new energy harvesting electromagnetic device using aerodynamic instability. *IEEE Transactions on Magnetics*, 45(10):4376–4379.
- [134] Kamakoti, R. and Shyy, W. (2004). Fluid–structure interaction for aeroelastic applications. *Progress in Aerospace Sciences*, 40(8):535–558.
- [135] Kareem, A. and Tamura, A. (2015). *Advanced structural wind engineering*. Springer.
- [136] Kareem, A. and Tamura, Y. (2013). *Advanced Structural Wind Engineering*. Springer.
- [137] Kassiotis, C., Ibrahimbegovic, A., Niekamp, R., and Matthies, H. G. (2011). Nonlinear fluid–structure interaction problem. part I: Implicit partitioned algorithm, nonlinear stability proof and validation examples. *Computational Mechanics*, 47(3):305–323.
- [138] Kavrakov, I., Argentini, T., Omarini, S., Rocchi, D., and Morgenthal, G. (2019). Determination of complex aerodynamic admittance of bridge decks under deterministic gusts using the vortex particle method. *Journal of Wind Engineering and Industrial Aerodynamics*, 193:103971.
- [139] Kavrakov, I. and Morgenthal, G. (2017). A comparative assessment of aerodynamic models for buffeting and flutter of long-span bridges. *Engineering*.

- [140] Kavrakov, I. and Morgenthal, G. (2018a). Aeroelastic analyses of bridges using a pseudo-3D vortex method and velocity-based synthetic turbulence generation. *Engineering Structures*, 176:825–839.
- [141] Kavrakov, I. and Morgenthal, G. (2018b). A synergistic study of a CFD and semi-analytical models for aeroelastic analysis of bridges in turbulent wind conditions. *Journal of Fluids and Structures*, 82:59–85.
- [142] Kim, D., Cossé, J., Cerdeira, C. H., and Gharib, M. (2013). Flapping dynamics of an inverted flag. *Journal of Fluid Mechanics*, 736.
- [143] Konstantinidis, E. and Balabani, S. (2008). Flow structure in the locked-on wake of a circular cylinder in pulsating flow: Effect of forcing amplitude. *International Journal of Heat and Fluid Flow*, 29(6):1567–1576.
- [144] Koumoutsakos, P. (2005). Multiscale flow simulations using particles. *Annu. Rev. Fluid Mech.*, 37:457–487.
- [145] Koumoutsakos, P., Leonard, A., and Pepin, F. (1994). Boundary conditions for viscous vortex methods. *Journal of Computational Physics*, 113(1):52–61.
- [146] Kudela, H. and Regucki, P. (2002). The vortex-in-cell method for the study of three-dimensional vortex structures. In *Tubes, Sheets and Singularities in Fluid Dynamics*, pages 49–54. Springer.
- [147] Kuethe, A. M. and Chow, C.-Y. (1986). *Foundations of aerodynamics*. Wiley New York.
- [148] Kumar, N. M., Subathra, M., and Cota, O. D. (2015). Design and wind tunnel testing of funnel based wind energy harvesting system. *Procedia Technology*, 21:33–40.
- [149] Kwon, S.-D. (2010). A T-shaped piezoelectric cantilever for fluid energy harvesting. *Applied Physics Letters*, 97(16):164102.
- [150] Larose, G. and D’auteuil, A. (2006). On the reynolds number sensitivity of the aerodynamics of bluff bodies with sharp edges. *Journal of Wind Engineering and Industrial Aerodynamics*, 94(5):365–376.
- [151] Larsen, A. and Walther, J. H. (1997). Aeroelastic analysis of bridge girder sections based on discrete vortex simulations. *Journal of Wind Engineering and Industrial Aerodynamics*, 67:253–265.
- [152] Larsen, A. and Walther, J. H. (1998). Discrete vortex simulation of flow around five generic bridge deck sections. *Journal of Wind Engineering and Industrial Aerodynamics*, 77:591–602.
- [153] Le, T.-N., Battini, J.-M., and Hjiiaj, M. (2011). Efficient formulation for dynamics of corotational 2D beams. *Computational Mechanics*, 48(2):153–161.
- [154] Leonard, A. and Koumoutsakos, P. (1993). High resolution vortex simulation of bluff body flows. *Journal of Wind Engineering and Industrial Aerodynamics*, 46:315–325.
- [155] Liu, G.-T., Wang, X.-J., Ai, B.-Q., and Liu, L.-G. (2004). Numerical study of pulsating flow through a tapered artery with stenosis. *Chinese Journal of Physics*, 42(4):401–409.

-
- [156] Liu, Z. and Kopp, G. A. (2011). High-resolution vortex particle simulations of flows around rectangular cylinders. *Computers & Fluids*, 40(1):2–11.
- [157] Marelli, S. and Capobianco, M. (2011). Steady and pulsating flow efficiency of a wastegated turbocharger radial flow turbine for automotive application. *Energy*, 36(1):459–465.
- [158] Marelli, S., Capobianco, M., and Zamboni, G. (2014). Pulsating flow performance of a turbocharger compressor for automotive application. *International Journal of Heat and Fluid Flow*, 45:158–165.
- [159] Matiko, J., Grabham, N., Beeby, S., and Tudor, M. (2013). Review of the application of energy harvesting in buildings. *Measurement Science and Technology*, 25(1):012002.
- [160] Matthies, H. G. and Steindorf, J. (2003). Partitioned strong coupling algorithms for fluid–structure interaction. *Computers & Structures*, 81(8-11):805–812.
- [161] Mazzoni, S., McKenna, F., Scott, M. H., Fenves, G. L., et al. (2006). Opensees command language manual. *Pacific Earthquake Engineering Research (PEER) Center*, 264.
- [162] McRobie, A., Morgenthal, G., Abrams, D., and Prendergast, J. (2013). Parallels between wind and crowd loading of bridges. *Phil. Trans. R. Soc. A*, 371(1993):20120430.
- [163] Meneghini, J. R. (1993). Numerical simulation of bluff body flow control using a discrete vortex method.
- [164] Michelin, S. and Doaré, O. (2013a). Energy harvesting efficiency of piezoelectric flags in axial flows. *Journal of Fluid Mechanics*, 714:489–504.
- [165] Michelin, S. and Doaré, O. (2013b). Energy harvesting efficiency of piezoelectric flags in axial flows. *Journal of Fluid Mechanics*, 714:489–504.
- [166] Michelin, S., Smith, S. G. L., and Glover, B. J. (2008). Vortex shedding model of a flapping flag. *Journal of Fluid Mechanics*, 617:1–10.
- [167] Milani, D. (2019). *Concepts of Adaptivity for Vortex Particle Methods and Applications to Bluff Body Aerodynamics*. PhD thesis, Bauhaus University Weimar.
- [168] Milani, D. and Morgenthal, G. (2018). Methods for controlling the local spatial and temporal resolution of vortex particle simulations of bluff body aerodynamics problems. *Computers & Fluids*, 166:225–242.
- [169] Ming, T. (2016). *Solar chimney power plant generating technology*. Academic Press.
- [170] Missoum, S., Dribusch, C., and Beran, P. (2010). Reliability-based design optimization of nonlinear aeroelasticity problems. *Journal of Aircraft*, 47(3):992–998.
- [171] Mitcheson, P. D., Yeatman, E. M., Rao, G. K., Holmes, A. S., and Green, T. C. (2008). Energy harvesting from human and machine motion for wireless electronic devices. *Proceedings of the IEEE*, 96(9):1457–1486.
- [172] Monprapussorn, T., Athisakul, C., and Chucheepsakul, S. (2007). Nonlinear vibrations of an extensible flexible marine riser carrying a pulsatile flow. *Journal of Applied Mechanics*, 74(4):754–769.

- [173] Morgenthal, E. I. (2005). Advances in numerical bridge aerodynamics and recent applications. 15(2):95–95.
- [174] Morgenthal, G. (2002). *Aerodynamic analysis of structures using high-resolution vortex particle methods*. PhD thesis.
- [175] Morgenthal, G., Corriols, A. S., and Bendig, B. (2014). A GPU-accelerated pseudo-3D vortex method for aerodynamic analysis. *Journal of Wind Engineering and Industrial Aerodynamics*, 125:69–80.
- [176] Morgenthal, G. and McRobie, A. (2002). A comparative study of numerical methods for fluid structure interaction analysis in long-span bridge design. *Wind & Structures*, 5(2):101–114.
- [177] Morgenthal, G. and Walther, J. H. (2007). An immersed interface method for the vortex-in-cell algorithm. *Computers & Structures*, 85(11-14):712–726.
- [178] Nakamura, Y. (1996). Vortex shedding from bluff bodies and a universal Strouhal number. *Journal of Fluids and Structures*, 10(2):159–171.
- [179] Nakamura, Y., Ohya, Y., Ozono, S., and Nakayama, R. (1996). Experimental and numerical analysis of vortex shedding from elongated rectangular cylinders at low reynolds numbers 200-103. *Journal of Wind Engineering and Industrial Aerodynamics*, 65(1-3):301–308.
- [180] Newmark, N. M. (1959). A method of computation for structural dynamics. *Journal of the Engineering Mechanics Division*, 85(3):67–94.
- [181] Ojo, O., Tan, D., Wang, Y.-C., Shoele, K., and Erturk, A. (2019). Aspect ratio effects in wind energy harvesting using piezoelectric inverted flags. In *Active and Passive Smart Structures and Integrated Systems XIII*, volume 10967, page 109670Q. International Society for Optics and Photonics.
- [182] Okajima, A., Yi, D., Sakuda, A., and Nakano, T. (1997). Numerical study of blockage effects on aerodynamic characteristics of an oscillating rectangular cylinder. *Journal of Wind Engineering and Industrial Aerodynamics*, 67:91–102.
- [183] Orrego, S., Shoele, K., Ruas, A., Doran, K., Caggiano, B., Mittal, R., and Kang, S. H. (2017). Harvesting ambient wind energy with an inverted piezoelectric flag. *Applied Energy*, 194:212–222.
- [184] Palacios, R. and Cesnik, C. (2005). Static nonlinear aeroelasticity of flexible slender wings in compressible flow. In *46th AIAA/ASME/ASCE/AHS/ASC Structures, Structural Dynamics and Materials Conference*, page 1945.
- [185] Park, J., Kim, K., Kwon, S., and Law, K. H. (2012). An aeroelastic flutter based electromagnetic energy harvester with wind speed augmenting funnel. In *Proceedings of the International Conference on Advances in Wind and Structures*, pages 26–29. Korea Advanced Inst. of Science and Technology Seoul, Korea.
- [186] Park, J., Morgenthal, G., Kim, K., Kwon, S.-D., and Law, K. H. (2014). Power evaluation of flutter-based electromagnetic energy harvesters using computational fluid dynamics simulations. *Journal of Intelligent Material Systems and Structures*, 25(14):1800–1812.

-
- [187] Parkinson, G. (1989). Phenomena and modelling of flow-induced vibrations of bluff bodies. *Progress in Aerospace Sciences*, 26(2):169–224.
- [188] Peng, Z. and Zhu, Q. (2009). Energy harvesting through flow-induced oscillations of a foil. *Physics of Fluids*, 21(12):123602.
- [189] Peskin, C. S. (1972). Flow patterns around heart valves: A numerical method. *Journal of Computational Physics*, 10(2):252–271.
- [190] Ploumhans, P., Daeninck, G., and Winckelmans, G. (2004). Simulation of three-dimensional bluff-body flows using the vortex particle and boundary element methods. *Flow, Turbulence and Combustion*, 73(2):117–131.
- [191] Ploumhans, P., Winckelmans, G., Salmon, J. K., Leonard, A., and Warren, M. (2002). Vortex methods for direct numerical simulation of three-dimensional bluff body flows: Application to the sphere at $re = 300, 500, \text{ and } 1000$. *Journal of Computational Physics*, 178(2):427–463.
- [192] Prendergast, J. and McRobie, F. (2006). Simulation of 2D unsteady wind by a vortex method and application to studying bluff body flow. In *7th UK Conference on Wind Engineering*, pages 1–4.
- [193] Prendergast, J. M. (2008). *Simulation of unsteady 2-D wind by a vortex method*. PhD thesis, University of Cambridge.
- [194] Priya, S. and Inman, D. J. (2009). *Energy harvesting technologies*, volume 21. Springer.
- [195] Qamar, A., Seda, R., and Bull, J. L. (2011). Pulsatile flow past an oscillating cylinder. *Physics of Fluids*, 23(4):041903.
- [196] Quaranta, G., Masarati, P., and Mantegazza, P. (2005). A conservative mesh-free approach for fluid-structure interface problems. In *International Conference for Coupled Problems in Science and Engineering, Greece*.
- [197] Rasmussen, J. T., Hejlesen, M. M., Larsen, A., and Walther, J. H. (2010). Discrete vortex method simulations of the aerodynamic admittance in bridge aerodynamics. *Journal of Wind Engineering and Industrial Aerodynamics*, 98(12):754–766.
- [198] Rossinelli, D., Bergdorf, M., Cottet, G.-H., and Koumoutsakos, P. (2010). GPU accelerated simulations of bluff body flows using vortex particle methods. *Journal of Computational Physics*, 229(9):3316–3333.
- [199] Rossinelli, D. and Koumoutsakos, P. (2008). Vortex methods for incompressible flow simulations on the GPU. *The Visual Computer*, 24(7-9):699–708.
- [200] Ryzhakov, P., Rossi, R., Idelsohn, S., and Oñate, E. (2010). A monolithic Lagrangian approach for fluid–structure interaction problems. *Computational Mechanics*, 46(6):883–899.
- [201] Sader, J. E., Cossé, J., Kim, D., Fan, B., and Gharib, M. (2016). Large-amplitude flapping of an inverted flag in a uniform steady flow – A vortex-induced vibration. *Journal of Fluid Mechanics*, 793:524–555.

- [202] Sanchez-Sanz, M., Fernandez, B., and Velazquez, A. (2009). Energy-harvesting microresonator based on the forces generated by the Kármán street around a rectangular prism. *Journal of Microelectromechanical Systems*, 18(2):449–457.
- [203] Sarpkaya, T. (2004). A critical review of the intrinsic nature of vortex-induced vibrations. *Journal of fluids and structures*, 19(4):389–447.
- [204] Scanlan, R. H. and Tomo, J. (1971). Air foil and bridge deck flutter derivatives. *Journal of Soil Mechanics & Foundations Div.*
- [205] Schlaich, J. (1995). *The solar chimney: electricity from the sun*. Edition Axel Menges.
- [206] Schlaich, J., Bergemann, R., Schiel, W., Weinrebe, G., et al. (2005). Design of commercial solar updraft tower systems—utilization of solar induced convective flows for power generation. *Journal of Solar Energy Engineering*, 127(1):117–124.
- [207] Schneck, D. and Ostrach, S. (1975). Pulsatile blood flow in a channel of small exponential divergence—I. The linear approximation for low mean Reynolds number. *Journal of Fluids Engineering*, 97(3):353–360.
- [208] Scott, M. H. and Filippou, F. C. (2007). Response gradients for nonlinear beam–column elements under large displacements. *Journal of Structural Engineering*, 133(2):155–165.
- [209] Selle, A., Rasmussen, N., and Fedkiw, R. (2005). A vortex particle method for smoke, water and explosions. In *ACM Transactions on Graphics (TOG)*, volume 24, pages 910–914. ACM.
- [210] Sessarego, M., Feng, J., Ramos-García, N., and Horcas, S. G. (2020). Design optimization of a curved wind turbine blade using neural networks and an aeroelastic vortex method under turbulent inflow. *Renewable Energy*, 146:1524–1535.
- [211] Sessarego, M., Ramos-García, N., Sørensen, J. N., and Shen, W. Z. (2017). Development of an aeroelastic code based on three-dimensional viscous–inviscid method for wind turbine computations. *Wind Energy*, 20(7):1145–1170.
- [212] Shelley, M., Vandenberghe, N., and Zhang, J. (2005). Heavy flags undergo spontaneous oscillations in flowing water. *Physical Review Letters*, 94(9):094302.
- [213] Shemer, L., Wygnanski, I., and Kit, E. (1985). Pulsating flow in a pipe. *Journal of Fluid Mechanics*, 153:313–337.
- [214] Shiels, D., Leonard, A., and Roshko, A. (2001). Flow-induced vibration of a circular cylinder at limiting structural parameters. *Journal of Fluids and Structures*, 15(1):3–21.
- [215] Shoele, K. and Mittal, R. (2016). Energy harvesting by flow-induced flutter in a simple model of an inverted piezoelectric flag. *Journal of Fluid Mechanics*, 790:582–606.
- [216] Silva-Leon, J., Cioncolini, A., Nabawy, M. R., Revell, A., and Kennaugh, A. (2019). Simultaneous wind and solar energy harvesting with inverted flags. *Applied Energy*, 239:846–858.
- [217] Simiu, E. and Scanlan, R. H. (1996). *Wind Effects on Structures: Fundamentals and Applications to Design*. Wiley New York.

-
- [218] Sirohi, J. and Mahadik, R. (2011). Piezoelectric wind energy harvester for low-power sensors. *Journal of Intelligent Material Systems and Structures*, 22(18):2215–2228.
- [219] Sirohi, J. and Mahadik, R. (2012). Harvesting wind energy using a galloping piezoelectric beam. *Journal of Vibration and Acoustics*, 134(1):011009.
- [220] Sodano, H. A., Inman, D. J., and Park, G. (2004). A review of power harvesting from vibration using piezoelectric materials. *Shock and Vibration Digest*, 36(3):197–206.
- [221] Sotiropoulos, F. and Yang, X. (2014). Immersed boundary methods for simulating fluid–structure interaction. *Progress in Aerospace Sciences*, 65:1–21.
- [222] Steggel, N. and Rockliff, N. (1997). Simulation of the effects of body shape on lock-in characteristics in pulsating flow by the discrete vortex method. *Journal of Wind Engineering and Industrial Aerodynamics*, 69:317–329.
- [223] Strømmen, E. (2010). *Theory of Bridge Aerodynamics*. Springer Science & Business Media.
- [224] Sun, W., Ding, Z., Qin, Z., Chu, F., and Han, Q. (2020). Wind energy harvesting based on fluttering double-flag type triboelectric nanogenerators. *Nano Energy*, 70:104526.
- [225] Tang, D., Yamamoto, H., and Dowell, E. (2003). Flutter and limit cycle oscillations of two-dimensional panels in three-dimensional axial flow. *Journal of Fluids and Structures*, 17(2):225–242.
- [226] Tang, L., Pai, M. P., et al. (2007). On the instability and the post-critical behaviour of two-dimensional cantilevered flexible plates in axial flow. *Journal of Sound and Vibration*, 305(1-2):97–115.
- [227] Tang, L., Païdoussis, M. P., and Jiang, J. (2009). Cantilevered flexible plates in axial flow: energy transfer and the concept of flutter-mill. *Journal of Sound and Vibration*, 326(1-2):263–276.
- [228] Tang, L., Zhao, L., Yang, Y., and Lefeuvre, E. (2015). Equivalent circuit representation and analysis of galloping-based wind energy harvesting. *IEEE/ASME Transactions on Mechatronics*, 20(2):834–844.
- [229] Taniike, Y. and Inaoka, H. (1988). Aeroelastic behavior of tall buildings in wakes. *Journal of Wind Engineering and Industrial Aerodynamics*, 28(1-3):317–327.
- [230] Taylor, G. W., Burns, J. R., Kammann, S., Powers, W. B., and Welsh, T. R. (2001). The energy harvesting Eel: A small subsurface ocean/river power generator. *IEEE Journal of Oceanic Engineering*, 26(4):539–547.
- [231] Taylor, I. and Vezza, M. (1999). Prediction of unsteady flow around square and rectangular section cylinders using a discrete vortex method. *Journal of Wind Engineering and Industrial Aerodynamics*, 82(1-3):247–269.
- [232] Teh, L. H. and Clarke, M. J. (1998). Co-rotational and Lagrangian formulations for elastic three-dimensional beam finite elements. *Journal of Constructional Steel Research*, 48(2-3):123–144.

- [233] Tian, F.-B., Dai, H., Luo, H., Doyle, J. F., and Rousseau, B. (2014). Fluid–structure interaction involving large deformations: 3D simulations and applications to biological systems. *Journal of Computational Physics*, 258:451–469.
- [234] Tolba, K. I. and Morgenthal, G. (2017). Pseudo three-dimensional simulation of aeroelastic response to turbulent wind using Vortex Particle Methods. *Journal of Fluids and Structures*, 72:1–24.
- [235] Tolba, K. I. and Morgenthal, G. (2018a). Modelling of inflow-conditions for vortex particle methods to simulate atmospheric turbulence and its induced aerodynamic admittance on line-like bluff bodies. *International Journal of Computational Fluid Dynamics*, 32(10):412–443.
- [236] Tolba, K. I. and Morgenthal, G. (2018b). Parallel scalability and efficiency of vortex particle method for aeroelasticity analysis of bluff bodies. *Computational Particle Mechanics*, 5(4):493–506.
- [237] Uchida, S. (1956). The pulsating viscous flow superposed on the steady laminar motion of incompressible fluid in a circular pipe. *Zeitschrift für Angewandte Mathematik und Physik (ZAMP)*, 7(5):403–422.
- [238] Van Loon, R., Anderson, P., Van de Vosse, F., and Sherwin, S. (2007). Comparison of various fluid–structure interaction methods for deformable bodies. *Computers & structures*, 85(11-14):833–843.
- [239] Varghese, S. S. and Frankel, S. H. (2003). Numerical modeling of pulsatile turbulent flow in stenotic vessels. *Journal of Biomechanical Engineering*, 125(4):445–460.
- [240] Vicente-Ludlam, D., Barrero-Gil, A., and Velazquez, A. (2014). Optimal electromagnetic energy extraction from transverse galloping. *Journal of Fluids and Structures*, 51:281–291.
- [241] Von Backström, T. W., Harte, R., Höffer, R., Krätzig, W., Kröger, D., Niemann, H., and Van Zijl, G. (2008). State and recent advances in research and design of solar chimney power plant technology. *VGB powertech*, 88(7):64–71.
- [242] Wall, W. A. (1999). Fluid-struktur-interaktion mit stabilisierten finiten elementen.
- [243] Wall, W. A. and Ramm, E. (1998). *Fluid Structure Interaction Based Upon a Stabilized (ALE) Finite Element Method*. SFB 404, Geschäftsstelle.
- [244] Walther, J. H. and Larsen, A. (1997). Two dimensional discrete vortex method for application to bluff body aerodynamics. *Journal of Wind Engineering and Industrial Aerodynamics*, 67:183–193.
- [245] Wang, D.-A., Chiu, C.-Y., and Pham, H.-T. (2012). Electromagnetic energy harvesting from vibrations induced by Kármán vortex street. *Mechatronics*, 22(6):746–756.
- [246] Wang, D.-A. and Ko, H.-H. (2010). Piezoelectric energy harvesting from flow-induced vibration. *Journal of Micromechanics and Microengineering*, 20(2):025019.
- [247] Wang, D.-A., Pham, H.-T., Chao, C.-W., and Chen, J. M. (2011). A piezoelectric energy harvester based on pressure fluctuations in Kármán vortex street. In *World Renewable Energy Congress-Sweden; 8-13 May; 2011; Linköping; Sweden*, number 057, pages 1456–1463. Linköping University Electronic Press.

-
- [248] Wang, J., Geng, L., Ding, L., Zhu, H., and Yurchenko, D. (2020). The state-of-the-art review on energy harvesting from flow-induced vibrations. *Applied Energy*, 267:114902.
- [249] Watanabe, Y., Suzuki, S., Sugihara, M., and Sueoka, Y. (2002). An experimental study of paper flutter. *Journal of Fluids and Structures*, 16(4):529–542.
- [250] Wei, C. and Jing, X. (2017). A comprehensive review on vibration energy harvesting: Modelling and realization. *Renewable and Sustainable Energy Reviews*, 74:1–18.
- [251] Weinstein, L. A., Cacan, M. R., So, P., and Wright, P. (2012). Vortex shedding induced energy harvesting from piezoelectric materials in heating, ventilation and air conditioning flows. *Smart Materials and Structures*, 21(4):045003.
- [252] Wong, H. (1980). Vortex-induced wake buffeting and its suppression. *Journal of Wind Engineering and Industrial Aerodynamics*, 6(1-2):49–57.
- [253] Wood, C., Gil, A., Hassan, O., and Bonet, J. (2010). Partitioned block-Gauss–Seidel coupling for dynamic fluid–structure interaction. *Computers & Structures*, 88(23-24):1367–1382.
- [254] Wu, T. and Kareem, A. (2011). Modeling hysteretic nonlinear behavior of bridge aerodynamics via cellular automata nested neural network. *Journal of Wind Engineering and Industrial Aerodynamics*, 99(4):378–388.
- [255] Wüchner, R., Kupzok, A., and Bletzinger, K.-U. (2007). A framework for stabilized partitioned analysis of thin membrane–wind interaction. *International Journal for Numerical Methods in Fluids*, 54(6-8):945–963.
- [256] Xie, J., Yang, J., Hu, H., Hu, Y., and Chen, X. (2012). A piezoelectric energy harvester based on flow-induced flexural vibration of a circular cylinder. *Journal of Intelligent Material Systems and Structures*, 23(2):135–139.
- [257] Xu, Y.-L. (2013). *Wind Effects on Cable-supported Bridges*. John Wiley & Sons.
- [258] Yamamoto, C. T., Meneghini, J. R., Saltara, F., Fregonesi, R. d. A., and Ferrari Jr, J. A. (2004). Numerical simulations of vortex-induced vibration on flexible cylinders. *Journal of Fluids and Structures*, 19(4):467–489.
- [259] Yan, Z., Abdelkefi, A., and Hajj, M. R. (2014). Piezoelectric energy harvesting from hybrid vibrations. *Smart Materials and Structures*, 23(2):025026.
- [260] Yang, Y., Zhao, L., and Tang, L. (2013). Comparative study of tip cross-sections for efficient galloping energy harvesting. *Applied Physics Letters*, 102(6):064105.
- [261] Zhang, W., Kwok, K., and Xu, Y. (1994). Aeroelastic torsional behaviour of tall buildings in wakes. *Journal of Wind Engineering and Industrial Aerodynamics*, 51(2):229–248.
- [262] Zhao, L., Tang, L., and Yang, Y. (2013). Comparison of modeling methods and parametric study for a piezoelectric wind energy harvester. *Smart Materials and Structures*, 22(12):125003.
- [263] Zhou, M., Chen, Q., Xu, Z., and Wang, W. (2019). Piezoelectric wind energy harvesting device based on the inverted cantilever beam with leaf-inspired extensions. *AIP Advances*, 9(3):035213.

- [264] Zhou, X., Wang, F., and Ochieng, R. M. (2010). A review of solar chimney power technology. *Renewable and Sustainable Energy Reviews*, 14(8):2315–2338.
- [265] Zhou, X., Yang, J., Xiao, B., and Shi, X. (2008). Special climate around a commercial solar chimney power plant. *Journal of Energy Engineering*, 134(1):6–14.
- [266] Zhu, L. and Peskin, C. S. (2002). Simulation of a flapping flexible filament in a flowing soap film by the immersed boundary method. *Journal of Computational Physics*, 179(2):452–468.
- [267] Zhu, Q. (2011). Optimal frequency for flow energy harvesting of a flapping foil. *Journal of Fluid Mechanics*, 675:495–517.
- [268] Zhu, Q., Haase, M., and Wu, C. H. (2009). Modeling the capacity of a novel flow–energy harvester. *Applied Mathematical Modelling*, 33(5):2207–2217.
- [269] Zhu, Q. and Peng, Z. (2009). Mode coupling and flow energy harvesting by a flapping foil. *Physics of Fluids*, 21(3):033601.

List of publications

Journal articles

- Chawdhury, S., and Morgenthal, G.: An extension of pseudo-3D vortex particle methods for aeroelastic interactions of thin-walled structures, 1st Revision submitted to Journal of Wind Engineering and Industrial Aerodynamics, 2020.
- Chawdhury, S., and Morgenthal, G.: A partitioned solver to simulate large-displacement fluid–structure interaction of thin plate systems for vibration energy harvesting. Journal of Computers & Structures 224 (2019), pp. 106110.
- Chawdhury, S., Milani, D., Morgenthal, G.: Modeling of pulsating incoming flow using vortex particle methods to investigate the performance of flutter-based energy harvesters. Journal of Computer & Structures 209 (2018), pp. 130-149.
- Chawdhury, S., Morgenthal, G.: Numerical simulations of aeroelastic instabilities to optimize the performance of flutter-based electromagnetic energy harvesters. Journal of Intelligent Material Systems and Structures, 29(4) (2018), pp. 479-495.
- Chawdhury, S., Morgenthal, G.: Flow Reproduction using Vortex particle Methods for Simulating Wake Buffeting Response of Bluff Structures. Journal of Wind Engineering and Industrial Aerodynamics 151 (2016), pp. 122-136.

Conference articles

- Morgenthal, G., Kavrakov, I., Chawdhury, S., Advancements in vortex particle methods for aeroelastic analysis of line-like structures, Baustatik–Baupraxis 14, 2020, Universität Stuttgart, 2020.
- Chawdhury, S., Morgenthal, G., A pseudo three-dimensional multi-slice numerical model to simulate wind-induced vibration of thin-walled roof systems, 7th ECCOMAS Thematic Conference on Computational Methods in Structural Dynamics and Earthquake Engineering (COMPDYN 2019), Crete, Greece, 2019.
- Chawdhury, S., Morgenthal, G., Numerical investigation of flexible beams for electromagnetic energy harvesting under the wakes from upstream cylinder, VII International Conference on Computational Methods for Coupled Problems in Science and Engineering, Rhode Island, Greece, 2017.
- Chawdhury, S., Morgenthal, G., Simulation of Aeroelastic Instabilities to Evaluate the Power Output of Flutter-based Electromagnetic Energy Harvesters, IABSE Spring Conference, Guangzhou, 2016.
- Chawdhury, S., Morgenthal, G., Flow Reproduction Using Vortex Particle Methods for Wake Buffeting Analysis of Bluff Structures, ICFMA 2015, 17th International Conference on Fluid Mechanics and Applications, Paris, 2015.
- Tolba, K. I., Morgenthal, G., Chawdhury, S., Wake flow reproduction in Vortex Particle Methods for simulating buffeting response, 6th International Symposium on Computational Wind Engineering, Hamburg, 2014.